

Topical Review

Recent progress in thin-film growth of Fe-based superconductors: superior superconductivity achieved by thin films

Masahito Sakoda¹, Kazumasa Iida²  and Michio Naito¹ 

¹ Department of Applied Physics, Tokyo University of Agriculture and Technology, Koganei, Tokyo 184-8588, Japan

² Department of Materials Physics, Nagoya University, Chikusa-ku, Nagoya 464-8603, Japan

E-mail: minaito@cc.tuat.ac.jp

Received 1 December 2017, revised 27 February 2018

Accepted for publication 11 April 2018

Published 27 July 2018



Abstract

The discovery of high- T_c superconductivity in Fe-based superconductors pioneered by Kamihara *et al* (2008 *J. Am. Chem. Soc.* **130** 3296–7) has triggered worldwide research efforts in both science and technology. High-quality epitaxial thin films of Fe-based superconductors are required to develop Fe-based superconducting devices, such as Josephson junctions and superconducting quantum interference devices, and also to develop Fe-based superconducting coated conductors (tapes) with high J_c under strong magnetic fields. Epitaxial films are also required for basic research to explore the intrinsic properties of Fe-based superconductors, since sizable bulk single crystals are difficult to grow for some of the Fe-based superconductors such as $LnFeAs(O,F)$ (Ln : lanthanoid element). There are several families of Fe-based superconductors: $Fe(Se,Te)$ with $T_c \sim 15$ K, $LiFeAs$ with $T_c \sim 18$ K, $(Ae,K)Fe_2As_2$ (Ae = alkaline earth element) with $T_c \sim 38$ K for $Ae = Ba$, and $LnFeAs(O,F)$ with $T_c \sim 55$ K for $Ln = Nd$ or Sm . Increasing the number of elements in compounds, the T_c becomes higher. Simultaneously, thin-film growth becomes more difficult in principle, and it was not imagined at the beginning of the research that thin-film growth of five-element compounds, $LnFeAs(O,F)$, could be realized quickly. At present, T_c as high as 58 K exceeding the highest T_c ever reported for bulk samples and high critical current density (J_c) over 3 MA cm^{-2} are obtained in $SmFeAs(O,F)$. In this topical review, we present an overview of the progress in thin-film growth of representative Fe-based superconductors over a decade, including a detailed description of the growth recipes for each family using molecular beam epitaxy or pulsed laser deposition. Furthermore, we present recent hot topics, such as monolayer $FeSe$ with T_c much higher than bulk T_c , though how high T_c can be reached has not been established. Other examples making use of the advantages specific to thin films such as stabilization of quasi-equilibrium phases, enhancement of T_c by epitaxial strain, etc will also be described.

Keywords: Fe-based superconductor, molecular beam epitaxy, pulsed laser deposition, thin film, pinning, monolayer, electric-double-layer transistor

(Some figures may appear in colour only in the online journal)

1. Introduction

Ten years have passed since the discovery of high- T_c superconductivity in Fe-based superconductors pioneered by Kamihara *et al* (2008). This discovery has had a considerable impact on the community of superconductivity for a number of reasons. The first is that the T_c of ~55 K is the second highest superconducting transition temperature in ambient pressure, next to the T_c of ~140 K of copper oxides.³ The second is that the key element in these superconducting compounds is Fe. Fe had been believed to be incompatible with superconductivity in most cases and, therefore there had only been very limited efforts in the past to look for superconducting materials containing Fe. Hence, it is interesting from a physics point of view to clarify the role of Fe in high- T_c superconductivity. The third is the variety of materials. Not only FeAs tetrahedron layers but also Fe-(As,P) or (Fe,Co)-As or Fe-(Se,Te) layers show high- T_c superconductivity. This is in contrast to cuprates, in which the CuO₂ planes are prerequisite for high- T_c superconductivity. Furthermore, it has turned out from the extensive efforts in the search for materials following the first discovery that there are rich structural variations, namely, plenty of block layers possible.

In recent years, significant efforts have also been made for the growth of single crystals and epitaxial films of Fe-based superconductors in order to acquire more reliable experimental data. For some Fe-based superconductors such as (Ba,K)Fe₂As₂, (Sr,K)Fe₂As₂, EuFe₂As₂, BaFe₂(As,P)₂, Ba(Fe,Co)₂As₂, LiFeAs, Na_{1-δ}FeAs, and Fe(Se,Te) it has been demonstrated that high-quality and sizable single crystals can be grown rather easily by the (self-)flux method. But single-crystal growth of other compounds is not easy. For example, the growth of SmFeAs(O,F) requires high pressure (~3 GPa) and high temperature (1350 °C–1450 °C), and the crystals thus obtained are typically ~1 mm in the *ab* plane (Karpinski *et al* 2009, Zhigadlo *et al* 2012). Remarkable progress has also been achieved in thin-film growth over these 10 years, the details of which we present in this review article.⁴ There are three purposes to growing high-quality films: basic research, wire (tape) application, and electronics application. The first can be demonstrated in the case of SmFeAs(O,F) as mentioned above. For this material the growth of epitaxial films may be easier, and the size of epitaxial films are much bigger (~10 × 10 mm) in the *ab* plane. Similar situations have been encountered in cuprates and MgB₂. In recent years, high-quality epitaxial films of novel superconductors have played a tremendous role in various fundamental experiments such as ordinary transport and magnetotransport (including quantum oscillations), optics in a wide frequency range from terahertz/far-infrared to ultraviolet (Chanda *et al* 2014), photoemission and x-ray

³ T_c ~ 200 K has recently been reported for H₃S under very high hydrostatic pressure (~200 GPa) (Drozdov *et al* 2015).

⁴ Especially in Japan, the ‘Transformative Research Project on Iron Pnictides’ (TRIP) led by the Japan Science and Technology Agency played a key role at the very initial stage of the thin-film research for Fe-based superconductors (2008–2011). Without this project, the present technical level of the thin-film growth of Fe pnictides/chalcogenides would not have been achieved. One of the authors (M N) joined this project.

absorption spectroscopy (Yamamoto *et al* 2004a, Oyanagi *et al* 2007, 2012), tunneling spectroscopy (Ueda *et al* 2005, Chen *et al* 2008), μ SR (Kojima *et al* 2014), penetration depth (Skinta *et al* 2002a, 2002b, Kim *et al* 2003), and critical current density measurements (Iida *et al* 2013b). Moreover, the use of thin films has enabled advanced experiments based on their advantages and possibilities, which cannot be explored in single crystals. They include strain and interface effects, dimensionality control via artificial layering, and introduction of pinning centers associated to the specific film growth mode or to particle additions. Finally, carrier doping by field-effect transistors, which has recently become a quite active research field, can be carried out almost exclusively on thin films.

With regard to the second wire application, Fe-based superconductors are favorable for high-field wire applications for several reasons: (i) high upper critical field (H_{c2}) and low anisotropy, (ii) robust grain boundaries, and (iii) acceptance of high density artificial defects. Hence, high performance of thin films of Fe-based superconductors on technical substrates and power-in-tube processed superconducting wires has been demonstrated. In this review article, we summarize the transport critical current properties of Fe-based superconducting thin films on various substrates as well as technical substrates and also discuss the pinning mechanisms.

With regard to the third electronics application, we should recognize the current situation correctly. At present, cuprates have the highest T_c . One may ask why we need to develop Fe-based Josephson junctions (JJs) in such situations. In the case of cuprates, the research on thin-film growth started immediately after their discovery (1987). The initial aim of the research was to build up the scientific and technological foundation of superconducting electronics operating at 77 K. At that time, there was no technique established to grow complex oxides such as high- T_c cuprates. So everyone started by growing thin films of YBa₂Cu₃O₇, which was similar to the initial situations in the research of Fe-based superconductors. During 1987–1990, there was remarkable progress in the growth of cuprates films, and the technical level reached a peak in early 1990s. Based on such mature thin-film technologies, the research then progressed to the fabrication of integrated JJ circuits employing a multilayer structure. In spite of enormous efforts worldwide over more than 10–15 years, however, cuprate-based JJ technology has not yet been completed. We still rely on the Nb-based JJ technology although the operating temperature of Nb JJs is as low as 4.2 K. So it is important to develop a reliable and robust technology to fabricate JJs operating at >20 K. The candidate materials may be MgB₂ and Fe-based superconductors. JJs are important not only in application to fabricate superconducting devices but also in basic science to probe the unconventional nature of pairing (*d*, *p*, *s*_±, multi-gap, etc), as applied to cuprates more than two decades ago (Tsuei *et al* 1994, Tsuei and Kirtley 2000). High-quality Fe-based JJs may explore new possibilities in such a direction (Golubov and Mazin 2012), and the preliminary work has already been reported (Chen *et al* 2010).

There are several families of Fe-based superconductors. Among them, *Ln*FeAs(O,F) (*Ln* = lanthanide element), doped *Ae*Fe₂As₂ (*Ae* = alkaline earth element), and Fe*Ch* (*Ch*: chalcogen) are the most intensively examined for

growing thin films. In this topical review, we present an overview of the progress in the thin-film growth of these representative Fe-based superconductors over a decade, including the detailed description of the growth recipes by molecular beam epitaxy (MBE) or pulsed laser deposition (PLD). The choice of substrates suitable to Fe-based superconducting films is also an important issue and is discussed in detail. Furthermore, we present recent hot topics, such as monolayer FeSe with T_c much higher than bulk T_c . Some other examples making use of advantages specific to thin films such as stabilization of quasi-equilibrium phases, enhancement of T_c by epitaxial strain, controlling T_c by piezoelectric substrates, etc will also be described. This review article is organized as follows. It starts in section 2 by the basic physics and chemistry of Fe-based superconductors, including the crystal structures, electronic phase diagram, elemental band structure, pairing mechanisms, etc. In section 3, the details of our molecular beam epitaxy technique of Fe-based superconductors are described, including the substrate issue. In sections 4–6, the growth of the $LnFeAs(O, F)$, doped $AeFe_2As_2$, and $FeCh$ families are described respectively, including our results and also representative results of other groups. Section 7 serves as a summary. Several review articles and monographs have been published. Some of them are focused on thin-film synthesis and applications (Hiramatsu *et al* 2009, 2012, Li *et al* 2011, Tanabe and Hosono 2012, Mele 2012, Haindl *et al* 2014, Sadovskii 2016, Imai *et al* 2017, Hosono *et al* 2017), which should also be referred to. There is also a review article of Josephson effects in Fe-based superconductors (Seidel 2011). More general ones include Izyumov and Kurmaev 2010, Paglione and Greene 2010, Mizuguchi and Takano 2010, Johnston 2010, Johrendt *et al* 2011, Hirschfeld *et al* 2011, Hosono and Kuroki 2015, Hosono *et al* 2015.

2. Basic physics and chemistry of Fe-based superconductors

2.1. Crystal structure

2.1.1. Crystal structures of the representative families. The first high- T_c ($T_c > 20$ K) iron-based superconductor is LaFeAs (O,F) with $T_c \sim 26$ K discovered by Kamihara *et al* (2008). The compounds have a ZrCuSiAs-type crystal structure (space group $P4/nmm$), as shown in figure 1(a). The same group (Hosono group) discovered rather low- T_c Fe-based superconductors such as LaFePO ($T_c \sim 4$ K) (Kamihara *et al* 2006), LaNiPO ($T_c \sim 3$ K) (Watanabe *et al* 2007), and LaNiAsO ($T_c = 2.4$ K) (Watanabe *et al* 2008) during 2006–2007. Before these works, the group was investigating transparent *p*-type oxychalcogenide semiconductors such as LaCuSO, of which LaFeAs(O,F) is isostructural (Hosono 2007). Soon after the discovery by Kamihara *et al*, the T_c was increased up to 55 K by replacement of a lanthanoid element (Ln) from La to Nd (Ren *et al* 2008a, 2008c) and to Sm (Ren *et al* 2008b, 2008c). We call these materials the ‘1111’ compounds in this review article, according to the atomic ratio. In the 1111 compounds,

anti-fluorite (or tetrahedron) Fe_2Pn_2 layers (Pn : pnictogen) and fluorite $Ln_2(O,F)_2$ layers stack alternately as can be seen in figure 1(a). The quaternary silicide arsenides ZrCuSiAs and HfCuSiAs were first reported in 1974 by Johnson and Jeitschko (1974). There were also some works performed on ZrCuSiAs-type Fe-based and related compounds before the works by the Hosono group (Kamihara *et al* 2006, 2008, Watanabe *et al* 2007, 2008). For example, Zimmer *et al* (1995) synthesized $LnFePO$, $LnRuPO$, and $LnCoPO$ and characterized their structures. But the superconductivity at $T_c \sim 4$ K of LaFePO was overlooked at that time.

The discovery of $LnFeAs(O,F)$ inspired strong interest in the search for new Fe-based superconductors with different crystal structures, and as a result, many families have been found over a short period of time. One representative family found in the quite early stage (May 2008) are the compounds, $(Ae,A)Fe_2As_2$ (A : alkaline element), called the ‘122’ compounds (Rotter *et al* 2008a, 2008b, Sasmal *et al* 2008). The highest T_c is ~ 38 K in $Ba_{0.65}K_{0.35}Fe_2As_2$. The compounds have the ThCr₂Si₂-type crystal structure (space group $I4/mmm$), as shown in figure 1(b). In the 122 compounds, tetrahedron Fe_2Pn_2 layers and plane Ae layers stack alternately. It is known that there are many superconducting compounds with the ThCr₂Si₂ structure. One well-known example is the ‘heavy fermion’ superconductor, CeCu₂Si₂, although its T_c is low, around 0.6 K. The $AeFe_2P_2$ compounds were first synthesized by Mewis (1980) but with no indication of superconductivity. Jeitschko *et al* (1987) reported new ThCr₂Si₂-type phosphides and arsenides with ruthenium (Ru) and osmium (Os) as the transition metal component (note that Ru and Os are located in the same column of the periodic table as Fe). They obtained $T_c \sim 4.1$ K for LaRu₂P₂, which was the highest of the ThCr₂Si₂-type compounds at the time. In the same article, they also reported the synthesis of AeRu₂P₂, AeRu₂As₂, AeOs₂P₂, and AeOs₂As₂. They examined the occurrence of superconductivity in these compounds, but no superconductivity was found down to 1.8 K. Some time later (1993), the nickel borocarbides such as LuNi₂B₂C and YPd₂B₂C, were shown to have relatively high T_c (Mazumdar *et al* 1993, Cava *et al* 1994a, 1994b). The borocarbides have a modified ThCr₂Si₂ structure (called the YNi₂B₂C structure), in which small carbon atoms occupy the interstitial site in the Th layer. The highest T_c is ~ 23 K in YPd₂B₂C. Their pairing mechanism, though not conclusive, has been regarded as a conventional electron–phonon interaction. In the $LnNi_2B_2C$ borocarbides, it has been claimed that T_c is sensitive to the B–Ni–B bond angle in the Ni₂B₂ tetrahedron (Mattheiss *et al* 1994, Siegrist *et al* 1994). The same trend appears to hold in Fe-based superconductors. Fe-based borocarbide superconductors instead of Ni-based ones, if synthesized, may certainly shed light on the connection of the pairing mechanism between superconducting borocarbides and Fe pnictides.

Another representative family is $FeCh$, called the 11 compounds. The superconductivity in FeSe ($T_c \sim 8.5$ K) (Hsu *et al* 2008) and successively $FeSe_{0.5}Te_{0.5}$ ($T_c \sim 14$ K) (Yeh *et al* 2008) were discovered by the Wu group soon after the announcement of the discovery of superconductivity in

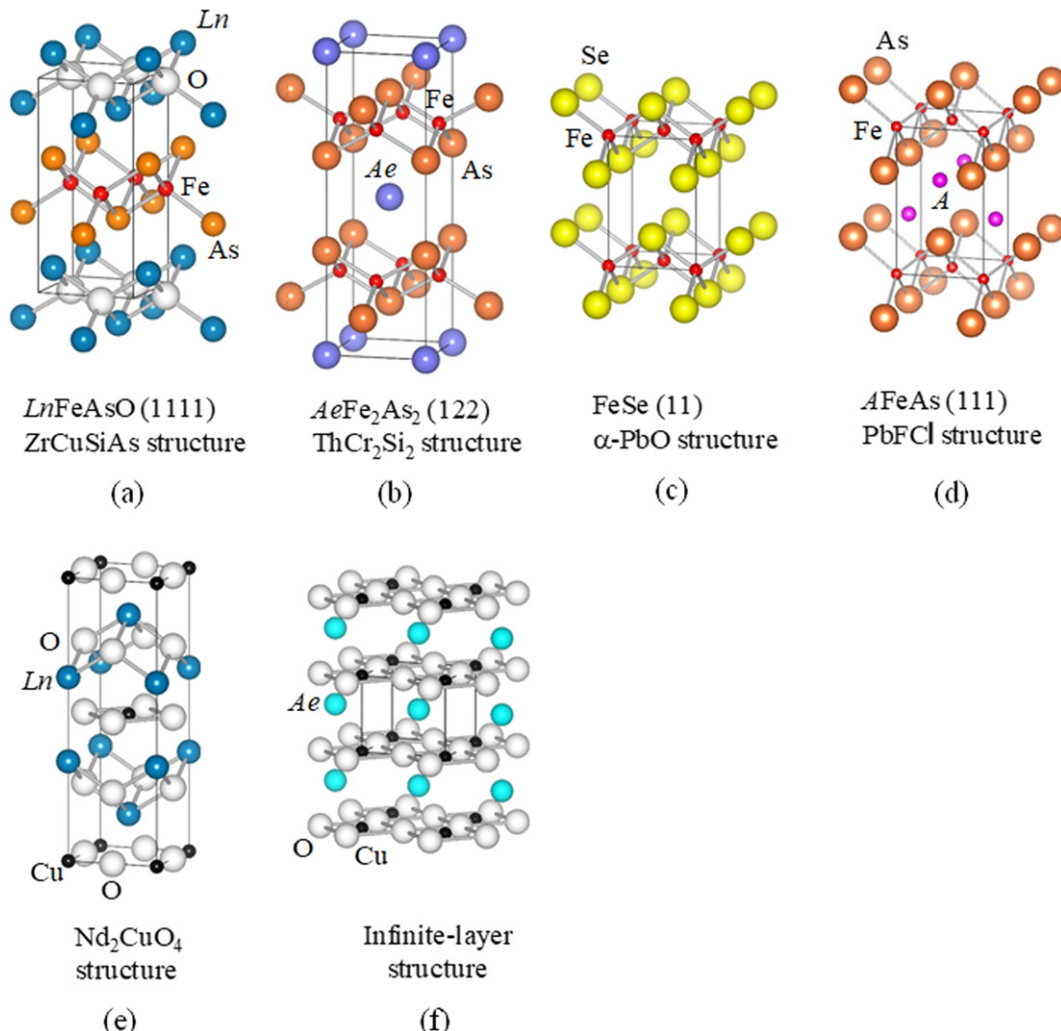


Figure 1. Crystal structures of the representative families of Fe-based superconductors: (a) 1111, (b) 122, (c) 11, and (d) 111 families. Some of the copper oxides have crystal structures similar to those of Fe-based superconductors: (e) Nd_2CuO_4 and (f) infinite-layer structures.

LaFeAs(O,F) by the Hosono group. At the beginning, it appeared that the T_c in Fe chalcogenides might not be as high as the T_c in Fe pnictides. But the T_c of FeSe can be raised substantially with the application of hydrostatic pressure and reaches 37 K at 10 GPa (Mizuguchi *et al* 2008, Medvedev *et al* 2009). The 11 compounds have the so-called (anti)- α -PbO-type crystal structure (space group $P4/nmm$). In these compounds, as shown in figure 1(c), divalent Fe ions are surrounded tetrahedrally by divalent chalcogen ions instead of trivalent pnictogen ions as seen in Fe pnictides. The structure of FeCh is regarded as a successive stack of neutral tetrahedron Fe_2Ch_2 layers by van der Waals interaction. It is similar in structure to the Fe_2Pn_2 layers in Fe pnictides, which, on the contrary, are negatively charged with positively charged block layers inserted in between. They are well-known compounds, but their superconductivity has never been examined since magnetic Fe was thought to be competitive with superconductivity. In FeCh, large molecules such as ethylenediamine (EDA) can be intercalated in the presence of alkaline ions (Li^+ , Na^+ etc) between neutral FeCh

layers (Burrard-Lucas *et al* 2013, Noji *et al* 2014). The intercalation raises the T_c up to 45 K.

The compounds closely related to the 11 family in the structure is AFeAs (A = alkaline element), called the 111 compounds. The structure of superconducting LiFeAs ($T_c = 18$ K) was first determined by Tapp *et al* (2008), and is shown in figure 1(d). It is referred to as the (anti-)PbFCl structure. The framework of the structure is the same as that of FeCh. The bare framework of Fe_2As_2 layers are not stable by itself but stabilized by small Li ions inserted at the interstitial site. The material with the highest T_c of the 111 family is $\text{Na}_{1-\delta}\text{FeAs}$, whose T_c reaches 25 K although it is strongly sample-dependent. The compounds of the 111 family are bulk superconductors in undoped, stoichiometric form. This feature is unique in that in other compounds (1111 and 122 families) critical to the high- T_c Fe_2As_2 layers is the need for a sufficient amount of chemical doping.

2.1.2. Chemical bonding. As seen in section 2.1.1, all of the Fe-based superconductors have related layered (quasi-2D) crystal

structures formed by successive stacking of blocks. One of the blocks common for all phases is isostructural (Fe_2Pn_2 or Fe_2Ch_2) molecular layers formed by FePn_4 or FeCh_4 tetrahedra. The other block is LnO layers in LnFeAs(O,F) , Ae layers in $(\text{Ae},\text{K})\text{Fe}_2\text{As}_2$, and no layer in FeCh . In this subsection, we describe the aspect of chemical bonding in the Fe-based superconductors. We take LnFeAsO as a representative example. The formal valence is $(\text{Ln}^{3+}\text{O}^{2-})(\text{Fe}^{2+}\text{As}^{3-})$, so there is an electron transfer between layers $[\text{LnO}]^{1+} \rightarrow [\text{FeAs}]^{1-}$. In the Ln_2O_2 layers, the $\text{Ln}-\text{O}$ bond is primarily ionic whereas in the Fe_2As_2 layers, the $\text{Fe}-\text{As}$ bond is predominantly covalent (partially ionic) as can be inferred from the directional bonding, and the $\text{Fe}-\text{Fe}$ bond is metallic. LnFeAsO can be regarded roughly as a stack of ionic $[\text{Ln}_2\text{O}_2]$ and covalent $[\text{Fe}_2\text{As}_2]$ layers (Shein and Ivanovskii 2009).

The situation somewhat resembles that in cuprates. One of the parent compounds of high- T_c cuprates, Nd_2CuO_4 , whose crystal structure is called as the ‘ Nd_2CuO_4 ’ structure by its own name, can be regarded as a stack of ionic $[\text{Nd}_2\text{O}_2]^{2+}$ and covalent $[\text{CuO}_2]^{2-}$ layers as can be seen in figure 1(e) (Müller-Buschbaum and Wollschläger 1975). The ionic layers in both LnFeAsO ($\text{Ln} = \text{Nd}$) and Nd_2CuO_4 are the same (fluorite $[\text{Nd}_2\text{O}_2]^{2+}$ layers), but the covalent layers are different: Fe_2As_2 tetrahedron layers versus square-planar CuO_2 layers. Both NdFeAsO and Nd_2CuO_4 can be superconducting by partial substitution of O by F: $T_c \sim 55$ K in NdFeAs(O,F) and $T_c \sim 27$ K in $\text{Nd}_2\text{Cu(O,F)}_4$ (James *et al* 1989). Similarly, one can correspond the AeFe_2As_2 family of Fe pnictides to the infinite-layer AeCuO_2 family of cuprates as shown in figure 1(f) (Siegrist *et al* 1988). In this case, AeFe_2As_2 can be superconducting by partial substitution of Ae by A (hole doping) whereas AeCuO_2 can be superconducting by partial substitution of Ae by Ln (electron doping) (Smith *et al* 1991).

2.2. Electronic phase diagram

The original crystal structures (at high temperatures ($T > 200$ K)) of the parent Fe pnictides, such as LnFeAsO and AeFe_2As_2 , are tetragonal as shown in section 2.1.1. But as the temperature is lowered, they exhibit a structural phase transition to an orthorhombic one at T_{struc} and subsequently an antiferromagnetic (AFM) ordering transition at T_N ($\leq T_{\text{struc}}$). Both the T_{struc} and T_N decrease with the doping in both the 1111 and the 122 compounds. With further doping, the superconductivity sets in at the critical dopant concentration (x_c) and is optimized with the highest T_c at x_{opt} . The situation in Fe pnictides resembles that in cuprates, in that the parent compounds are AFM and the superconductivity appears by suppressing the AFM ordering by doping. One difference is that the parent Fe pnictides stay metallic down to low temperatures (even below T_N) whereas most of the parent copper oxides are a Mott–Hubbard insulator (or more strictly a charge-transfer insulator).⁵

Figure 2(a) shows a phase diagram by Huang *et al* (2008a) of $\text{LaFeAsO}_{1-x}\text{F}_x$ ($T_c^{\max} = 26$ K). In this article, the T_{struc} and

T_N were determined from the neutron diffraction experiments on polycrystalline samples. Luetkens *et al* (2008) obtained almost identical results for $\text{LaFeAsO}_{1-x}\text{F}_x$. In the experiments by Luetkens *et al*, μ SR and Mössbauer spectroscopy were employed as magnetic local probes whereas x-ray diffraction (XRD) experiments to detect the orthorhombic splitting have been used as a structural probe. As can be seen from figure 2(a), the T_{struc} is ~ 160 K in the parent LaFeAsO and gradually decreases with the F concentration, x . The T_{struc} suddenly drops to zero at $x \approx 0.05$. The T_N is ~ 140 K in the parent LaFeAsO and gradually decreases in parallel to the T_{struc} . The T_N also drops suddenly to zero at $x \approx 0.04$, which is slightly lower than $x \approx 0.05$ for T_{struc} . The data in figure 2(a) indicates that a long-range AFM order disappears as a function of doping before superconductivity appears. On the other hand, the orthorhombic phase extends into the superconductivity dome in $\text{LaFeAsO}_{1-x}\text{F}_x$.

The phase diagrams for some other LnFeAs(O,F) have been reported, although there is no systematic data available on the Ln dependence. The observation in $\text{LaFeAsO}_{1-x}\text{F}_x$ is typical for many LnFeAs(O,F) compounds, but the fine details differ for each Ln and also some discrepancies exist among the reports by different groups (see figure 2). Figure 2(b) shows the phase diagram for $\text{CeFeAsO}_{1-x}\text{F}_x$ ($T_c^{\max} = 46$ K) and (c) and (d) for $\text{SmFeAsO}_{1-x}\text{F}_x$ ($T_c^{\max} = 56$ K). In $\text{CeFeAsO}_{1-x}\text{F}_x$ (Zhao *et al* 2008), the drop in both T_{struc} and T_N is not discontinuous, which is different from the behavior of $\text{LaFeAsO}_{1-x}\text{F}_x$. The T_{struc} decreases gradually and disappears at around $x = 0.1$ when superconductivity is already well developed. On the other hand, the T_N rapidly and essentially vanishes before the emergence of superconductivity for $x > 0.06$. The results again indicate that although superconductivity in $\text{CeFeAsO}_{1-x}\text{F}_x$ can survive in the low-temperature orthorhombic phase, it appears to compete with the static magnetic order.

A more complex situation takes place in $\text{SmFeAsO}_{1-x}\text{F}_x$. In figures 2(c) and (d), the phase diagrams reported by the two groups are compared. Figure 2(c) by Maeter *et al* (2012) is roughly similar to the figure 2(b) for $\text{CeFeAsO}_{1-x}\text{F}_x$. In contrast, figure 2(d) by Martinelli *et al* (2011) is considerably different from the others (Margadonna *et al* 2009a, Kamihara *et al* 2010). The T_{struc} exhibits a very gradual decrease with x and is kept as high as 125 K at $x = 0.22$. In the case of $\text{SmFeAsO}_{1-x}\text{F}_x$, the possible coexistence of superconductivity and magnetism in the 1111 compounds is a delicate and controversial issue.

Next we turn to the phase diagram of the 122 compounds. There are many similarities in the phase diagram between the 1111 and 122 compounds. For example, the parent BaFe_2As_2 shows structural and magnetic transitions simultaneously at $T_{\text{struc}} = T_N = 142$ K (Rotter *et al* 2008b, Huang *et al* 2008b, Johrendt and Pöttgen 2009). The substitution of either of K for Ba or P for As or Co for Fe drives BaFe_2As_2 superconducting. The first case corresponds to hole doping to the Fe_2As_2 layers, the second to isovalent doping, and the third to electron doping. The T_c^{\max} is 38 K for K substitution, 30 K for P substitution (Nakajima *et al* 2012), and 25 K for Co substitution (Nandi *et al* 2010). The phase diagrams of these compounds are

⁵ An exception has recently been found, namely, parent Ln_2CuO_4 with the Nd_2CuO_4 structure is metallic and superconducting (Naito *et al* 2016).

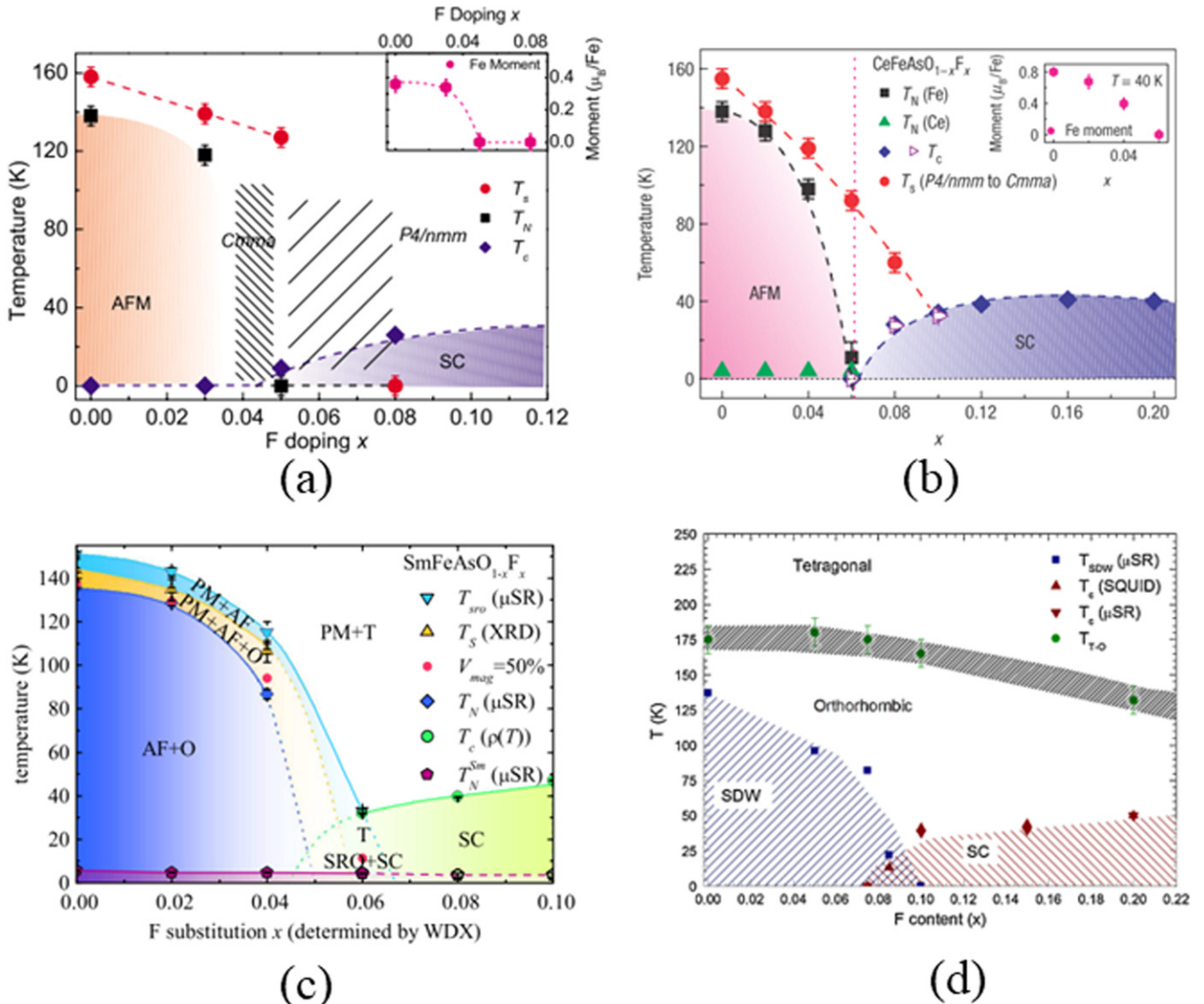


Figure 2. Electronic phase diagram of $Ln\text{FeAsO}_{1-x}\text{F}_x$ with different Ln : (a) $Ln = \text{La}$. Reprinted figure with permission from Huang *et al* (2008a), Copyright 2008 by the American Physical Society. (b) $Ln = \text{Ce}$. Reprinted by permission from Springer Nature: Nature Materials (Zhao *et al* 2008), Copyright 2008. (c) $Ln = \text{Sm}$ (reproduced with permission from Maeter *et al* (2012), and (d) $Ln = \text{Sm}$ (Martinelli *et al* 2011). Reprinted figure with permission from Martinelli *et al* (2011), Copyright 2011 by the American Physical Society.

summarized in figure 3. In the 122 family, $T_{\text{struc}} = T_N$ or $T_{\text{struc}} \geq T_N$ (i.e., T_N is nearly equal to but only slightly lower than T_{struc}) holds, which is a behavior distinguished from the 1111 family, where T_N is lower than T_{struc} . Furthermore, there is a substantial range of x in which superconductivity and the magnetic ordering do coexist in the 122 compounds. If the regions of the magnetic and the superconducting phases do overlap, the question is whether they coexist in the same volume or side by side due to mesoscopic phase separation. If the former is the case, the pairing via spin fluctuation is most likely in the Fe-based superconductors. However, the study of the pressure effect for BaFe_2As_2 appears to indicate definitely that the superconducting and magnetic phases separate (Yamazaki *et al* 2010). At present the issue is still being debated and is unsettled.

The phase diagram of the 11 compounds somewhat differs from those of the 1111 and 122 compounds, and this will

be addressed in section 6.5 in conjunction with the suppression of phase separation via thin-film synthesis.

2.3. Electronic structure

2.3.1. Band structure. Band calculations have been done independently by several groups immediately after high- T_c superconductivity was found in LaFeAs(O,F) . Even the first-principles band calculation was done by Lebègue (2007) for LaOFeP ($T_c \sim 4$ K) in 2007 prior to the discovery of LaFeAs(O,F) . The results are roughly in agreement with one another. Here we discuss the essence of the electronic structure of Fe-based superconductors based on the results on LaFeAsO by Kuroki *et al* (2008, 2009), Hosono and Kuroki (2015). They performed first-principles band calculation with the Quantum-ESPRESSO package (Giannozzi *et al* 2009), and then constructed the maximally localized Wannier functions.

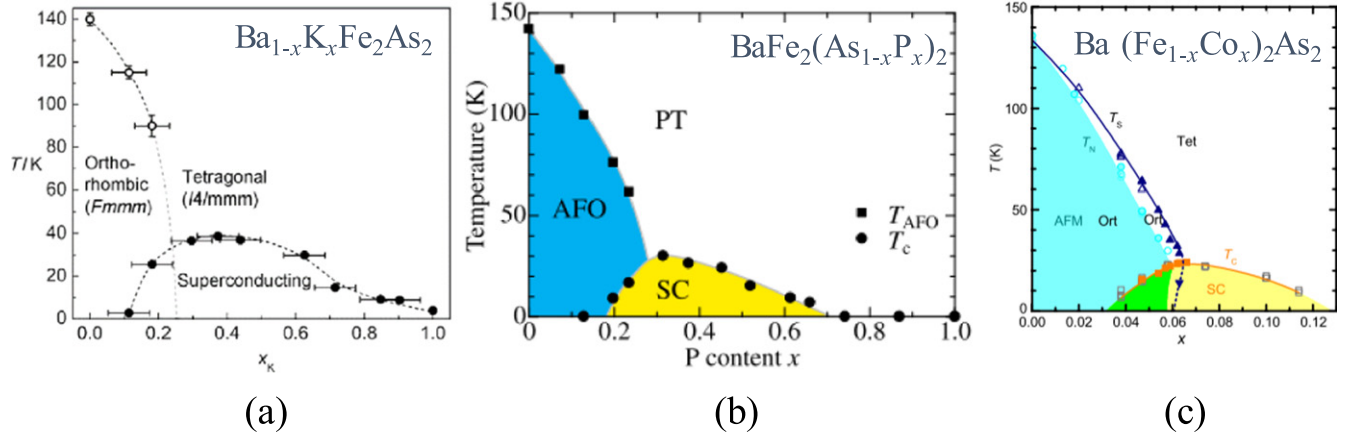


Figure 3. Electronic phase diagram of the 122 family: (a) $\text{Ba}_{1-x}\text{K}_x\text{Fe}_2\text{As}_2$ (Rotter *et al* 2008b (John Wiley & Sons. Copyright © 2008 WILEY-VCH Verlag GmbH & Co. KGaA, Weinheim)), (b) $\text{BaFe}_2(\text{As}_{1-x}\text{P}_x)_2$ (reproduced with permission from Nakajima *et al* 2012), and (c) $\text{Ba}(\text{Fe}_{1-x}\text{Co}_x)_2\text{As}_2$. Reprinted figure with permission from Nandi *et al* (2010), Copyright 2010 by the American Physical Society. $\text{Ba}_{1-x}\text{K}_x\text{Fe}_2\text{As}_2$ corresponds to hole doping to the Fe_2As_2 layers, $\text{BaFe}_2(\text{As}_{1-x}\text{P}_x)_2$ to isovalent doping, and $\text{Ba}(\text{Fe}_{1-x}\text{Co}_x)_2\text{As}_2$ to electron doping.

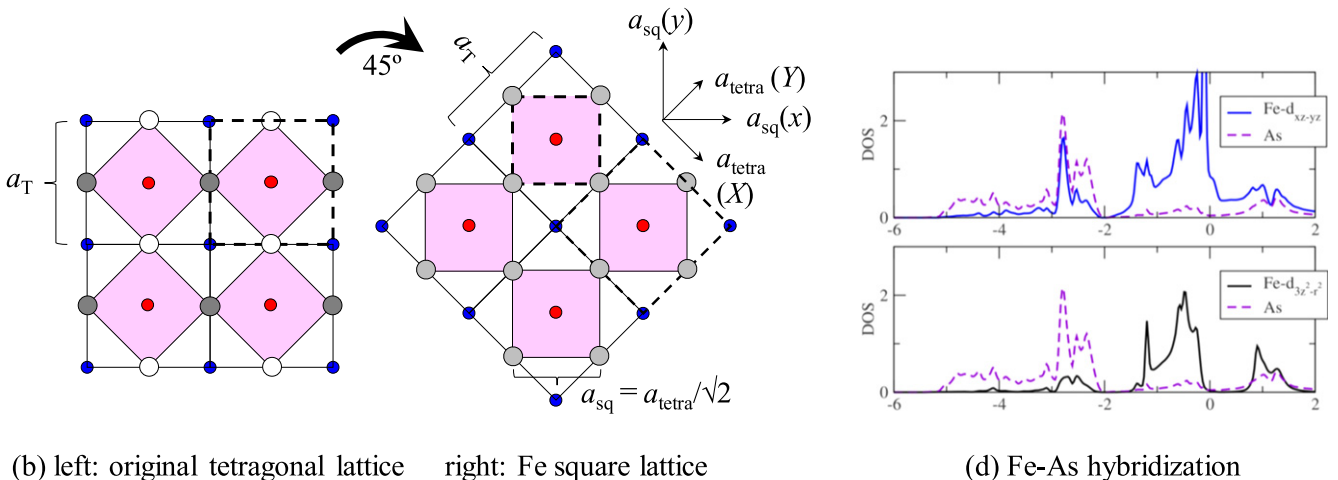
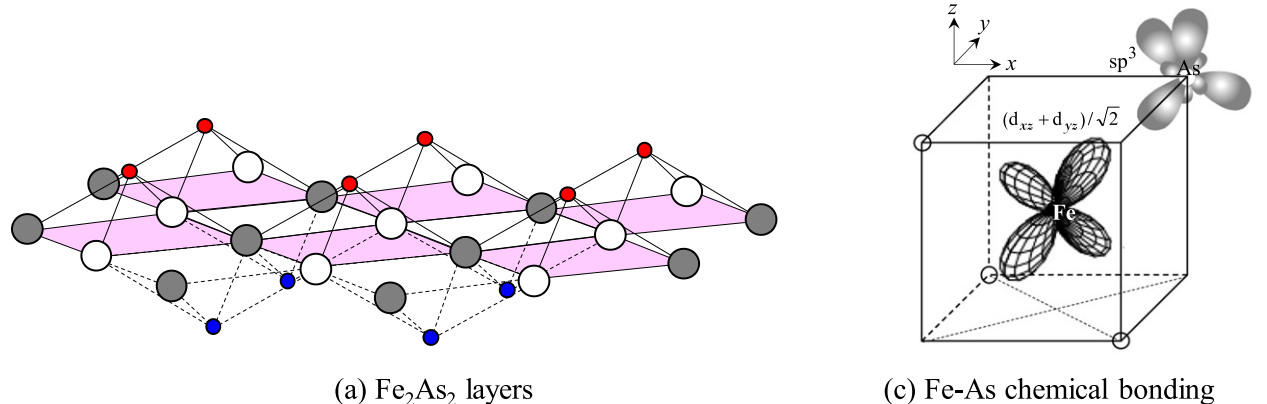


Figure 4. Basic structural chemistry of LaFeAsO: (a) Fe_2As_2 layer, (b) relation between original tetragonal lattice and Fe square lattice, (c) schematic picture of chemical bonding between $\text{Fe } 3d_{x^2-y^2}$ and $\text{As } 4sp^3$, (d) partial densities of states of the $\text{Fe-}d$ orbitals (solid lines) and $\text{As-}p$ orbitals (dashed lines). (d) Reprinted figure with permission from Vildosola *et al* (2008), Copyright 2008 by the American Physical Society.

LaFeAsO has a tetragonal layered structure, in which Fe atoms are arrayed on a square lattice. All Fe atoms appear to be equivalent. Because of the tetrahedral coordination of As, however, there are two Fe atoms (marked by white and gray) per unit cell, which are inequivalent from a crystallographical point of view as can be seen in figure 4(a). Each of the two Fe

sites in the unit cell has five orbital symmetries (1: d_{3Z2-R2} , 2: d_{XZ} , 3: d_{YZ} , 4: d_{X2-Y2} , 5: d_{XY} , where X, Y, Z refer to those for the original tetragonal unit cell). So, as a total, ten 3d orbitals appear in the calculated band (ten-band model). This complex situation can somewhat be simplified by noting that each Fe atom has the same local arrangement of other atoms

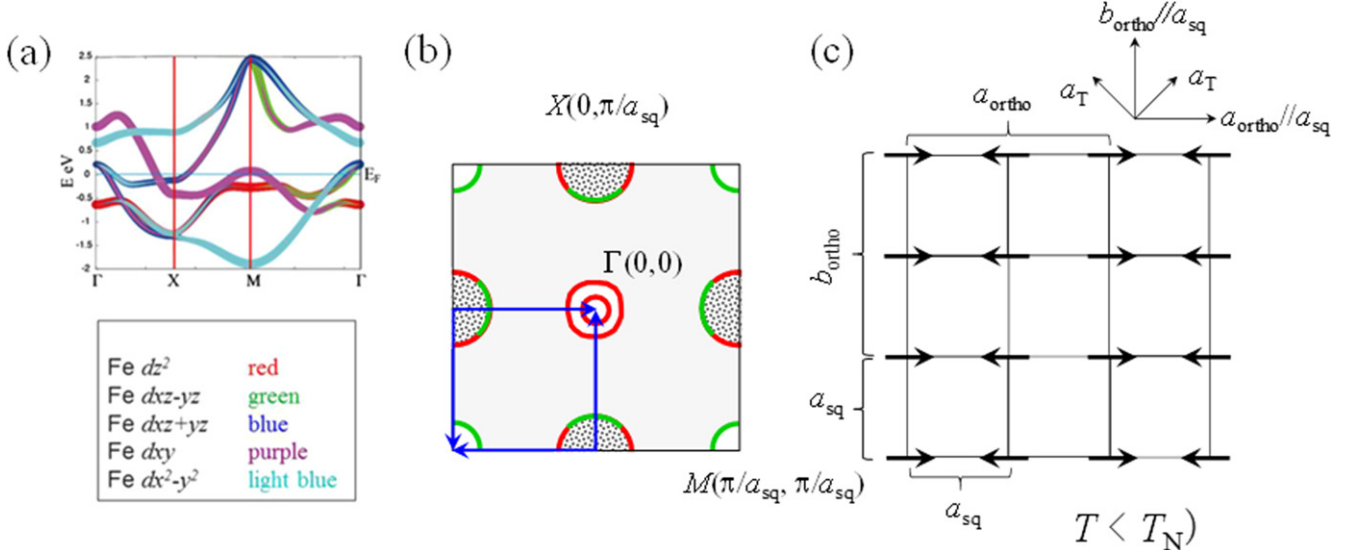


Figure 5. (a) Electronic band structure and (b) Fermi surface for LaFeAsO in the unfolded BZ zone. The Fermi surfaces drawn by red lines have a dominantly d_{xz} and d_{yz} orbital character, while the Fermi surfaces drawn by green lines have a dominantly d_{xy} orbital character. In (c), the spin structure in the SDW phase ($T < T_N$) is demonstrated. (a) and (b) Reprinted from Hosono and Kuroki (2015), Copyright 2015, with permission from Elsevier.

(Pn or Ch) and the two Wannier orbitals in each unit cell are equivalent. Then it is smart to take a unit cell that contains only one orbital per symmetry, which results in an effective five-band model on a square lattice, where the x and y axes are rotated by 45° from $X-Y$ (see figure 4(b)). The Brillouin zone (BZ) is unfolded by this procedure (the BZ area becomes doubled). This is the setting traditionally used in the description of the electronic properties of FeAs-type compounds. The resultant bands and Fermi surface are reproduced in figures 5(a) and (b). In the unfolded BZ, there are two hole pockets at Γ , two electron pockets (four half cylinders) at X , and one hole pocket (four quarter cylinders) at M . The total volume confined within the electron cylinders at X is equal to the sum of the volumes within two hole cylinders at Γ plus one hole cylinder at M and is ~ 0.13 electrons per formula unit (Singh and Du 2008).

Based on the five-band model (five-orbital model), let us now take a more intuitive view of the structure of Fe $3d$ states, which play a major role in the formation of the electronic properties of Fe pnictides. In a free Fe ion in an As tetrahedron, the five-fold degenerate $3d$ orbitals— d_{x2-y2} , d_{3z2-r2} , d_{xz} , d_{yz} , d_{xy} —split into the e_g doublet (d_{x2-y2} , d_{3z2-r2}) and t_{2g} triplet (d_{xz} , d_{yz} , d_{xy}) if the As tetrahedron is regular. In tetrahedral crystal field, the t_{2g} level is higher in energy than the e_g level. Of these five orbitals, the lobes of $d_{xz\pm yz}$ ($d_{xz} \pm d_{yz}$) are directed at As, so substantial hybridization is expected as shown in figure 4(c). On the other hand, the lobes of d_{x2-y2} and d_{3z2-r2} are not directed at As, which can be regarded as non-bonding orbitals. The d_{xy} orbital is in between. Partial contributions of these different orbitals to the total Fe $3d$ density of states have been calculated by Vildosola *et al* (2008) for LaOFeAs. The results are shown in figure 4(d). While the dominant electronic character near the Fermi level is due to Fe, a strong mixing between the $d_{xz\pm yz}$ (and also d_{xy} , which is not shown) and As $4p$ orbitals is

apparent in the range of energy of -3 to -2 eV, where the As $4p$ band is strongly peaked (Haule *et al* 2008). The result can be regarded as arising from their large hybridization of Fe $3d$ orbitals and the As $4p$ orbitals. Such a view can be also supported from the insignificant weight of the d_{x2-y2} and d_{3z2-r2} orbitals in this energy range.

2.3.2. Fermi surface nesting and spin density wave (SDW).

Many of the parent Fe pnictides exhibit structural and magnetic phase transitions successively as described in section 2.2. Here we discuss the long-range AFM structure realized in parent Fe pnictides. The parent compounds show a resistivity anomaly at T_{struc} and T_N but stay metallic in contrast to the parent copper oxides. Therefore, Fe^{2+} spins in Fe pnictides are most probably of a more itinerant character than Cu^{2+} spins in copper oxides, which are supposed to be localized by strong Coulomb repulsion (large Mott–Hubbard U) between electrons. The itinerant character of Fe^{2+} spin is also in accord with its magnetic moment as small as ~ 0.3 – 0.4 μ_B in LaFeAsO (de la Cruz *et al* 2008). In general, one can regard the AFM order in itinerant electronic systems as an SDW, and it is possible to argue the AFM ordering based on the nesting of a Fermi surface. As seen in the band calculations based on the Fe square lattice (figure 5(b)), the Fermi surface consists mainly of two hole pockets (outer and inner) at Γ and two electron pockets at X , which are similar in size (there is one additional hole pocket at M). If the electron pockets at X are shifted by the \mathbf{Q} vector, either $\mathbf{q}_1 = (\pi/a_{\text{sq}}, 0)$ or $\mathbf{q}_2 = (0, \pi/a_{\text{sq}})$, it is almost overlaid with the hole pockets at Γ or M . We call such wave vectors (Q vectors) ‘nesting vectors’ as indicated by the arrows in figure 5(b). The nesting is important in determining the wave-vector dependence of magnetic susceptibility, in general. The generalized susceptibility (or response function) for frequency ω and wave vector \mathbf{q} can be expressed for the simplest non-interacting

electrons as

$$\chi(\mathbf{q}, \omega) = \sum_{\mathbf{q}} \frac{f_{\mathbf{p}} - f_{\mathbf{p}+\mathbf{q}}}{\hbar\omega + \varepsilon_{\mathbf{p}} - \varepsilon_{\mathbf{p}+\mathbf{q}}} = \sum_{\mathbf{q}} \frac{f_{\mathbf{p}}^X - f_{\mathbf{p}+\mathbf{q}}^{\Gamma(\text{or } M)}}{\hbar\omega + \varepsilon_{\mathbf{p}}^X - \varepsilon_{\mathbf{p}+\mathbf{q}}^{\Gamma(\text{or } M)}}, \quad (2.1)$$

where $\varepsilon_{\mathbf{p}}$ and $f_{\mathbf{p}}$ is the energy and Fermi distribution function for the state with the momentum, \mathbf{p} . The static susceptibility, $\chi(\mathbf{q}, \omega \rightarrow 0)$, is enhanced at the nesting vector ($\mathbf{q} = \mathbf{Q}$) and the charge density wave or SDW with the corresponding wave vector is stabilized. In the case of Fe pnictides, an SDW state is stabilized with lattice distortion accompanied. The resultant spin structure is shown in figure 5(c). Since there are two nesting vectors possible, \mathbf{q}_1 and \mathbf{q}_2 , the other spin structure rotated by 90° is possible. The SDW is accompanied by orthorhombic lattice distortion as shown in figure 5(c), with the orthorhombic a -axis parallel to the spin direction and the orthorhombic b -axis perpendicular to it. The a -axis lattice distance is slightly longer than the b -axis lattice distance ($a_{\text{ortho}} = 5.7099 \text{ \AA}$, $b_{\text{ortho}} = 5.6820 \text{ \AA}$ at 2 K in LaFeAsO) (Lynn and Dai 2009).

2.4. Pairing mechanism

Next we give a brief description of the current understanding of the pairing mechanism in Fe-based superconductors. The equation for the superconducting gap, $\Delta(\mathbf{k})$, can be written in the form in momentum space,

$$\Delta(\mathbf{k}) = - \sum_{\mathbf{k}} V(\mathbf{k} - \mathbf{k}') \frac{\tanh[2E(\mathbf{k}')/2k_B T_c]}{2E(\mathbf{k}')} \Delta(\mathbf{k}'), \quad (2.2)$$

where $V(\mathbf{k} - \mathbf{k}')$ is the pairing interaction and $E(\mathbf{k})$ is the dispersion of the quasiparticle excitation (Hosono and Kuroki 2015). In the case of conventional superconductors, the pairing interaction is mediated by phonons, and is attractive ($V < 0$). On the other hand, the pairing interaction is repulsive ($V > 0$) when it is mediated by the spin fluctuation. In the case of $V > 0$, the $\Delta(\mathbf{k})$ has to change the sign to satisfy equation (2.2), such as the d -wave gap in cuprates.

The theoretical models for spin-mediated pairing have dominated over those for the charge-mediated one as the high- T_c mechanism in Fe pnictides since the materials are close to magnetism. As discussed in section 2.3, the SDW-type ordering in the compounds has been explained by the nesting of the hole and electron Fermi surfaces. The same type but dynamic spin fluctuation leads to spin-mediated pairing. This is because the pairing interaction, $V(\mathbf{k} - \mathbf{k}')$, is proportional to spin susceptibility, $\chi_s(\mathbf{q} = \mathbf{k} - \mathbf{k}', \omega)$, (Miyake *et al* 1988), which is enhanced at $\mathbf{q}_1 = (\pi/a_{\text{sq}}, 0)$ or $\mathbf{q}_2 = (0, \pi/a_{\text{sq}})$. The frequency ω should be finite since not static distortion but dynamic fluctuation is important for mediating pairing, but $\hbar\omega$ should be much smaller than the typical electron energy, $\varepsilon_{\mathbf{k}}$. So $\chi_s(\mathbf{k} - \mathbf{k}', \omega = 0)$ may be approximated by $\chi_s(\mathbf{k} - \mathbf{k}', \omega = 0)$. More rigorous random phase approximation (RPA) calculations have been performed by Kuroki *et al* (2008) and showed that $\chi_s(\mathbf{k})$ has peaks around $(k_x, k_y) = (\pi/a_{\text{sq}}, 0)$ and $(0, \pi/a_{\text{sq}})$ as shown in figure 6(a). Figure 6(b) compares schematic images of the

pairing in real space for Fe pnictides and for copper oxides. In Fe pnictides, next-nearest-neighbor pairing takes place with no sign change in the lobes in real space, which is not d -wave pairing but so-called s_{\pm} pairing ($\Delta(\mathbf{k}) = \Delta_0 \cos(k_x a_{\text{sq}}) \cos(k_y a_{\text{sq}})$). The absolute value of $\Delta(\mathbf{k})$ is maximized at $(0, 0)$, $(\pi/a_{\text{sq}}, 0)$, $(0, \pi/a_{\text{sq}})$, $(\pi/a_{\text{sq}}, \pi/a_{\text{sq}})$ in momentum space and the nodes of the gap do not intersect the Fermi surfaces. In copper oxides, in contrast, nearest-neighbor pairing takes place with sign changes in the lobes, which is d -wave pairing ($\Delta(\mathbf{k}) = \Delta_0 [\cos(k_x a) - \cos(k_y a)]$). The absolute value of $\Delta(\mathbf{k})$ is maximized at $(\pi/a, 0)$, $(0, \pi/a)$ and the nodes of the gap intersect the Fermi surfaces.

2.5. Structural parameters controlling T_c

The T_c of Fe-based superconductors ranges from a few to 56 K and shows a strong material dependence. For example, the T_c of $Ln\text{FeAs(O,F)}$ depends strongly on Ln : the T_c increases from La to Sm and decreases from Gd to Dy with a maximum around Sm where $T_c = 56$ K. The situation is quite different from that in cuprates for $Ln\text{Ba}_2\text{Cu}_3\text{O}_7$, which exhibit a little change in T_c ranging from 90 K–96 K. It has been claimed immediately after the discovery of high- T_c superconductivity in Fe pnictides that the material dependence of T_c may be attributed to the difference in the local structure. So far, the As–Fe–As bond angle, α , and the pnictogen height, h_{anion} , from the Fe plane are proposed as the structural parameters controlling the T_c .

2.5.1. T_c versus bond angle. Figure 7(a) is a summary of the T_c as a function of the (Pn or Ch)-Fe-(Pn or Ch) bond angle α (Lee *et al* 2008, 2012). Here the maximum T_c for each system and the corresponding bond angles are plotted to compare the T_c at the optimum doped level. For example, in the 1111 systems, the bond angle α approaches 109.47° at $Ln = Nd$. At this bond angle, the FeAs_4 tetrahedron becomes regular. Obviously, T_c is the highest at $\alpha = 109.47^\circ$. This tendency is also observed in other systems such as the 122 system. In figure 7(a), ‘the more regular FeAs_4 tetrahedron, the higher T_c ’ appears to hold. As mentioned in section 2.1.1, a similar empirical trend has been proposed for $Ln\text{Ni}_2\text{B}_2\text{C}$ borocarbide superconductors, where the NiB_4 tetrahedron in the Ni_2B_2 molecular layers is covalent ideally with the B–Ni–B angle of 109.47° (Mattheiss *et al* 1994, Siegrist *et al* 1994).

2.5.2. T_c versus pnictogen height. Margadonna *et al* (2009b) claimed that the correlation between the T_c and bond angle does not hold for FeSe under pressure. This compound has FeSe_4 tetrahedra with a sizable distortion away from regularity ($\alpha \sim 104^\circ$, 5.5° away from a regular tetrahedron). The T_c of FeSe substantially increases with pressure. The structure is also compressed significantly with increasing pressure in an anisotropic way: at 9 GPa, the interlayer Se–Se distance shrinks most steeply by 9.1% whereas the intralayer Fe–Se and Se–Se distances in the FeSe_4 tetrahedron shrink by 2.9% and 3.8%, respectively. The intralayer distortion results in a slight reduction (from 104.5° at 0 GPa to 104.0° at 4 GPa) in the bond angle, α , which is shown by the broken line in

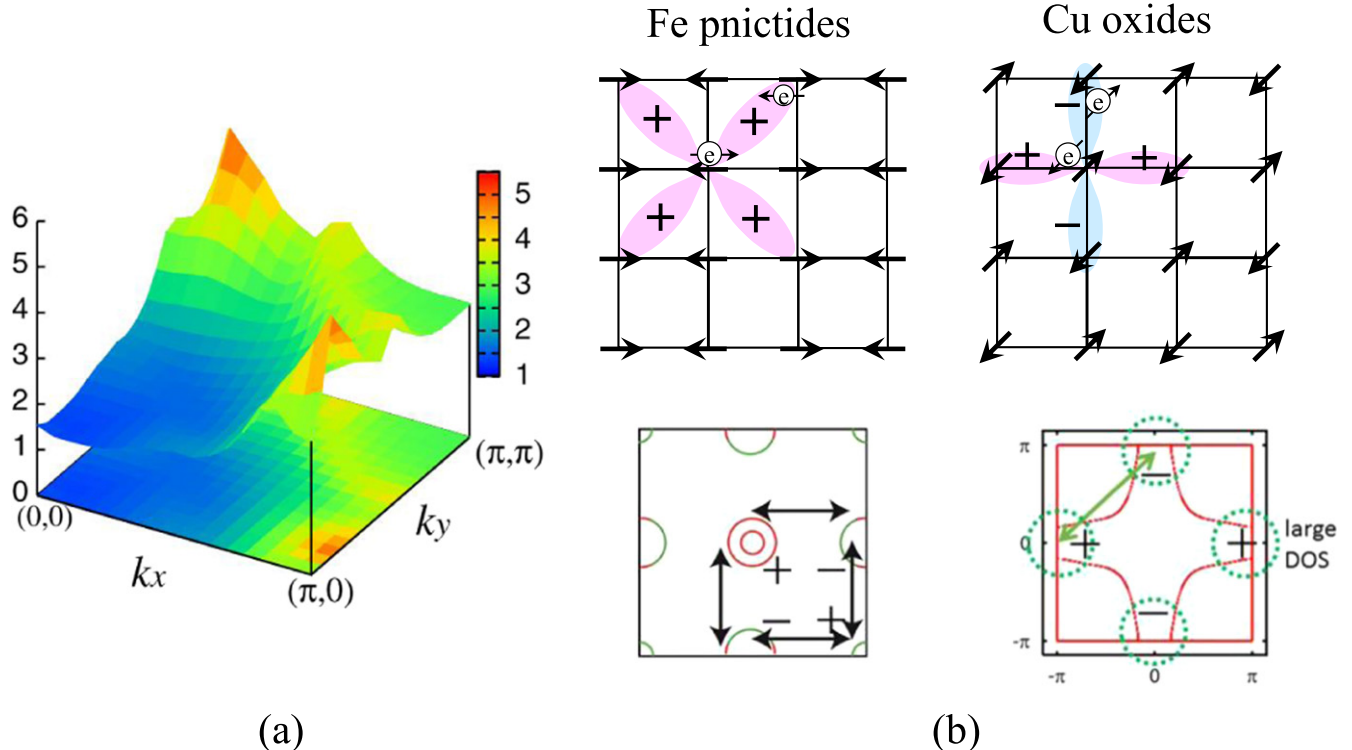


Figure 6. (a) Spin susceptibility (χ_s) calculated by RPA, which has peaks around $(k_x, k_y = (\pi/a_{sq}, 0), (0, \pi/a_{sq}))$. (b) Correspondence between real-space pairing and momentum-space gap functions for Fe-based superconductors (left) and for cuprate superconductors (right). (a) Reprinted figure with permission from Kuroki *et al* (2008), Copyright 2008 by the American Physical Society, and (b) Reprinted from Hosono and Kuroki (2015) with a slight modification, Copyright 2015, with permission from Elsevier.

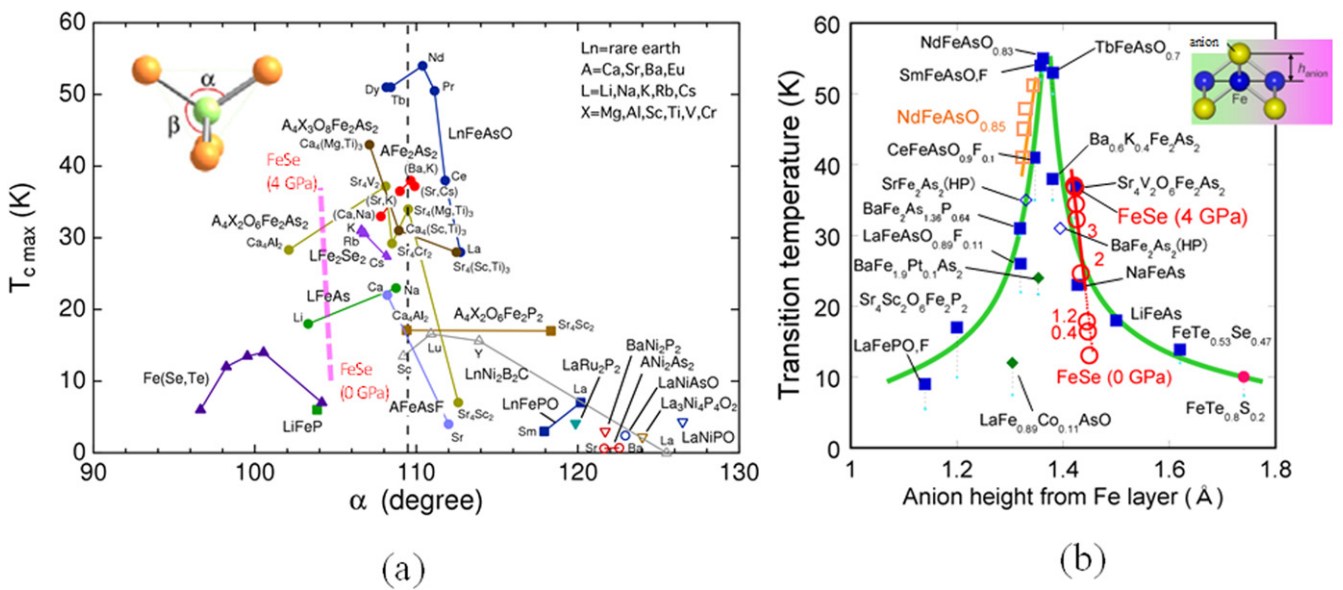


Figure 7. Two trends for the T_c versus structure in Fe-based superconductors. (a) Maximum T_c versus the bond angle α (reprinted from Lee *et al* (2012), Copyright 2012, with permission from Elsevier) and (b) maximum T_c versus anion height for various Fe-based superconductors (reproduced from Mizuguchi *et al* (2010) © IOP Publishing Ltd. All rights reserved.) The anion height, h_{anion} , is defined in the inset. In (a), the data for FeSe under pressure is indicated by a pink thick broken line. In (b), large symbols indicate the onset temperature whereas small light-blue circles indicate the zero-resistivity temperatures at ambient pressure. Filled squares are the data at ambient pressure, open diamonds the data of SrFe₂As₂ and BaFe₂As₂ under the optimal pressure, open squares the data of NdFeAsO_{0.85} under high pressure, open circles the data of FeSe under high pressure, a filled circle the data of FeTe_{0.8}S_{0.2}, and filled green diamonds the data of Pt-doped BaFe₂As₂ and Co-doped LaFeAsO.

figure 7(a). Increasing pressure, the T_c rises with the α being reduced, which is in contradiction to the above empirical trend between the T_c and bond angle that holds for the FeAs system. Then a different trend was proposed by Mizuguchi *et al* (2010), Okabe *et al* (2010), which revealed the relationship of T_c with the Se height. The application of pressure results initially in the increase of T_c and the reduction of the Se height, but a further increase of pressure above 5 GPa lowers T_c and increases the Se height. The T_c is inversely proportional to the Se height. However, this statement is contradictory to the behavior observed in other compounds. In some pnictides, T_c is higher with increasing the pnictogen height. So the overall behavior can be drawn as shown in figure 7(b), which shows the maximum T_c of each system as a function of the anion height, h_{anion} . Increasing the h_{anion} , the T_c of Fe-based superconductors initially increases and reaches a maximum (~ 56 K) at a height of 1.38 Å, corresponds to SmFeAs(O,F). Then, exceeding the optimum $h_{\text{anion}} \sim 1.38$ Å, T_c decreases with increasing the h_{anion} .

3. Molecular beam epitaxy growth of Fe-based superconductors

3.1. Basic technique

One of the authors (M N) started the MBE growth of high- T_c cuprates in 1990, and, since then, he and his colleagues have grown many copper or non-copper complex oxides and also MgB₂ (Naito *et al* 1997, Ueda and Naito 2003). Therefore, the TAT (Tokyo University of Agriculture and Technology) group employed an MBE technique for the growth of Fe-based superconductors.

MBE has been a primary tool used for the thin-film growth of III-V semiconductors, such as GaAs and InP, employed in a variety of optoelectronic devices. The III/V atomic ratio of the films is essentially self-adjusted to the stoichiometric value owing to the volatility of the group V elements: excessive As or P re-evaporates from the growth surfaces. This self-adjustment mechanism retarded the development of composition control techniques in thin-film growth, which is a main reason why MBE did not spread as a versatile thin-film growth technique of multi-cation compounds. The discovery of high- T_c cuprates ~ 30 years ago changed the situation, and a substantial amount of effort has been performed for the MBE growth of complex oxides (oxide MBE) over two or three decades. The growth of multi-component compounds, including oxides, by MBE posed many challenges, the primary of which is precise composition control of the constituent elements. This demand has led to the development of real-time *in situ* composition control techniques for evaporation fluxes.

A quartz crystal microbalance (QCM) measures mass flux and is the most widely used technique in vapor sensing although it is not always powerful in the growth of multi-cation compounds. The reason is because QCM has no material selectivity; thus, different materials deposited on the same QCM

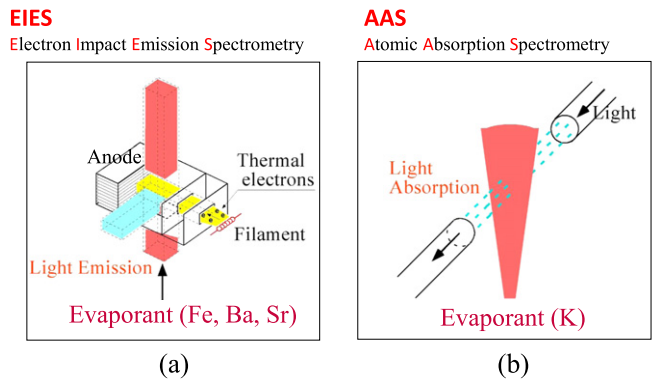


Figure 8. Schematics of EIES (a) and AAS (b).

sensor cannot be distinguished. The material (or element) selectivity is prerequisite for rate monitoring in MBE growth of multi-cation compounds. Therefore, one has to choose a rate monitoring scheme based on mass spectrometry or atomic spectroscopy. For the former, quadrupole mass spectrometers (QMS) were employed in the past (Chang *et al* 1973, Edlinger *et al* 1988, Fischer *et al* 1988, Koprio *et al* 1988), but the problem is that, because of a large drift in time of mass-selected signals at the spectrometer, frequent calibration of the signal against actual evaporation flux is required (Benerofe *et al* 1994). For the latter, electron impact emission spectrometry (EIES) and atomic absorption spectrometry (AAS) have been utilized. In EIES (Lu and Lightner 1977, Yamamoto *et al* 2013), as shown in figure 8(a), the impact of ~ 200 eV electrons on evaporants at the sensor head causes the emission of photons, whose wavelength is specific to the element and quantity is proportional to the evaporant density. The photons (lights) emitted are guided to the detectors located outside the MBE chamber via optical fibers. The detectors are photomultiplier tubes, in front of which optical band-pass filters are inserted. The band-pass filters discriminate the wavelength of the lights and allow element-specific detection of the optical signals. Nowadays, the EIES rate controller is commercially available as Guardian (Inficon) (Lu *et al* 2008) although trial-and-error processes are prerequisite on the researcher side to make it provide superior performance. AAS is another promising technique (Matijasevic *et al* 1991, Klausmeier-Brown *et al* 1992, Benerofe *et al* 1994, Lu and Guan 1995). In AAS, classic AAS is performed on the evaporant stream (figure 8(b)). In standard AAS, the light source is a hollow cathode lamp (HCL) with its cathode made of the same material as it has to be measured in the evaporant stream. The HCL, when energized, generates the characteristic atomic emission. The light from the HCL, after mechanically chopped at a few hundred Hz, is passed directly through the evaporant stream in a vacuum chamber, typically just in front of the substrate position, via optical viewport windows. AAS has the same advantages of material selectivity and non-intrusive sensing as EIES; furthermore, it operates in limitless pressure. The problem with AAS is the linearity problem since Beer's law gives a linear relation only in a limited vapor density range. The use of

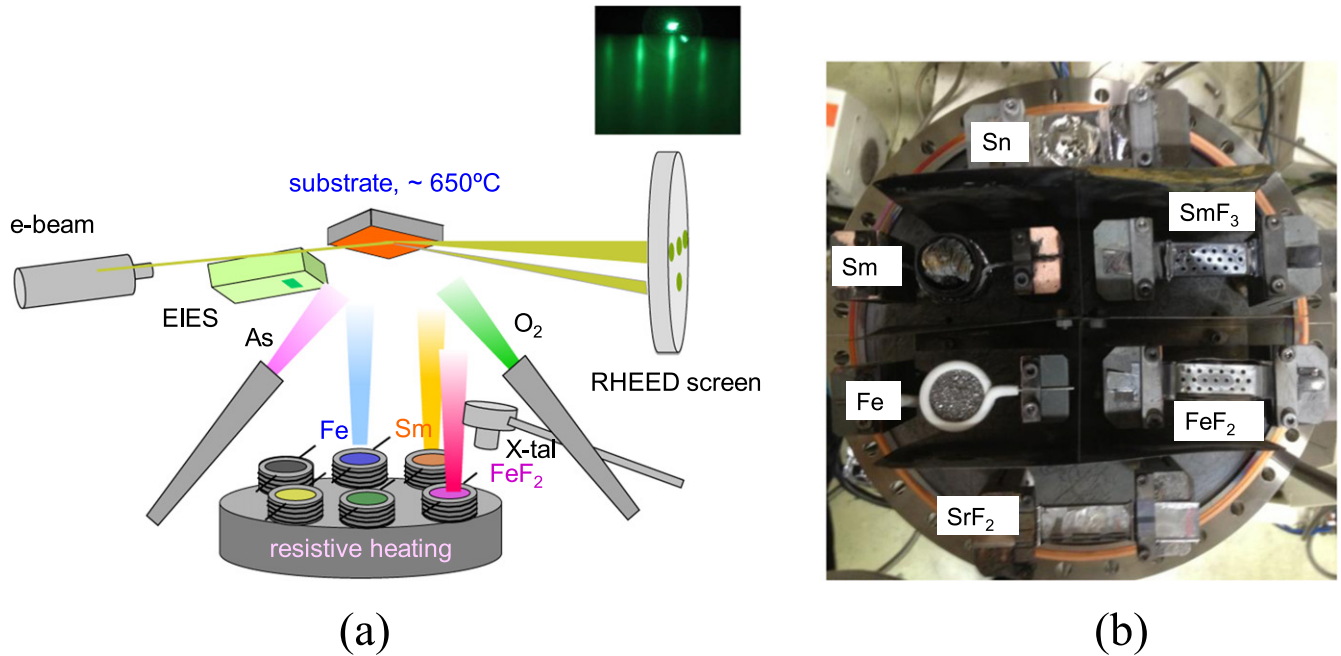


Figure 9. (a) Schematic of the MBE system at TAT and (b) photograph of the source flange.

tunable diode lasers to replace HCL should eliminate this problem since their line-widths are much narrower (Wang *et al* 1995, 1996, 1997, 1999).

The films of all the Fe-based superconductors were grown at TAT in a customer's designed MBE chamber (base pressure of $\sim 2 \times 10^{-9}$ Torr) equipped with high-sensitivity EIES and AAS systems. Figure 9 shows a schematic of the MBE system at TAT and a photograph of the source flange. All the elements (Fe, Sm, Ba, Sr, As, Se, etc) except for K were supplied from pure metal sources by resistive heating (W/Ta baskets or boats or homemade effusion cells). Fe has a high sublimation temperature of 998 °C required for vapor pressure of 10^{-5} Torr and is quite reactive at high temperatures. Therefore, it is difficult to evaporate by resistive heating. We evaporated the Fe using an alumina-coated tungsten basket (bare tungsten does not stand).

Elemental K is very reactive and is quite difficult to handle in air. The reactivity of alkaline elements increases moving down the periodic table: Li < Na < K < Rb < Cs. Elemental Li can be handled in air without much danger, but elemental K cannot. Initially, K was supplied from a pure metal source using a homemade effusion cell. But we had a small explosion in the cell once when venting the chamber while the effusion cell of K was still warm (probably ~ 70 °C–100 °C). It is noteworthy that the melting temperature of K is as low as 63.5 °C. Then the TAT group stopped using elemental K. There are two ways to supply K in a vacuum chamber from relatively stable materials. One is to use alkali-metal dispensers (SAES Getters) and the other is to use K-containing stable alloys such as Ga–K, In–K, and Sn–K. In the former, the dispensers contain K₂CrO₄ with a reducing agent (Zr 84%–Al 16%), which releases K metal when heated in a vacuum. We used this method in the past for MBE growth of (Ba,K)BiO₃ (Yamamoto *et al* 2004b).

This method may be suitable for the growth of oxides but, we thought, maybe not for the growth of (Ba,K)Fe₂As₂. Then we made the latter choice, and supplied K from relatively stable In–K alloy (In₈K₅). The In–K binary phase diagram shows that In₈K₅ has a melting temperature as high as 480 °C, but according to our experience, K starts to be released already at around 350 °C. No contamination by In is likely to occur because the vapor pressures of In and K at 350 °C are quite different ($\sim 10^{-12}$ Torr for In versus ~ 1 Torr for K). Initially, In₈K₅ ingots were prepared by our colleague via reacting In and K placed in an Al₂O₃ crucible in a sealed quartz tube. Later, however, we used a quicker way. Elemental K and elemental In (roughly 8:5) were immersed in a heptane-filled Al₂O₃ crucible of a homemade K-cell and they are alloyed directly in the crucible by heating the K-cell in vacuum.⁶

As regards the rate control of each cation flux, we employed EIES for most of the cation elements such as Fe, Sm, Ba, and Sr except for the alkaline elements. We found that EIES does not measure the flux of alkaline elements properly, so we used AAS for K. Each flux is calibrated by a QCM inserted into the substrate holder position in advance (the substrate holder is swung up during calibration). The accuracy of rate control is $\sim 10^{-2}$ Å s⁻¹ or better for all cation elements. All the fluxes were controlled via feedback loops to the power supplies for resistive heaters. Se and As are supposed to have a strong atomic emission line at approximately $\lambda = 2000$ Å, but we did not observe an emission signal. This may be because Se and As do not evaporate in the atomic state but rather in the cluster molecule state. Hence, the Se

⁶ The role of heptane is not to expose K to air. Heptane can be pumped away rather easily during evacuation. If one uses Ga instead of In, one can immerse K ingots in Ga (liquid at ambient temperatures) with no need for heptane.

Table 1. Details of the evaporation sources and flux measurements of the MBE growth of Fe-based superconductors.

Source	Heater	Crucible	Liner inserted between heater and crucible	Flux measurement
Fe	Fe	Alumina-coated W basket	None	EIES
Sm	Sm	W basket	Ta	EIES
Ba	Ba	W basket	Ta	EIES
Sr	Sr	W basket	Ta	EIES
K	In-K alloy	Effusion cell	Quartz or alumina	AAS
Li	Li	Effusion cell	Alumina	AAS
As	As	Effusion cell	Quartz or Pyrex	QMS and IG
Se	Se	W basket	Quartz or Pyrex	QCM
SmF ₃	SmF ₃	Ta boat	None	QCM
CaF ₂	CaF ₂	Ta boat	None	QCM
FeF ₂	FeF ₂	Ta boat	None	QCM

Table 2. Structure and lattice parameters of the substrates commonly used in the growth of Fe-based superconductors.

Substrate	Structure	Crystal system	Lattice parameter (Å)	Atomic distance at surface (Å)
r-cut Al ₂ O ₃	Corundum	Rhombohedral	$a_0 = 5.128, \alpha = 55^\circ 20'$	3.48
MgO(001)	NaCl	Cubic	4.212	4.212
MgAl ₂ O ₄ (001)	Spinel	Cubic	8.083	4.042
YAlO ₃ (110)	Pseudo-perovskite	Orthorhombic	$a_0 = 5.179, b_0 = 5.329, c_0 = 7.370$	3.715
LaAlO ₃ (001)	Pseudo-perovskite	Rhombohedral	$a_0 = 5.356, \alpha = 60^\circ 06'$	3.790
(LaAlO ₃) _{0.3} (Sr ₂ TaAlO ₆) _{0.7} (LSAT) (001)	Perovskite	Cubic	3.868	3.868
CaF ₂ (001)	CaF ₂	Cubic	5.463	3.863
SrF ₂ (001)	CaF ₂	Cubic	5.800	4.101
BaF ₂ (001)	CaF ₂	Cubic	6.200	4.384

flux is controlled by a quartz crystal thickness monitor and the As flux was controlled by the cell temperature with monitoring the arsenic partial pressure (P_{As}) by a QMS and an ion gauge (IG). The oxygen atmosphere during the growth of the 1111 compounds was set by introducing 0.1–0.2 sccm of O₂ through a stainless steel tube directed at a substrate and the flow was controlled by a mass flow controller. Table 1 summarizes the details of the evaporation for each element or compound.

3.2. Substrates

Table 2 summarizes the substrates used for the thin-film growth of Fe-based superconductors. At the beginning, most of thin-film growth was performed with familiar oxide substrates, which have been used for the growth of oxide films. But, later (2009), it turned out that fluoride substrates appear to be superior to oxide substrates in growing films of some of the Fe-based superconductors. Then, fluoride substrates, especially CaF₂, have been frequently used. One problem with fluoride substrates is their fragility. In this review article, (LaAlO₃)_{0.3}(Sr₂TaAlO₆)_{0.7} is abbreviated as LSAT, but other substrate materials are not abbreviated.

4. Growth of 1111 films

4.1. Early efforts by PLD

The first high- T_c Fe-based superconductor, LaFeAs(O,F), was discovered during the course of the extensive research on the transparent conducting compounds, $LnM^{2+}OPn^{3-}$, (Ln : trivalent lanthanide cations, M^{2+} : divalent cations, Pn^{3-} : trivalent pnictogen anions) conducted by the Hosono group (Kamihara *et al* 2008). Therefore, a few attempts at the film growth of 1111 compounds such as LaZnOPn were already reported before 2008. Kyanuma *et al* (2008) grew LaZnOPn ($Pn = P$, As) films on MgO. They deposited amorphous precursor layers by PLD at ambient temperatures and post-annealed them in an evacuated silica glass tube at 1000 °C. The resultant films were out-of-plane and also in-plane aligned due to solid-state epitaxy (they called this method ‘reactive solid-phase epitaxy’). With such circumstances, film growth of the 1111 materials was attempted immediately after the first report of superconductivity in LaFeAs(O,F) in spite of the quinary compounds.

The first attempt at growing LaFeAs(O,F) thin films was made by Hiramatsu *et al* (2008a). They examined several processes, including reactive solid-phase epitaxy that

successfully applied to LaZnOPn and also simple PLD growth. Initially, they employed an ArF excimer laser ($\lambda = 193$ nm) in their processes, but during this period they could not obtain a film containing even a small portion of the LaFeAsO phase. Finally, they succeeded in obtaining the epitaxial films of LaFeAsO by simple PLD, in which the excitation source for PLD was changed from the ArF excimer laser to a second harmonic (2ω) Nd:YAG (yttrium aluminum garnet) laser ($\lambda = 532$ nm). Besides, they stressed another critical factor for the successful growth, which is the high phase purity of PLD targets. The LaFeAsO phase has never been obtained in deposited films whenever even a small amount of wide-bandgap impurities such as La₂O₃ and LaOF were present in the targets. These wide-bandgap impurities appeared to be selectively transferred to the film. Eventually they obtained out-of-plane and in-plane aligned films of nearly single-phase LaFeAsO at the optimum growth temperature of 780 °C on the (001) face of the MgO, MgAl₂O₄, and LSAT substrates. However, no films showed superconductivity down to 2 K due probably to insufficient or no F content in the films despite a high concentration of F (10 at%) in the PLD target.

Almost one month later,⁷ Backen *et al* (2008) reported epitaxial LaFeAs(O,F) thin films on MgO(001) and LaAlO₃(001) by employing a two-step process, in which LaFeAs(O,F) precursor films were deposited at room temperature by ablating LaFeAsO_{1-x}F_x ($x = 0.1$ and 0.25) sintered targets using a KrF excimer laser ($\lambda = 248$ nm), followed by *ex situ* annealing in an evacuated quartz tube. After the optimization of annealing conditions, superconducting LaFeAs(O,F) thin films with an onset T_c up to 11 K were realized. However, zero resistance could not be achieved. After further optimization of the two-step process, fully superconducting LaFeAs(O,F) thin films with $T_c^{\text{on}} - T_c^{\text{end}} = 28$ K–20 K were grown on LaAlO₃(001) (Haindl *et al* 2010). Furthermore it turned out from the investigation of the transport properties of a polycrystalline LaFeAs(O,F) film that it showed weak-link behavior, indicating that super-current flow is blocked severely by high-angle grain boundaries. This observation spurred research into grain boundary issues over pnictide superconductors.

The two-step process usually produced polycrystalline films, but some of the LaFeAs(O,F) films were grown epitaxially (Kidszun *et al* 2010). The detailed microstructural analyses revealed that an epitaxial LaOF layer was present between the LaFeAs(O,F) film and the LaAlO₃ substrate (Kidszun *et al* 2011). Additionally, a polycrystalline LaOF was observed on top of the LaFeAs(O,F) epitaxial layer. Here the epitaxial relation is (001)[100]_{LaFeAs(O,F)} || (001)[110]_{LaOF} || (001)[100]_{LaAlO₃}. A key to epitaxial growth of LaFeAs(O,F) is the formation of a LaOF seed layer. However, the formation of epitaxial LaOF takes place in a rather uncontrollable manner.

⁷ The submission date of Hiramatsu *et al* (2008a) was 31 July 2008, whereas the submission date of Backen *et al* (2008) was 26 August 2008.

4.2. First success by MBE

The early attempts by PLD suggested that it is not easy to grow superconducting films of 1111 compounds. A major breakthrough in the film growth of 1111 compounds was achieved by the Nagoya group employing MBE (Kawaguchi *et al* 2009, 2010). Within two and half years from the first report on superconducting LaFeAs(O,F), they grew superconducting NdFeAs(O,F) films with T_c^{on} as high as 48 K by MBE. They supplied all the elements from solid sources (no gas source) charged in Knudsen cells: Fe, As, NdF₃, and Fe₂O₃ (Kawaguchi *et al* 2009). Here, Fe₂O₃ was used as an oxygen source since Fe₂O₃ heated at 500 °C ~ 800 °C releases oxygen accompanied by its reduction to Fe₃O₄. In their MBE growth of NdFeAs(O,F) films, first, an approximately 3000 Å thick GaAs buffer layer was grown at 610 °C on a GaAs(001) substrate, subsequently NdFeAs(O,F) was grown at 650 °C–670 °C. The growth rate of NdFeAs(O,F) was as low as 150 Å h⁻¹ and all the films in their first article were 150 Å thick. The growth window for P_{O_2} and P_{As} to prepare single-phase films of Nd-1111 is quite narrow, though reproducible, even if the cation ration Nd:Fe is stringently adjusted to 1:1. NdF₃ instead of Nd was chosen as the Nd source in order to supply fluorine.⁸ The amount of fluorine supplied was much more than that required for NdFeAsO_{0.8}F_{0.2}. In their first article, however, they were unable to obtain any superconducting film but obtained fluorine-free NdFeAsO films. The reason was clarified in their second paper.

In their first article, the growth time, t_g , was fixed to 1 h whereas in the second article, t_g was varied systematically from 1–6 h (Kawaguchi *et al* 2010). Figure 10(a) shows the out-of-plane θ –2θ XRD patterns of Nd-1111 thin films grown with different t_g but all other parameters were identical. The films grown for $t_g \leq 3$ h were single phased, but some impurity peaks appeared with increasing the growth time further. In particular, the formation of the NdOF phase is apparent for the $t_g = 5$ and 6 h films. The XRD (102) ϕ -scan confirmed that the Nd-1111 phase was grown epitaxially on a GaAs substrate. The corresponding ρ – T data are shown in figure 10(b). As seen in the figure, the resistivity of the films grown for $t_g \leq 4$ h showed semiconducting behavior without a trace of superconductivity whereas the films grown for $t_g = 5$ and 6 h exhibited clear superconducting transitions with the highest $T_c^{\text{on}} - T_c^{\text{end}} = 48$ K–42 K for the latter film. The difference between the films grown for $t_g \leq 4$ h and $t_g \geq 5$ h can be attributed to the fluorine content in the films. Electron probe microanalysis (EPMA) of the films showed that no fluorine was found in the films with $t_g \leq 4$ h while a certain amount of fluorine was contained in the films with $t_g = 5$ and 6 h.

Based on their results of the Auger depth profile, they discussed why fluorine was observed only in the films that were grown with long t_g . Figure 10(c) is a plot of the intensities of the Auger signals as a function of the sputtering time

⁸ NdF₃ is easier to evaporate than Nd. It requires ~900 °C for NdF₃ to get a vapor pressure of 10^{-4} Torr whereas it requires 1062 °C for Nd. Furthermore, Nd readily oxidizes during the growth of Nd-1111, making stable evaporation difficult.

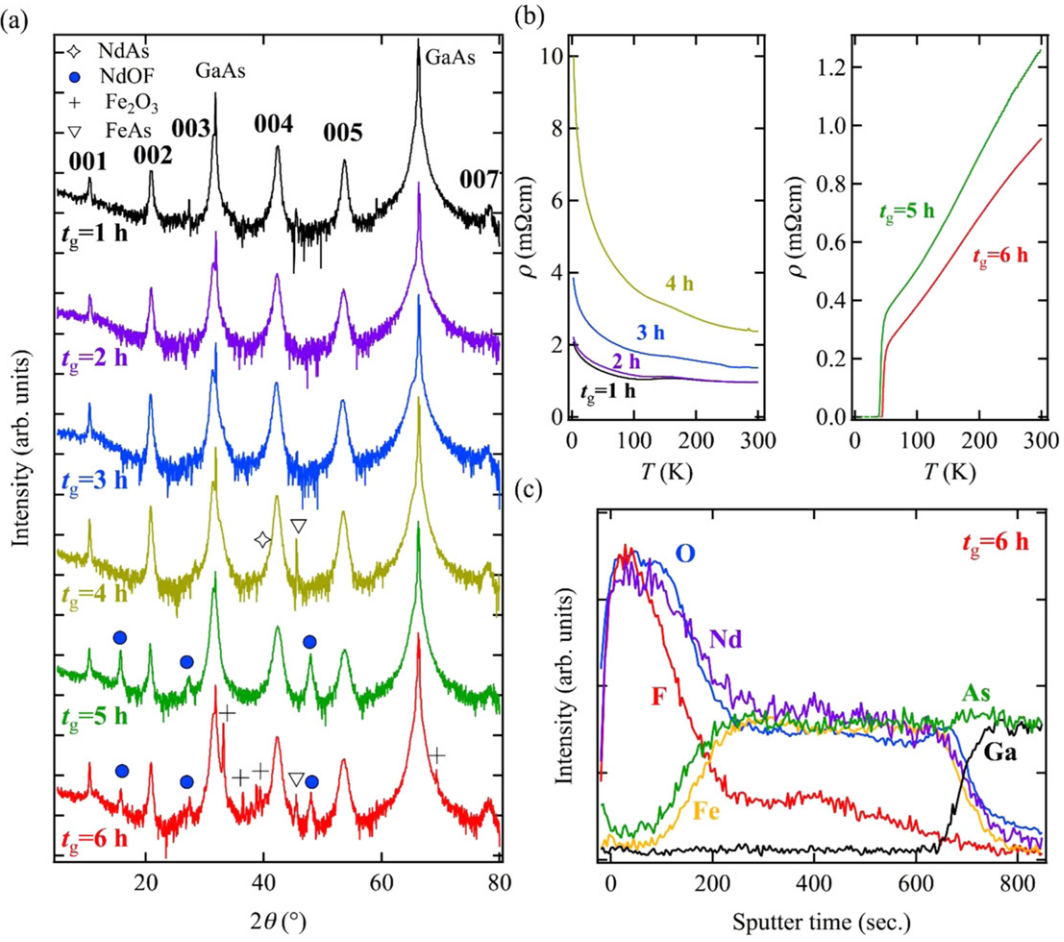


Figure 10. (a) XRD patterns of the films fabricated with different growth times t_g . All films were fabricated under the same growth conditions except for t_g . (b) Temperature dependence of resistivity of the Nd-1111 films grown with (left) $t_g \leq 4$ h and (right) $t_g \geq 5$ h. The films grown with $t_g = 5$ and 6 h exhibited a clear superconducting transition: $T_c^{on} - T_c^{end} = 45$ K–38 K for the film with $t_g = 5$ h and $T_c^{on} - T_c^{end} = 48$ K–42 K for the film with $t_g = 6$ h. (c) Auger depth-profile analysis of the Nd-1111 film grown for 6 h. The intensity of the Auger signal is plotted as a function of sputtering time. Redrawn with some modifications based on the data of figures 1, 2, and 4 in Kawaguchi *et al* (2010).

(t_{sp}) for the film with $t_g = 6$ h. One can see steep rises in the Nd, O, and F content near the surface ($t_{sp} \leq 200$ s), which was accompanied by the depletion of the Fe and As content. This observation implies that the NdOF phase, that was observed in the XRD patterns of the films with $t_g = 5$ and 6 h, was formed at the end of the film growth. Indeed, the reflection high-energy electron diffraction (RHEED) pattern during the growth suggested that Nd-1111 was grown until $t_g \sim 4$ h but later a different phase, presumably NdOF, was predominant. In their MBE growth, NdF₃ is used as the Nd source, which means that the supplied amount of F is three times larger than Nd. Therefore, the formation of the NdFeAsO phase during the early stage of the film growth is unusual. It is reported that fluorine can react with GaAs forming GaF₃ and GaF₅ thus formed sublimes above about 550 K (~280 °C). So, in their MBE growth, the reaction, NdF₃ + Ga → Nd + GaF₃, takes place at the initial stage of the film growth with GaF₃, one of the by-products, immediately sublimated, resulting in the formation of F-free NdFeAsO. With the increase in the film thickness, however, it becomes increasingly difficult for fluorine to reach the GaAs surface and some of the fluorine remained unreacted with Ga.

When the amount of fluorine exceeded a certain level, the growth of NdOF was thermodynamically more favorable. Using the same technique, they also prepared superconducting LaFeAs(O,F) films but with $T_c^{on} - T_c^{end}$ as low as 4.5 K–2.0 K (Kawaguchi *et al* 2011b).

In the above MBE growth by the Nagoya group, Ga in GaAs substrates plays an important role as the F-getter at the initial stage of the film growth. This means that the growth on other substrate materials may not be possible with similar growth parameters. Furthermore, even on GaAs substrates, the fluorine doping process is not straightforward and lacks good controllability. Then they decided to use a Ga molecular beam as a getter, and succeeded in growing Nd-1111 films on MgO substrates (Kawaguchi *et al* 2011a). Thin films were grown by supplying Fe, As, NdF₃, and Ga using Fe₂O₃ as an oxygen source. The growth rate of Nd-1111 was 150 Å h⁻¹ as in the previous articles. According to EPMA, the fluorine intensity of the films decreased with increasing P_{Ga} , indicating that Ga indeed worked as a fluorine-getter. With no or low Ga beam supplied, the Nd-1111 phase did not form. On the other hand, with an appropriate amount of Ga supplied during the growth, single-phase Nd-1111 films were obtained but

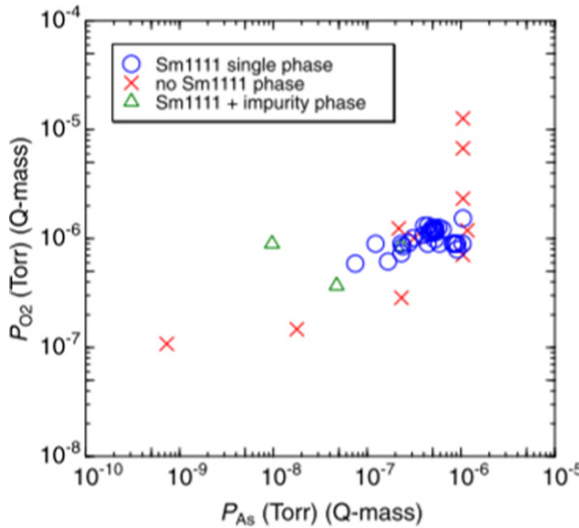


Figure 11. Growth window of the formation of SmFeAsO in the $P_{\text{As}} - P_{\text{O}_2}$ plane for the MBE growth on the LaAlO₃ substrates. All the films were grown at $T_s = 650^\circ\text{C}$ with the Sm:Fe flux ratio ($r_{\text{Sm}/\text{Fe}}$) optimized. The circles, triangles, and crosses denote the formation of the single-phase Sm-1111 phase, the formation of Sm-1111 films with impurity phases, and no 1111 phase formation, respectively. Reproduced with permission from Ueda *et al* (2012b). Copyright (2012) The Japan Society of Applied Physics.

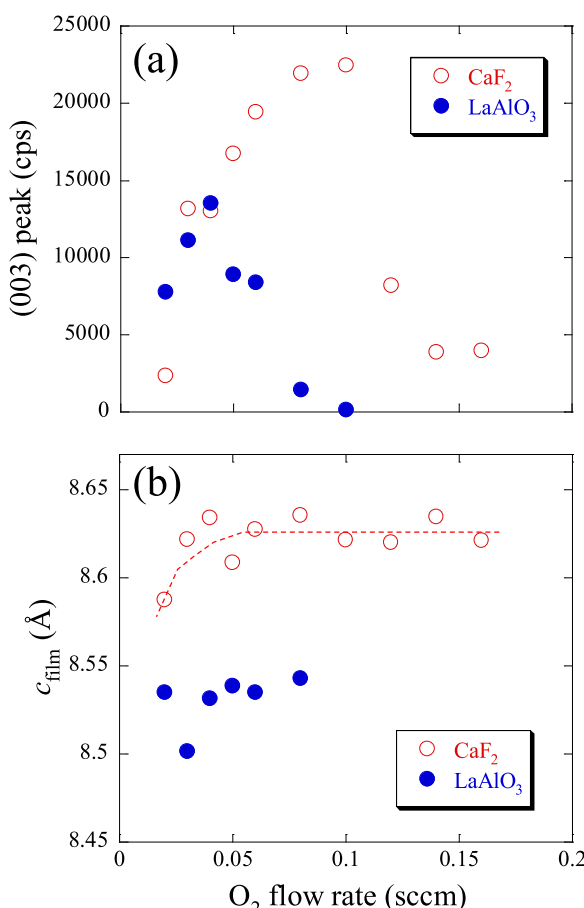


Figure 12. (a) Peak intensity of the (003) XRD reflection and (b) the c -axis lattice parameter (c_{film}) of the SmFeAsO films as a function of the O₂ flow rate. The results for the films grown on CaF₂ and LaAlO₃ substrates are compared.

with no F content (namely, no superconductivity) in the films. In order to induce superconductivity in the films, an NdOF overlayer (~ 10 nm) on top of F-free NdFeAsO is required. In their study, an NdOF layer was intentionally grown on top of the Nd-1111 thin film by closing the shutters of Fe, As, and Ga after growing Nd-1111, but continuing the supply of NdF₃ and oxygen (from Fe₂O₃) for another 1 h. These observations seem to suggest that the NdOF overlayer plays a crucial role in doping fluorine to the Nd-1111 phase. Employing the overlayer technique, they obtained $T_c^{\text{on}} - T_c^{\text{end}} = 45\text{K} - 41\text{K}$ on MgO, and later $T_c^{\text{on}} - T_c^{\text{end}} = 56\text{ K} - 52\text{ K}$ on CaF₂ (Uemura *et al* 2012).

4.3. Two-step growth at TAT: fluorine diffusion from an SmF₃ overlayer

4.3.1. Growth optimization of pristine SmFeAsO films (growth temperature, P_{O_2} , P_{As} , etc). Following the report of MBE growth of NdFeAs(O,F) by the Nagoya group, the TAT group started the MBE growth of 1111 compounds in 2010. At first, we attempted growing F-free SmFeAsO films (Ueda *et al* 2011a, 2012b, Takeda *et al* 2012, Takano *et al* 2012). In our MBE growth, the simplest growth route was adopted, and all the films were by codepositing elemental Sm, Fe, and As in an oxygen atmosphere. Sm instead of Nd was chosen since the vapor pressure of Sm is much higher than that of Nd. Namely, it requires only 573 °C for Sm to reach the vapor pressure of 10⁻⁴ Torr whereas 1062 °C is required for Nd.

The evaporation rates were 0.70 and 0.25 Å s⁻¹ for Sm and Fe, respectively, which correspond to the molar ratio of Sm:Fe = 1:1. These rates yield 850 Å thick films by 10 min deposition, amounting to a film growth rate of 1.4 Å s⁻¹, which is much faster than the growth rate employed by the Nagoya group.⁹ The fine adjustment of the Sm to Fe flux ratio ($r_{\text{Sm}/\text{Fe}}$) is critical in obtaining single-phase films with good superconducting properties reproducibly. In our routine growth, starting from these nominal rates, the rates were fine-tuned toward optimizing the crystallinity and the superconductivity. Although the XRD peaks of the 1111 phase appear in a wide range of $r_{\text{Sm}/\text{Fe}}$, a stringent adjustment of the cation flux ratio within $\pm 10\%$ is required to grow single-phase SmFeAs(O,F) films with high T_c and a sharp superconducting transition.

With regard to the growth temperature (T_s), c -axis oriented single-phase films of SmFeAsO can be obtained in the wide range of 540 °C–680 °C. In this range of T_s , the XRD peaks sharpen and the kink in the ρ – T curve at T_N becomes more prominent with increasing T_s . Therefore, most of the growth has been performed at 650 °C–680 °C, which is close to the optimum T_s (650 °C–670 °C) employed in the growth of NdFeAsO by the Nagoya group (Kawaguchi *et al* 2009).

⁹ An error was found in the calculations of the growth rate in our early publications on both Sm-1111, Ba(Sr)-122, FeSe films (Agatsuma *et al* 2010, Takeda *et al* 2010, 2012, Ueda *et al* 2011a, 2011b, 2012a, 2012b, Takano *et al* 2012). The correct rate is half of the value given in these references. Correcting this error results in half the film thickness and also resistivity. The corrected film thickness was confirmed by cross-sectional scanning electron microscopy.

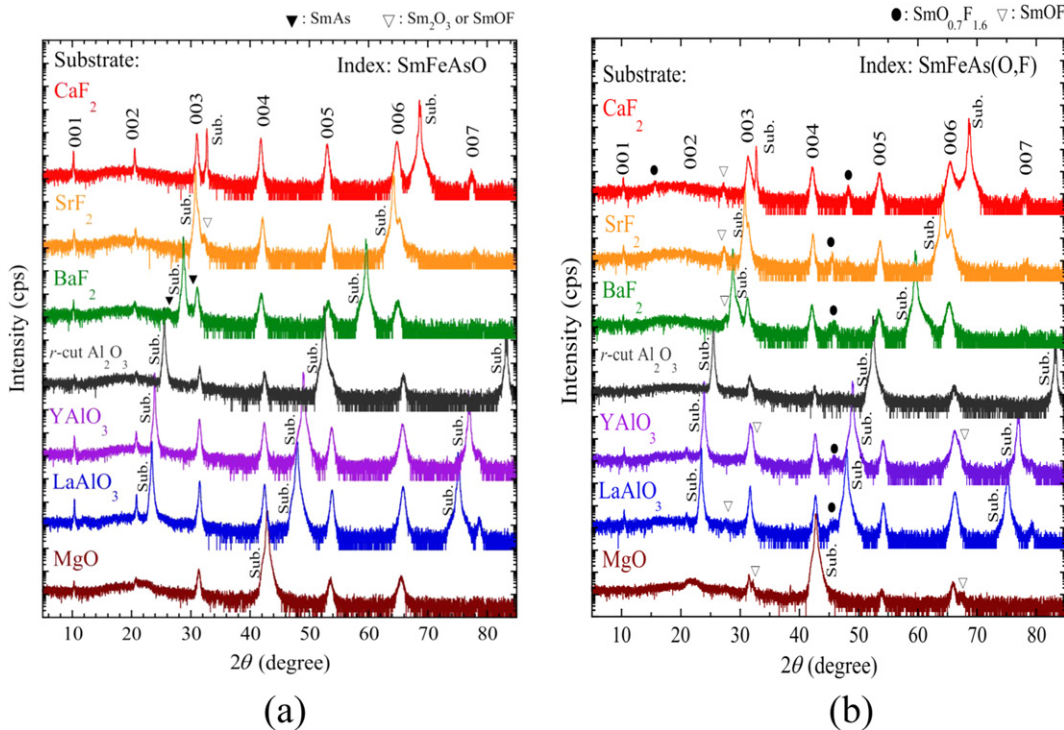


Figure 13. θ - 2θ XRD profiles of the SmFeAsO films on seven substrates (CaF_2 , SrF_2 , BaF_2 , r -cut Al_2O_3 , YAlO_3 , LaAlO_3 , and MgO): (a) before F diffusion and (b) after F diffusion. Reprinted from Takano *et al* (2012), Copyright 2012, with permission from Elsevier.

Table 3. FWHM, $\Delta\omega$, of the ω scan (rocking curve) for the (003) reflection (the (004) reflection was used for the film on SrF_2 because of the overlap of the (003) reflection of the film and the (002) reflection of the substrate) and, $\Delta\phi$, of the ϕ scan for the (102) reflection in SmFeAsO films on various substrates.

Substrate	FWHM $\Delta\omega$ of the (003)	FWHM $\Delta\phi$ of the (102)
CaF_2	0.35°	~0.50°
SrF_2	1.0°	~1.2°
BaF_2	2.0°	~2.2°
LaAlO_3	0.82°	~1.1°
YAlO_3	1.0°	~1.4°
MgO	2.4°	~3.0°
r -cut Al_2O_3	4.1°	—

Next, the arsenic and oxygen fluxes (P_{As} and P_{O_2}) were optimized. LnFeAsO is composed of four elements, namely, two cations and two anions. The situation is different from that for cuprates, for example, $\text{YBa}_2\text{Cu}_3\text{O}_7$, which is also composed of four elements, but three cations and one anion. The stoichiometry can be adjusted artificially for cations but is not straightforward for anions. This is because the (physical and chemical) sticking coefficients of anions depend not only on the substrate temperature but also on the fluxes of other cations and also anions supplied simultaneously. A further problem was that there was no report for the thermodynamic phase diagram for SmFeAsO. Therefore, the optimization of P_{As} and P_{O_2} was made by trial and error. The growth window in the $P_{\text{As}} - P_{\text{O}_2}$ plane thus obtained at $T_s = 650^\circ\text{C}$ on the LaAlO_3 substrates is demonstrated in figure 11 (Ueda *et al* 2012b). There is only a very narrow window of oxygen

partial pressure ($P_{\text{O}_2} \approx 1 \times 10^{-6}$ Torr) where single-phase SmFeAsO can be obtained. Slightly excessive P_{O_2} results in the formation of SmOF whereas insufficient P_{O_2} results in the formation of SmAs. Stringent control of the oxygen atmosphere during thin-film growth is of extreme importance for reproducible growth of high-quality thin films. On the other hand, the window of P_{As} is relatively wide. From XRD measurements, well-defined peaks of the Sm-1111 phase were observed in a wide range of P_{As} from 1×10^{-8} to 1×10^{-6} Torr.

The window of P_{O_2} for the Sm-1111 phase formation is not only narrow but also substrate dependent (Takeda *et al* 2012). Since elemental Fe is quite reactive at high temperatures, it reacts with substrates and thereby extracts oxygen from oxide substrates and fluorine from fluoride substrates. The optimum O_2 flow in the growth of SmFeAsO films on LaAlO_3 and CaF_2 is compared in figure 12, in which (a) the XRD peak intensity of the (003) reflection and (b) the c -axis lattice parameter (c_{film}) of the films are plotted against the O_2 flow rate. The XRD peak intensity is maximized at the O_2 flow rate of ~ 0.04 sccm on LaAlO_3 and at $0.08 \sim 0.10$ sccm on CaF_2 .¹⁰ The reason for the lower O_2 flow rate required on LaAlO_3 is that oxygen is partially supplied from a substrate. With regard to the c_{film} in figure 12(b), the c_{film} ($\approx 8.54 \text{ \AA}$) on LaAlO_3 , which is close to or may be slightly longer than the bulk values ($c_{\text{bulk}} \approx 8.50 \text{ \AA}$ and $a_{\text{bulk}} \approx 3.935 \text{ \AA}$), is almost independent of the O_2 flow rate. On the other hand, all the films on CaF_2 are heavily distorted

¹⁰ The optimum rate is somewhat different from our past result in Takeda *et al* (2012). This is because the gas line had a leak in the past experiments.

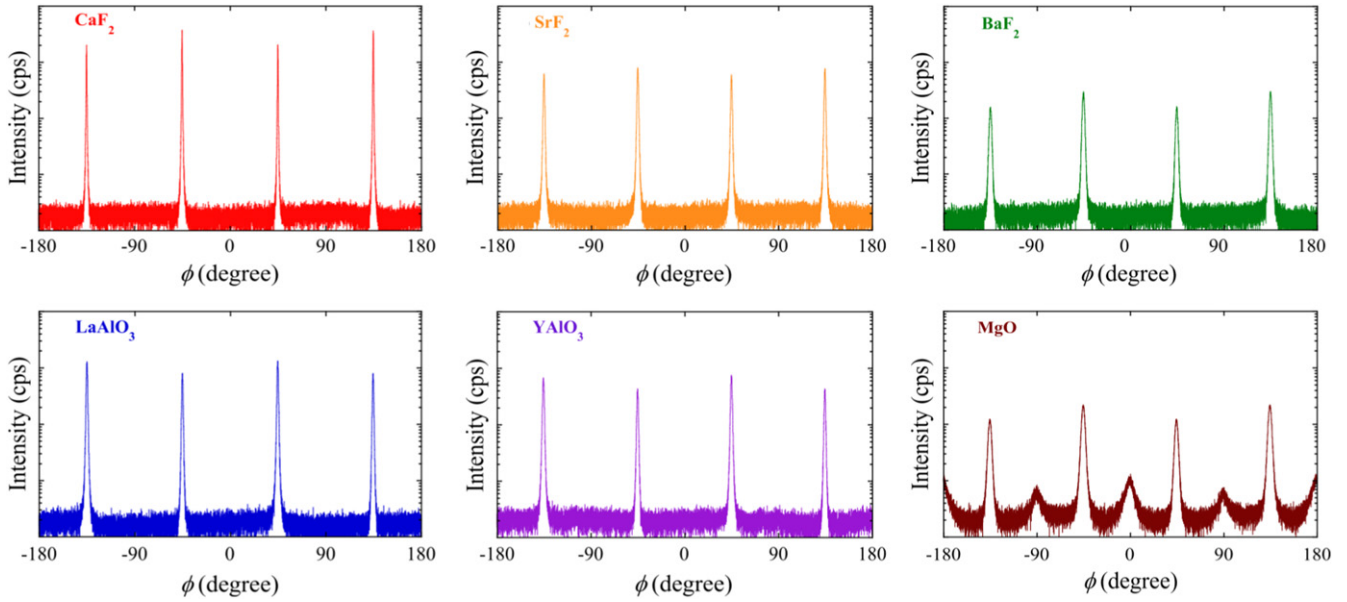


Figure 14. ϕ -scan XRD profiles of the (102) reflection of the as-grown SmFeAsO films on six substrates (CaF₂, SrF₂, BaF₂, LaAlO₃, YAlO₃, and MgO). Reprinted from Takano *et al* (2012), Copyright 2012, with permission from Elsevier.

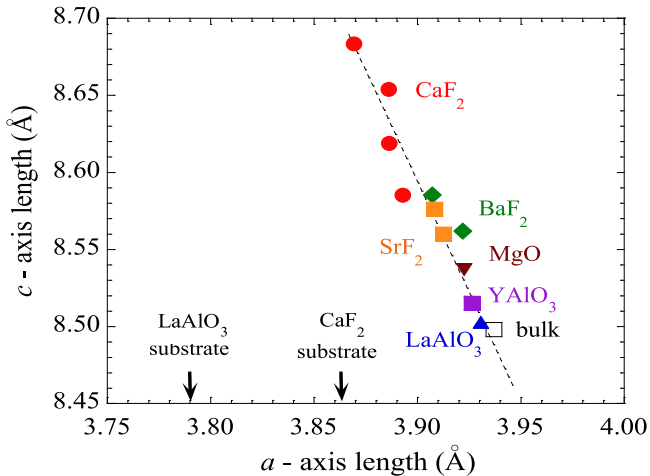


Figure 15. Lattice parameters (c_{film} and a_{film}) of the SmFeAsO films on six substrates deduced from the XRD measurements. The lattice parameters of the bulk samples are also included (empty square). Reprinted from Takano *et al* (2012), Copyright 2012, with permission from Elsevier.

from the bulk crystal structure and have significantly longer c_{film} (≈ 8.60 – 8.65 Å). Furthermore, the c_{film} gradually shortens with reducing the O₂ flow rate below 0.05 sccm on CaF₂. The c -axis lattice parameter is a measure of the F content in films, namely, decreases with x in $Ln\text{FeAsO}_{1-x}\text{F}_x$. The shortened c_{film} indicates the fluorine intake from CaF₂ in the films. These observations are a clear indication of the occurrence of the interdiffusion of oxygen or fluorine from substrates to films. In accordance with these observations, F-free SmFeAsO films on fluoride substrates show a resistivity kink at T_N shifted to a lower temperature and sometimes exhibit a superconducting transition whereas the films on oxide substrates show behavior similar to the one observed in the parent bulk samples.

4.3.2. Substrate dependence. Next, the substrate dependence of the growth of SmFeAsO films is presented. The TAT group has grown SmFeAsO films on various substrates and made a detailed comparison of films on different substrates in the structure and the superconductivity (Takano *et al* 2012). Figure 13(a) shows the θ - 2θ XRD patterns of SmFeAsO thin films grown on seven substrates, CaF₂, SrF₂, BaF₂, *r*-cut Al₂O₃, YAlO₃, LaAlO₃, and MgO. All other growth parameters such as $r_{\text{Sm}/\text{Fe}}$, P_{O_2} , and P_{As} were optimized for each film growth. All the films are nearly single phased (in the films on SrF₂ and BaF₂, small impurity peaks of SmAs or SmOF are seen) and c -axis oriented. The full width at half maximum (FWHM), $\Delta\omega$, of the ω scan (rocking curve) for the (003) reflection of the SmFeAsO thin films on seven substrates are summarized in table 3. Figure 14 shows the ϕ -scan of the (102) peak of the SmFeAsO films on the six substrates other than the *r*-cut Al₂O₃. In-plane alignment of the films was also confirmed by the four-fold symmetry observed in the ϕ -scan profile except for the films on MgO and *r*-cut Al₂O₃. The SmFeAsO film on MgO contained 45° rotated grains, as seen in figure 14, and the film on *r*-cut Al₂O₃ was not in-plane aligned. The FWHM values, $\Delta\phi$, for the (102) reflection of the SmFeAsO films are also included in table 3. As can be seen in this table, the XRD results demonstrate that the SmFeAsO films on CaF₂ are superior in crystalline quality compared to the films on other substrates.

The lattice parameters (c_{film} and a_{film}) of these films (except for the a_{film} of the film on *r*-cut Al₂O₃) evaluated from the XRD measurements are summarized in figure 15. One can see a trend in this figure in that the films on all the substrates have slightly longer c_{film} and slightly shorter a_{film} than those reported for bulk samples denoted by the empty square. Of these films, the films on CaF₂ have the longest c_{film} and the shortest a_{film} although there is a wide spread in c_{film} and a_{film} . The highly crystalline films grown on CaF₂ typically have

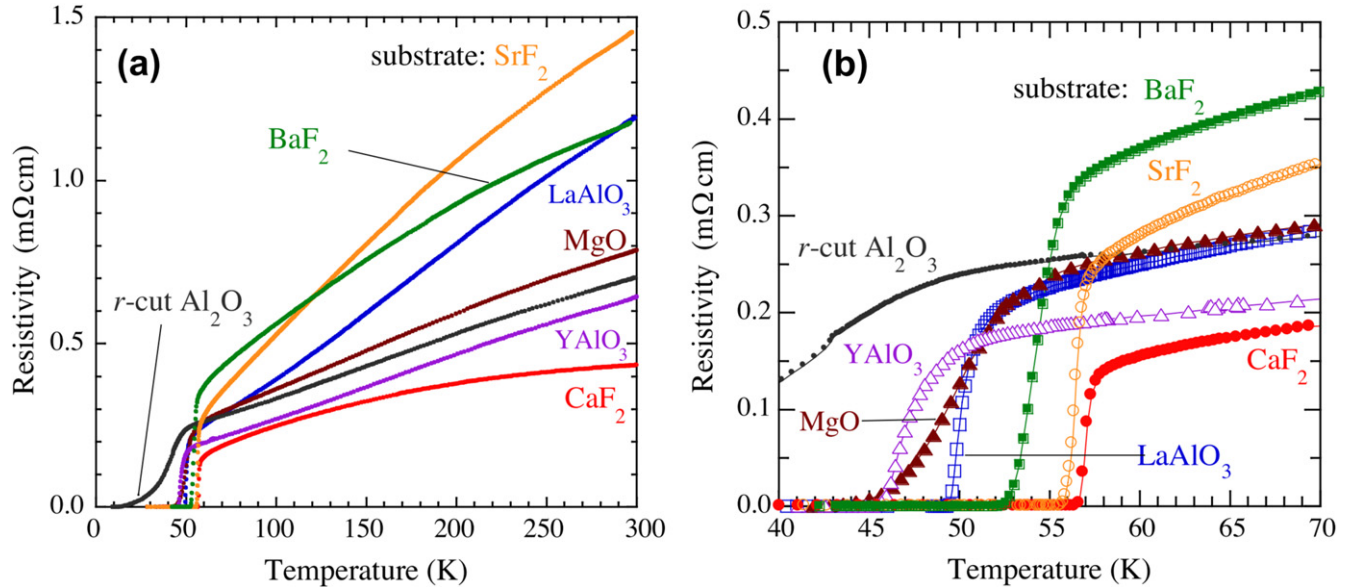


Figure 16. (a) Resistivity versus temperature (ρ - T) curves and (b) superconducting transitions of the SmFeAs(O,F) films after F diffusion on seven substrates. Reprinted from Takano *et al* (2012), Copyright 2012, with permission from Elsevier.

$c_{\text{film}} \approx 8.62\text{--}8.65 \text{\AA}$ and $a_{\text{film}} \approx 3.87\text{--}3.88 \text{\AA}$. The a_{film} is close to the Ca–Ca distance ($a_{\text{sub}}/\sqrt{2} = 3.863 \text{\AA}$) of CaF₂ (see table 2), suggesting that in-plane compressive strain is introduced into the films by the lattice mismatch. Furthermore, the large mismatch of the thermal expansion coefficient (α) between the CaF₂ and Fe pnictides may reinforce in-plane compressive strain as observed in Ba(Fe_{1-x}Co_x)₂As₂ films on CaF₂ (Iida *et al* 2016). It is well established in the growth of oxide films that in-plane compression leads to out-of-plane expansion due to the Poisson effect (Sato and Naito 1997). Epitaxial strain tends to be relaxed in SmFeAsO films with poorer crystallinity.

The structural distortion on other substrates may not be explained by epitaxial strain. This is firstly because the a_{bulk} of SmFeAsO is far from the a_{sub} of the substrates. Furthermore, the a_{sub} of SrF₂, BaF₂, and MgO is longer than the a_{bulk} of SmFeAsO, and hence tensile strain should be introduced into a film, leading to longer a_{film} and shorter c_{film} . But the observations are opposite as seen in figure 15. At present, no clear explanation for the origin of compressive strain on these substrates can be given although the above-mentioned thermal expansion mismatch is one possibility.

4.3.3. High $T_c \sim 58 \text{ K}$ in SmFeAsO films achieved via fluorine diffusion from an SmF₃ overlayer. Next, the results on fluorine diffusion to SmFeAsO films via an SmF₃ overlayer are presented. The F diffusion process of the TAT group is simple: a $\sim 250 \text{ \AA}$ thick SmF₃ overlayer is deposited on an SmFeAsO film at $T_s = 650 \text{ }^\circ\text{C}$ and subsequently the film is kept at the same temperature for 30 min (Takeda *et al* 2012). The entire process does not need to be done *in situ*, but old SmFeAsO films once exposed to air can be used for this experiment and almost identical results were obtained. Other fluorides such as NdF₃, CaF₂, and FeF₂ were tested as an overlayer on SmFeAsO. NdF₃ works as well as SmF₃. In

contrast, with CaF₂, F diffusion hardly occurs at $\sim 650 \text{ }^\circ\text{C}$, and with FeF₂, a severe reaction between SmFeAsO and FeF₂ takes place, yielding a substantial amount of Fe₂As. The results with CaF₂ and FeF₂ were much inferior to those with SmF₃ or NdF₃.

Figure 13(b) shows the XRD patterns of SmFeAs(O,F) films on seven substrates after F diffusion. Even if the films were single phase before F diffusion, impurity phases such as SmOF and SmO_{0.7}F_{1.6} always appeared after F diffusion. The diffraction peaks of Sm-1111 showed a shift to a higher angle and some broadening after F diffusion, indicating that F substitutes partially for the O site in SmFeAsO but not very uniformly. The c_{film} decreased by 0.03–0.06 \AA , amounting to F doping by more than $x = 0.2$ in SmFeAsO_{1-x}F_x. The $\Delta\omega$ and $\Delta\phi$ increased, for example, in films on CaF₂ from 0.35° and 0.50° to 0.81° and 0.88°, respectively.

Figure 16(a) shows the ρ - T curves of F-diffused SmFeAsO thin films on seven substrates, and figure 16(b) shows an enlarged view of a superconducting transition. The highest T_c obtained so far on each substrate is $T_c^{\text{on}} - T_c^{\text{end}} = 57.8 \text{ K} - 56.4 \text{ K}$ on CaF₂, 57.3 K–55.5 K on SrF₂, 56.4 K–51.8 K on BaF₂, 48.2 K–10.2 K on *r*-cut Al₂O₃, 48.7 K–45.1 K on YAlO₃, 50.3 K–49.3 K on LaAlO₃, and 55.3 K–41.7 K on MgO. The T_c^{on} of the films on CaF₂ and SrF₂ may exceed the highest T_c^{on} reported in bulk samples. In general, the T_c^{on} of films on fluoride substrates is higher than that on oxide substrates. This result suggests that fluoride substrates are more suitable than oxide substrates for obtaining better superconductivity in SmFeAs(O,F) films. In the growth of *Ln*FeAs(O,F), fluorine diffusion both from an SmF₃ overlayer and a fluoride substrate enriches the F concentration in a film to the level exceeding the limit allowed in bulk synthesis. By contrast, oxygen diffusion from an oxide substrate dilutes the F concentration in a film.

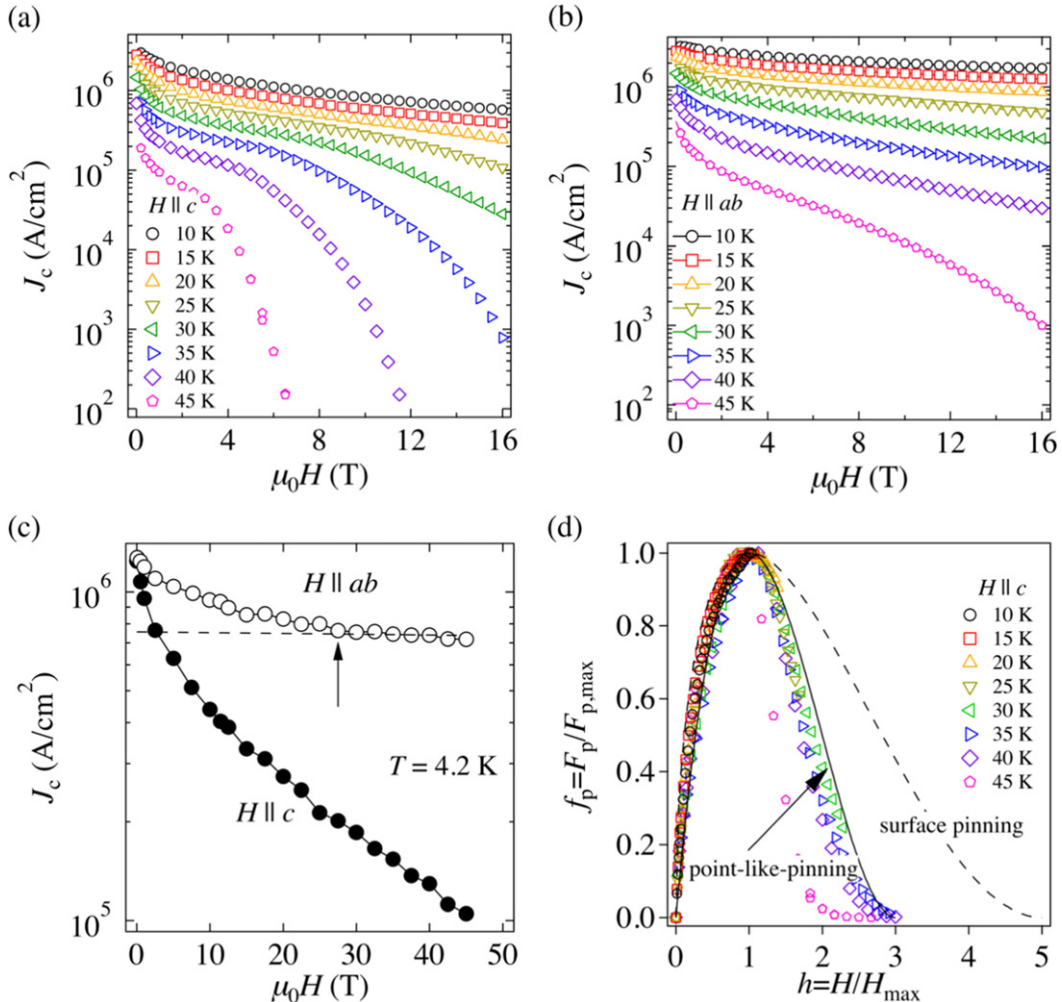


Figure 17. In-field J_c properties of an epitaxial SmFeAs(O,F) film on a SrF₂(001) substrate at various temperatures for (a) $H \parallel c$ and (b) $H \parallel ab$ measured at the National High Magnetic Field Laboratory, FL, USA. Permission courtesy of Chiara Tarantini. (c) Field dependence of a SmFeAs(O,F) on CaF₂(001) substrate for $H \parallel c$ and $H \parallel ab$ at 4.2 K. The data are taken from Iida *et al* (2013b). (d) The normalized pinning force density is plotted as a function of h .

4.3.4. High $J_c \sim 3 \text{ MA cm}^{-2}$ in F-diffused SmFeAs(O,F). As discussed in the previous sections, high- T_c , epitaxial SmFeAs(O,F) thin films can be grown by two-step growth, which offers a great opportunity for exploring transport properties. In fact, similar transport properties of a SmFeAs(O,F) single crystal using a microbridge realized by focused ion beam have already been reported by Moll *et al* (2010), but our measurements on thin films revealed the in-field transport properties in much higher fields up to 45 T (Iida *et al* 2013b).

The in-field critical current densities (J_c) of an epitaxial SmFeAs(O,F) thin film (~85 nm) on a SrF₂ substrate up to 16 T for both major crystallographic directions are summarized in figures 17(a) and (b). As can be seen, self-field J_c exceeded 1 MA cm⁻² below 30 K. Due to Joule heating, self-field J_c could not be measured at 10 K although the experiment showed that the film is capable of carrying self-field J_c over 3 MA cm⁻². In-field J_c for both major crystallographic directions is almost at a comparable level to a SmFeAs(O,F) single crystal (Moll *et al* 2010). In figure 17(a), the J_c for $H \parallel c$ is always low compared to the J_c for $H \parallel ab$ indicative of the presence of anisotropic flux pinning in the

material. The J_c for $H \parallel c$ is monotonously decreased with magnetic field as observed in usual superconductors. On the other hand, for $\mu_0 H > 5$ T, the J_c for $H \parallel ab$ becomes insensitive to H at $T < 15$ K. Such a weak magnetic field dependence of the J_c for $H \parallel ab$ is more obvious, when the measurement temperature is lowered to 4.2 K (figure 17(c)). The J_c for $H \parallel ab$ is observed to decrease gradually with H and it shows an almost constant value of $7.5 \times 10^5 \text{ A cm}^{-2}$ for $\mu_0 H > 28$ T. This observation can be described quantitatively by the competition model between extrinsic and intrinsic pinning (Awaji *et al* 1999). The intrinsic pinning will be discussed in more detail in section 4.3.5. It can be seen that extrinsic pinning is dominant up to 28 T. Over 28 T, intrinsic pinning strength exceeds that of the the extrinsic one.

4.3.5. Pinning mechanism. In order to gain information on vortex pinning, the pinning force density (F_p) is analyzed. As stated above, the intrinsic pinning starts to be active at low temperatures for $H \parallel ab$. Therefore, we analyze the pinning force density only for $H \parallel c$ by a modified Dew-Hughes model (Dew-Hughes 1974). In figure 17(d), we plot the

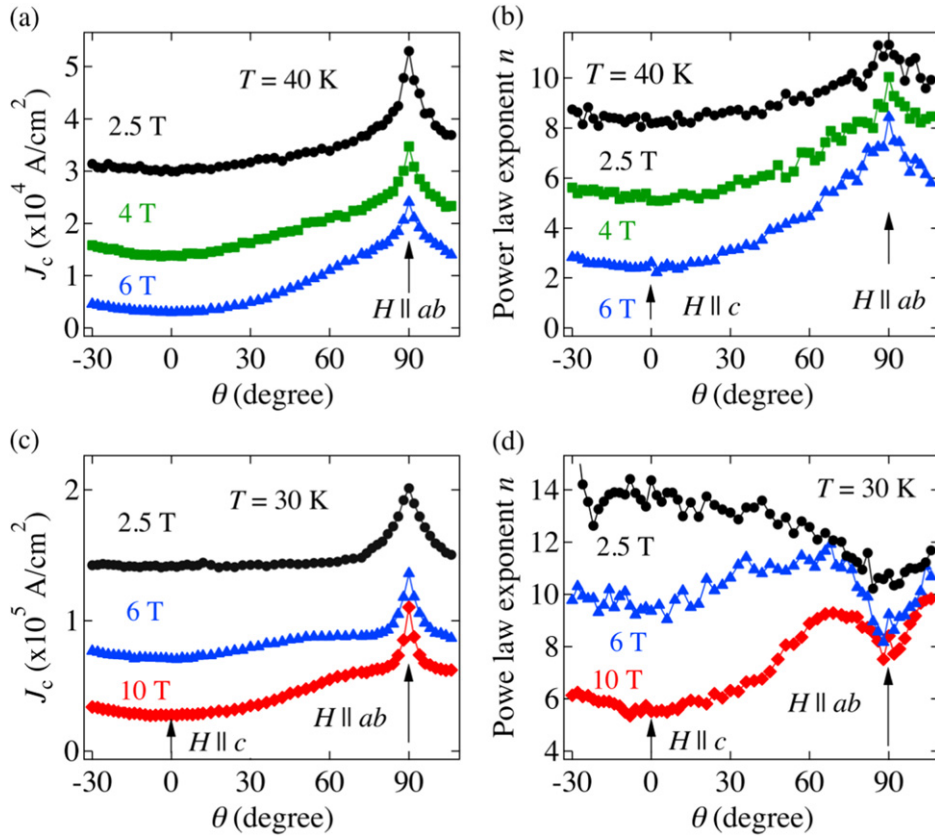


Figure 18. (a) Angular and field dependences of J_c for a SmFeAs(O,F) on CaF_2 and (b) the corresponding n at 40 K. (c) Angular and field dependences of J_c for a SmFeAs(O,F) on CaF_2 and (d) the corresponding n at 30 K. Reproduced from (Iida *et al* 2013b), CC BY 3.0.

normalized pinning force density ($f_p = F_p/F_{p,\max}$) versus $h = H/H_{\max}$, where $F_{p,\max}$ is the maximal pinning force density and H_{\max} is the applied field at which F_p is the maximal value. It is clear that the f_p data in the low-field regime are located in between the point-like pinning (crystal defects like vacancies) and surface pinning (2D defects parallel to the c -axis, involving twin boundaries or dislocation array). Here, the point-like pinning can be described by

$$f_p = \frac{9}{4}h\left(1 - \frac{h}{3}\right)^2, \quad (4.1)$$

whereas the surface pinning is

$$f_p = \frac{25}{16}h^{0.5}\left(1 - \frac{h}{5}\right)^2. \quad (4.2)$$

For the high-field regime, the data almost fall onto the point-like pinning curve. These results suggest that both point-like pinning and surface pinning are present and the former is predominant at high fields in SmFeAs(O,F) films.

For $H \parallel ab$, we analyzed the E - J curves for determining J_c . On the assumption that superconductors have no weak link, an E - J curve is described by the power law relation $E \sim J^n$, where the exponent n contains information on the pinning potential. Therefore, J_c scales the exponent n . Figures 18(a) and (b) show the angular dependence of J_c for a SmFeAs(O,F) film on CaF_2 at 40 K and the corresponding exponent n value. Relatively a sharp maximum and a broad minimum of J_c and n were observed at

$H \parallel ab$ and $H \parallel c$, respectively. Hence, the angular dependence of J_c has a similar trend to $n(\theta)$. At 30 K, however, this tendency is violated in the range of θ close to 90° (figures 18(c) and (d)). We associate this with the vortex trapping reported in Tarantini *et al* 2016, where vortices form a staircase structure with segments locked into the ab plane connected by vortex kinks (Civale *et al* 2005) (figure 19(a)). Hence, intrinsic pinning (modulation of superconducting order parameter along the c -axis) starts to be active between 30 K and 40 K, which matches the transition temperature of Abrikosov–Josephson vortices in SmFeAs(O,F) single crystals (Iida *et al* 2013b, Moll *et al* 2013). A dip of n is a consequence of kink excitation of vortex. To observe the vortex lock-in more clearly, the angular dependences of J_c and n were measured at a fixed large magnetic field of 10 T as a function of temperature. As can be seen in figure 19(c), a tiny peak within a dip of n emerged below 20 K due to vortex lock-in (figure 19(a)) and grew with decreasing temperature in accord with $\text{YBa}_2\text{Cu}_3\text{O}_{7-\delta}$ (Awaji *et al* 2011) and NdFeAs(O,F) (Tarantini *et al* 2016).

4.4. One-step growth of LnFeAs(O,F) : overview

In the previous subsection, it has been demonstrated that the F diffusion via an LnF_3 overlayer is quite a promising route in obtaining high- T_c and high- J_c plain films of LnFeAs(O,F) . However, the F diffusion via LnF_3 -overlayer approach has a problem: there is an undesired layer of LnOF on the surface of films. Our measurement of the conductance of SmFeAs(O,F)

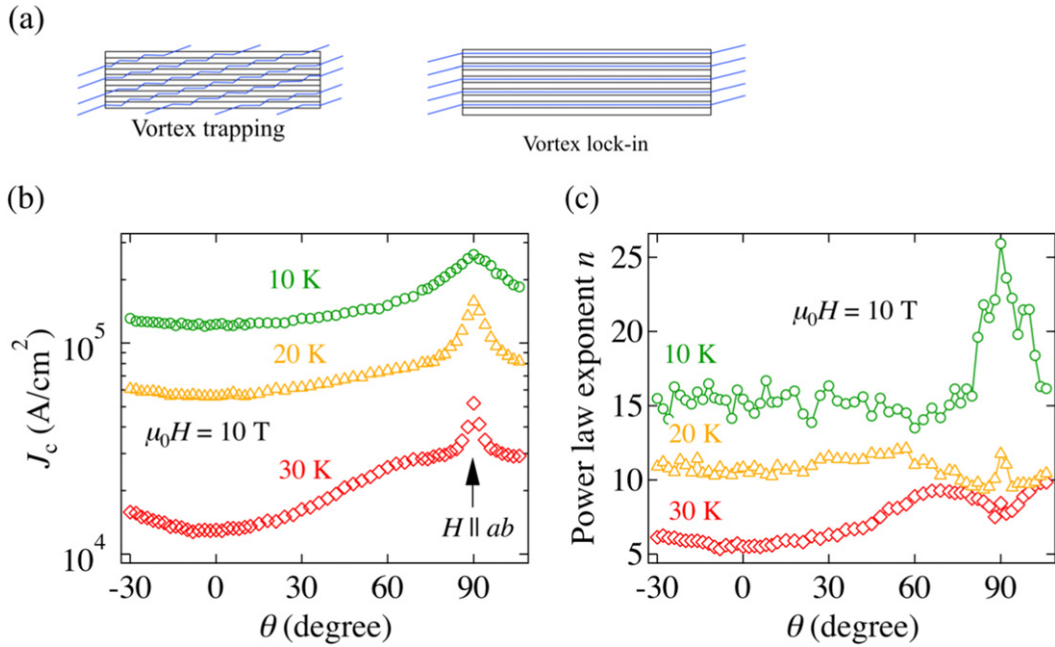


Figure 19. (a) Schematic illustration of vortex trapping and vortex lock-in for SmFeAs(O,F). (b) Angular dependence and temperature of J_c of a SmFeAs(O,F) on CaF₂ and (c) the corresponding exponent n . Field strength was fixed at 10 T.

films prepared by two-step growth as a function of thickness revealed that a ~ 225 Å thick non-conducting layer is present at the top surface. This degraded layer causes a serious problem for multilayer deposition required for fabricating sandwich-type JJs. Furthermore, the SmF₃ overlayer approach for F diffusion is not able to control the F concentration in films. To avoid these problems, it is important to establish a one-step growth technique of superconducting *Ln*-1111 films without post-growth F diffusion.

In the following subsections, the one-step MBE growth of SmFeAs(O,F) films is described. The key issue in one-step growth is how to supply fluorine. In the growth of oxide films, O₂ gas, sometimes activated such as atomic O or O₃, is introduced into a vacuum chamber. By contrast, it is not realistic to introduce F₂ or HF gas into a chamber. In general, there are the following three routes to supply fluorine to films.

Method 1: post-growth F diffusion from a fluoride overlayer.

Method 2: F diffusion from a fluoride substrate or a fluoride bottom layer.

Method 3: deposition with F-containing gas or solid.

Method 1 was described in the previous section. Method 2 may provide the simplest way among one-step growth methods. Similarly to method 1, F is introduced to films by diffusion but from the bottom so an undesired non-superconducting layer on the surface of films may not be present. In fact, as mentioned in section 4.3.1, the diffusion from fluoride substrates such as CaF₂, SrF₂, BaF₂ is substantial and can be enhanced with reducing P_{O2} during growth. The TAT group demonstrated that the $T_c^{on} - T_c^{end}$ reaches 26.5 K–9.5 K, 30.0 K–23.0 K, and 51.5 K–43.0 K on CaF₂, SrF₂, and BaF₂, respectively. Similar results have also been obtained by PLD. Haindl *et al* (2016) reported *in situ* growth of superconducting SmFeAs(O,F) thin films (up to $T_c^{on} - T_c^{end} \sim 35$ K–22 K) on

CaF₂(001) by PLD. One can expect that F diffusion is facilitated in thinner films with higher growth temperatures. Therefore they increased the growth temperature (T_s) to 860 °C and reduced the film thickness down to 300–500 Å. These observations seem to indicate that a substantial amount of F diffuses to the films from fluoride substrates and that fair superconductivity may be obtained by optimization of P_{O2} during growth.

With regard to method 3, from a safety point of view, one needs to use solid-state fluorine sources. A few candidates have been proposed as a solid-state fluorine source such as LnF₃, FeF₂, and FeF₃. Of these fluorides, LnF₃ and FeF₂ sublime without decomposition at ~ 900 °C and ~ 800 °C, respectively, whereas FeF₃ decomposes thermally at 150 °C–200 °C by releasing F-containing gas. Although the thermal decomposition reaction for FeF₃ is not well established, it is conjectured that $2\text{FeF}_3 \rightarrow 2\text{FeF}_2 + \text{F}_2$ (or 2F) in ideal circumstances. Then molecular-F₂ assisted growth (or atomic-F assisted growth) appears to be possible without handling toxic and dangerous fluorine gas. Furthermore, unlike subliming LnF₃ and FeF₂, cation elements and fluorine are supplied to a film independently, so it appears that FeF₃ may be more ideal as a fluorine source. However, it has turned out in our recent work that the actual situations are not so simple. The gaseous species released from thermal decomposition of FeF₃ turned out to be mainly HF. The reason is that FeF₃ is highly hydroscopic and contains a substantial amount of water even in reagents sold as so-called ‘anhydrous’. The issues involved in the use of FeF₃ are addressed below.

In the following subsections, the one-step growth of SmFeAs(O,F) films using SmF₃, FeF₂, and FeF₃ performed at TAT are described. We describe only the results with SmF₃ in detail and give a brief summary of the results with subliming FeF₂ and with thermally decomposing FeF₃ for comparison.

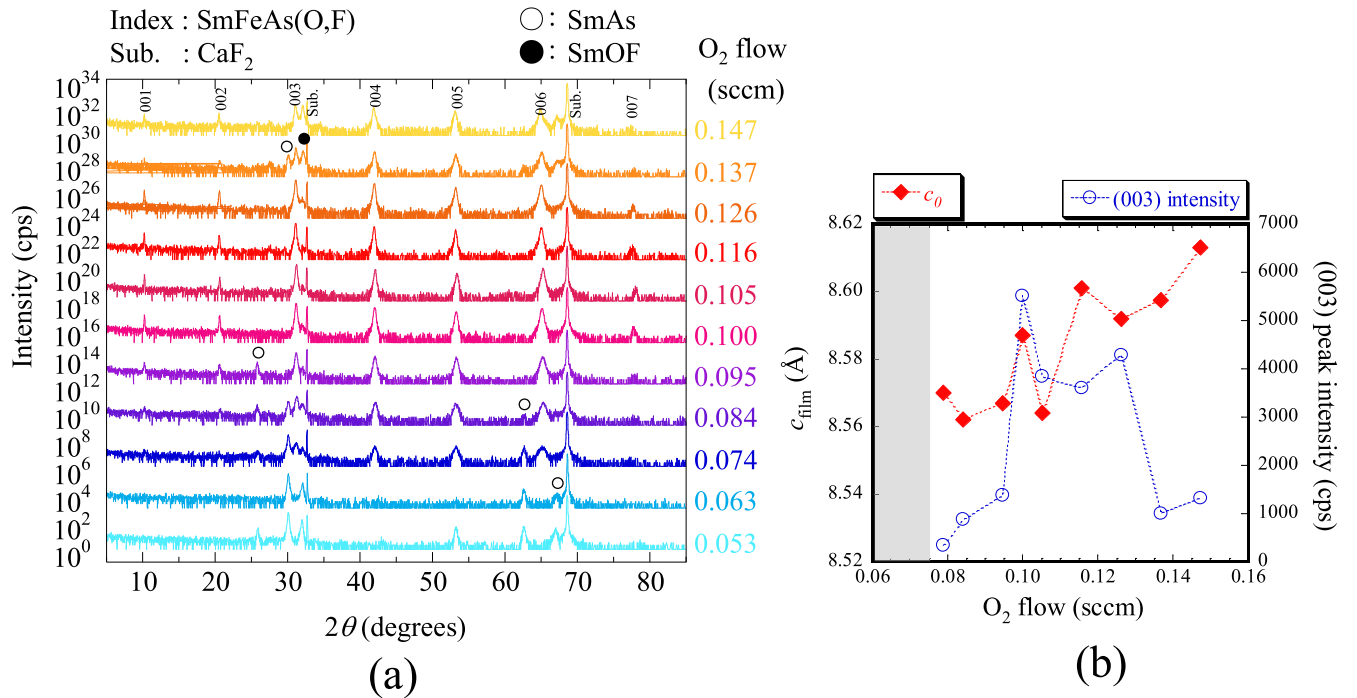


Figure 20. (a) XRD patterns of the SmFeAs(O,F) films grown on CaF₂ substrates with different O₂ flow rates using SmF₃ as the fluorine source. (b) The c_{film} and (003) peak intensity are plotted as functions of the O₂ flow rate.

This is because the results of the one-step growth of SmFeAs(O,F) with either FeF₂ or FeF₃ are described in the full-length articles by Sugawara *et al* (2014) and Sakoda *et al* (2017).

Before going into our one-step growth, the activity for the one-step growth by the Nagoya group is briefly described (Chihara *et al* 2015). As mentioned above, the Nagoya group achieved the growth of F-free NdFeAsO films by codepositing Fe, As, NdF₃, and Ga in oxygen atmosphere. As the next step, they attempted growing F-doped NdFeAsO by adjusting the supply of O₂ and Ga. However, their initial attempt did not provide films showing any signs of superconductivity. As the reason of this ill behavior, they pointed out that even with the high growth temperature of 800 °C, migration was insufficient. They identified the origin of low migration as a significant amount of N₂ in their MBE chamber during growth, which is released from the heated pyrolytic boron nitride (pBN) crucible used for the Fe source (Chihara *et al* 2015). Then, they changed the pBN crucible to an Al₂O₃ one, and the amount of N₂ was greatly reduced. After this improvement, the one-step growth of NdFeAs(O,F) was realized and superconducting NdFeAs(O,F) films with their best $T_c^{\text{on}} - T_c^{\text{end}} = 50 - 40$ K were grown on MgO. However, precipitates were observed on the film surface, indicating that further optimization was necessary.

4.5. One-step growth of SmFeAs(O,F) assisted by subliming SmF₃ at TAT

This subsection describes the details of our one-step growth of SmFeAs(O,F) assisted by subliming SmF₃. Our initial and struggled attempts at growing SmFeAs(O,F) with SmF₃ were briefly described in an earlier short publication (Ueda

et al 2012a), but substantial progress was achieved later and at present superconducting SmFeAs(O,F) films with T_c over 50 K can be grown reproducibly. The key for reproducible growth is the stable supply of SmF₃ with a very low rate (0.1 ~ 0.2 Å s⁻¹).

The respective evaporation rates of Sm and Fe for F-free SmFeAsO were 0.70 and 0.25 Å s⁻¹. In our one-step growth of SmFeAs(O,F) using SmF₃, the rates were set so as to grow SmFeAsO_{0.79}F_{0.21} films, i.e., the rates of Sm, SmF₃, and Fe were 0.65, 0.08, and 0.25 Å s⁻¹, respectively. CaF₂ substrates were used in most of the growth. With these rates, first the growth conditions such as substrate temperature and O₂ flow rate were optimized, and then the attempt at controlling the F content in films was performed.

4.5.1. Growth optimization. SmFeAs(O,F) films were grown at different substrate temperatures ($T_s = 604$ °C–720 °C). The XRD peaks of Sm-1111 are observed in all the films grown at this range of T_s , but the peaks are substantially broad in the films grown at $T_s = 604$ °C indicative of the lower crystallinity. On the other hand, the peaks of secondary phases such as SmAs and SmOF are prominent in the films grown at $T_s \geq 695$ °C. The films grown at $T_s = 645$ °C and 670 °C are nearly single phased with sharp peaks. The ρ -T measurements showed that the films grown at $T_s \geq 670$ °C showed high T_c over 50 K whereas the films grown at $T_s < 670$ °C showed lower T_c . From the XRD and ρ -T, the optimum T_s was judged to be 670 °C, which is almost identical to the T_s for the growth of F-free SmFeAsO.

Next, the O₂ flow rate was optimized. Figure 20 summarizes the XRD results for the SmFeAs(O,F) films grown with different flow rates (0.05 ~ 0.15 sccm) of O₂ gas which

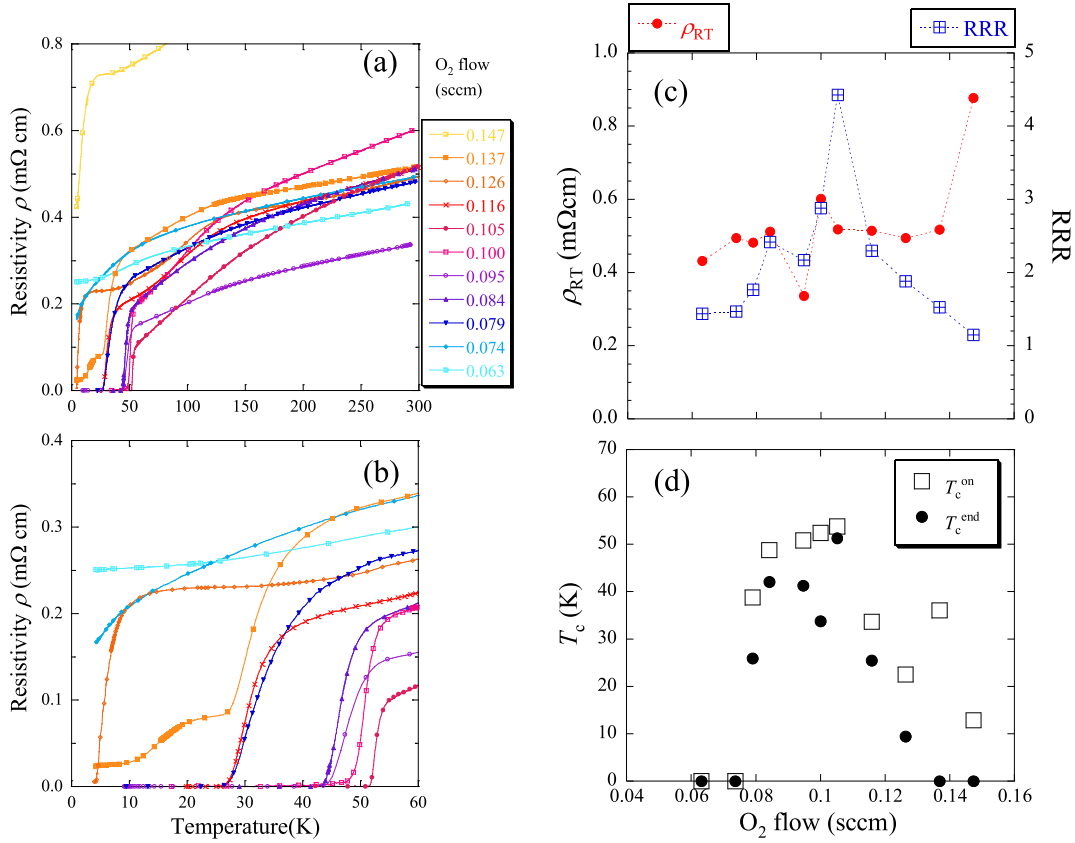


Figure 21. (a) Resistivity versus temperature (ρ - T) curves and (b) superconducting transitions of the SmFeAs(O,F) films grown on CaF_2 substrates with different O_2 flow rates using SmF_3 as the fluorine source. In (c) ρ_{RT} and RRR and in (d) T_c^{on} and T_c^{end} are plotted as functions of the O_2 flow rate.

are introduced to the MBE chamber: (a) XRD patterns and (b) c_{film} and the (003) intensity as functions of the O_2 flow rate. Figure 21 summarizes the corresponding transport data of the films: (a) ρ - T curves and (b) superconducting transition. In figures 21(c) and (d) the room-temperature resistivity ρ_{RT} , residual resistivity ratio (RRR), and T_c are plotted as functions of the O_2 flow rate. The XRD peaks of Sm-1111 appear with the O_2 flow ≥ 0.07 sccm (figure 20(a)). But a substantial amount of impurity peaks such as SmAs and SmOF are also seen. SmAs is a main impurity in the case of insufficient oxygen flow rates whereas SmOF is a main impurity in the case of excessive oxygen flow rates. It is not easy to grow single-phase films. In this series of films, the O_2 flow rate of 0.105 sccm provides the best film in that the XRD pattern showing a high intensity of the Sm-1111 peaks with a small number of impurity peaks and furthermore the T_c is the highest ($T_c^{on} - T_c^{end} = 54.6$ K – 51.0 K). Excessive O_2 flow rates (> 0.11 sccm) rapidly elongate the c_{film} and reduce T_c , eventually leading to nonsuperconductivity. In $\text{SmFeAsO}_{1-x}\text{F}_x$, the c_{film} shortens with x , so the elongated c_{film} is an indication of the reduced F content in the films.

4.5.2. F doping dependence. Next the fluorine doping dependence was examined. The rate of SmF_3 was monitored by a QCM (section 3.1, Inficon, IC6), which has a collimator directed at the SmF_3 source so as not to see other sources. In fact, because of the small signal-to-noise ratio and

slow response of the QCM, the SmF_3 rate, R_{SmF_3} , (typically 0.1 – 0.2 Å s $^{-1}$) is difficult to control via a feedback loop to a power supply. Therefore, the SmF_3 source was heated by a constant power mode, and the R_{SmF_3} was calculated from the accumulated thickness for 9 min out of the growth time (10 min). The variations of the resultant XRD and ρ - T of films with R_{SmF_3} are roughly systematic, confirming that our compromised method works rather well.

Figure 22(a) shows the XRD patterns of $\text{SmFeAsO}_{1-x}\text{F}_x$ films grown with different R_{SmF_3} from 0.02 – 0.33 Å s $^{-1}$. The XRD patterns show that the films are nearly single phased for R_{SmF_3} up to 0.20 Å s $^{-1}$. Figure 22(b) is a plot of the c_{film} and the (003) peak intensity of the films as a function of R_{SmF_3} . The c_{film} decreases almost linearly with R_{SmF_3} up to ~ 0.10 Å s $^{-1}$, then tends to flatten and finally goes up after the minimum of $c_{\text{film}} = 8.555$ Å at $R_{\text{SmF}_3} = 0.15$ Å s $^{-1}$. This observation seems to indicate that the F content in the films can be controlled by R_{SmF_3} to some extent but only in the range of a low R_{SmF_3} up to ~ 0.15 Å s $^{-1}$. The resultant shrinkage of c_{film} by changing R_{SmF_3} from 0.00 – 0.15 Å s $^{-1}$ is as large as ~ 0.07 Å. Such large shrinkage cannot be explained by the F doping alone since the shrinkage of the c_{film} by F doping from $x = 0.00$ to $x = x_{\text{sl}}$ (solubility limit) is 0.03 – 0.04 Å in the bulk samples. The large shrinkage of the c_{film} observed may be explained by assuming that in-plane compressive epitaxial strain prevailing in the parent SmFeAsO on CaF_2 tends to be relaxed with increasing F doping. Figures 23(a) and (b) show the corresponding ρ - T curves and

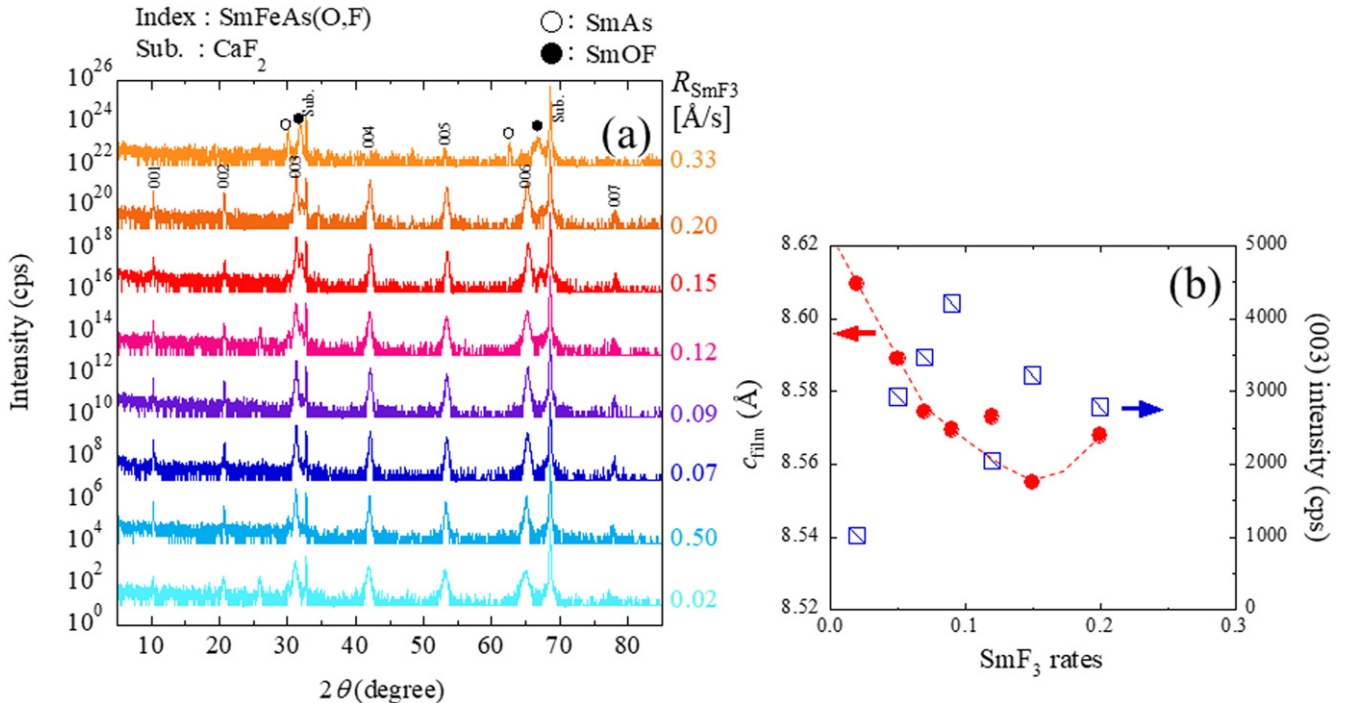


Figure 22. (a) XRD patterns of the SmFeAs(O,F) films grown on CaF₂ substrates with different R_{SmF_3} using SmF₃ as the fluorine source. In (b), the film and (003) peak intensity are plotted as functions of R_{SmF_3} .

superconducting transitions of these films, respectively. With an excessive supply of SmF₃, first, superconductivity starts to deteriorate (increased ρ and reduced T_c) at $R_{\text{SmF}_3} = 0.20 \text{ \AA s}^{-1}$, where the c_{film} starts to elongate, and eventually the Sm-1111 phase disappears as seen in the XRD pattern of the film grown with $R_{\text{SmF}_3} = 0.33 \text{ \AA s}^{-1}$ (see figure 22(a)).

The nominal relationship between R_{SmF_3} and x is $x = 2.7 \times R_{\text{SmF}_3}$, so $R_{\text{SmF}_3} = 0.05 \sim 0.10 \text{ \AA s}^{-1}$, corresponding nominally to $x = 0.135 \sim 0.27$. But the actual F content in the SmFeAsO_{1-x}F_x films is not easy to evaluate. A comparison with the results of bulk synthesis is not straightforward for the following reasons. First, there is large scattering among the bulk results reported by several groups (Liu *et al* 2008, Margadonna *et al* 2009a, Kamihara *et al* 2010, Fujioka *et al* 2013), for example, the solubility limit, x_{sl} , of F shows the following variation: 0.08 in Kamihara *et al* (2010), 0.14 in Fujioka *et al* (2013), and 0.20 in Liu *et al* (2008) and Margadonna *et al* (2009a). Second, the lattice parameters are usually a good measure for x , but those of the SmFeAsO_{1-x}F_x films are heavily modified by epitaxial strain and cannot be used for the evaluation of x . The T_c value and $\rho-T$ curve may be used for a rough evaluation of x . Comparing our data of the films in figure 23 with the bulk data by Liu *et al* (2008), the T_c and $\rho-T$ curves of the films grown with $R_{\text{SmF}_3} = 0.05$ and 0.07 \AA s^{-1} appear to correspond to those for bulk samples with $x = 0.14$ and 0.20 , respectively. If this is the case, the actual x may be close to the nominal x . However, the c_{film} as a function of R_{SmF_3} shows a saturating tendency near $R_{\text{SmF}_3} \sim 0.15 \text{ \AA s}^{-1}$, so in this range, the actual x in the films may be lower than the nominal x . A further supply of SmF₃ ($R_{\text{SmF}_3} \geq 0.20 \text{ \AA s}^{-1}$) elongates the c_{film} , which is not the behavior expected from Vegard's law. Thus, in

the growth of SmFeAsO_{1-x}F_x with SmF₃, x does not vary with R_{SmF_3} in a simple manner.

T_c versus R_{SmF_3} is summarized in figure 23(c). The T_c rapidly goes up at R_{SmF_3} above 0.05 \AA s^{-1} and also rapidly comes down at R_{SmF_3} exceeding 0.15 \AA s^{-1} . It is possible to grow films with $T_c^{\text{on}} > 50 \text{ K}$ at $R_{\text{SmF}_3} = 0.07 \sim 0.15 \text{ \AA s}^{-1}$, but it requires finer control of R_{SmF_3} to obtain films with intermediate T_c ($\sim 10 \sim 40 \text{ K}$). Of the films shown in figure 23, the film grown with $R_{\text{SmF}_3} = 0.15 \text{ \AA s}^{-1}$ shows the highest $T_c^{\text{on}} - T_c^{\text{end}} = 57.0 \text{ K} - 53.9 \text{ K}$ with $\rho(300 \text{ K}) = 580 \mu\Omega\text{cm}$ ($\text{RRR} = \rho(300 \text{ K})/\rho(60 \text{ K}) = 4.50$) whereas the film grown with $R_{\text{SmF}_3} = 0.07 \text{ \AA s}^{-1}$ shows the lowest $\rho(300 \text{ K}) = 320 \mu\Omega\text{cm}$ ($\text{RRR} = 3.07$) with $T_c^{\text{on}} - T_c^{\text{end}} = 53.9 \text{ K} - 50.5 \text{ K}$. These values are substantially improved from those obtained by our initial attempt with SmF₃ (Ueda *et al* 2012a). Furthermore, at present, such quality of films can be grown with fair reproducibility.

4.6. One-step growth of SmFeAs(O,F) assisted by subliming FeF₂ at TAT

In this subsection, the one-step growth with subliming FeF₂ is briefly described, which is essentially quite similar to the growth with subliming SmF₃ in many aspects (Sugawara *et al* 2014). For example, excessive P_{O_2} during growth reduces the F content in films, and higher T_s ($\geq 700 \text{ }^\circ\text{C}$) makes it more difficult to prepare single-phase films due to the appearance of a substantial amount of impurity phases. Here, a few differences in the growth with FeF₂ and SmF₃ are pointed out.

- The growth temperature can be lowered down to $645 \text{ }^\circ\text{C}$. $T_s = 645 \text{ }^\circ\text{C}$ is sufficient to grow high- T_c ($> 50 \text{ K}$) SmFeAs(O,F) films with FeF₂ whereas $T_s \geq 670 \text{ }^\circ\text{C}$ is required with SmF₃. This makes it easier to

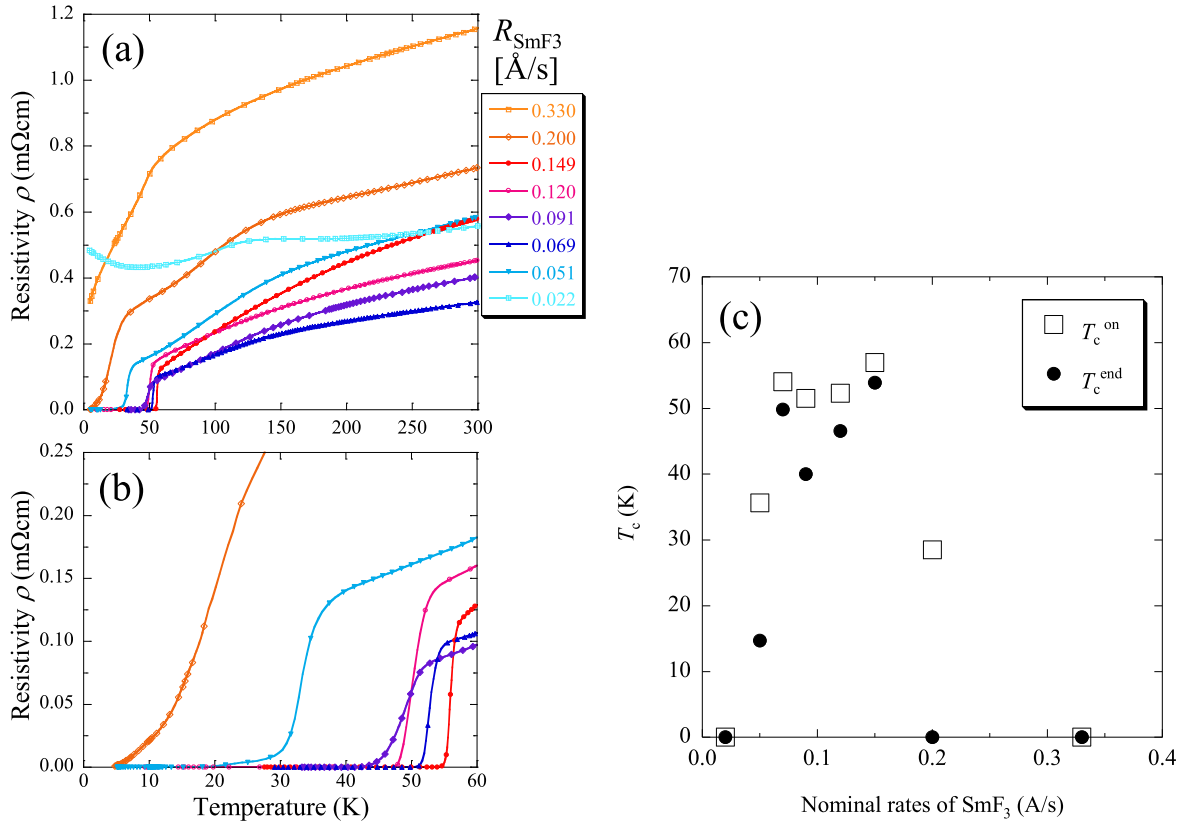


Figure 23. (a) Resistivity versus temperature (ρ - T) curves and (b) superconducting transitions of the SmFeAs(O,F) films grown on CaF_2 substrates with different $R_{\text{SmF}3}$ using SmF_3 as the fluorine source. In (c), T_c^{on} and T_c^{end} are plotted as functions of $R_{\text{SmF}3}$.

grow single-phase high- T_c films with FeF_2 than with SmF_3 , which is one of the advantages of FeF_2 .

- The window of the O_2 flow rate in the growth with FeF_2 is a little wider, in that excessive O_2 flow rate deteriorates superconductivity more gradually, than in the growth with SmF_3 .
- The actual F content (x) in the films appears to be substantially lower than the nominal x in the growth with FeF_2 . For example, in order to grow $\text{SmFeAsO}_{0.80}\text{F}_{0.20}$ films, the nominal rates for Sm, Fe, and FeF_2 are 0.70, 0.225, and 0.08 \AA s^{-1} , respectively. The films grown with these rates were underdoped and not superconducting, and the FeF_2 rate to obtain films with $T_c > 50 \text{ K}$ had to be set to $R_{\text{FeF}2} \geq 0.185 \text{ \AA s}^{-1}$, which is more than twice the nominal rate. This may indicate that F in FeF_2 is easier to lose (evaporate?) than F in SmF_3 . This observation may be related to our experience that FeF_2 is not suitable as an overlayer of SmFeAsO in two-step growth. Both subliming SmF_3 and FeF_2 can produce highly crystalline high- T_c SmFeAs(O,F) films but the growth window may be somewhat wider with FeF_2 than with SmF_3 according to our experience.

4.7. One-step growth of SmFeAs(O,F) assisted by thermally decomposing FeF_3 at TAT

In this subsection, the growth of SmFeAs(O,F) films with FeF_3 is briefly described (Sakoda *et al* 2017). As mentioned above,

FeF_3 releases F-containing gas via thermal decomposition at 150°C – 200°C . But the decomposition reaction is not a simple one ($2 \text{FeF}_3 \rightarrow 2\text{FeF}_2 + \text{F}_2$ or 2F). FeF_3 is known to be highly hydroscopic, and trihydrate $\text{FeF}_3 \cdot 3\text{H}_2\text{O}$ as well as anhydrous FeF_3 are commercially available. The anhydrous form of FeF_3 was used in our thin-film growth. In reality, however, even anhydrous FeF_3 contains a lot of H_2O , which is released during heating in vacuum. In order to evaluate the partial pressure of fluorine-containing species and H_2O during heating, the TAT group performed thermal desorption spectroscopy (TDS) on some of commercially available anhydrous FeF_3 reagents.

4.7.1. TDS on FeF_3 . TDS was carried out in our tubular vacuum furnace system. Figure 24(a) shows a schematic of our TDS system. The system consists of a quartz tube ($30 \text{ mm}\phi$) connected to a large diffusion pump (EO6, Edwards) with a QMS (RGA100, Stanford Research Systems) attached to the vacuum tubing between the furnace and pump. The quartz tube can be heated by an external tubular furnace. An FeF_3 pellet ($\sim 3 \text{ g}$), which was pulverized to increase the surface area was then put in an aluminum crucible, and placed in a quartz tube. The partial pressures of representative species detected at the QMS were monitored as a function of the furnace temperature while ramping up the temperature by 1°C min^{-1} . The results are shown in figure 24(b), which plots the partial pressures of F, F_2 , HF, O_2 , and H_2O . First of all, it should be mentioned that the results of TDS on FeF_3 differed for each reagent examined, namely, the quality of FeF_3 is reagent-manufacturer dependent and lot-dependent even though the

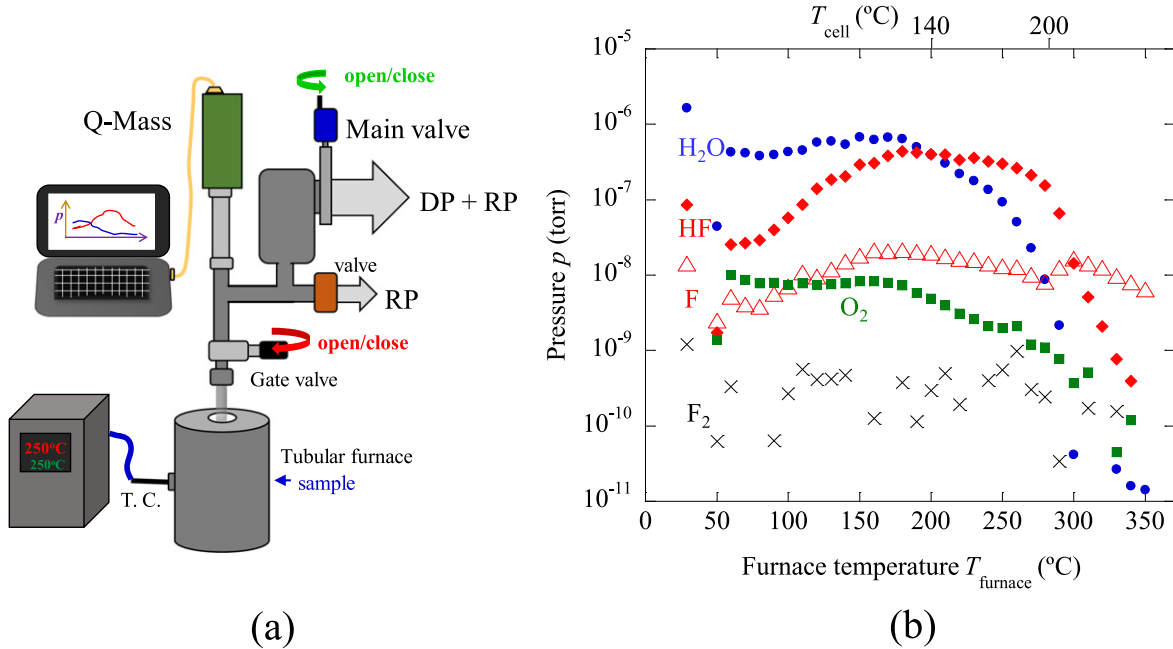


Figure 24. (a) Schematic of our TDS system and (b) plots of the partial pressures of F , F_2 , HF , O , O_2 , and H_2O detected at the QMS as a function of the furnace temperature while ramping up the temperature by $1\text{ }^{\circ}\text{C min}^{-1}$. The partial pressures indicated as F , F_2 , HF , O_2 , and H_2O correspond to the signal at the QMS of $M = 19$, 38 , 20 , 32 , and 18 , respectively. Reprinted from Sakoda *et al* (2017), with the permission of AIP Publishing.

reagents were made by the same manufacturer. In some cases, the signal of water is much more prominent than in figure 24(b).

The F_2 signal is below our detection limit. On the other hand, the partial pressure of F , $P(\text{F})$, is detectable and $P(\text{HF})$ is substantially higher than $P(\text{F})$. Both increase at $T_{\text{furnace}} > 100\text{ }^{\circ}\text{C}$. Then, the $P(\text{F})$ gradually decreases at $T_{\text{furnace}} > 150\text{ }^{\circ}\text{C}$ whereas $P(\text{HF})$ shows a plateau at $T = 150\text{ }^{\circ}\text{C} \sim 250\text{ }^{\circ}\text{C}$, followed by a rapid decrease at $T_{\text{furnace}} > 300\text{ }^{\circ}\text{C}$. The surprising observation is that the partial pressure of H_2O is the highest up to $T_{\text{furnace}} \sim 200\text{ }^{\circ}\text{C}$ among the species released from ‘anhydrous’ FeF_3 . $P(\text{H}_2\text{O})$ falls rapidly at $T_{\text{furnace}} > 250\text{ }^{\circ}\text{C}$ and the degassing of water almost completes at $T \sim 300\text{ }^{\circ}\text{C}$. $P(\text{HF})$ diminishes in almost the same temperature range. The behavior suggests that HF is released by the chemical reaction in the presence of water, $4\text{FeF}_3 + 2\text{H}_2\text{O} \rightarrow 4\text{FeF}_2 + 4\text{HF} + \text{O}_2$. It is most likely that F is supplied dominantly in the form of HF to a film in our growth with FeF_3 . Our TDS results indicate that $T_{\text{furnace}} = 200\text{ }^{\circ}\text{C} \sim 280\text{ }^{\circ}\text{C}$ is an appropriate heating temperature range for FeF_3 in the growth of SmFeAs(O,F) films, which corresponds to the effusion cell temperature, T_{cell} , of $140\text{ }^{\circ}\text{C} \sim 200\text{ }^{\circ}\text{C}$.¹¹ It should be noted that for reproducible growth it is necessary to degas the FeF_3 source in the MBE chamber at $T_{\text{cell}} \sim 140\text{ }^{\circ}\text{C}$ for 5 days before film growth,

4.7.2. Fluorine doping dependence. Next we describe the method of how to control the F content (x) in films. In

the case of subliming FeF_2 or SmF_3 as a fluorine source, the sublimation rate of FeF_2 or SmF_3 was varied by monitoring with a QCM in order to control x . But in the case of FeF_3 , since only gaseous species are released from the source, the monitoring with a QCM is not possible. Furthermore, it turned out that reproducible and quantitative monitoring of gaseous fluorine-containing species by QMS is also difficult. Therefore, the feed rate of fluorine-containing species was varied simply by changing the T_{cell} of FeF_3 . As mentioned above, the quality of FeF_3 is reagent-manufacturer dependent and lot-dependent, so the following data were collected in a straight series of growths carried out with the same FeF_3 source and without the breaking vacuum of the main chamber.

Figure 25 is a summary of the results, and shows the variation with T_{cell} of (a) XRD patterns, (b) c_{film} and the (003) peak intensity, (c) $T_c^{\text{on}} - T_c^{\text{end}}$, (d) $\rho - T$, and (e) superconducting transition. The T_{cell} varied from $150\text{ }^{\circ}\text{C} - 220\text{ }^{\circ}\text{C}$. As can be seen in figure 25(a), the films grown with $T_{\text{cell}} \leq 170\text{ }^{\circ}\text{C}$ are nearly single phased whereas both SmOF and SmAs impurities become prominent for higher T_{cell} , especially above $200\text{ }^{\circ}\text{C}$. Figure 25(b) summarizes the c_{film} and the peak intensity of the (003) reflection as a function of T_{cell} . The c_{film} is longer than 8.60 \AA at $T_{\text{cell}} \leq 160\text{ }^{\circ}\text{C}$, indicating that the F content in the films is very small, which is consistent with the presence of the resistivity kink in these films as can be seen in figure 25(d). In the range of T_{cell} from $160\text{ }^{\circ}\text{C} - 185\text{ }^{\circ}\text{C}$, one can see the shrinkage of the c_{film} with increasing T_{cell} , in spite of some scattering of the data. The c_{film} at $T_{\text{cell}} = 185\text{ }^{\circ}\text{C}$ is 8.5590 \AA . This indicates that F doping proceeds with increasing T_{cell} from $160\text{ }^{\circ}\text{C}$ up to $185\text{ }^{\circ}\text{C}$. In the films grown with $T_{\text{cell}} \geq 190\text{ }^{\circ}\text{C}$, the scattering

¹¹ Our TDS was not carried out in an MBE chamber, but rather in a separate vacuum furnace system. The thermometer (thermocouple) readings are different for these two systems, which are roughly calibrated. The rough correspondence between the two temperatures (T_{furnace} and T_{cell}) is indicated in figure 24(b).

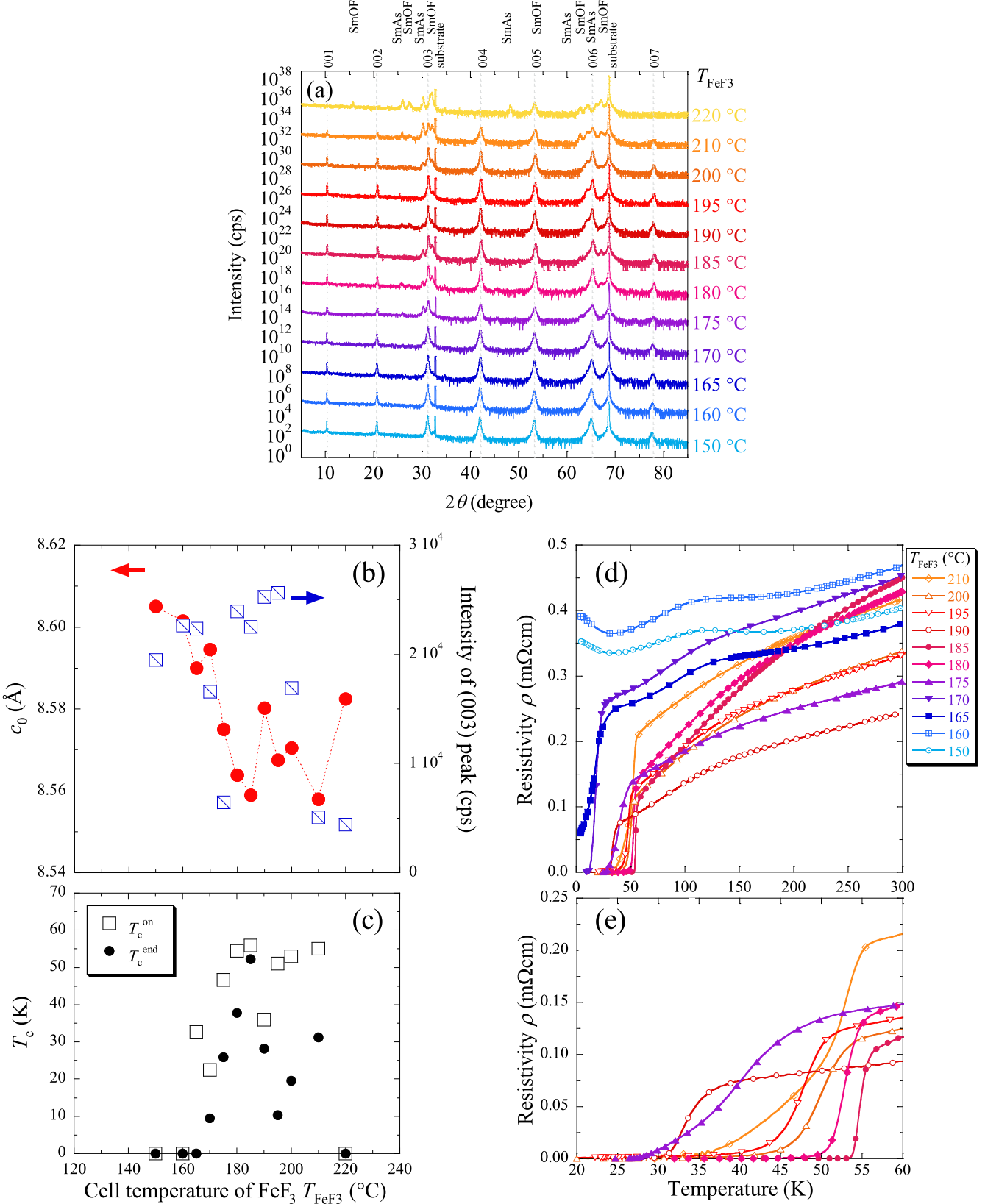


Figure 25. Fluorine doping dependences of the $\text{SmFeAs}(\text{O},\text{F})$ films grown on CaF_2 substrates using FeF_3 as the fluorine source: the variations with T_{cell} of (a) XRD patterns, (b) c_{film} and the (003) peak intensity, (c) $T_c^{\text{on}} - T_c^{\text{end}}$, (d) $\rho - T$, and (e) superconducting transition. This series of films was grown at $T_s = 670$ °C on CaF_2 with P_{O_2} and P_{As} optimized. The T_{cell} varied from 150 °C–220 °C. Reprinted from Sakoda *et al* (2017), with the permission of AIP Publishing.

Table 4. Comparison of the fluorine sources, FeF_3 , FeF_2 , and SmF_3 , used in the growth of the SmFeAs(O,F) films: growth windows and highest T_c 's. The growth window for pristine SmFeAsO is also included for comparison.

SmFeAs(O,F)				
	SmFeAsO	FeF_2	SmF_3	FeF_3
T_s ($^\circ\text{C}$)	540–680	645–720	670–720	670 ± 10
p_{As} (Torr)	$\sim 10^{-8}$	$\sim 10^{-7}$	$\sim 10^{-7}$	$\sim 10^{-8}$
O_2 flow (sccm)	0.07–0.14	0.08–0.13	0.09–0.13	0.06
T_c^{on} (K)		56.1–54.0	57.0–53.9	55.9–52.3
$-T_c^{\text{end}}$ (K)				

of the data is too large to extract a trend. With a further increase of T_{cell} above 200°C , the 1111 phase starts to decompose.

As can be seen in figure 25(e), superconductivity is observed at $T_{\text{cell}} = 165^\circ\text{C} \sim 210^\circ\text{C}$. Figure 25(c) is a summary of T_c as a function of T_{cell} , demonstrating that the $T_c^{\text{on}} - T_c^{\text{end}}$ increases with T_{cell} up to 185°C . For the T_{cell} above 190°C , although the T_c^{on} remains high, the T_c^{end} shows a rapid decrease and large scattering. This behavior of T_c is in accordance with the structural data. Summarizing the results using FeF_3 as the fluorine source, nearly single-phase films of SmFeAs(O,F) with $T_c^{\text{on}} - T_c^{\text{end}}$ as high as $55.9\text{ K} - 52.3\text{ K}$ can be grown but the reproducibility and systematics are crucially dependent on the quality of the ‘anhydrous’ FeF_3 reagents.

4.8. Comparison of the growth with SmF_3 , FeF_2 , and FeF_3

Finally, the fluorine sources (SmF_3 , FeF_2 , and FeF_3) in the growth of SmFeAs(O,F) films are compared. Table 4 summarizes the parameters in the SmFeAs(O,F) growth using SmF_3 , FeF_2 , and FeF_3 and the resultant T_c . The table also includes the growth parameters of F-free SmFeAsO for comparison. In figures 26(a) and (b) the XRD peak intensity of the (003) reflection and the T_c are plotted against T_s . The (003) reflection intensity grows above $T_s \sim 630^\circ\text{C}$, 600°C , and 660°C in the growth with SmF_3 , FeF_2 , and FeF_3 , respectively. In accordance with this structural result, the superconductivity is optimized at $T_s \sim 670^\circ\text{C}$ or higher, 645°C or higher, and 670°C with SmF_3 , FeF_2 , and FeF_3 , respectively. In the growth with FeF_3 , the window of T_s to grow single-phase films is narrow and restricted to $670^\circ\text{C} \pm 10^\circ\text{C}$ whereas there is some window for the T_s in the growth with SmF_3 and FeF_2 . A higher $T_s (> 670^\circ\text{C})$ in the growth with SmF_3 or FeF_2 sometimes produces films with slightly higher T_c^{on} , possibly due to F diffusion from CaF_2 substrates. But it is not always better in that it becomes more and more difficult to obtain single-phase films free from SmOF and SmAs impurities. So films are usually grown at $T_s = 670^\circ\text{C}$ even with SmF_3 or FeF_2 .

Other differences are the optimum O_2 flow and P_{As} . As regards the P_{As} , the optimal window is one order of

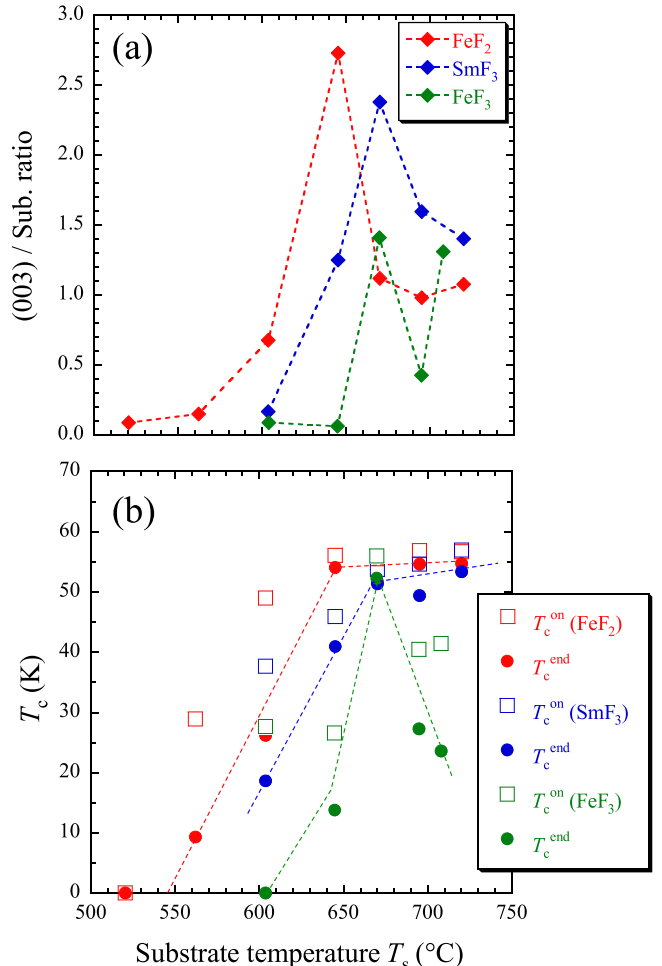


Figure 26. Comparison of the SmFeAs(O,F) films grown with different fluorine sources, FeF_3 , FeF_2 , and SmF_3 : (a) (003) peak intensity and (b) $T_c^{\text{on}} - T_c^{\text{end}}$ of the resultant films as functions of T_s . In (a), the (003) peak intensity is divided by the intensity of the (002) reflection of the CaF_2 substrate. The reason for this normalization is to correct for the change in the intensity of incident x-ray, which decreases gradually by aging and returns back by replacement to a new tube. In fact, the films included in this figure have been prepared over 4 years and the aged x-ray tube has been replaced once to a new one.

magnitude lower in the growth of SmFeAs(O,F) films using FeF_3 than the P_{As} window in the growth using SmF_3 or FeF_2 , and is comparable to the optimal P_{As} in the growth of pristine SmFeAsO . The optimum O_2 flow rate also depends on the F source as shown in figure 27. The optimum O_2 flow rate is substantially lower in the growth with FeF_3 than the growth with FeF_2 or SmF_3 , which may be partly because O_2 is released in the thermal decomposition of FeF_3 with H_2O ($4\text{FeF}_3 + 2\text{H}_2\text{O} \rightarrow 4\text{FeF}_2 + 4\text{HF} + \text{O}_2$), and is used for the formation of SmFeAs(O,F) . As can be seen in table 4, the best $T_c^{\text{on}} - T_c^{\text{end}}$ obtained with FeF_3 are comparable to those with FeF_2 or SmF_3 , but the ‘yield’ to obtain such high T_c may be in the order of $\text{FeF}_2 > \text{SmF}_3 > \text{FeF}_3$. The inferior yield of SmFeAs(O,F) with FeF_3 is mainly due to the large amount of

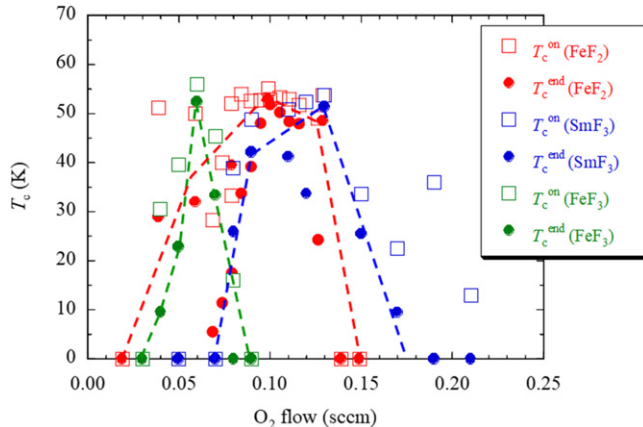


Figure 27. Comparison of the window of the oxygen flow rate for the films grown with three fluorine sources. The $T_c^{\text{on}} - T_c^{\text{end}}$ are plotted as functions of the oxygen flow rate.

H_2O contained in commercially available ‘anhydrous’ Fe_3 reagents. If truly anhydrous FeF_3 is available, the situation may be improved significantly.

5. Growth of 122 films

5.1. Growth of $(\text{Ba},\text{K})\text{Fe}_2\text{As}_2$ and $(\text{Sr},\text{K})\text{Fe}_2\text{As}_2$ films

In this section, we review the growth of the films of the 122 phase. We start with the film growth of $(\text{Ae},\text{K})\text{Fe}_2\text{As}_2$ ($\text{Ae} = \text{Ba}$ or Sr). As compared with $\text{Ln}\text{FeAs(O,F)}$, $(\text{Ae},\text{K})\text{Fe}_2\text{As}_2$ consists of fewer elements, and especially contains only one anion (As) so thin films of these compounds appear to be easier to grow than thin films of $\text{Ln}\text{FeAs(O,F)}$. In fact, sizable ($\sim 10 \times 10$ mm in the lateral dimension and a few mm thick) bulk single crystals of $(\text{Ae},\text{K})\text{Fe}_2\text{As}_2$ can be grown either by using FeAs as the self-flux or Sn flux under ambient pressure. However, the growth of $(\text{Ae},\text{K})\text{Fe}_2\text{As}_2$ films is not easy but is as difficult as or more difficult than the growth of $\text{Ln}\text{FeAs(O,F)}$ films.

5.1.1. Attempt by post-annealing. Only three groups (the Sungkyunkwan University group in Korea, the TAT group, and the Hosono group) have reported the growth of $(\text{Ae},\text{K})\text{Fe}_2\text{As}_2$ films. As demonstrated below, several groups succeeded in growing thin films of 122 compounds other than $(\text{Ae},\text{K})\text{Fe}_2\text{As}_2$ such as $\text{BaFe}_2(\text{As,P})_2$ or $\text{Ba}(\text{Fe,Co})_2\text{As}_2$. So the difficulty is specific to the growth of $(\text{Ae},\text{K})\text{Fe}_2\text{As}_2$, where the volatility of K presents a serious problem. In order to avoid this problem, the Sungkyunkwan University group prepared superconducting $(\text{Ba},\text{K})\text{Fe}_2\text{As}_2$ films by a post-annealing technique (Lee *et al* 2010a, 2014), which is similar to the technique employed in early efforts for the film growth of cuprates and MgB_2 . In their growth, precursor thin films of BaFe_2As_2 were deposited on $\text{LaAlO}_3(001)$ or Al_2O_3 (*c*-cut) substrates at room temperature by means of PLD (a KrF excimer laser), then they were put into a quartz tube with K metal in an Ar atmosphere. The encapsulated quartz ampoule was annealed in a furnace at 725°C for 40 min. The resultant

films were *c*-axis oriented and showed a superconducting transition with $T_c^{\text{on}} - T_c^{\text{end}} = 40.0\text{ K}-37.5\text{ K}$, which appeared to be a promising result. One poor characteristic was high resistivity due probably to many scattering centers arising from the grain boundaries: the $\rho(300\text{ K})$ of the films was as high as $3\text{ m}\Omega\text{cm}$, namely, ten times higher than the value of bulk single crystals.

Recently, Hiramatsu *et al* (2014b) and Hatakeyama *et al* (2016) developed a new solid-phase epitaxy technique to prepare thin films of the end member, KFe_2As_2 . Instead of annealing precursors in K vapor in a sealed quartz tube, they embedded KFe_2As_2 precursors (K-enriched) in KFe_2As_2 powders in a custom-made alumina vessel and cover. The vessel and cover were tightly pressed to each other by clenching with alumina bolts and nuts so as not to lose K by vaporization even by annealing at temperatures as high as 1000°C . The whole assembly was placed in a gas-tight stainless steel tube filled with dry Ar and annealed in a furnace. All the processes were done in a dry and inert glove box. Initially they employed lattice-matched LSAT substrates, with which KFe_2As_2 films severely reacted even at 700°C , so they changed the substrates to MgO , then obtained epitaxial films of KFe_2As_2 . Since the resultant films degraded quickly in air, XRD measurements were carried out using an O-ring sealed sample carrier filled with dry Ar.

5.1.2. MBE growth of $(\text{Ba},\text{K})\text{Fe}_2\text{As}_2$ and $(\text{Sr},\text{K})\text{Fe}_2\text{As}_2$ films at TAT

The TAT group grew $(\text{Ba},\text{K})\text{Fe}_2\text{As}_2$ and $(\text{Sr},\text{K})\text{Fe}_2\text{As}_2$ films *in situ* by MBE (Agatsuma *et al* 2010, Takeda *et al* 2010, Ueda *et al* 2011b, Yamagishi *et al* 2011). The evaporation rate of Fe was fixed at 0.50 \AA sec^{-1} , and 5 min deposition results in 620 \AA thick $\text{Sr}_{1-x}\text{K}_x\text{Fe}_2\text{As}_2$ and 650 \AA thick $\text{Ba}_{1-x}\text{K}_x\text{Fe}_2\text{As}_2$ films. The K flux was supplied about twice as much as the required amount in order to compensate for re-evaporation: the flux ratio of Ba (or Sr) : K was set to $1 - x : 2x$ in the growth of $(\text{Ba}_{1-x}\text{K}_x)\text{Fe}_2\text{As}_2$ or $(\text{Sr}_{1-x}\text{K}_x)\text{Fe}_2\text{As}_2$. The substrates used were mostly *r*-cut Al_2O_3 since the substrate dependence is weak in contrast to the case of $\text{Ln}\text{FeAs(O,F)}$. The films containing a large content of K degrade quickly (for one to several minutes, depending on x) in air, therefore, the films were coated with polystyrene resin (called ‘Q-dope’) diluted by toluene immediately after taking the films out of the MBE chamber.

The MBE growth of pristine SrFe_2As_2 and BaFe_2As_2 without K is easy, and *c*-axis oriented epitaxial films with an apparent resistivity kink due to the magnetic transition can be obtained at $T_s \geq \sim 450^\circ\text{C}$ and in a wide range of P_{As} ($1 \times 10^{-7} \sim 5 \times 10^{-6}$ for BaFe_2As_2 and roughly one order higher for SrFe_2As_2). Although the XRD peaks of the 122 phase are not observed in the films grown at $T_s \leq \sim 400^\circ\text{C}$, the resistivity kink is still observed in the films grown at $T_s \sim 350^\circ\text{C}$, indicating that the polycrystalline 122 phase consisting of very small grains forms at this temperature.

As mentioned above, K is highly volatile, and accordingly K is not incorporated in films grown at $T_s > 400^\circ\text{C}$.

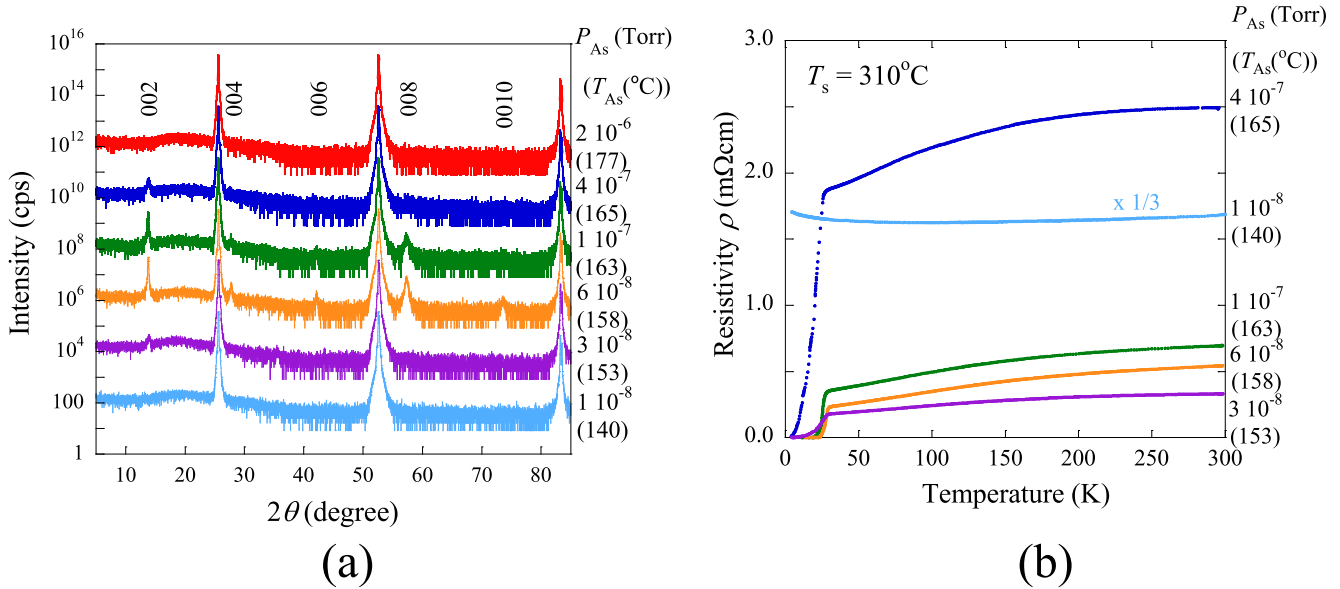


Figure 28. (a) XRD patterns and (b) ρ - T curves of the (Sr,K)Fe₂As₂ films grown at $T_s = 310$ °C with different As fluxes (P_{As}) from 1×10^{-8} Torr to 2×10^{-6} Torr. The As cell temperatures (T_{As}) are also indicated. Reprinted from Agatsuma *et al* (2010), Copyright 2010, with permission from Elsevier.

Hence, the growth of K-containing 122 films needs to be done at $T_s \leq \sim 400$ °C. However, lowering T_s alone did not produce superconducting (Sr,K)-122 or (Ba,K)-122 films. In fact, the films neither contained K nor crystallized in the 122 phase at $T_s \sim 300$ °C if P_{As} was kept at the values optimized for pristine films. A substantial reduction of P_{As} from these values is required for incorporating K into films.

Figure 28 shows the first results of the superconducting films of (Sr,K)-122. Figure 28(a) shows the XRD patterns of the (Sr,K)-122 films grown at $T_s = 310$ °C in different P_{As} . No peak of the 122 phase in the XRD pattern is observed in the film grown with $P_{\text{As}} = 2 \times 10^{-6}$ Torr. However, by the reduction of P_{As} down to 4×10^{-7} Torr, the XRD peaks of the 122 phase appeared and the peak positions confirmed that K is incorporated in the film. The intensity of the XRD peaks became stronger when P_{As} was reduced to 6×10^{-8} Torr. However, a further reduction of P_{As} resulted in weaker XRD peaks, and the 122 phase did not form for P_{As} below 1×10^{-8} Torr. The c_{film} of the films also elongates with lowering P_{As} . The elongation of the c_{film} indicates that more K is incorporated in the films, since the c_{bulk} almost linearly increases with x in Sr_{1-x}K_xFe₂As₂ and also in Ba_{1-x}K_xFe₂As₂ according to the bulk data. Figure 28(b) shows the corresponding ρ - T curves of the films. The film grown in $P_{\text{As}} = 6 \times 10^{-8}$ Torr has a resistivity of around 0.5 mΩcm at 300 K and shows a broad superconducting transition with $T_c^{\text{on}} - T_c^{\text{end}} = 29.2$ K–22.4 K while the film grown in $P_{\text{As}} = 3 \times 10^{-8}$ Torr has lower resistivity (0.3 mΩcm at 300 K) but with a long transition tail.

A more detailed study of the P_{As} dependence on the structural and superconducting properties of the (Sr,K)-122 films was performed, and the results are summarized in figure 29. This figure shows (a) the XRD peak intensity of the (002) reflection, (b) c_{film} , (c) $T_c^{\text{on}} - T_c^{\text{end}}$ as a function of the

As cell temperature (T_{As}), and (d) the variation of the ρ - T curves with T_{As} . All the films in this figure were grown at $T_s = 315$ °C with the setting of the rate aimed at $x \sim 0.45$. The As cell temperature can be converted to P_{As} based on the calibration curve, which varies in time, depending on the amount of As in the cell, but in a short period the same calibration curve can be used if one bears a possible slight drift in mind. The rough correspondence between T_{As} and P_{As} is shown in the upper part of figure 29(a). The films of almost single phased (Sr,K)-122 can be obtained in the relatively wide range of T_{As} between 140 °C and 170 °C. As can obviously be seen in figure 29(a), however, the films with strong XRD peak intensity are obtained only in a very narrow range (154 °C–160 °C) of T_{As} . Figure 29(b) shows the c_{film} versus T_{As} . Except for the data points for the $T_{\text{As}} = 160$ °C and 172 °C, one can see a clear trend of the c_{film} increasing from ~ 13.0 – 13.18 Å with lowering T_{As} . The c_{film} increase continues below $T_{\text{As}} = 150$ °C, where the XRD intensity becomes very weak. With the data for the c_{bulk} of the bulk samples ($c_{\text{bulk}} = 12.3226 + 1.5161x$ [Å]) in Sr_{1-x}K_xFe₂As₂ (Lv *et al* 2009), the K concentration in the films could be evaluated. The x value increased from about 0.45–0.55 with lowering T_{As} from 166 °C–133 °C. Of the scattered data points, the data for $T_{\text{As}} = 160$ °C were reproducible. Two films grown at $T_{\text{As}} = 160$ °C peeled off by themselves although no good adhesion of the Sr_{1-x}K_xFe₂As₂ films to the *r*-cut sapphire substrates was commonly seen, and we could not measure the resistivity of these films. The two films also showed the value of the c_{film} substantially deviated from the trend line. The growth at $T_{\text{As}} = 160$ °C could be singular.

Figure 29(d) shows the corresponding ρ - T data. The transport properties did not change with T_{As} as drastically as the structural properties did. All films grown with $T_{\text{As}} = 139$ °C–172 °C showed a superconducting transition,

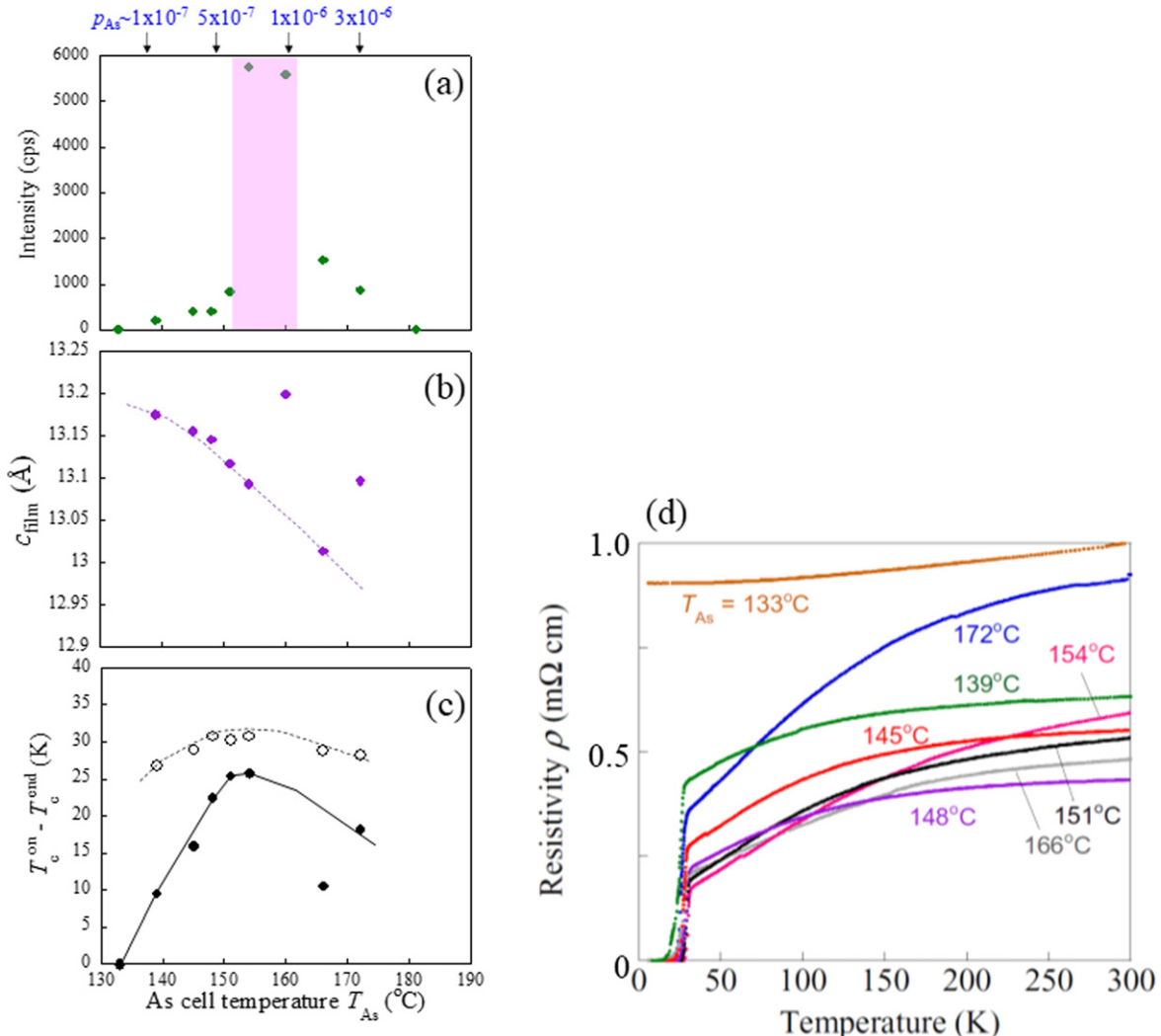


Figure 29. Structural and superconducting data for the $\text{Sr}_{1-x}\text{K}_x\text{Fe}_2\text{As}_2$ films ($x \sim 0.45$) grown in different P_{As} . The films were grown at $T_s = 310^{\circ}\text{C}$ with different As cell temperatures, $T_{\text{As}} = 133^{\circ}\text{C} \sim 172^{\circ}\text{C}$. The XRD peak intensity of (a) the (002) reflection, (b) c_{film} , and (c) T_{c} are plotted against T_{As} . The $\rho-T$ curves of the films are shown in (d). Reprinted from Ueda *et al* (2011b), Copyright 2011, with permission from Elsevier.

and one can see a difference only in the transition width and RRR. Figure 29(c) summarizes the $T_{\text{c}}^{\text{on}} - T_{\text{c}}^{\text{end}}$ of the films. The film grown at $T_{\text{As}} = 154^{\circ}\text{C}$ showed the best properties, $T_{\text{c}}^{\text{on}} - T_{\text{c}}^{\text{end}} = 30.8\text{ K} - 25.8\text{ K}$ and $\text{RRR} = R(300\text{ K})/R(T_{\text{c}}^{\text{on}}) = 3.56$.

Further optimization of the growth conditions such as a slight increase in the growth temperature to 340°C resulted in substantial improvement of the superconducting properties of the films. Our best film of (Sr,K)-122 showed a fairly sharp superconducting transition with $T_{\text{c}}^{\text{on}} - T_{\text{c}}^{\text{end}} = 33.2\text{ K} - 30.0\text{ K}$ and $\rho(300\text{ K}) = 400\text{ }\mu\Omega\text{cm}$. The film had a $c_{\text{film}} = 13.04\text{ \AA}$, corresponding to $x = 0.465$, which is close to the optimum composition for $\text{Sr}_{1-x}\text{K}_x\text{Fe}_2\text{As}_2$. Our best T_{c} of (Sr,K)-122 is slightly lower than the value ($\sim 36\text{ K}$) reported for bulk single crystals. A similar optimization has been performed for (Ba,K)-122 growth. Our best (Ba,K)-122 film grown at $T_s = 340^{\circ}\text{C}$ showed $T_{\text{c}}^{\text{on}} - T_{\text{c}}^{\text{end}} = 38.3\text{ K} - 35.5\text{ K}$ and $\rho(300\text{ K}) = 300\text{ }\mu\Omega\text{cm}$. The film had a

$c_{\text{film}} = 13.28\text{ \AA}$, corresponding to $x = 0.335$, which is close to the optimum composition for $\text{Ba}_{1-x}\text{K}_x\text{Fe}_2\text{As}_2$.

5.1.3. Systematic x dependence in $\text{Ba}_{1-x}\text{K}_x\text{Fe}_2\text{As}_2$ films.

Next we attempted to grow $\text{Ba}_{1-x}\text{K}_x\text{Fe}_2\text{As}_2$ films with x varied from 0.0–1.0, and examined the x dependence of the films. Figure 30(a) shows the XRD patterns of the $\text{Ba}_{1-x}\text{K}_x\text{Fe}_2\text{As}_2$ films with $x_r = 0.0 - 1.0$ grown on *r*-cut Al_2O_3 . Here we denoted the nominal doping level by x_r , which represents the flux ratio of Ba : K ($1 - x_r : 2x_r$). The BaFe_2As_2 films were grown at $T_s = 580^{\circ}\text{C}$ in $P_{\text{As}} = 2 \sim 4 \times 10^{-7}$ Torr and the K-doped $\text{Ba}_{1-x}\text{K}_x\text{Fe}_2\text{As}_2$ films were grown at $T_s = 340^{\circ}\text{C}$ in $P_{\text{As}} = 2 \sim 4 \times 10^{-8}$ Torr (Takeda *et al* 2010). The XRD patterns reveal only the (00*l*) reflections of the 122 phase, indicating that the films are single phased and *c*-axis oriented. A streaky RHEED pattern was observed during growth, indicating that the films grown are in-plane aligned and smooth. The XRD peaks,

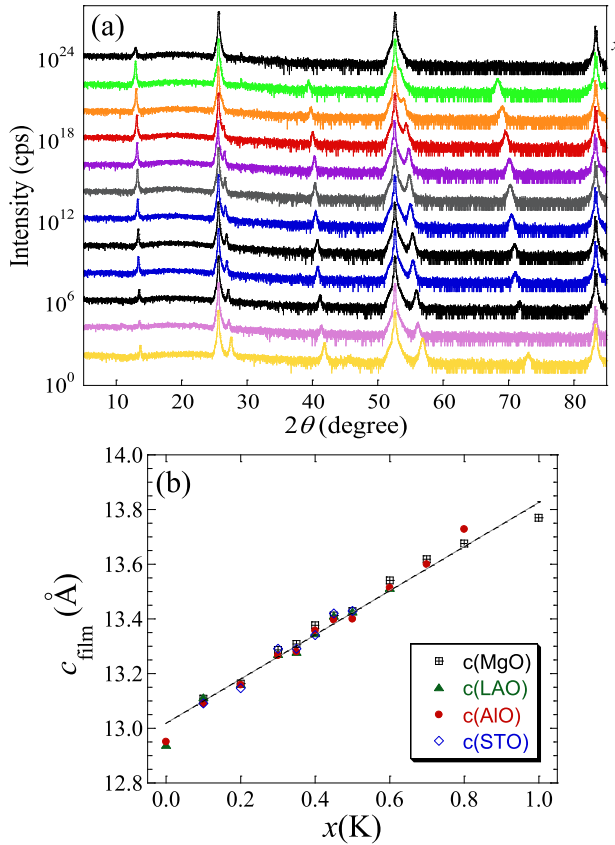


Figure 30. (a) XRD patterns of $\text{Ba}_{1-x}\text{K}_x\text{Fe}_2\text{As}_2$ films grown on *r*-cut Al_2O_3 with $x_r = 0.0\text{--}1.0$. The c_{film} of $\text{Ba}_{1-x}\text{K}_x\text{Fe}_2\text{As}_2$ films grown on *r*-cut Al_2O_3 , MgO , LaAlO_3 , and SrTiO_3 are plotted as a function of x_r in (b). The values reported for the bulk samples are denoted by the dashed line. (a) Rotter *et al* (2008b) John Wiley & Sons. Copyright © 2008 WILEY-VCH Verlag GmbH & Co. KGaA, Weinheim. (b) Reprinted from Yamagishi *et al* (2011), Copyright 2011, with permission from Elsevier.

especially higher $(00l)$, of the KFe_2As_2 films are faint, probably due to the rapid degradation of KFe_2As_2 films in air, which did not allow the evaluation of a reliable c_{film} . The coating of Q-dope did not work well for films with high K doping levels.

Figure 30(b) shows the c_{film} versus x_r relationship of $\text{Ba}_{1-x}\text{K}_x\text{Fe}_2\text{As}_2$ films grown on various substrates. The data points of the thin films are close to the values reported for the bulk samples in Rotter *et al* (2008b), which are denoted by the dashed line. It should also be noted that one sees almost no substrate dependence of the c_{film} , implying that the films have no epitaxial strain.

Figure 31 shows the doping dependence of the superconducting and transport properties of the $\text{Ba}_{1-x}\text{K}_x\text{Fe}_2\text{As}_2$ films. Figure 31(a) shows an enlarged view of the superconducting transition. The absolute value of the resistivity is not reliable due to the degradation of the films, especially with high x_r , in air. So we plotted the normalized resistance ($R(T)/R(300 \text{ K})$) as a function of temperature. A systematic evolution of the normalized resistance curves with x can be seen up to $x_r = 0.7$. Figures 31(b) and (c) summarize the K

doping dependence of the $\text{Ba}_{1-x}\text{K}_x\text{Fe}_2\text{As}_2$ films: (b) T_c and (c) $r = R(300 \text{ K})/R(T_c^{\text{on}})$ (or $r = R(300 \text{ K})/R(4.2 \text{ K})$ for the non-superconducting film) as a function of the doping level, x_c , where x_c denotes the actual doping level deduced from the c_{film} , using a linear interpolation of $c_{\text{bulk}} = 13.0168 + 0.8118x$ reported for the bulk $\text{Ba}_{1-x}\text{K}_x\text{Fe}_2\text{As}_2$ samples (Rotter *et al* 2008b). The T_c is the highest for $x_c \sim 0.30$, $T_c^{\text{on}} = 38.3 \text{ K}$ ($T_c^{\text{end}} = 35.5 \text{ K}$). Further K doping gradually reduces T_c , eventually to $\sim 10 \text{ K}$ at $x_c = 0.82$. A few articles reported T_c versus x_c for $\text{Ba}_{1-x}\text{K}_x\text{Fe}_2\text{As}_2$ using bulk polycrystalline samples or single crystals. The results differed substantially: optimum x (x_{opt}) ~ 0.35 in Rotter *et al* (2008b) and $x_{\text{opt}} \sim 0.50$ in Chen *et al* (2009) though the highest T_c is almost the same, 38 K–39 K. Our T_c versus x_c curve is close to the one obtained by Rotter *et al* (2008b) but not to the others (Luo *et al* 2008, Chen *et al* 2009).

5.2. Growth of $(\text{Ba},\text{Ln})\text{Fe}_2\text{As}_2$ by PLD

The partial substitution of divalent alkaline earth ions (Ba^{2+} and Sr^{2+}) by monovalent alkaline ions (K^+ and Na^+) dopes holes in the FeAs layer whereas the partial substitution of alkaline earth ions by trivalent lanthanide ions (Ln^{3+}) should dope electrons in the FeAs layer. But $(\text{Ba}_{1-x}\text{Ln}_x)\text{Fe}_2\text{As}_2$ has not been synthesized in the form of bulk. Katase *et al* (2012a) attempted electron doping by fabricating $(\text{Ba}_{1-x}\text{La}_x)\text{Fe}_2\text{As}_2$ thin films by PLD. This study also proved one of the advantages of thin-film growth which is that it stabilizes non-equilibrium phases.

As stated above, $(\text{Ba}_{1-x}\text{La}_x)\text{Fe}_2\text{As}_2$ bulk targets have not been fabricated. Hence, La-added BaFe_2As_2 pellets with various doping levels were prepared and served as PLD targets. $(\text{Ba}_{1-x}\text{La}_x)\text{Fe}_2\text{As}_2$ thin films were fabricated on $\text{MgO}(001)$ substrates by PLD with a second harmonics of Nd:YAG laser. The growth temperature was fixed at $850 \text{ }^\circ\text{C}$. All the films were grown in cube-on-cube epitaxy with high phase purity. Here the La content (x) of the films was determined by EPMA.

Resistivity traces for all the films are shown in figure 32(a). The resistivity anomaly due to the magnetic transition was shifted to lower temperatures as the La doping (x) was increased. At $x = 0.08$ the film showed superconductivity and the superconducting transition temperature T_c is observed to increase with increasing x . The highest T_c of 22.3 K was recorded at $x = 0.13$. Based on the resistivity data, the electronic phase diagram of $(\text{Ba}_{1-x}\text{La}_x)\text{Fe}_2\text{As}_2$ was constructed (figure 32(b)). Interestingly, the phase diagram of the $(\text{Ba}_{1-x}\text{La}_x)\text{Fe}_2\text{As}_2$ thin film is almost identical to that of the $\text{Ba}(\text{Fe}_{1-x}\text{Co}_x)_2\text{As}_2$ thin film, which will be presented below, in the underdoped regime. On the other hand, the superconductivity of $(\text{Ba}_{1-x}\text{La}_x)\text{Fe}_2\text{As}_2$ was suppressed faster than that of $\text{Ba}(\text{Fe}_{1-x}\text{Co}_x)_2\text{As}_2$ in the overdoped regime.

Katase *et al* (2013) further extended their studies to various rare-earth (Ln : Ce, Pr, Nd and Sm) doping into BaFe_2As_2 . All the $(\text{Ba}_{1-x}\text{Ln}_x)\text{Fe}_2\text{As}_2$ thin films were prepared by PLD using the same setup and deposition conditions as stated above. All the rare-earth elements except for Sm were successfully doped into the Ba-site in epitaxial BaFe_2As_2 thin

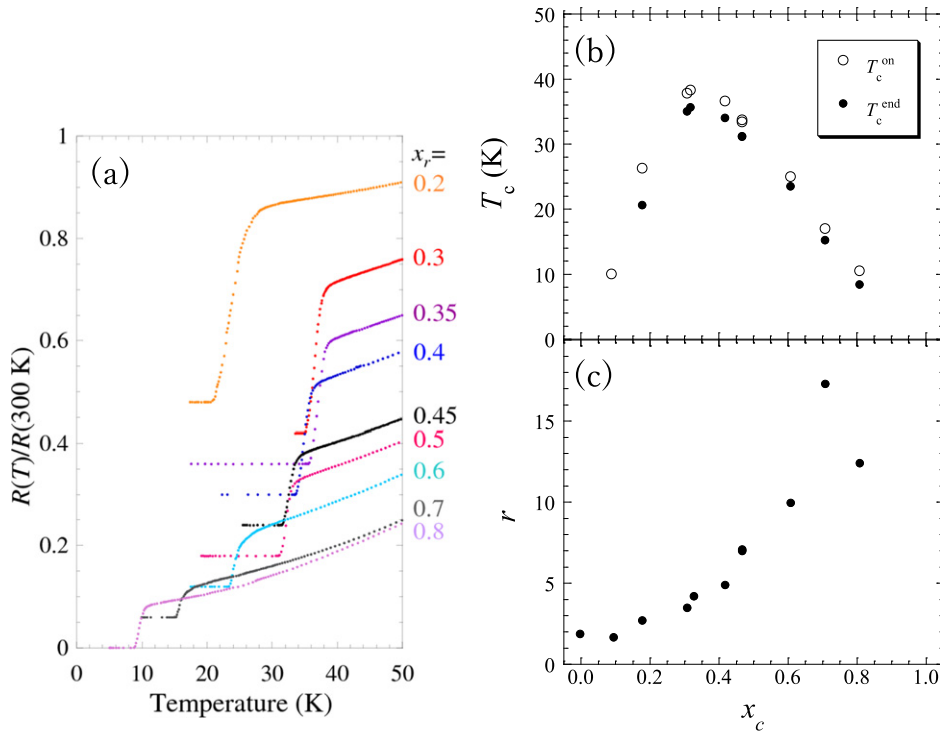


Figure 31. (a) Superconducting transition in $\text{Ba}_{1-x}\text{K}_x\text{Fe}_2\text{As}_2$ with x systematically varied. The vertical axis is the normalized resistance ($R(T)/R(300 \text{ K})$). For clarity, normalized resistance curves are shifted vertically by 0.06 units successively. The films with $x_r = 0.0\text{--}0.7$ were grown on r -cut Al_2O_3 and the film with $x_r = 0.8$ was grown on MgO . In (b) and (c), the doping dependence of the $\text{Ba}_{1-x}\text{K}_x\text{Fe}_2\text{As}_2$ films are summarized: (b) T_c and (c) $r = R(300 \text{ K})/R(T_c^{\text{on}})$ (or $r = R(300 \text{ K})/R(4.2 \text{ K})$ for the non-superconducting films). The data are plotted as a function of x_c . The highest T_c is attained at $x_c \sim 0.30$. Reprinted from Yamagishi *et al* (2011), Copyright 2011, with permission from Elsevier.

films. The solubility limit for Ce, Pr, and Nd were 0.30, 0.28, and 0.20, respectively, as determined by EPMA. The different solubility limit is due to the ionic size mismatch between Ln and Ba. The T_c^{on} values are 13.4 K for $Ln = \text{Ce}$ and 6.2 K for $Ln = \text{Pr}$.

5.3. Growth of Ca-based 122 films

As described in the previous sections, high-quality Ba-122 epitaxial thin films have been readily fabricated by many groups. In contrast, CaFe_2As_2 thin films have not been studied well so far. A fundamental problem is the high vapor pressure of Ca, which leads to difficulty in controlling the film stoichiometry. Nevertheless, Katase *et al* (2012b) made a first attempt to grow CaFe_2As_2 films by PLD using a stoichiometric target $\text{Ca}(\text{Fe}_{0.97}\text{Co}_{0.03})_2\text{As}_2$ but did not succeed. It seems to be difficult to grow CaFe_2As_2 thin films by PLD due mainly to the high vapor pressure of Ca. Since then, the research activity into CaFe_2As_2 thin films declined. After the discovery of high- T_c over 40 K in $(\text{Ca},\text{La})\text{Fe}_2\text{As}_2$ (Lv *et al* 2011, Gao *et al* 2011, Saha *et al* 2012, Kudo *et al* 2013), however, the research into CaFe_2As_2 thin films gained renewed interest.

Iida *et al* (2018) implemented the Fe-buffer layer for facilitating the phase formation of CaFe_2As_2 . Figure 33 exhibits the out-of-plane x-ray diffraction pattern of $\text{CaFe}_2\text{As}_2/\text{Fe}$ bilayers on $\text{MgO}(001)$ substrates.¹² CaFe_2As_2

¹² The description of bilayers is defined as $\text{CaFe}_2\text{As}_2/\text{Fe}$, where the primary layer represents Fe and the second layer (i.e., CaF_2As_2) is deposited on the primary layer.

thin films were deposited on Fe-buffered MgO by ablating CaFe_2As_2 and Pr-doped CaFe_2As_2 sintered pellets using a KrF excimer laser (frequency of 7 Hz and energy density of 3 J cm^{-2}) at 675°C . The details of the Fe-buffer layer preparation was found in Thersleff *et al* (2010). It is clear from figure 33 that the $(00l)$ reflections of CaFe_2As_2 together with the (hhk) reflections of FeAs are observed except for the substrate and Fe peaks, indicative of loss of Ca. Hence, employing a Ca-rich PLD target may lead to phase-pure CaFe_2As_2 . Nevertheless, these results highlight a phase formation of CaFe_2As_2 by PLD. However, Pr may not be incorporated into CaFe_2As_2 , since no peak shifts between CaFe_2As_2 and Pr-doped CaFe_2As_2 are observed. The superconductivity for both $(\text{Ca},\text{Pr})\text{Fe}_2\text{As}_2$ and CaFe_2As_2 thin films was not confirmed in resistivity measurements down to 2 K.

Hatano *et al* (2016) reported the first successful growth of phase-pure and epitaxial CaFe_2As_2 on $\text{CaF}_2(001)$ and LSAT(001) substrates by MBE using Ca, Fe, and As solid sources. The key to successful growth was to control the Ca flux precisely and to employ relatively low deposition temperatures between 600°C and 700°C . Although a flux ratio of $P_{\text{Ca}}/P_{\text{Fe}} \sim 0.5$ produced CaFe_2As_2 , a certain amount of impurities were detected due probably to the loss of Ca. Hence, the flux ratio was increased to $P_{\text{Ca}}/P_{\text{Fe}} \sim 1.0$ in order to compensate for the loss of Ca. As a result, phase-pure and c -axis oriented CaF_2As_2 films were grown on most of the substrates (figure 34(a)). CaO was detected as an impurity phase when the films were deposited on $\text{SrTiO}_3(001)$ and $\text{LaAlO}_3(001)$. The ϕ -scan of the (103)

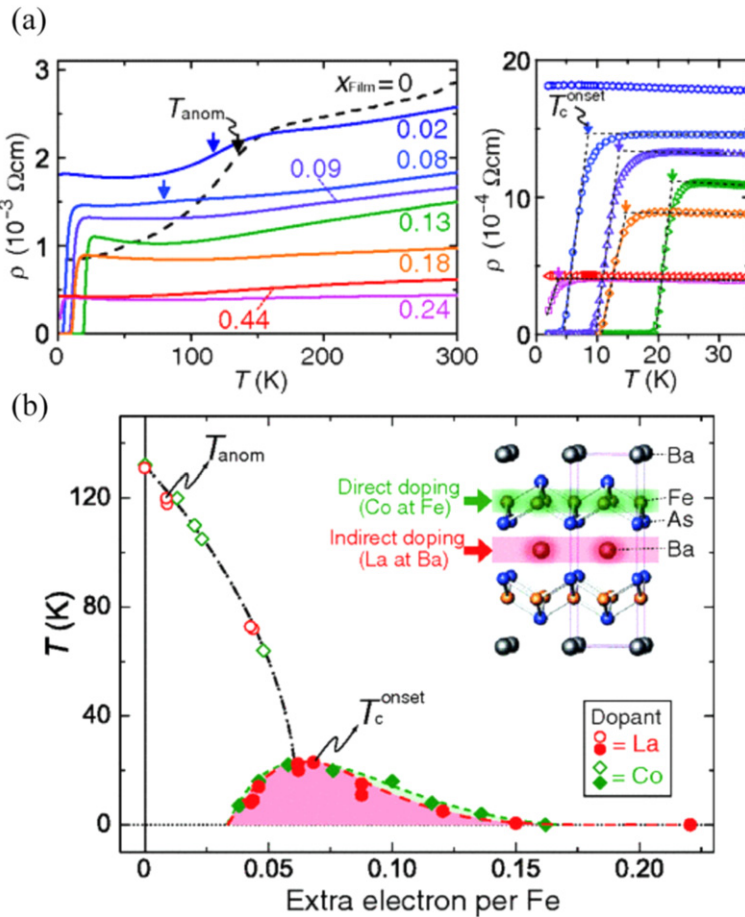


Figure 32. (a) Resistivity curves of the $(\text{Ba}_{1-x}\text{La}_x)\text{Fe}_2\text{As}_2$ thin films. (b) Electronic phase diagram of the $(\text{Ba}_{1-x}\text{La}_x)\text{Fe}_2\text{As}_2$ thin films. The corresponding phase diagram of the $\text{Ba}(\text{Fe}_{1-x}\text{Co}_x)_2\text{As}_2$ thin films is also shown for comparison. Reprinted figure with permission from Katase *et al* (2012a), Copyright 2012 by the American Physical Society.

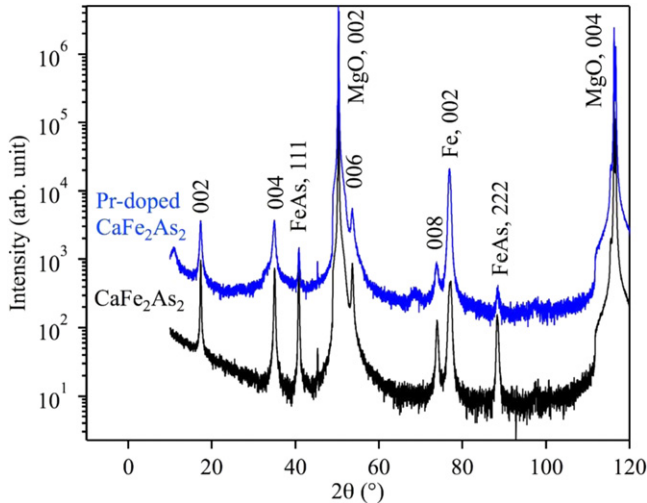


Figure 33. Out-of-plane x-ray (Co-K α radiation) diffraction patterns of $\text{CaFe}_2\text{As}_2/\text{Fe}$ bilayers prepared by PLD on $\text{MgO}(001)$ substrates: the upper trace represents Pr-doped CaFe_2As_2 and the lower one is pristine CaFe_2As_2 .

reflection revealed that 45° rotated grains were present for the films prepared on the LaAlO_3 , SrTiO_3 , MgAl_2O_4 , and MgO substrates (figure 34(b)). One would expect strain-driven

superconductivity as demonstrated by Engelmann *et al* (2013b). Indeed, the c -axis lattice constant for all the films were elongated irrespective of the lattice mismatch and hence strain was exerted into the films (figure 34(c)). It has been reported that in-plane compressive strain (i.e., elongation of the c -axis due to the Poisson effect) reduces the k_z dispersion of the Fe $3d_{xz/yz}$ orbitals, leading to an increase in T_{SDW} (T_N) (Iida *et al* 2016). In fact, the T_{SDW} of all the films were higher than that of single crystals (figure 35(b)). Hence, in-plane compressive strain is not favorable for superconductivity. However, some of the films showed a sign of superconductivity at low temperatures (figure 35(a)). Among them, CaFe_2As_2 on MgAl_2O_4 exhibited an aging effect: the superconducting transition was pronounced after 12 days. On the other hand, CaFe_2As_2 on LSAT did not show any sign of an aging effect and hence high stability, although the film had an almost similar c -axis length and T_{SDW} to those of the CaFe_2As_2 on MgAl_2O_4 . A structural assessment by XRD revealed that CaFe_2As_2 on LSAT showed high crystallinity ($\Delta\omega \sim 0.18^\circ$ and $\Delta\phi \sim 0.24^\circ$). Hence, it can be speculated that the films on MgAl_2O_4 absorbed H_2O due to defects in structure or to poor crystalline quality, leading to a local strain and hence inducing superconductivity.

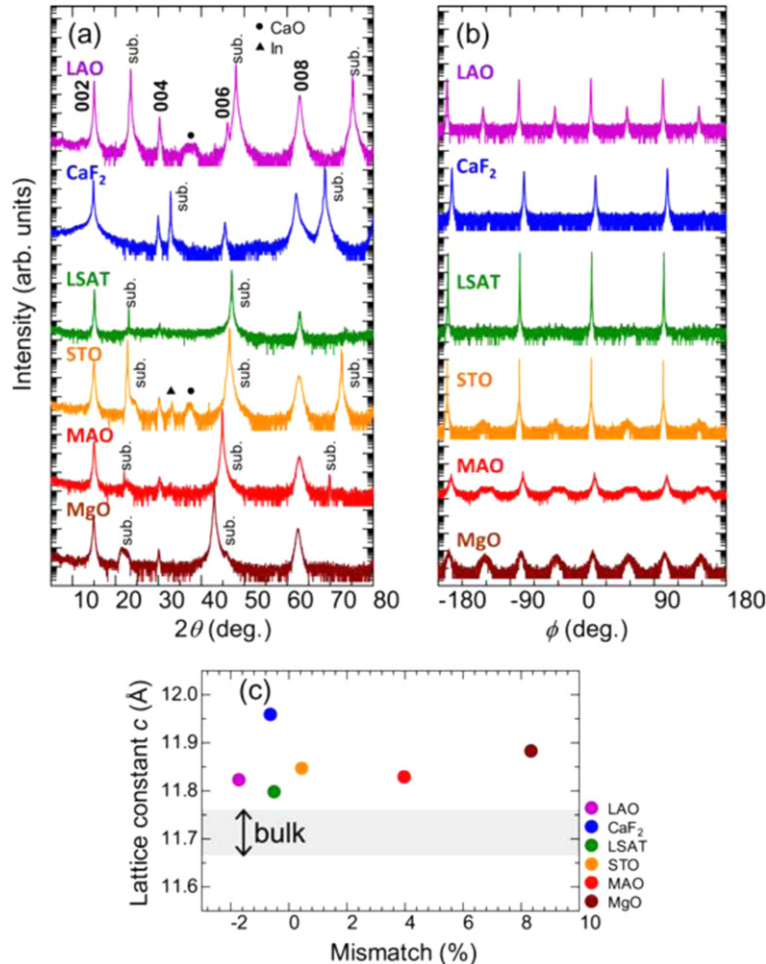


Figure 34. (a) X-ray $\theta/2\theta$ scans of CaFe₂As₂ thin films deposited by MBE on various substrates and (b) the corresponding ϕ scan of the (103) reflection. (c) The c -axis lattice parameter as a function of lattice mismatch. LAO, STO, and MAO are the abbreviations for LaAlO₃, SrTiO₃, and MgAl₂O₄, respectively. The lattice mismatch was calculated by $100 \times (a_{\text{sub}} - a_{\text{Ca-122}})/a_{\text{Ca-122}}$, where a_{sub} and $a_{\text{Ca-122}}$ were the substrate lattice parameter and the a -axis of CaFe₂As₂ (Ca-122). Reproduced Hatano *et al* (2016). © IOP Publishing Ltd. All rights reserved.

5.4. Growth of BaFe₂(As,P)₂

5.4.1. Growth of BaFe₂(As,P)₂ by PLD. Although epitaxial (Ba_{1-x}K_x)Fe₂As₂ thin films can be fabricated by MBE (see section 5.1.2), it seems to be difficult to grow biaxial textured K-doped BaFe₂As₂ thin films by *in situ* PLD due to the difficulty in incorporating volatile K into the Ba-site. In such circumstances, there is a considerable interest in BaFe₂(As_{1-x}P_x)₂, since this material is the second highest T_c (~ 31 K) in the Ba-122 system (Kasahara *et al* 2010). Most importantly, P is a low vapor pressure compared with K, expecting a good controllability of the film stoichiometry. Indeed, Adachi *et al* (2012) reported the epitaxial growth of P-doped BaFe₂As₂ thin films on MgO(001) substrates by PLD. The sintered polycrystalline BaFe₂(As_{0.6}P_{0.4})₂ disk was ablated with a second harmonic (2 ω) Nd:YAG laser at a frequency of 10 Hz. The resultant film showed a T_c of 26.5 K and a high self-field critical current density (J_c) of 3.5 MA cm⁻² at 4.2 K. Additionally, the in-field J_c properties

of P-doped BaFe₂As₂ were better than that of Co-doped BaFe₂As₂, above 10 K. Following this study, several papers were published. Note that a Nd:YAG (2 ω) laser was used for all the research.

Miura *et al* (2013b) investigated the effect of the P content on the superconducting properties of BaFe₂(As_{1-x}P_x)₂ thin films on MgO. The maximal T_c (28.9 K) was achieved for the film prepared from the stoichiometric BaFe₂(As_{0.66}P_{0.33})₂ target. The phosphorous content of the resultant film was $x = 0.28$, indicative of the stoichiometric transfer from the target to the film not having been preserved. The optimally P-doped BaFe₂As₂ thin film showed the lowest upper critical field (H_{c2}) anisotropy ($\gamma_{Hc2} = 1.54$) as well as the highest irreversibility field.

Adachi *et al* (2014) prepared BaFe₂(As_{1-x}P_x)₂ films on LSAT(001) and obtained the highest T_c ($T_c^{\text{on}} = 30.6$ K) among the PLD-processed BaFe₂(As_{1-x}P_x)₂ despite a lack of P content ($x = 0.144$). The film has longer a_{film} (~ 3.954 Å) than a_{bulk} (3.92 Å) and appears to be given tensile

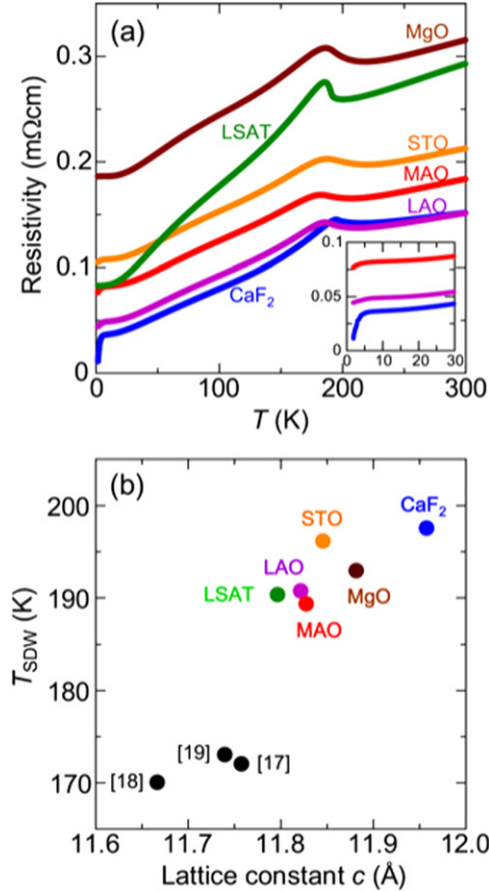


Figure 35. (a) Resistivity traces of MBE-grown CaFe₂As₂ thin films as a function of temperature. (b) Relationship between T_{SDW} and the c -axis lattice parameter. The data of the bulk samples [17], [18], and [19] are also plotted for comparison. Here [17], [18], and [19] correspond to the data by Ronning *et al* (2008), Ni *et al* (2008), and Goldman *et al* (2008), respectively. Reproduced from Ronning *et al* (2008) and Hatano *et al* (2016). © IOP Publishing Ltd. All rights reserved.

strain despite $a_{\text{sub}}(\text{LSAT}) < a_{\text{bulk}}$. The authors speculated that the presence of reaction layer between the film and LSAT observed by transmission electron microscopy (TEM) may be a reason for such high T_c accompanied with in-plane tensile stress.

5.4.2. $\text{BaFe}_2(\text{As}_{1-x}\text{P}_x)_2$ grown by MBE and epitaxial strain effect. High-quality epitaxial BaFe₂(As_{1-x}P_x)₂ thin films have been also realized on MgO(001) by the Nagoya group employing MBE (Sakagami *et al* 2013). The highest T_c was nearly 30 K, although the P content was lower than the optimally P-doped BaFe₂As₂ single crystal. Later, Kawaguchi *et al* (2014) constructed an electronic phase diagram of BaFe₂(As_{1-x}P_x)₂ thin films on both LaAlO₃(001) and MgO (001), as depicted in figure 36. They grew films on LaAlO₃ at 710 °C. However, higher growth temperatures between 800 °C and 900 °C were required for the growth of films on MgO. As can be seen, the superconducting dome of the films on the LaAlO₃ substrates is almost identical to that of single crystals, whereas the corresponding dome for the films on the MgO substrates is shifted to a lower P content. The authors

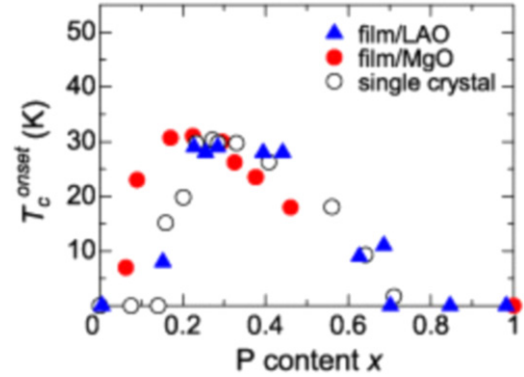


Figure 36. Superconducting domes (i.e., T_c versus P-doping level) of the BaFe₂(As_{1-x}P_x)₂ thin films prepared by MBE on LaAlO₃(001) and MgO(001). Reproduced from Kawaguchi *et al* (2014). © IOP Publishing Ltd. All rights reserved.

explained the shift of the superconducting dome by in-plane tensile strain that changes the local structure. It was reported that in-plane tensile strain increases the k_z dispersion of the Fe $3d_{xz/yz}$ orbitals on the Fermi surface hole pockets, which leads to the decrease in T_N (Iida *et al* 2016). The degree of the shift in the superconducting dome correlates with T_N : lower T_N pulls the superconducting dome towards the underdoped side.

5.4.3. Grain boundary properties. The Nagoya group also prepared a P-doped BaFe₂As₂ thin film on a [001]-tilt MgO bicrystal substrate with a misorientation angle of $\theta_{\text{GB}} = 24^\circ$ by MBE (Sakagami *et al* 2013). The I - V characteristics of the P-doped BaFe₂As₂ grain boundary junction are shown in figure 37(a). At 2 K, an $I_c R_N$ product of 37.4 μV was obtained, where I_c is the Josephson critical current and R_N is the normal resistance of the barrier. Correspondingly, an R_{NA} value of $1.3 \times 10^{-10} \Omega \text{ cm}^{-2}$ was calculated, where A is the cross-sectional area of the barrier, indicative of the metallic nature of the grain boundary. Figure 37(b) shows how self-field J_c of P-doped BaFe₂As₂ is affected by θ_{GB} . On the assumption that P-doped BaFe₂As₂ has the same critical angle (θ_c) as Co-doped BaFe₂As₂ (Katase *et al* 2011b), where J_c starts to fall off exponentially, both films are almost identical to one another in the decay rate of inter-grain J_c . It is noted that the absolute value of J_c is substantially higher for P-doped BaFe₂As₂ than for Co-doped BaFe₂As₂, which will be discussed in section 5.4.4.

5.4.4. Pinning enhancement. Kurth *et al* (2015) reported a high self-field J_c of 6.3 MA cm^{-2} at 4.2 K for P-doped BaFe₂As₂ thin film prepared by MBE on MgO(001), despite its clean microstructure. Chemical analysis by EPMA revealed a P content of $\text{P}/(\text{As}+\text{P}) = 0.22$ for the resultant film. Although the P level is lower than the optimal doping for single crystals, the film showed a high T_c of 30.7 K due to the in-plane tensile strain as discussed in section 5.4.2. This means that the doping level for the film is optimal on MgO. It was reported that vortex core energy of flux lines is enhanced close to the optimal P doping (Putzke *et al* 2014). Hence, the

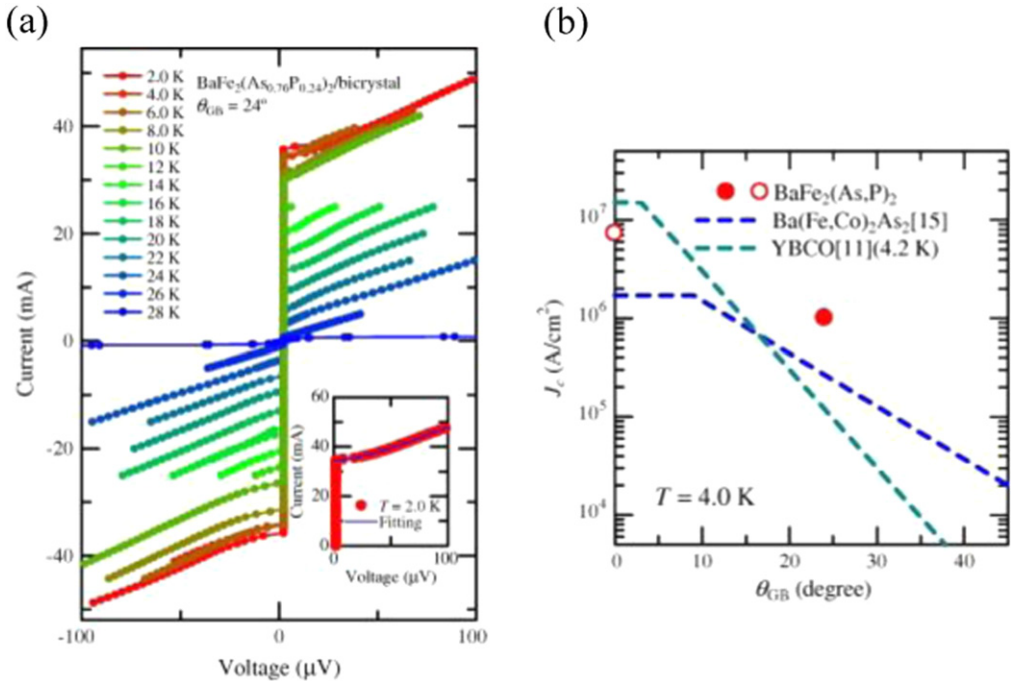


Figure 37. (a) I - V curves of a P-doped BaFe_2As_2 grain boundary junction with $\theta_{\text{GB}} = 24^\circ$. The inset represents the fitting curve to the I - V measured at 2 K. (b) Misorientation angle (θ_{GB}) dependence of the self-field J_c for an optimally P-doped BaFe_2As_2 thin film measured at 4 K. For comparison, Co-doped BaFe_2As_2 and $\text{YBa}_2\text{Cu}_3\text{O}_7$ data were also plotted. Reprinted from Sakagami *et al* (2013), Copyright 2013, with permission from Elsevier.

authors claimed that the unexpected high J_c was attributed to a strong enhancement of the vortex core energy at optimal P doping.

Miura *et al* (2013a) reported that in-field J_c properties of a PLD-grown $\text{BaFe}_2(\text{As}_{0.72}\text{P}_{0.28})_2$ thin film are suppressed faster than Co-doped BaFe_2As_2 with c -axis correlated defects (i.e. pinning centers), which are described below (section 5.5.4), at given field and temperature. The authors relate this poor J_c property of P-doped BaFe_2As_2 to the low density of c -axis correlated defects. Indeed, their hypothesis was justified by the experimental observation that no peak was observed for $H \parallel c$ in the angular dependence of the J_c measurements. In order to improve the J_c properties, Miura *et al* (2013b) introduced BaZrO_3 into P-doped BaFe_2As_2 , which is the same tactics for pinning improved $\text{YBa}_2\text{Cu}_3\text{O}_7$ by BaZrO_3 (MacManus-Driscoll *et al* 2004). As a result, nano-sized BaZrO_3 particles were dispersed into P-doped BaFe_2As_2 matrices, which led to a significant enhancement of in-field J_c (figure 38(a)). As can be seen, the J_c for BaZrO_3 -added $\text{BaFe}_2(\text{As}_{1-x}\text{P}_x)_2$ thin films were improved in the whole angular range compared with a pristine $\text{BaFe}_2(\text{As}_{1-x}\text{P}_x)_2$ film (figure 38(b)).

Sato *et al* (2014) proposed another approach for the improvement of the vortex pinning. First, the authors investigated the optimum growth temperature (T_s) for P-doped BaFe_2As_2 on $\text{MgO}(001)$ by PLD at a fixed growth rate of $\sim 3 \text{ \AA s}^{-1}$. They concluded that epitaxial films are obtained in the temperature range of $1000^\circ\text{C} \leqslant T_s \leqslant 1100^\circ\text{C}$. After the optimization of T_s they also investigated the effect of the growth rate on the microstructures. Figure 39

shows the cross-sectional bright-field scanning transmission electron microscopy (STEM) images of P-doped BaFe_2As_2 epitaxial films employing different growth rates. Clearly, the film grown at a growth rate of 2.2 \AA s^{-1} contained a number of c -axis correlated (vertical) defects (figure 39(a)). On the other hand, most of the defects in the film grown at 3.3 \AA s^{-1} are tilted from the substrate normal (figure 39(b)). Chemical analysis proved that the composition of those defects is the same as that of film matrix (figures 39(c) and (d)). Therefore, those defects are edge/threading dislocations or domain boundaries. The angular dependence of J_c for P-doped BaFe_2As_2 epitaxial films reflects these microstructures. The lower growth rate (2.2 \AA s^{-1}), which produced a number of vertical defects, results in a large c -axis peak of J_c . Accordingly the film grown at a growth rate of 2.2 \AA s^{-1} showed good in-field J_c performances at 4.2 K: J_c for both major crystallographic directions exceeding 1 MA cm^{-2} at 6 T.

Sato *et al* (2016) also prepared P-doped BaFe_2As_2 thin films on technical substrates on which a textured MgO template was deposited by ion beam assisted deposition (IBAD- MgO). In this investigation, they employed two different IBAD- MgO templates: one was $\Delta\phi_{\text{MgO}} = 4^\circ$ (well-aligned) and the other was $\Delta\phi_{\text{MgO}} = 8^\circ$ (poorly aligned). The TEM characterizations revealed that the texture of the MgO transferred to the P-doped BaFe_2As_2 thin films created dislocation networks. Furthermore, the film on the poorly aligned IBAD- MgO contained a higher density of grain boundaries with small misorientation angles (θ_{GB}) compared with the film on the well-aligned IBAD- MgO .

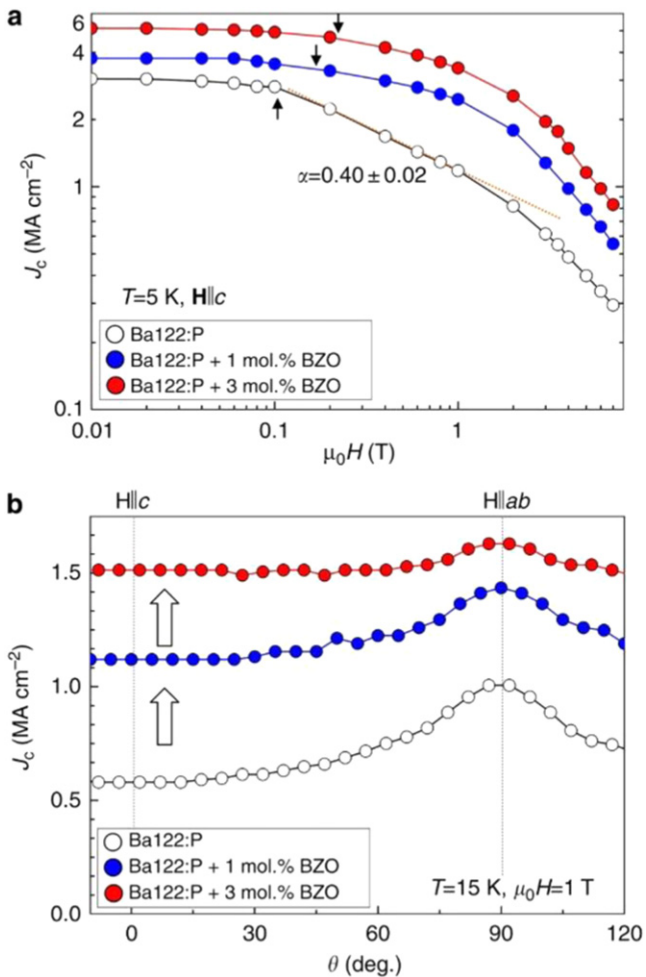


Figure 38. (a) J_c - H properties of optimally P-doped BaFe_2As_2 thin films with BaZrO_3 (BZO) addition measured at 5 K. The arrows represent the transition field from the single vortex pinning state to weak collective pinning state, which is gradually increased by BZO addition. (b) Angular dependence of J_c for the corresponding films measured at 15 K under a magnetic field of 1 T. The arrows indicate the J_c enhancement by BZO addition. Reprinted by permission from Springer Nature: Nature Communications (Miura *et al* 2013b) Copyright 2013 CC BY 3.0.

Based on the relationship between θ_{GB} and the averaging dislocation spacing, the respective θ_{GB} for the films on the well-aligned and poorly aligned IBAD-MgO were calculated to be 1.3° – 2.4° and 3.6° – 5.9° ¹³. On the assumption that the critical grain boundary misorientation angle (θ_c) for the P-doped BaFe_2As_2 is the same as for the Co-doped BaFe_2As_2 , namely 9° , the dislocation networks mentioned above enhance the vortex pinning. Hence, one can expect that the in-field J_c properties of the film on the poorly aligned IBAD-MgO are superior to those of the film on the well-aligned template. In fact, this hypothesis was experimentally proved, as shown in figure 40. Later, it was reported that grain boundaries work as flux pinning by analyzing the pinning force density (Iida *et al* 2017). At 12 K, both films showed almost the same in-field J_c , even though the T_c^{zero} of the film on the poorly aligned IBAD-MgO was 19 K, 4 K lower than the film on the well-aligned template. Further optimized

P-doped BaFe_2As_2 on the poorly aligned IBAD-MgO has higher in-field J_c properties than MgB_2 and NbTi at 4.2 K, and similar to Nb_3Sn above 20 K (figure 40(e)).

5.5. Growth of $\text{Ba}(\text{Fe}_{1-x}\text{Co}_x)_2\text{As}_2$ by PLD

5.5.1. Film growth. Among the PLD-processed Fe-based superconducting thin films, Co-doped BaFe_2As_2 (Ba-122) has been most well studied thanks to its easy preparation and high stability at an ambient condition. To date, six groups have fabricated high-quality epitaxial Co-doped Ba-122 thin films by PLD. Table 5 summarizes the deposition conditions of the six groups for Co-doped Ba-122 thin films. The first epitaxial Co-doped Ba-122 thin films were fabricated on LSAT using a second harmonic Nd:YAG laser by Katase *et al* (2009). The film showed an atomically flat terrace-and-step surface. Most importantly, Co-doped Ba-122 is highly stable against H_2O vapor compared with Co-doped SrFe_2As_2 , which has spurred the progress of the research into Co-doped Ba-122 thin films.

One month later, Iida *et al* (2009) reported the growth of Co-doped Ba-122 thin films on the (001) face of various substrates (SrTiO_3 , LSAT, LaAlO_3 , and YAlO_3) using a KrF excimer laser for exploring the effect of strain on T_c . All the films except on YAlO_3 were epitaxially grown. Particularly the film on SrTiO_3 showed the smallest FWHM in the ϕ -scan of the (103) reflection, indicative of the good texture of the film. Additionally, the film showed the highest T_c (24.5 K) owing to the in-plane strain ($c/a \sim 3.34$). It is notable that the T_c almost linearly increased with c/a . However, SrTiO_3 becomes electrically conducting in ultrahigh vacuum at high temperatures due to the creation of oxygen vacancies, which may become an obstacle to transport measurements particularly near the normal-superconducting transition. Later, it was also reported that textured Fe was present at the interface between the films and substrates (Iida *et al* 2010, Hänisch *et al* 2011), which led to the implementation of an Fe buffer layer for the epitaxial growth of Co-doped Ba-122 (Thersleff *et al* 2010).

During the same period, Lee *et al* (2009) reported Co-doped Ba-122 grain boundary junctions using [001]-tilt SrTiO_3 bicrystal substrates (see below). This study also demonstrated that SrTiO_3 may become a good template for epitaxial growth of Co-doped Ba-122. Later, this hypothesis was proved to be true by realizing high crystalline quality Co-doped Ba-122 on SrTiO_3 -buffered LSAT (Lee *et al* 2010b).

The implementation of both buffer layers (i.e., SrTiO_3 and Fe) produces high-quality epitaxial Co-doped Ba-122 thin films. These results were also supported by microstructural analysis: it was reported that FeAs tetrahedron coherently bonds with Fe for $\text{Ba}(\text{Fe}_{1-x}\text{Co}_x)_2\text{As}_2$ /Fe bilayers (Thersleff *et al* 2010). Furthermore, the bonding of the FeAs layer to the SrO layer in SrTiO_3 was confirmed in $\text{SrTiO}_3/\text{Ba}(\text{Fe}_{1-x}\text{Co}_x)_2\text{As}_2/\text{SrTiO}_3$ superlattice (Lee *et al* 2013). The use of buffer layers widens the choice of

¹³ The θ_{GB} was calculated by the following relation, $D = |b|/2 \sin(\theta_{GB}/2)$, where D is the average spacing between dislocations and $|b|$ is the norm of the Burgers vector.

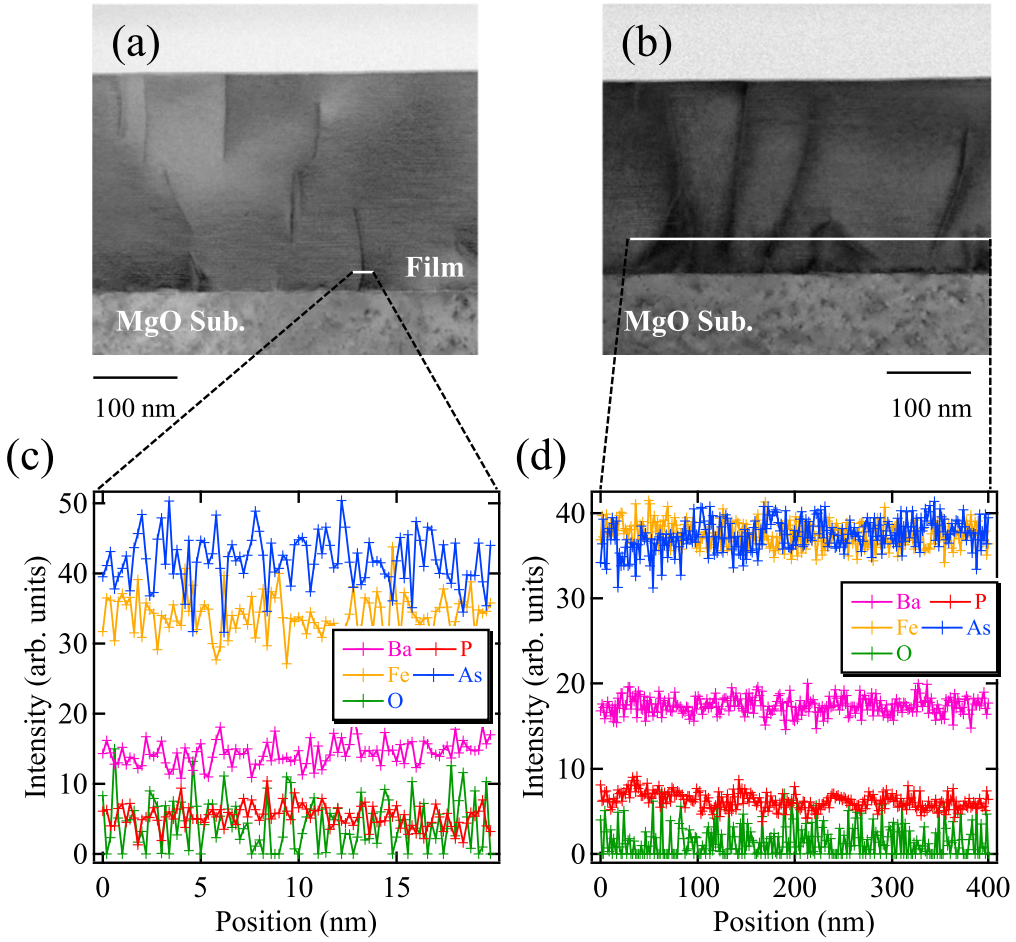


Figure 39. Cross-sectional STEM view of the P-doped BaFe_2As_2 epitaxial thin films at a growth rate of (a) 2.2 \AA s^{-1} and (b) 3.9 \AA s^{-1} . For both films, defects perpendicular to the substrate are clearly seen, however, their density is different. (c) and (d) display the results of an STEM-EDXS line scan along the horizontal white lines shown in (a) and (b). The figure is redrawn with some modifications based on the data taken from figure 4 in Sato *et al* (2014).

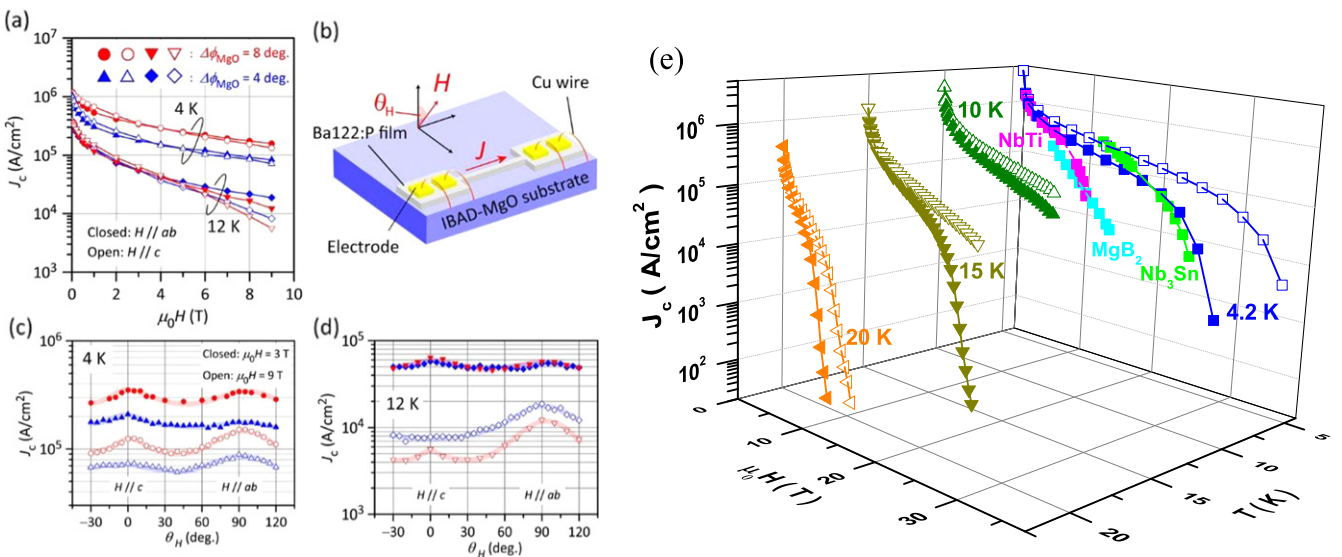


Figure 40. In-field J_c properties of the P-doped BaFe_2As_2 epitaxial films on IBAD-MgO with different in-plane mosaicity. (a) J_c - H properties measured at 4 K and 12 K. (b) Schematic illustration of the configuration of the sample for transport measurements. (c) Angular dependence of J_c measurements at 4 K and (d) 12 K. The closed and open symbols represent $\mu_0 H = 3 \text{ T}$ and 9 T , respectively. Reproduced from Sato *et al* 2016. CC BY 4.0. (e) J_c - H - T properties of P-doped BaFe_2As_2 on technical substrates at different temperatures for $H \parallel c$ (closed symbols) and $H \parallel ab$ (open symbols). The data are taken from Iida *et al* 2017. For comparison, the data for MgB_2 (Li *et al* 2013), NbTi (Boutboul *et al* 2006 and Kanithi *et al* 2014), and Nb_3Sn (Parrell *et al* 2005) are also shown.

Table 5. Brief summary of the conditions for the PLD deposition of $\text{Ba}(\text{Fe}_{1-x}\text{Co}_x)_2\text{As}_2$ films employed by six different institutions, where TIT, CAS, and GIST represent Tokyo Institute of Technology, Chinese Academy of Science, and Gwangju Institute of Science and Technology, respectively. The reference numbers are as follows: [1] Katase *et al* (2009), [2] Katase *et al* (2010), [3] Hiramatsu *et al* (2014a), [4] Mohan *et al* (2010), [5] Katase *et al* (2011a), [6] Lee *et al* (2009), [7] Lee *et al* (2010b), [8] Tarantini *et al* (2014), [9] Iida *et al* (2009), [10] Trommler *et al* (2010), [11] Thersleff *et al* (2010), [12] Iida *et al* (2011b), [13] Rehm *et al* (2013), [14] Engelmann *et al* (2013b), [15] Engelmann *et al* (2013a), [16] Kurth *et al* (2013), [17] Trommler *et al* (2014), [18] Iida *et al* (2016), [19] Lei *et al* (2014), [20] Yuan *et al* (2017b), and [21] Lee *et al* (2017).

Group	Laser	Pressure	Substrates	T_s (°C)
TIT	ArF (193 nm) [3]	5×10^{-7} Pa	LSAT [1, 2, 3], MgO [4]	700 °C [1], 850 °C [2, 3, 4, 5]
	KrF (248 nm) [3]		IBAD-MgO [5]	
	Nd:YAG (532 nm) [1, 2, 4, 5]			
	Nd:YAG (1064 nm)[3]			
University Wisconsin-Madison	KrF(248 nm)	$3 \times 10^{-5} \sim 3 \times 10^{-5}$ Pa	SrTiO ₃ [6]	730 °C–750 °C
IFW Dresden	KrF (248 nm)	1×10^{-7} Pa	SrTiO ₃ and BaTiO ₃ buffered various substrates (LSAT, LaAlO ₃ , GdScO ₃ , Si) [7] CaF ₂ [8] LSAT [9, 11], SrTiO ₃ [9] LaAlO ₃ [9] YAlO ₃ [9], MgO [11, 18] SrTiO ₃ -buffered PMN-PT [10] Fe-buffered MgO [11] Fe-buffered IBAD-MgO [12] Fe-buffered MgAl ₂ O ₄ [13, 14, 15] BaF ₂ [16], SrF ₂ [16], CaF ₂ [16, 18] Fe/MgO/PMN-PT [17], MgO [11, 18]	620 °C–850 °C
Temple University	KrF (248 nm)	$8 \times 10^{-4} \sim 5 \times 10^{-5}$ Pa	LSAT [19], LaAlO ₃ [19] MgO [19], SrTiO ₃ [19] BaF ₂ [19], CaF ₂ [19]	725 °C
CAS GIST	KrF (248 nm)	1.3×10^{-5} Pa	CaF ₂ [20]	700 °C
	KrF (248 nm)	4×10^{-5} Pa	CaF ₂ [21]	700 °C

substrates and enables growing $\text{Ba}(\text{Fe}_{1-x}\text{Co}_x)_2\text{As}_2$ on any substrate. Indeed, epitaxial Co-doped and undoped Ba-122 thin films have been deposited on Fe-buffered IBAD-MgO (Iida *et al* 2011b), Fe-buffered MgAl₂O₄(001) (Rehm *et al* 2013, Engelmann *et al* 2013a, 2013b) and SrTiO₃-buffered Si(001) (Lee *et al* 2010b).

However, Katase *et al* (2010) reported that high- J_c (self-field J_c of 4 MA cm⁻² at 4 K) Co-doped Ba-122 epitaxial thin films were prepared directly on LSAT(001) substrates using a second harmonic Nd:YAG laser by further optimization of the growth parameters. Furthermore, epitaxial $\text{Ba}(\text{Fe}_{1-x}\text{Co}_x)_2\text{As}_2$ thin films were also realized on MgO(001) substrates despite a large lattice mismatch of 6% (Mohan *et al* 2010). Recently, Iida *et al* (2016) also reported that epitaxial Ba($\text{Fe}_{1-x}\text{Co}_x$)₂As₂ thin films with various x were prepared on MgO using a KrF excimer laser.

Later, Hiramatsu *et al* (2014a) investigated the effect of laser wavelength of PLD on the crystalline quality and J_c properties of Co-doped Ba-122 on LSAT substrates. They concluded that the key to epitaxial growth with good crystalline quality is the precise control of the deposition rate ($3 \sim 4 \text{ \AA s}^{-1}$) regardless of laser wavelength. Fully optimized Co-doped Ba-122 thin films prepared by three different lasers (i.e., different wavelength) showed a high self-field J_c of over

2 MA cm⁻² at 2 K. The J_c of Co-doped Ba-122 prepared by a second harmonic Nd:YAG laser possessed slightly higher values at the intermediate field due probably to the high density of defects, which works as flux pinning centers.

Kurth *et al* (2013) successfully deposited epitaxial Co-doped Ba-122 thin films on CaF₂, SrF₂, and BaF₂ without buffer layers using a KrF excimer laser, demonstrating that fluoride substrates are generic substrates suitable for the epitaxial growth of Ba-122. Later, other groups (University of Wisconsin-Madison, Temple University, and Chinese Academy of Science and Gwangju Institute of Science and Technology) also reported the successful growth of epitaxial Co-doped Ba-122 thin films on CaF₂ by PLD (Tarantini *et al* 2014, Lei *et al* 2014, Yuan *et al* 2017b, Lee *et al* 2017).

5.5.2. Grain boundary properties. As already stated in section 5.5.1, Co-doped Ba-122 bicrystal junctions have been fabricated by Lee *et al* (2009) using [001]-tilt bicrystal SrTiO₃ substrates with different misorientation angles. Lee *et al* (2009) demonstrated that the critical angle for which the exponential decay of the inter-grain J_c set in was around 5°, and concluded that Co-doped Ba-122 showed a weak link behavior, which is similar to cuprates, necessitating biaxial

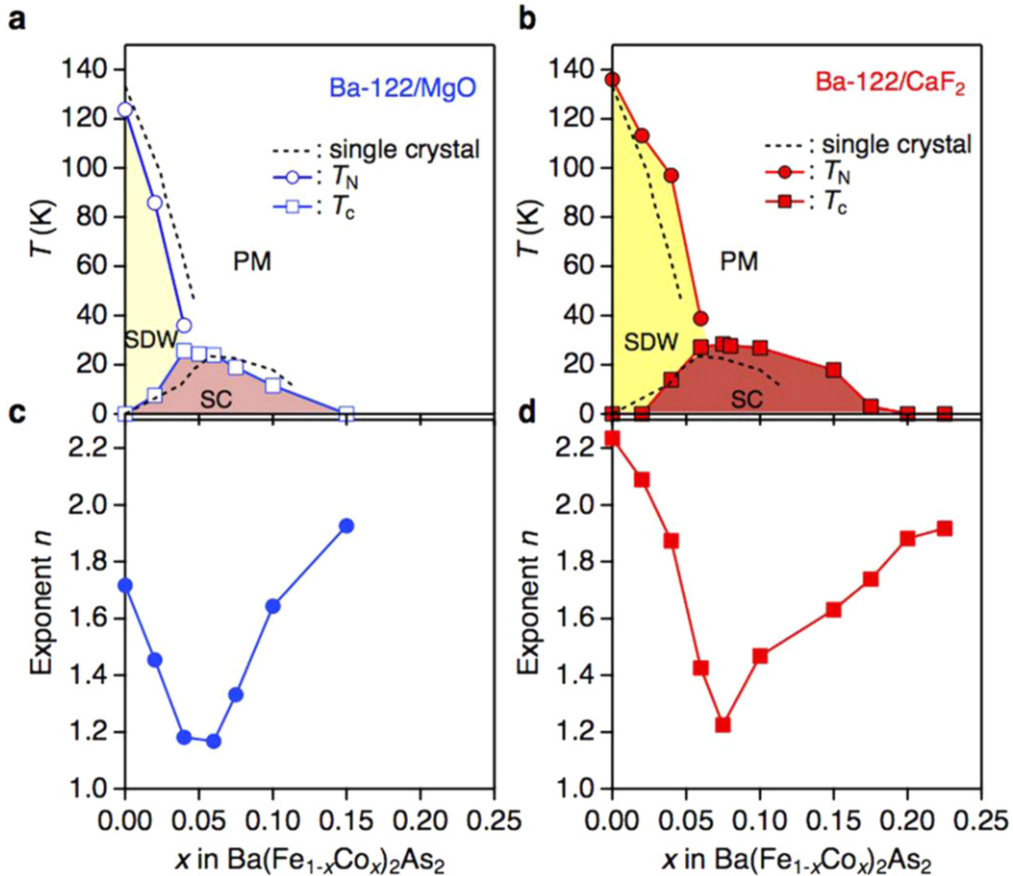


Figure 41. Electronic phase diagrams of Co-doped Ba-122 thin films grown on (a) MgO(001) and (b) CaF₂(001) substrates. The T_N and T_c denote the AFM and the superconducting transition temperatures, respectively. SDW, PM, and SC are the SDW, paramagnetic, and superconducting phases, respectively. Values for the exponent n taken from the resistivity data $\rho = \rho_0 + AT^n$ in the paramagnetic state: (c) Ba-122/MgO and (d) Ba-122 on CaF₂. Reproduced from Iida *et al* (2016). CC BY 4.0.

textured growth of Co-doped Ba-122 for high J_c . Subsequently, however, Katase *et al* (2011b) reported that the corresponding angle was 9° for Co-doped Ba-122 on MgO and LSAT. The difference between the results of the two groups may originate from the use of SrTiO₃ substrates. It is reported that oxygen vacancy in SrTiO₃ is created at high temperature under a high vacuum condition. On the assumption that oxygen diffuses through the grain boundary, the grain boundary region is oxidized and works as the current blocker. A detailed microstructural analysis is necessary to clarify this speculation.

Katase *et al* (2011b) investigated Co-doped Ba-122 bicrystal junctions in a wide range of misorientation angles (up to $\theta_{GB} = 45^\circ$) on MgO and LSAT. Unlike YBa₂Cu₃O₇, the inter-grain J_c was almost constant over $\theta_{GB} \geq 30^\circ$. Additionally, a high inter-grain J_c of 10^5 A cm^{-2} at 4 K was recorded, which is higher than that of YBa₂Cu₃O₇. They also concluded the metallic nature of the grain boundary. All of these properties are highly beneficial for wire applications. On the other hand, it is not favorable for electronic device applications since the metallic nature of junction barriers indicates the junction resistance is low.

5.5.3. Epitaxial strain effect. The electronic phase diagram of Co-doped Ba-122 is affected by epitaxial strain (figure 41) (Iida *et al* 2016). As can be seen, the optimal concentration of Co was around 0.05 for $\text{Ba}(\text{Fe}_{1-x}\text{Co}_x)_2\text{As}_2$ on MgO, whereas the corresponding composition for single crystals was around 0.08. Additionally, the whole phase diagram (i.e., superconducting dome and the AFM transition temperature) was shifted to the lower Co regime compared with single crystals (figure 41(a)). According to the band structure calculation, biaxial in-plane strain had an impact on the Fermi surface similar to Co doping. Indeed, the structural characterization of $\text{Ba}(\text{Fe}_{1-x}\text{Co}_x)_2\text{As}_2$ thin films on MgO revealed that the in-plane tensile strain was present. It was also reported that tensile strain is present for $\text{BaFe}_2(\text{As}_{1-x}\text{P}_x)_2$ on MgO and the superconducting dome was shifted to lower P content as discussed in section 5.4.2.

The resistivity curves of $\text{Ba}(\text{Fe}_{1-x}\text{Co}_x)_2\text{As}_2$ in the paramagnetic state were fitted by the following power law relation, $\rho = \rho_0 + AT^n$. In figure 41(c) the evaluated exponent $n(x)$ was plotted as a function of Co content. As can be seen, the exponent $n(x)$ for the thin films is a ‘V’-shape with a minimal value of $n = 1$ at around $x = 0.05$. Simultaneously, the highest T_c was observed at $x = 0.05$.

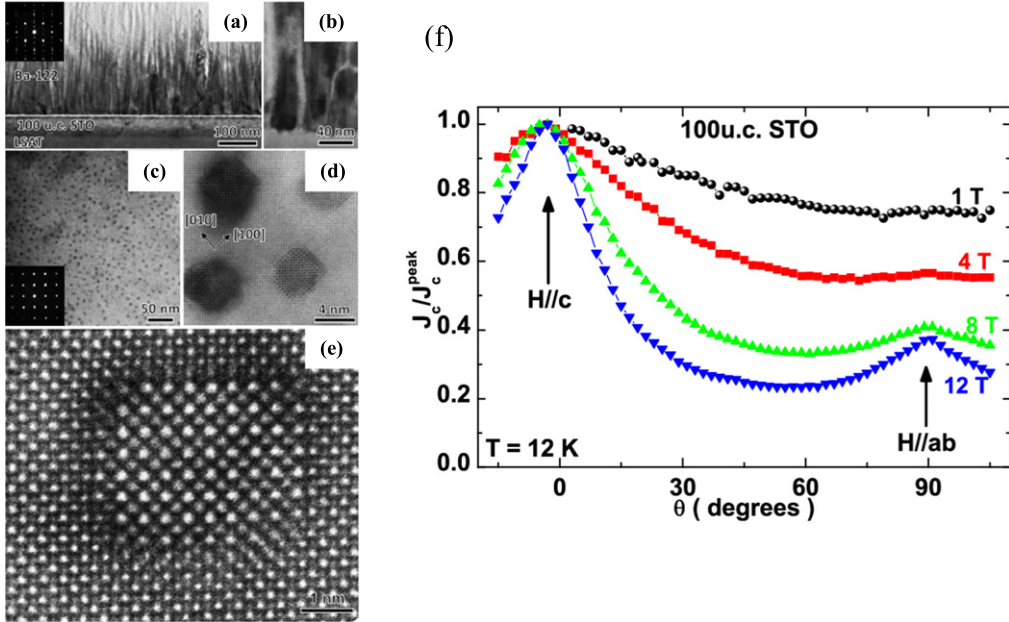


Figure 42. (a) Cross-sectional TEM image of Co-doped Ba-122 film grown on 100 unit-cell SrTiO₃/LSAT. This image is viewed along the [100] zone axis. The inset at the top left is the corresponding SAED pattern. (b) A magnified region of the line defects near the film/SrTiO₃ interface. (c) The planar-view bright-field TEM image viewed along the [001] zone axis. The corresponding SAED pattern inset at the bottom left shows a single-crystal pattern. (d) A high-resolution STEM image of (c) showing the structure of the nanopillars in the Ba-122 film. (e) A high-angle annular dark-field (Z-contrast) image showing the atomic structure of an epitaxial nanopillar in the Ba-122 film. Reprinted from Zhang *et al* (2011a), with the permission of AIP Publishing. (f) Normalized J_c at different applied field for Co-doped Ba-122 grown on 100 unit-cell SrTiO₃/LSAT at $T = 12$ K. Reprinted with permission from Tarantini *et al* (2010). Copyright 2010, AIP Publishing LLC.

This composition may correspond to the AFM quantum critical point (QCP), where the AFM transition temperature (T_N) goes to zero. It was reported that Co-doped Ba-122 has such an AFM QCP from several experimental observations (Ning *et al* 2014, Meingast *et al* 2012, Fernandes *et al* 2013).

On the other hand, the superconducting dome of the Ba(Fe_{1-x}Co_x)₂As₂ on LSAT is nearly identical to those of the single crystals due probably to strain-free films (Katase *et al* 2012b). A similar observation in MBE-processed BaFe₂(As_{1-x}P_x)₂ thin films on LaAlO₃ has been reported (Kawaguchi *et al* 2014). The authors argued that the films contained grains rotated by 45°, which may completely relax the strain.

Compared to the in-plane tensile strain, the in-plane compressive strain gives an opposite effect on the electronic phase diagram (figure 41(b)). The presence of the compressive strain in Ba(Fe_{1-x}Co_x)₂As₂ on CaF₂ was confirmed by structural analysis. The origin of compressive strain was the thermal expansion mismatch and the lattice mismatch (Iida *et al* 2016). In general, the large thermal expansion coefficient (e.g., CaF₂: 18.4×10^{-6} K⁻¹, LSAT: 8.2×10^{-6} K⁻¹, MgO: 10.0×10^{-6} K⁻¹, Co-doped Ba-122: 8.0×10^{-6} K⁻¹) of the substrates introduces in-plane compression to films (Lei *et al* 2014). As can be seen in figures 41(b) and (d), the compressive strain slightly increased the T_N and shifted the superconducting dome as well as the AFM QCP to higher Co doping in comparison with single crystals.

Based on the above results, one can clearly see that the shift of the superconducting dome correlates well with the T_N . Higher T_N pushes the superconducting dome toward higher

Co content, whereas lower T_N pulls the superconducting dome toward lower Co content.

5.5.4. J_c and pinning mechanisms. Lee *et al* (2010b) reported high-quality Co-doped Ba-122 single-crystal thin films on SrTiO₃-buffered LSAT. The resultant film showed a high self-field J_c of 4.5 MA cm⁻² at 4.2 K with strong *c*-axis flux pinning. The origin of the *c*-axis correlated pinning is the high density of the nanopillars of BaFeO₂ with an average size of 4–5 nm (figure 42) (Zhang *et al* 2011a), which is reminiscent of self-assembled nanorods BaZrO₃ in YBa₂Cu₃O₇ matrices (MacManus-Driscoll *et al* 2004). As can be seen, BaFeO₂ nanopillars grew epitaxially on the SrTiO₃ buffer layer as well as the surrounding Co-doped Ba-122. Albeit Co-doped Ba-122 on SrTiO₃-buffered LSAT is microstructurally similar to YBa₂Cu₃O₇ with BaZrO₃ nanorods, a distinct difference is present: the former showed a high tolerance of T_c against the high density of pinning centers (e.g., $T_c^{\text{end}} = 21.5$ K with more than 5% of volume fraction of BaFeO₂) and the latter exhibited a substantial decrease in T_c by a small content of BaZrO₃, which is ascribed to local strain caused by line defects (BaZrO₃). It has been reported that BaFeO₂ nanopillars grow coherently with Co-doped Ba-122 without structural degradation (Zhang *et al* 2011a), whereas BaZrO₃ nanorods induce local strain surrounding YBa₂Cu₃O₇, reducing T_c by a few kelvin.

Co-doped Ba-122 with self-assembled BaFeO₂ nanopillars showed an anomalous *c*-axis peak in the angular dependence of J_c measurements (figure 42(f)) (Tarantini

et al 2010). It is clear that the J_c for $H \parallel c$ (hereafter $J_c(H \parallel c)$) is always higher than that for $H \parallel ab$ ($J_c(H \parallel ab)$). Such inverse J_c anisotropy (i.e., $J_c(H \parallel c) > J_c(H \parallel ab)$) is due to the c -axis correlated flux pinning. Indeed, the flux pinning analysis for $H \parallel c$ using a Dew-Hughes model suggested a strong vortex core pinning by a dense array of nanoscale defects (Tarantini *et al* 2010).

Co-doped Ba-122 on LSAT(001) and MgO(001) substrates without SrTiO₃ buffer layers also exhibited a good in-field J_c properties (Katase *et al* 2010, Hiramatsu *et al* 2014a, Maiorov *et al* 2011, Mohan *et al* 2010, 2011). Both films prepared on LSAT and MgO showed a large c -axis peak in J_c , which is similar to the results reported in Lee *et al* (2010b) and Tarantini *et al* (2010). However, inverse J_c anisotropy disappeared at a relatively low field compared with the films with self-assembled BaFeO₂ nanopillars. It was also reported that grain boundaries act as the correlated flux pinning (Hänisch *et al* 2014). Figure 43 displays the cross-sectional view of the Co-doped Ba-122 deposited on LSAT(001). It is clear that most of the grain boundaries are almost straight throughout the Co-doped Ba-122. Additionally, Fe precipitates were present at the grain boundaries. Those defects created c -axis peaks in the J_c although the absolute J_c values were not very large.

Lee *et al* (2013) reported artificially layered superlattice structures in Co-doped Ba-122 using two different insertion layers, SrTiO₃ and non-doped (ND)-Ba-122. For SrTiO₃/Co-Ba-122 superlattice, the structural modulation along the film thickness was observed (figures 44(a) and (b)). Furthermore, the SrTiO₃/Co-Ba-122 superlattice did not have the c -axis correlated defects. In the case of ND-Ba-122/Co-Ba-122 multilayers, ND-Ba-122 grew laterally aligned but discontinuously (figure 44(c)). In addition, the c -axis correlated defects were present as can be seen in figure 44(d). The angular dependence of J_c reflects these unique microstructures. Due to the lack of c -axis correlated pinning, the SrTiO₃/Co-Ba-122 superlattice did not show a c -axis J_c peak in contrast to a very sharp J_c peak for $H \parallel ab$. The ND-Ba-122/Co-Ba-122 multilayer showed higher J_c than the SrTiO₃/Co-Ba-122 superlattice in all angular ranges. Later, the in-field J_c performance of ND-Ba-122/Co-Ba-122 multilayers has been improved by modifying the ND-Ba-122 PLD target (containing high oxygen content), resulting in an almost isotropic J_c over 10^5 A cm⁻² at 4.2 K and 20 T and a maximal pinning force density $F_{p,\max}$ of around 50 GN m⁻³ were recorded (Tarantini *et al* 2012). Further improvements in the pinning performance have been made by depositing ND-Ba-122/Co-Ba-122 multilayers on CaF₂ substrates, leading to a record high $F_{p,\max}$ of around 84 GN m⁻³ at 22.5 T and 4.2 K (Tarantini *et al* 2014).

Quite recently, Lee *et al* (2017) fabricated Co-doped Ba-122 thin films with BaZrO₃ (BZO) nanorods by PLD. They employed Co-doped Ba-122 targets with BZO (2 ~ 8 mol.%). The film with 2 mol% BZO showed a high J_c of over 1 MA cm⁻² at 13 T ($H \parallel c$) and 4.2 K, and the corresponding pinning force density reached around 170 GN m⁻³ at 13 T.

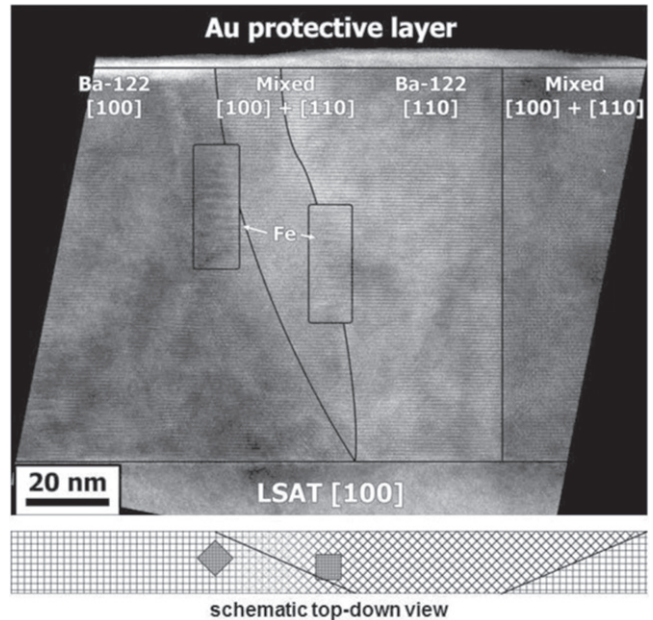


Figure 43. Cross-sectional TEM image of the Co-doped Ba-122/LSAT film, revealing a sharp substrate-film interface, 45°[001] tilt grain boundaries (vertical black lines) and round c -axis elongated Fe precipitates (encircled) near or within the grain boundaries. The image was taken in the (100) pole. Below the TEM image is a schematic top-down view illustrating the orientation of grain boundaries and Fe particles, deduced from Moiré contrasts. Reprinted with permission from Hänisch *et al* (2014). Copyright 2014, AIP Publishing LLC.

5.5.5. T_c control by piezoelectric substrate. Strain-driven changes in the superconducting properties have been widely studied in thin films. Commonly the lattice mismatch between a substrate and a film has been utilized to yield in-plane compressive or tensile strain, depending on the sign of the lattice mismatch. An alternative approach is to use single crystalline piezoelectric Pb(Mg_{1/3}Nb_{2/3})_{0.72}Ti_{0.28}O₃ (PMN-PT) substrates, which are capable of controlling in-plane strain dynamically. Trommler *et al* (2010) reported the epitaxial growth of optimally Co-doped Ba-122 on SrTiO₃-buffered PMN-PT. In order to avoid a possible chemical reaction between PMN-PT and Co-doped Ba-122, a 20 nm thick SrTiO₃ buffer layer was deposited on PMN-PT (001). The superconducting transition temperature T_c of the Co-doped Ba-122 was shifted after the application of an electrical field, $E = \pm 6.6$ kV cm⁻¹. Although a clear change in T_c was observed, the amount of shift (0.2 K for $\varepsilon_{ab} = 0.017\%$) was small due to the reduced response of PMN-PT at low temperatures. In-plane strain $\varepsilon_{ab} = 0.12\%$ at 10 kV cm⁻¹ at 300 K was decreased by 50% at 90 K and by 80% at 20 K. Later, the buffer architecture was modified (Co-doped Ba-122/Fe/MgO/PMN-PT), resulting in a large shift of T_c (0.6 K for $\varepsilon_{ab} = 0.035\%$) (Trommler *et al* 2014).

5.6. Superconductivity in pristine BaFe₂As₂ by epitaxial strain

Applying external pressure to pristine BaFe₂As₂ (Ba-122) samples induces superconductivity (Kimber *et al* 2009).

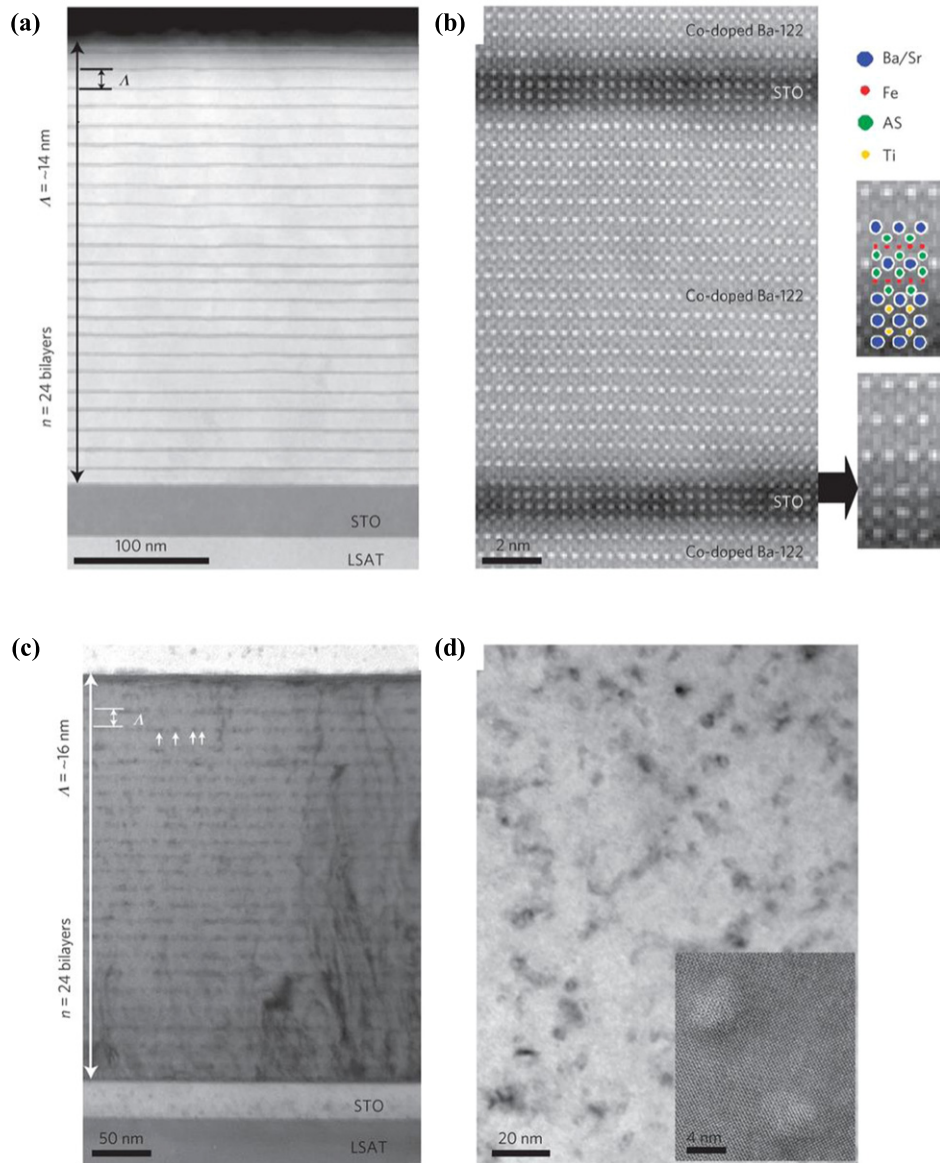


Figure 44. (a) High-angle annular dark-field (HAADF) image of the $\langle 100 \rangle$ projection of (SrTiO₃ (1.2 nm)/Co-doped Ba-122 (13 nm)) \times 24. (b) Enlarged view of (a). (c) Cross-sectional TEM image of the $\langle 100 \rangle$ projection of (ND-Ba-122 (3 nm)/Co-doped Ba-122 (13 nm)) \times 24. Arrows indicate nanoparticle arrays in the Co-Ba-122 layer along the ab axis. (d) Planar-view TEM image of (ND-Ba-122 (3 nm)/Co-doped Ba-122 (13 nm)) showing c -axis correlated (vertical) defects. Inset: high-resolution image of the vertical defects. Reproduced by permission from Springer Nature: Nature Materials (Lee *et al* 2013) Copyright 2013.

Particularly uniaxial pressure efficiently suppresses the SDW order and hence induces a high T_c (35 K) (Yamazaki *et al* 2010, Duncan *et al* 2010, Sefat 2011). Engelmann *et al* (2013b) reported the realization of superconductivity in parent Ba-122 by purely epitaxial strain. In figure 45(a), the structural characterization of Ba-122 films on Fe-buffered MgAl₂O₄(001) is summarized. For a 10 nm Ba-122 film (S₁₀), the (206) reflection of MgAl₂O₄ and the (109) and (1011) reflections of Ba-122 were located at the same Q_x value, indicating that the in-plane lattice parameter of Ba-122 and MgAl₂O₄ were identical to each other. The a_{film} of the sample S₁₀ was 4.04 Å, which was substantially larger than that of the Ba-122 polycrystalline target ($a = 3.96 \text{ \AA}$). Hence, the in-plane tensile strain was

introduced into the Ba-122 layer. Indeed, the out-of-plane lattice parameter of S₁₀ was 12.67 Å, much smaller than the Ba-122 target ($c = 13.014 \text{ \AA}$) due to the Poisson effect. However, this relation was violated as the Ba-122 thickness was increased to 60 nm (S₆₀), which infers that the in-plane strain was relieved in the sample S₆₀. Figures 45(a) and (b) show the temperature dependence of magnetic susceptibility and resistance for Ba-122. It is clear that Ba-122 with a thickness less than 30 nm showed an onset T_c of 35 K with a large transition width. However, the tiny value of diamagnetic signal at low temperatures suggested a very small amount of superconducting volume. Further increasing the layer thickness of Ba-122 led to reducing T_c and finally the superconductivity disappeared.

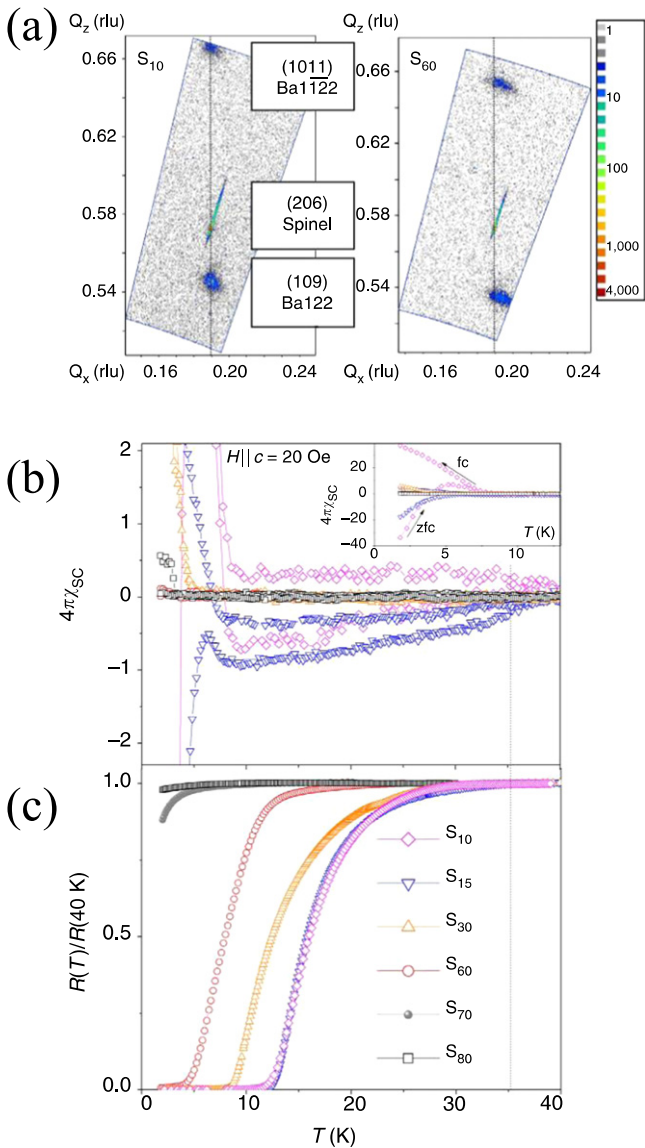


Figure 45. (a) Reciprocal space maps of samples S₁₀ and S₆₀. Relaxation processes for sample S₆₀ are clearly seen as a shift in the Ba-122 reflections with respect to the substrate peak. The line is a guide for the eyes. (b) Temperature dependence of the dimensionless magnetic susceptibility $\chi_{SC}(T) = [m(T) - m(40 \text{ K})]/V_{\text{Ba-122}}H$ in the superconducting state of the films with different thicknesses, where $m(T)$ is the sample magnetic moment, $V_{\text{Ba-122}}$ is the volume of the Ba-122 layer, and H is the applied magnetic field (data are not corrected for demagnetization factors). The inset shows the region of the bulk SC. (c) Temperature dependence of the normalized resistance $R(T)/R(40 \text{ K})$ of the investigated thin films in zero magnetic field. Reprinted by permission from Springer Nature: Nature Communications (Engelmann *et al* 2013b). Copyright 2013.

6. Growth of the 11 films

As mentioned in section 2, the superconductivity in FeSe ($T_c \sim 8.5 \text{ K}$) and FeSe_{0.5}Te_{0.5} ($T_c \sim 14 \text{ K}$) was discovered by the Wu group (Hsu *et al* 2008, Yeh *et al* 2008). At the beginning, their T_c appeared to be substantially lower than that in Fe pnictides. But soon after, it was found that the T_c of FeSe reaches 38 K by applying pressure (Mizuguchi *et al* 2008, Medvedev *et al* 2009). Furthermore, in 2012, the

Chinese groups (Wang *et al* 2012, Liu D *et al* 2012) reported a signature of superconductivity with T_c higher than 50 K in monolayer FeSe films on SrTiO₃ substrates, from $\rho-T$ measurements as well as the observation of a gap-like feature most likely due to superconductivity by scanning tunnel spectroscopy (STS) and angle-resolved photoemission spectroscopy (ARPES). The results have led to the expectation of FeSe breaking the superconducting transition temperature record of Fe-based superconductors ($T_c \sim 56 \text{ K}$ of SmFeAs(O,F)) or even to reach $T_c > 77 \text{ K}$. Since then, ultrathin FeSe films have become one of the hot issues in the research of Fe-based superconductors.

Even before the emergence of such a hot issue, thin-film growth of the 11 system involving FeSe, FeTe, FeS, Fe(S,Te), and Fe(Se,Te) has been quite active. The reasons are that the compounds are less toxic than other systems such as the 122 and 1111 systems, and additionally, the 11 system contains only FeCh tetrahedron, indicative of the simplest crystal structures among Fe-based superconductors. These features are favorable for both fundamental and applied research. Historically, FeSe thin films have been fabricated on GaAs substrates for possible spintronics applications (Takemura *et al* 1997, Liu *et al* 2007). However, the superconductivity in FeSe on GaAs was not reported.

6.1. PLD growth of Fe(Se,Te)

In this subsection, we overview the PLD growth of Fe(Se,Te) films. FeSe_{1-x}Te_x thin films were first grown by Wu *et al* (2009) by a PLD technique. They prepared FeSe_{1-x}Te_x thin films on MgO(001) with $x = 0, 0.1, 0.3, 0.5, 0.7$, and 0.9 using a KrF excimer laser at substrate temperature (T_s) varied from 250 °C–500 °C. The XRD patterns showed only $(00l)$ peaks, indicating that their films were *c*-axis preferred orientation. As the Te content increases, a gradual shift of $(00l)$ peaks to a lower angle was observed due to the relatively larger ionic radius of Te. However, for the low- x samples such as those with $x = 0.1$ and 0.3 , the $(00l)$ peak broadened. The bulk samples with low Te content tend to phase-separate into FeTe and FeSe, and it is difficult to have single-phased FeSe_{1-x}Te_x with low x (Yeh *et al* 2008). For the thin-film samples, although the XRD peaks did not show clear splitting, the broadening of the XRD peaks suggests non-uniform substitution of Te to Se sites. The *c*-axis lattice parameters of films are smaller than those of the bulk with the same nominal Te concentration, suggesting that the x in FeSe_{1-x}Te_x thin films is slightly lower (higher Se/Te ratio) than that of the bulk target. The ϕ -scan of the (101) and (203) peaks showed two kinds of domains (major and minor) with four-fold symmetry, which are rotated by 45° to each other. The orientation relationship in the major (minor) domain is FeSe[100] || MgO[110] (FeSe[100] || MgO[100]). Figure 46 shows the $\rho-T$ curves of the films with different x . The $\rho-T$ behavior changes from metallic to semiconducting behavior as x increases, which is consistent with the results for bulk samples. All films show a sharp superconducting transition at low temperature, except for the FeSe film. As compared with the T_c of the bulk samples, the T_c of the films is suppressed

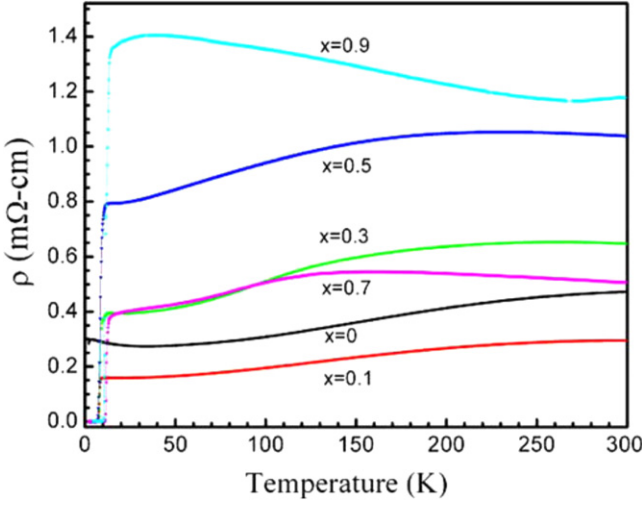


Figure 46. Temperature dependences of the resistivity of $\text{FeSe}_{1-x}\text{Te}_x$ films. The $\rho-T$ behavior changes from metallic to semiconducting as Te concentration increases. A sharp superconducting transition occurs at low temperature, except in the pure FeSe film. Reprinted from Wu *et al* (2009), Copyright 2009, with permission from Elsevier.

significantly at low x , in particular in the FeSe film, which only shows a slight resistive drop near 2 K. The T_c of the films approaches the bulk T_c for higher x . In relation to this observation, Wu *et al* (2009) demonstrated a substantial reduction of T_c with decreasing thickness, especially in the films with x . For example, the FeSe thin films show no true zero resistance unless the film is thicker than 3000 Å. In contrast, $\text{FeSe}_{0.5}\text{Te}_{0.5}$ films show true zero resistance for thicknesses >1000 Å. The strong thickness dependence of T_c is unlikely from the lattice parameter change due to epitaxial strain in thinner films because the strain is mostly relaxed due to the large lattice mismatch between $\text{Fe}(\text{Se},\text{Te})$ and MgO . Wu *et al* (2009) suspected that a possible cause of the observed results is the suppression of the structural transformation from tetragonal to orthorhombic at low temperatures in thinner films on tetragonal substrates.

Subsequently Bellingeri *et al* (2010) demonstrated that T_c can be increased in $\text{FeSe}_{0.5}\text{Te}_{0.5}$ films up to 21 K, significantly higher than the bulk value (~ 14 K). They fabricated epitaxial $\text{FeSe}_{0.5}\text{Te}_{0.5}$ thin films with different thicknesses (12–6000 Å) by PLD (KrF excimer laser) on different substrates (LaAlO_3 , SrTiO_3 , Y-stabilized ZrO_2). Figure 47(a) shows the thickness dependence of T_c . Their structural analyses indicated that the c_{film} (5.84–5.89 Å) is smaller than the bulk values ($c_{\text{bulk}} = 5.995$ Å) but it is almost independent of the film thickness. On the other hand, the a_{film} , which is also smaller than the bulk value ($a_{\text{bulk}} = 3.809$ Å), shows a significant change with the film thickness. The a_{film} shrinks rapidly (from 3.79–3.72 Å) with the film thickness increased from 12–2000 Å, irrespective of the substrate cell parameter. Then it elongates gradually with the film thickness increased from 2000–6000 Å. As shown in figure 47(b), the T_c is linearly related to the a_{film} : the T_c is higher for shorter a_{film} . The highest $T_c = 21$ K is obtained at 2000 Å, where the a_{film} is the shortest.

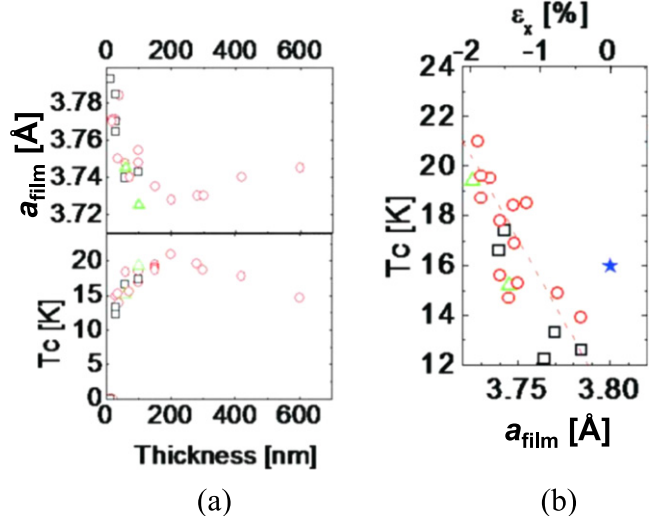


Figure 47. (a) a_{film} and T_c plotted as a function of film thickness for $\text{FeSe}_{0.5}\text{Te}_{0.5}$ films on various substrates (LaAlO_3 : red circle, SrTiO_3 : black square, Y:ZrO_2 green triangle). The T_c reaches a maximum value of 21 K for a thickness of about 2000 Å, where the a_{film} becomes minimum. (b) The data in (a) is replotted in the form of T_c versus a_{film} . The star represents the bulk value, and ε_x is defined as $(a_{\text{film}} - a_{\text{bulk}})/a_{\text{bulk}}$. Reprinted with permission from Bellingeri *et al* (2010). Copyright 2010, AIP Publishing LLC.

Many research groups have focused on $\text{Fe}(\text{Se},\text{Te})$, except for monolayer FeSe, due to the highest T_c in the bulk form. To date, various substrates such as oxides and fluorides have been tested for the growth of 11 thin films. Among the studies, SrTiO_3 and CaF_2 substrates have been frequently implemented (Si *et al* 2009, Bellingeri *et al* 2009, Imai *et al* 2010, Tsukada *et al* 2011, Chen *et al* 2012, Braccini *et al* 2013, Imai *et al* 2015, Yuan *et al* 2015a, 2015b, Seo *et al* 2017). Employing CaF_2 also yielded high-quality FeSe (no Te) thin films with T_c^{end} up to 11.4 K (Nabeshima *et al* 2013). Interestingly, a KrF excimer laser has been used for most of the thin-film growths by PLD. However, the optimum growth temperature varies from 230 °C–550 °C, which is still puzzling. Nevertheless, several important findings have been obtained, which are briefly summarized below.

- T_c of $\text{Fe}(\text{Se},\text{Te})$ thin films can be tuned by strain (Bellingeri *et al* 2010),
- High H_{c2} exceeding 50 T and its low anisotropy at low temperatures (Tarantini *et al* 2011),
- Inter-grain J_c across the grain boundary for $\text{Fe}(\text{Se},\text{Te})$ is not much reduced: the critical angle for which inter-grain J_c starts to fall off exponentially is as large as 9° (Si *et al* 2015, Sarnelli *et al* 2017).
- In the PLD growth of FeCh , unlike the PLD growth of oxides such as $\text{YBa}_2\text{Cu}_3\text{O}_7$, the target's composition is not transferred to the film's composition. It has been demonstrated that the chemical composition of $\text{Fe}(\text{Se},\text{Te})$ thin films stays around $\text{Se:Te} = 7:3$ even if the target composition is $\text{FeSe}_{0.5}\text{Te}_{0.5}$ (Yuan *et al* 2017a, Seo *et al* 2017). This observation is essentially in accord with the tendency that the PLD films have a higher Se/Te ratio than the targets as pointed out above by Wu *et al* (2009). Additionally, this composition corresponds to the

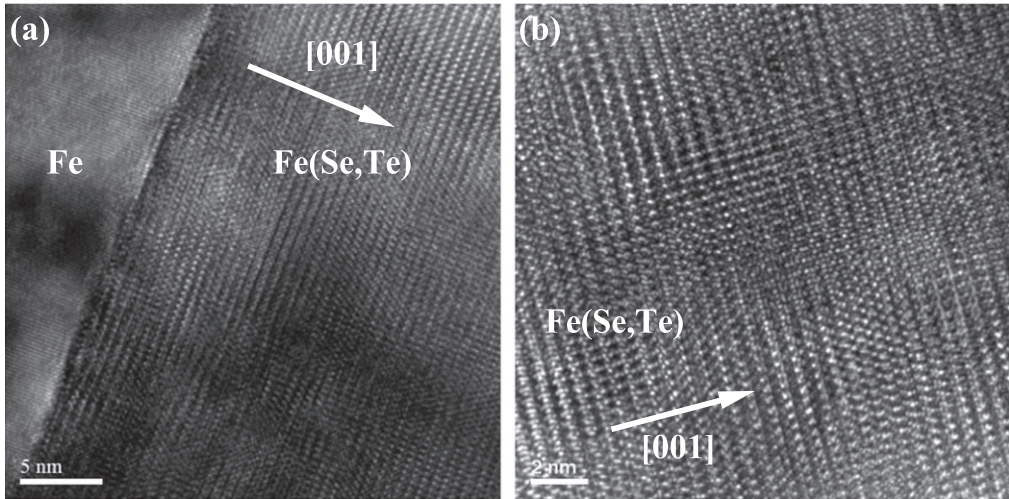


Figure 48. (a) Cross-sectional bright-field TEM image of Fe(Se,Te) thin film grown on Fe-buffered MgO in the vicinity of interface. (b) High-resolution TEM micrograph of the Fe(Se,Te) thin film. Reprinted figure with permission from Iida *et al* (2013a), Copyright 2013 by the American Physical Society.

optimum level where the maximum T_c was observed (see below, Imai *et al* 2015, Seo *et al* 2017). Seo *et al* (2017) also calculated the formation energy of FeSe, $\text{FeSe}_{0.5}\text{Te}_{0.5}$, and FeTe to explain the preferential formation of $\text{FeSe}_{0.7}\text{Te}_{0.3}$ films by PLD. As a result, the respective formation energies for FeSe, $\text{FeSe}_{0.5}\text{Te}_{0.5}$, and FeTe were -3.4 , -3.2 , and -3.0 eV. The authors concluded that FeSe has stronger binding than $\text{FeSe}_{0.5}\text{Te}_{0.5}$, or FeTe, and hence Fe preferentially bonds Se rather than Te in PLD.

6.2. Buffer layers for PLD

In this subsection, we focus on the PLD-processed 11 thin films by employing various buffer layers. The growth of 11 thin films on various single crystalline substrates, their growth conditions, and superconducting properties have been reviewed by Li *et al* (2011) and Mele (2012).

6.2.1. Fe buffer layer. Similarly to Co-doped Ba-122, Fe-buffer layer has been implemented for the epitaxial growth of Fe(Se,Te) thin films (Iida *et al* 2011a, Iida *et al* 2013a). Fe was deposited on MgO at room temperature by PLD using a KrF excimer laser, followed by post-annealing at 750°C *in situ*. Then Fe-buffered MgO was cooled to 450°C for the deposition of Fe(Se,Te). Here, Fe(Se,Te) single crystal with a nominal composition of Fe:Se:Te = 2:1:1 was used as a PLD target. TEM revealed clean interface between Fe-buffer layer and Fe(Se,Te) (figure 48), which is similar to the Ba-122/Fe bilayer system (Thersleff *et al* 2010). The resultant film showed high crystallinity (FWHM of the (001) rocking curve, $\Delta\omega_{(001)} = 0.73^\circ$, and average $\Delta\phi$ of the (101) reflection $\sim 0.97^\circ$). Additionally the film has a

higher T_c of 17.3 K than single crystals ($T_c = 13.6\text{ K}$) due to compressive strain.

6.2.2. Ba-122 buffer layer. Iida *et al* (2018) implemented Co-doped Ba-122 as a buffer layer for the growth of Fe(Se,Te). Shown in figures 49(a)–(c) are the RHEED patterns of Fe(Se,Te) fabricated on Co-doped Ba-122/Fe buffer layers. Note that the respective growth temperatures for Co-doped Ba-122 and Fe(Se,Te) were 750°C and 450°C . The respective thicknesses for Fe(Se,Te), Co-doped Ba-122 and Fe are 1000 \AA , 500 \AA and 200 \AA in nominal. Each RHEED image exhibited a streaky pattern indicating that smooth surfaces and epitaxy were realized for Fe(Se,Te), Co-doped Ba-122, and Fe. Out-of-plane x-ray diffraction patterns showed only $(00l)$ reflections for Fe(Se,Te), Co-doped Ba-122, and Fe together with MgO (figure 49(d)). These results highlighted that Ba-122 can be used as a potential buffer layer for epitaxial growth of the 11 system. Recently, Haindl *et al* (2016) also reported the use of Ba-122 as a buffer layer for the growth of SmFeAsO.

6.2.3. Non-superconducting Fe(Se,Te) buffer layer. It was reported that deposition temperature higher than 380°C yielded non-superconducting but biaxial textured Fe(Se,Te) on MgO (Molatta *et al* 2015). Hence, non-superconducting Fe(Se,Te) is a good candidate for a buffer layer for homoepitaxial Fe(Se,Te) superconducting layers. The primary deposition at 400°C by PLD produced non-superconducting Fe(Se,Te) (200 \AA). And then the second deposition was carried out at low temperatures in the range of $240^\circ\text{C} \leq T \leq 320^\circ\text{C}$ for a superconducting Fe(Se,Te) layer ($1200 \pm 300\text{ \AA}$). The high- T deposited Fe(Se,Te) buffer layer was grown cube-on-cube on MgO. Then the secondary superconducting Fe(Se,Te) was grown homo-epitaxially on the non-superconducting Fe(Se,Te) buffer layer. The T_c of the homoepitaxial Fe(Se,Te) layer was $>16\text{ K}$, which is higher

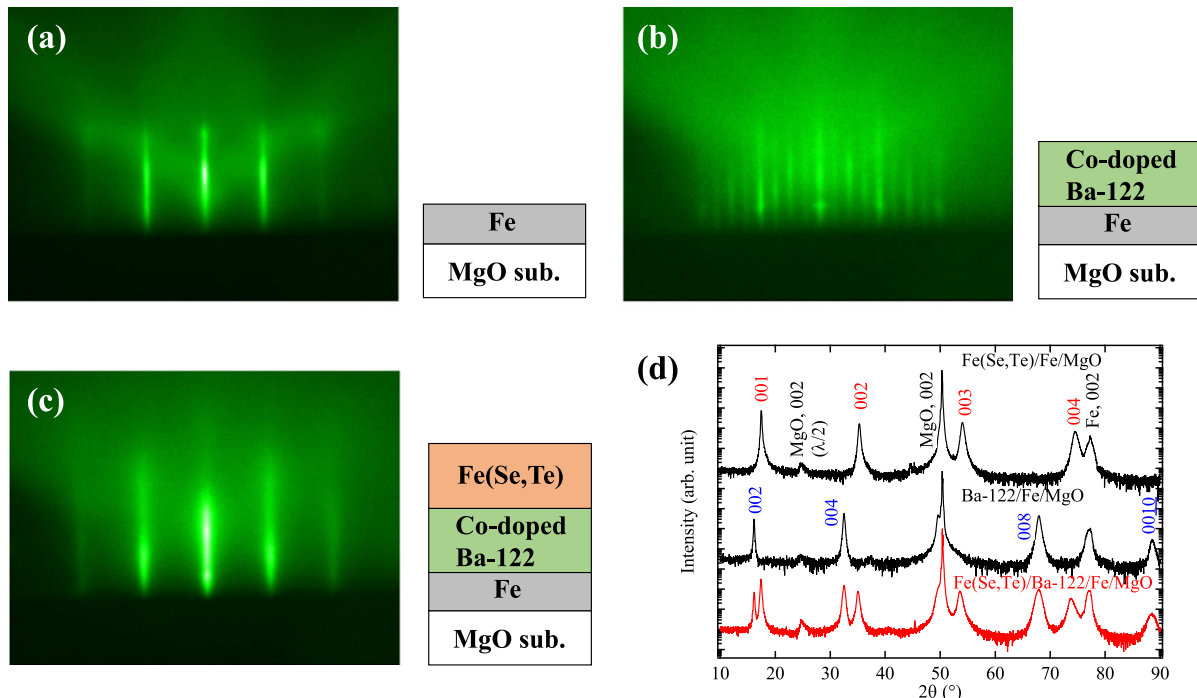


Figure 49. (a) RHEED patterns of the Fe on MgO deposited at room temperature, followed by annealing at 750 °C. (b) Co-doped Ba-122 deposited on Fe-buffered MgO at 750 °C, and (c) Fe(Se,Te) deposited on Co-doped Ba-122/Fe buffer layers at 450 °C. (d) Out-of-plane x-ray diffraction patterns for the Fe(Se,Te) thin film fabricated on Co-doped Ba-122/Fe buffer layers. For comparison, the diffraction patterns of the Fe(Se,Te)/Fe/MgO and the Co-doped Ba-122/Fe/MgO are also shown.

than the PLD target T_c (11 K). A similar idea was previously reported, in which the FeSe layer was deposited between $\text{FeSe}_{0.6}\text{Te}_{0.4}$ and a CaF_2 substrate (Ichinose *et al* 2013).

6.2.4. CaF_2 buffer layer. Fluoride substrates such as CaF_2 and SrF_2 are generic templates for producing ‘11,’ ‘122,’ and ‘1111’ epitaxial thin films with excellent superconductivity as stated in sections 4 and 5. Hence, the use of those materials as a buffer layer is a natural choice. Indeed, superconducting Fe(Se, Te) epitaxial thin films have been successfully deposited by PLD on CaF_2 -buffered LaAlO_3 , - CaF_2 , and -LSAT (Ichinose *et al* 2013, Yuan *et al* 2017a). Albeit many triangular-shaped CaF_2 was observed at the Fe(Se,Te)/ CaF_2 interface, the top surface of Fe(Se,Te) was quite smooth. Here, the IFW (Leibniz Institute for Solid State and Materials Research Dresden) group grew Fe(Se,Te) thin films on CaF_2 -buffered LSAT using the melt-processed $\text{FeSe}_{0.5}\text{Te}_{0.5}$ bulk sample as the PLD target. The resultant composition of all films was $\text{FeSe}_{0.7}\text{Te}_{0.3}$ confirmed by energy dispersive x-ray spectroscopy (EDX). It was found that even thin CaF_2 buffer layer improved T_c and also crystallinity of $\text{FeSe}_{0.7}\text{Te}_{0.3}$ (Yuan *et al* 2017a).

6.2.5. CeO_2 buffer layer. The lattice parameter of CeO_2 ($a/\sqrt{2} = 3.82 \text{ \AA}$) is comparable to that of Fe(Se,Te) (3.801 \AA), leading to a small lattice mismatch. Indeed, an Fe(Se,Te) layer grew almost coherently on CeO_2 -buffered SrTiO_3 (figure 50) (Ozaki *et al* 2016). Additionally, no interstitial Fe, which works as a pair breaker, was observed, leading to a high T_c^{end} of 18 K.

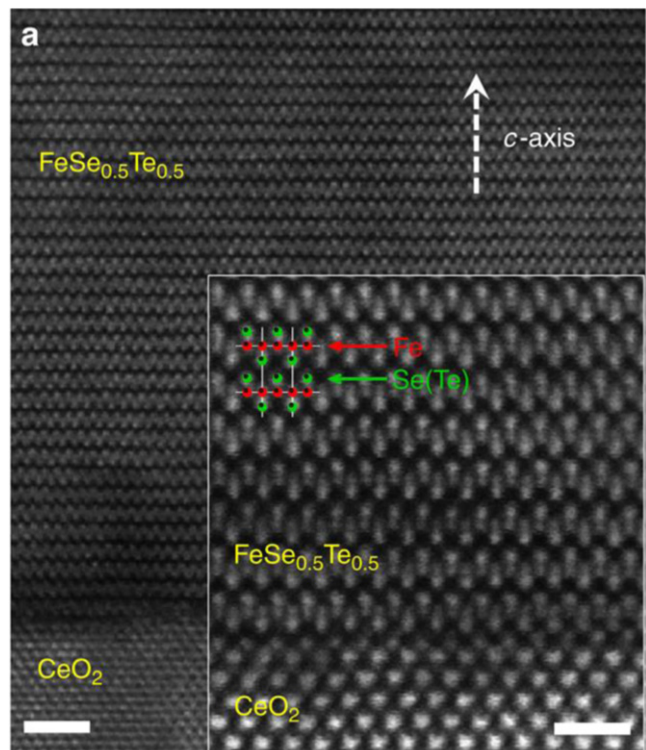


Figure 50. STEM-HAADF images of the representative Fe(Se,Te) film on the CeO_2 buffer layer (scale bar, 20 \AA). Inset: high-resolution image at the interface between CeO_2 and Fe(Se,Te) (scale bar, 10 \AA). Reproduced from Ozaki *et al* (2016). CC BY 4.0.

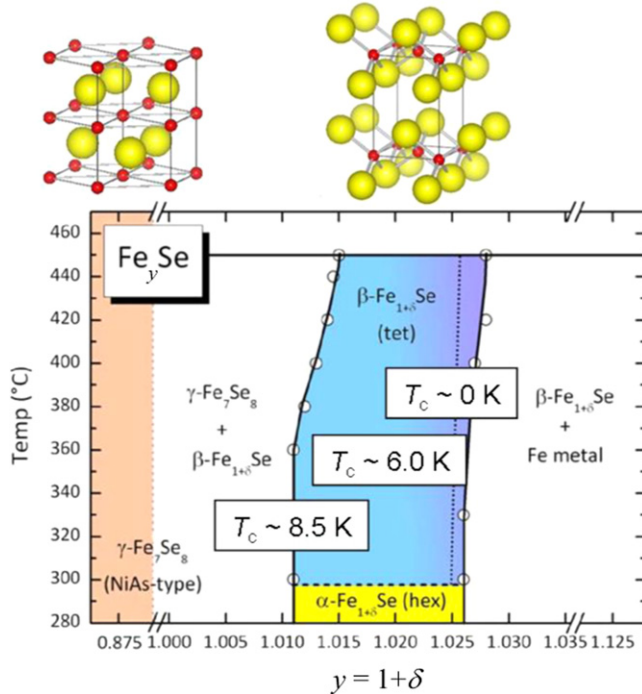


Figure 51. Thermodynamic phase diagram for binary Fe_ySe with $y \sim 1.0$. At the top of the figure, the crystal structures of $\beta\text{-FeSe}$ and $\gamma\text{-Fe}_7\text{Se}_8$ are shown. Reproduced figure with permission from McQueen *et al* (2009), Copyright 2009 by the American Physical Society.

The implementation of CeO_2 as a buffer layer also opens another opportunity for realizing an $\text{Fe}(\text{Se},\text{Te})$ coated conductor: $\text{Fe}(\text{Se},\text{Te})$ deposited on CeO_2/Y -stabilized ZrO_2 buffered technical substrates (Si *et al* 2013). The transport properties of those films are discussed in section 6.4.

6.3. MBE growth of FeSe at TAT

PLD has focused on the preparation of $\text{Fe}(\text{Se},\text{Te})$ films, as described in sections 6.1 and 6.2. An early attempt to grow Te-free FeSe films by MBE was undertaken by the TAT group (Agatsuma *et al* 2010). At first glance, the MBE growth of binary FeSe films *might* be much easier than the growth of the 1111 and 122 systems. For example, the growth of III-V semiconductors such as GaAs has been established, where the sticking coefficient of the group V elements is self-limited owing to their volatility, as mentioned in section 3.1. However, the growth of FeSe is not this case since the most Se-richest phase in the Fe-Se binary phase diagram is FeSe_2 with the pyrite structure. It appears that Se all sticks on the growth surface in the growth with the Fe:Se flux ratio nearly equal to 1:1, so stringent flux control is required. The thermodynamic phase diagram of FeSe makes matters more difficult. According to the phase diagram (figure 51) created by McQueen *et al* (2009), four phases appear for the Fe:Se ratio of nearly 1:1. The first is tetragonal $\beta\text{-Fe}_{1+\delta}\text{Se}$, which is the superconducting phase. The second and third are hexagonal $\alpha\text{-Fe}_{1+\delta}\text{Se}$ and $\gamma\text{-Fe}_7\text{Se}_8$, which are not superconducting. And the last is elemental Fe. The single-phase tetragonal $\beta\text{-Fe}_{1+\delta}\text{Se}$ is obtained below 455 °C in a very narrow range of

δ of 0.010–0.025 (slightly rich in Fe). Within this single-phase region, T_c varies from 8.5 K at $\delta = 0.010$ to 0 K at $\delta = 0.025$. Another problem is that the preparation of superconducting films of $\text{FeSe}_{1-x}\text{Te}_x$ with low x , especially $x = 0.0$, is difficult as mentioned in the above PLD work by Wu *et al* 2009. It turned out that the MBE growth of superconducting FeSe films, except for ultrathin films, is as difficult as the MBE growth of the 1111 and 122 films.

In these situations, the TAT group adopted a combinatorial approach. As shown in the inset of figure 52, they prepared four films in the same run with substrate holder rotation intentionally being stopped. The four films are given different compositions: Se rich near the Se source and Fe rich near the Fe source. Figure 52 shows the XRD patterns and $\rho-T$ curves of the four films (1000 Å thick) grown at $T_s \sim 350$ °C on *r*-cut Al_2O_3 .¹⁴ All films are metallic and show a substantial drop in resistivity although zero resistivity was not attained. The T_c^{on} reaches 13 K for the Se-rich film although the XRD showed that this film is a mixture of $\beta\text{-FeSe}$ and $\gamma\text{-Fe}_7\text{Se}_8$. Our observation is in accord with the trend found in bulk synthesis by McQueen *et al* (2009).

6.4. J_c and pinning mechanisms

6.4.1. Grain boundary issue. Si *et al* (2015) investigated the effect of the misorientation angle on the inter-grain J_c for PLD-processed $\text{Fe}(\text{Se},\text{Te})$ thin films using [001]-tilt SrTiO_3 bicrystals, on which a CeO_2 buffer layer was prepared. It was revealed that the critical angle (θ_c) for which J_c starts to decrease exponentially is around 9°. Later Sarnelli *et al* (2014, 2017) also reported similar results. Additionally, inter-grain J_c is almost constant for $\theta_{\text{GB}} \geq 30^\circ$. These results are almost the same as those for Co-doped Ba-122. Large θ_c as well as high H_{c2} and its low anisotropy are favorable for high-field magnet applications. Hence, several attempts at fabricating $\text{Fe}(\text{Se},\text{Te})$ wires and tapes have been demonstrated. For instance, $\text{Fe}(\text{Se},\text{Te})$ thin films have been deposited on technical substrates such as Hastelloy tapes, on which biaxially aligned MgO templates are fabricated by IBAD- MgO (Si *et al* 2011), and rolling-assisted biaxially textured substrates (RABiTS) with a CeO_2/Y -stabilized $\text{ZrO}_2/\text{Y}_2\text{O}_3$ buffer layer (Si *et al* 2013). The former showed a low $T_c^{\text{end}} \sim 11$ K probably due to the large lattice misfit between $\text{Fe}(\text{Se},\text{Te})$ and MgO . Nevertheless, the tapes showed almost isotropic J_c-H properties (J_c exceeding 10^4 A cm^{-2} at 4.2 K and 25 T for both $H \parallel c$ and $H \parallel ab$). On the other hand, the superconducting properties of the latter are much improved ($T_c^{\text{end}} \sim 18$ K). Although the FWHM value of the (101) peak ϕ -scan for $\text{Fe}(\text{Se},\text{Te})$ on RABiTS is as large as 6°, transport J_c at 4.2 K was quite high: self-field J_c exceeded 1 MA cm^{-2} and in-field J_c under $\mu_0 H = 30$ T for $H \parallel c$ was around 0.08 MA cm^{-2} . The pinning force analysis of the resultant film indicated that point defects

¹⁴ At the growth temperatures above 500 °C, we found that a substantial reaction between Fe and O in substrates takes place, yielding insulating films.

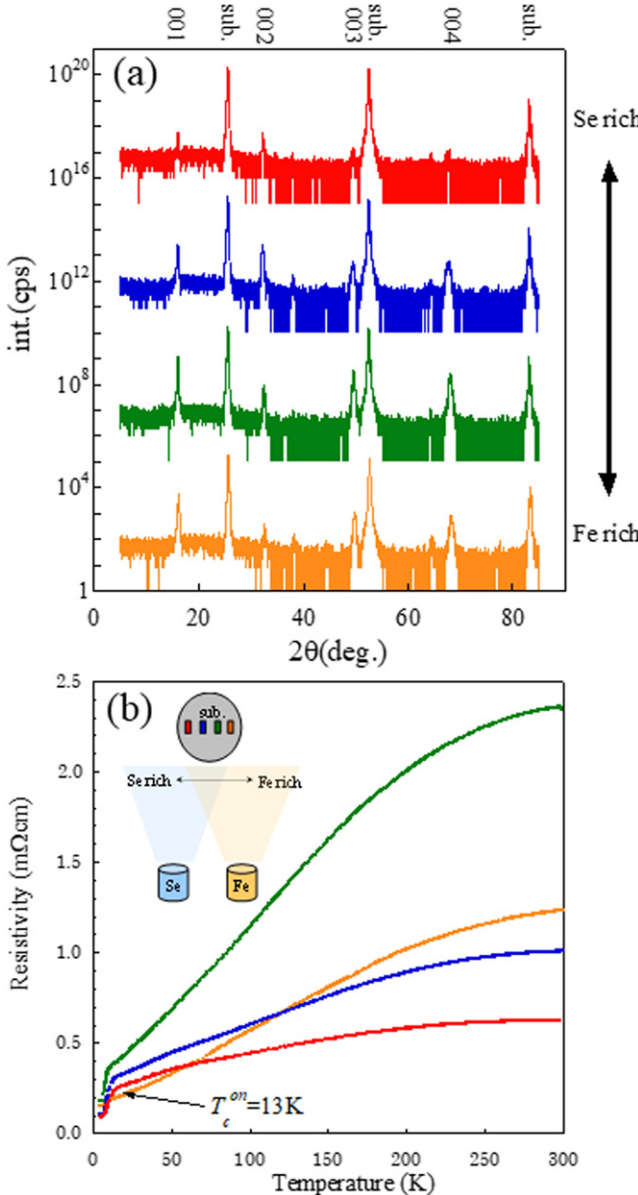


Figure 52. (a) XRD patterns and (b) $\rho-T$ curves of the FeSe films grown on *r*-cut Al_2O_3 prepared with composition gradation: Fe-richest film (orange) to Se-richest film (red). The inset in (b) shows a schematic illustration for composition gradation. Reprinted from Agatsuma *et al* (2010), Copyright 2010, with permission from Elsevier.

play a major role in improving J_c for both crystallographic directions.

6.4.2. High- J_c Fe(Se,Te) thin films. Tsukada *et al* (2011) reported a high in-field J_c of $4.2 \times 10^4 \text{ A cm}^{-2}$ at 14 T and 4.5 K for Fe(Se,Te) on $\text{CaF}_2(001)$ by PLD. Later several groups also reported high performances of J_c-H of Fe(Se,Te) on $\text{CaF}_2(001)$ by PLD (Mele *et al* 2012, Braccini *et al* 2013, Yuan *et al* 2015a, 2015b). Potentially, Fe(Se,Te) is capable of carrying a high J_c of over 3 MA cm^{-2} , as revealed by low-temperature scanning Hall-probe microscopy (LT-SHPM)

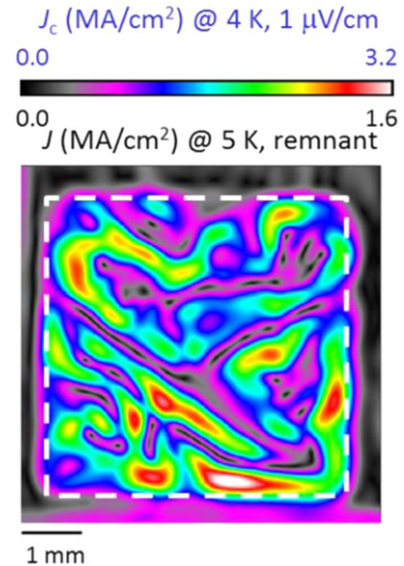


Figure 53. In-plane distribution of J_c in the Fe(Se,Te) film visualized by LT-SHPM at 5 K in a remanent stage. Reprinted with permission from Braccini *et al* (2013), Copyright 2013, AIP Publishing LLC.

(Braccini *et al* 2013). As can be seen in figure 53, the maximum J_c was locally beyond 3 MA cm^{-2} . Microstructural analysis of Fe(Se,Te) thin films on CaF_2 by TEM revealed some defects with a lateral size of about $50 \times 200 \text{ \AA}$ ($5 \times 20 \text{ nm}$) (Braccini *et al* 2013, Yuan *et al* 2015b). The authors claimed such defects led to the high J_c as well as the isotropic angular dependence of J_c .

Inverse J_c anisotropy rather than isotropic one was observed in Fe(Se,Te) on $\text{SrTiO}_3(001)$ (Bellingeri *et al* 2012), which is a similar observation in Co-doped Ba-122 on SrTiO_3 -buffered LSAT (see section 5.5.4). Shown in figure 54(a) is the STM tomography of Fe(Se,Te) fabricated on $\text{SrTiO}_3(001)$ by PLD. A high density of nanorods with a diameter of 20 \AA (2 nm) was observed. Due to such defects the angular dependence of J_c showed a large peak at $H \parallel c$ at all temperatures (figure 54(b)).

In order to further improve the pinning properties, low-energy protons (190 keV, dose of $1 \times 10^{15} \text{ p cm}^{-2}$) were irradiated to Fe(Se,Te) on CeO_2 -buffered $\text{SrTiO}_3(001)$ (Ozaki *et al* 2016). Cascade defects in Fe(Se,Te) were successfully introduced, which created nanoscale compressive strain, resulting in an increase of T_c by ~ 0.5 K. Additionally, J_c and hence the pinning force density F_p for both crystallographic directions were substantially improved (figure 55).

6.5. Tensile-strain-induced superconductivity in FeTe films and metastable $\text{FeSe}_{1-x}\text{Te}_x$ films with low x

The thin-film fabrication technique is very important in raising T_c by epitaxial strain and it is also a powerful tool for searching new materials. The film fabrication process is a thermodynamically non-equilibrium one, which is effective for stabilizing metastable phases. In this subsection, two

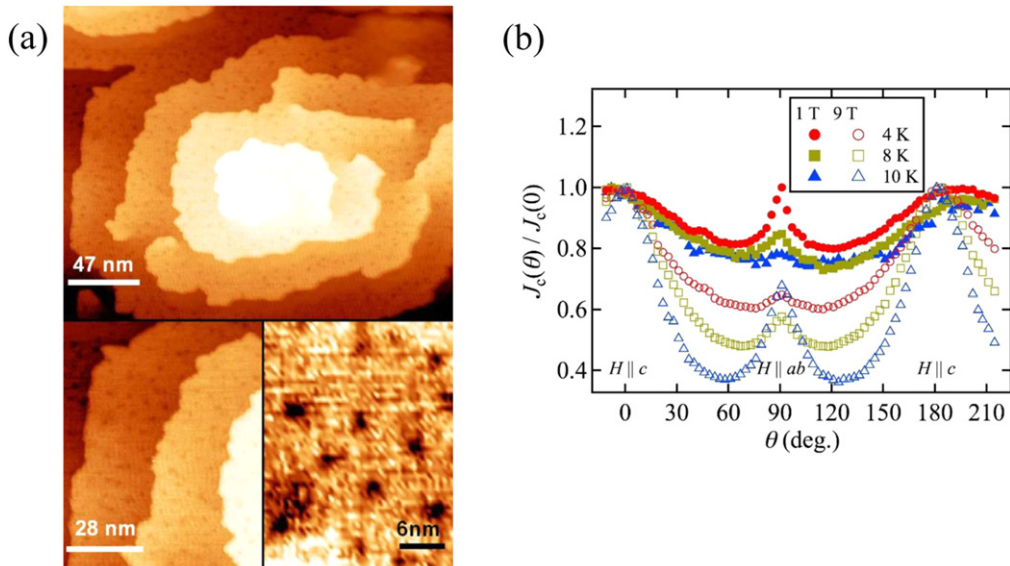


Figure 54. (a) STM image of the Fe(Se,Te) film fabricated on SrTiO₃(001). Reprinted from Bellingeri *et al* (2012), with the permission of AIP Publishing. (b) Angular dependence of the normalized J_c at various temperatures and fields. Redrawn with some modifications based on figure 3 in Bellingeri *et al* (2012).

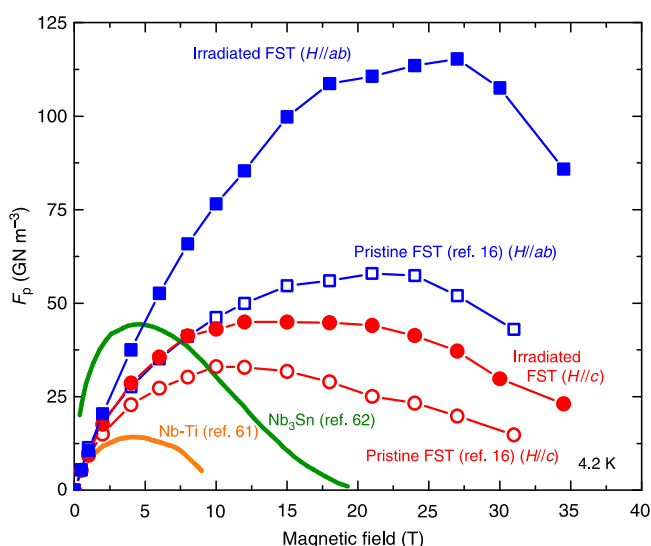


Figure 55. Pinning force density for the Fe(Se,Te) film before and after 190 keV proton irradiation with $1 \times 10^{15} \text{ p cm}^{-2}$ at 4.2 K, compared with NbTi and Nb₃Sn wires. Reproduced from Ozaki *et al* (2016). CC BY 4.0.

examples illustrating the advantage of thin-film synthesis are demonstrated.

The first example is tensile-stain-induced superconductivity in FeTe. FeTe is not superconducting in bulk form at ambient pressure or under high pressure, but superconductivity of 13 K was achieved in FeTe which is in the form of thin films and under tensile stress, as demonstrated by Han *et al* (2010). They fabricated FeTe films by PLD (XeCl excimer laser) at $\sim 540^\circ\text{C}$ on various substrates (LSAT, MgO, SrTiO₃, and LaAlO₃). Targets with excess Te by 40% (FeTe_{1.4}) were used to compensate for the loss of volatile Te in FeTe films. The films were epitaxial (c -axis oriented) and

single phased as revealed by XRD. The c -axis lattice constant of the FeTe films ($c_{\text{film}} \sim 6.25\text{--}6.28 \text{ \AA}$) was slightly smaller than the bulk value ($c_{\text{bulk}} \sim 6.3 \text{ \AA}$), irrespective of the substrate. This indicates that tensile strain appears to have been introduced into the films but not by epitaxial stress due to the lattice mismatch. Although Han *et al* (2010) did not figure out a clear origin of tensile strain, they commented that the Te(Se)-Te(Se) bonds between the adjacent FeTe (FeSe) layers are van der Waals force, so these compounds are easier to be compressed out of plane than stretched. The thickness dependencies revealed a maximum of T_c^{end} at 900 Å, suggesting that the critical thickness for pseudomorphic growth of these in-plane tensile films is 900 Å. The highest $T_c^{\text{on}} - T_c^{\text{end}} = 13.0 \text{ K} - 9.1 \text{ K}$ was obtained for the film on MgO.

A second example is the suppression of the phase separation in FeSe_{1-x}Te_x films with low x . As mentioned in section 6.1, the bulk samples with low x favor phase separation into FeTe and FeSe. Imai *et al* (2015) investigated a systematic change in the physical properties of films with x and compared the phase diagram with that of bulk single crystals. FeSe undergoes a structural transition from tetragonal to orthorhombic at a structural transition temperature ($\sim 90 \text{ K}$) and does not show any long-range magnetic order at ambient pressure, which is quite in contrast to other iron-based superconductors, where a structural and a magnetic phase transition occur almost simultaneously. Another end member material FeTe shows a structural transition from tetragonal to monoclinic at $\sim 70 \text{ K}$ and simultaneously develops a bccollinear antiferromagnetic order. The reported phase diagram for FeSe_{1-x}Te_x bulk samples is summarized in figure 56(a). Phase separation occurs at $0.1 \leq x \leq 0.4$ and single-phase samples with these compositions are not available. This has been a serious problem for the systematic investigation of the Te doping

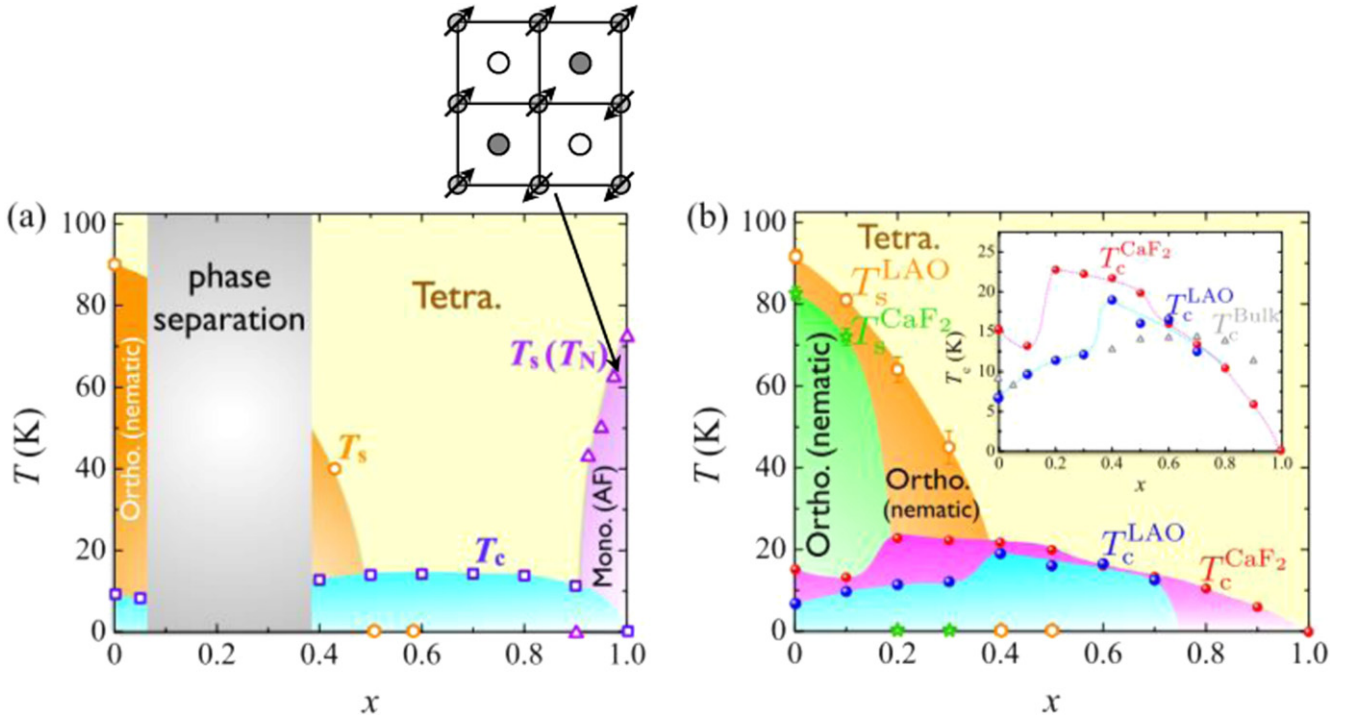


Figure 56. Phase diagrams of (a) bulk samples and (b) films of $\text{FeSe}_{1-x}\text{Te}_x$. Blue circles (red circles) and orange hexagons (light-green stars) represent the T_c^{on} and T_{struc} of the $\text{FeSe}_{1-x}\text{Te}_x$ thin films fabricated on LaAlO_3 (CaF_2), respectively. In the inset, the dependence of T_c^{on} on Te content x is enlarged. The dashed curves in the inset are guides for the eye. The words ‘ortho.’, ‘tetra.’, ‘mono.’, and ‘AF’ are abbreviations for orthorhombic, tetragonal, monoclinic, and antiferromagnetic phases, respectively. The magnetic structure in FeTe (referred to as ‘bicollinear’ spin ordering) is illustrated in the top of (a). Reproduced from Imai *et al* (2017). CC BY 4.0.

dependence. Imai *et al* (2017) recently demonstrated that phase separation can be suppressed in $\text{FeSe}_{1-x}\text{Te}_x$ thin films with these compositions fabricated on CaF_2 at T_s as low as 280 °C by PLD (KrF laser). The thin-film phase diagram is shown in figure 56(b). On CaF_2 , a superconducting transition is observed in all films except for FeTe films. The highest T_c is ~23 K at $x = 0.2$, whereas on LaAlO_3 the highest T_c is ~19 K at $x = 0.4$. These values of T_c are larger than the highest $T_c \sim 15$ K observed in $\text{FeSe}_{1-x}\text{Te}_x$ bulk samples at $x = 0.5$. The suppression of T_c at $x < 0.4$ for the films on LaAlO_3 indicates that a trace of phase separation survives on this substrate. CaF_2 plays an important role in suppressing the phase separation.

6.6. Monolayer films

Next, we present recent hot topics on the 11 films such as possible high T_c over 50 K in monolayer FeSe films and electric double-layer transistors (EDLTs) in ultrathin FeSe films. The first is the recent experiments on high- T_c superconductivity in ultrathin FeSe films carried out by the Chinese groups (Wang *et al* 2012, Liu *et al* 2012, Tan *et al* 2013, He *et al* 2013).

In 2012, Wang *et al* (2012) reported that one unit cell (1-UC) thick FeSe films grown on SrTiO_3 substrate by MBE showed signatures of a superconducting transition above 50 K, in STS as well as in $\rho-T$ measurements. 1-UC FeSe films for STS measurements were grown by coevaporation on conducting Nb-doped $\text{SrTiO}_3(001)$ substrates. Before growth, the

substrates were annealed in Se beam at 950 °C. The FeSe films were grown by coevaporating Fe and Se from standard Knudsen cells with a flux ratio of approximately 1:10 at 450 °C. The Fe flux was approximately 0.06 molecular-layer min⁻¹. The FeSe thin films were gradually annealed to 550 °C by several steps. Their flux ratio of 1:10 is different from our ratio 1:1 employed for the growth of thicker FeSe films as mentioned in section 6.3. 1-UC FeSe along the c -axis is made of a Se-Fe-triple layer and has a thickness of 5.5 Å. Their STS measurement on the one-UC FeSe at 4.2 K reveals a signature of superconductivity as shown in figure 57(a), namely, almost zero conductance at $-5 \text{ mV} \leq V_{\text{bias}} \leq 5 \text{ mV}$ and conductance peaks at $V_{\text{bias}} = \pm 20$ and $\pm 9 \text{ mV}$. If one assigns 20 mV to Δ/e , the gap value is almost one order of magnitude larger than $\Delta \sim 2.2 \text{ meV}$ reported for thick (300 Å) FeSe films on graphene ($T_c \sim 9$ K) (Song *et al* 2011). The temperature dependence of the tunnel spectrum was also measured, and the gap structure was visible up to 43 K. They found that the second UC and thicker films showed no superconductivity, and the observed superconductivity is limited to the very first unit cell of the film above the interface. They also attempted measuring the superconducting properties directly by transport measurements. In this case, the 5-UC FeSe film was grown on insulating $\text{SrTiO}_3(001)$ substrates, then covered with a 200 Å thick amorphous Si protection layer for *ex situ* measurements. The $R-T$ behavior shown in figure 57(b) is supposed to represent that of the bottom 1-UC FeSe . According to their definition of the onset of superconductivity, T_c^{on} is ~53 K.

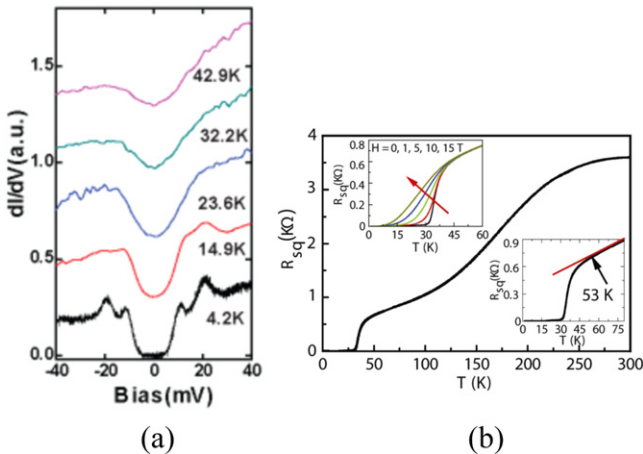


Figure 57. (a) dI/dV tunneling spectra of 1-UC FeSe on a Se-annealed Nb-dope SrTiO_3 substrate at different temperatures. At 4.2 K, pronounced superconducting coherence peaks appear at ± 20.1 and ± 9 mV, respectively. From 4.2 K–23.6 K, there is no obvious change in the gap size and the superconducting gap is still clearly visible at 42.9 K. Measurements at higher temperatures (77 K) were attempted, but no reliable spectra could be obtained due to very large thermal drifting in the STM system. (b) The R - T for the 1-UC FeSe on insulating SrTiO_3 surface. Upper inset: R - T curves at various magnetic fields applied in parallel to the c -axis. Lower inset: the definition of T_c^{on} . Reproduced from Wang *et al* (2012). © 2012 Chinese Physical Society and IOP Publishing Ltd.

Subsequently, the same group reported ARPES studies on 1-UC FeSe (Liu *et al* 2012). They investigated the electronic structure and superconducting gap in 1-UC FeSe. The Fermi surface topology is distinct from other Fe-based superconductors, and consists only of electron-like pockets near the X point in the unfolded BZ (equivalently the M point in the folded BZ, we refer to this point as X_{unfold} below, see figure 5(b)) without indication of any Fermi surface around the zone center. A similar Fermi surface has been observed in $A_x\text{Fe}_2\text{Se}_2$ ($A = \text{K}, \text{Cs}, (\text{Tl}, \text{Rb})$), except that electron (not hole) pockets exist also at the Γ point in these compounds. The superconducting gap, as estimated from symmetrizing the energy distribution curves as commonly used in high- T_c cuprates, is 15 meV and nearly isotropic, and it closes at $T_c \sim 55$ K. The results are overall in accord with the first report by Wang *et al* (2012).

The highest T_c reported so far is 109 K, which was obtained from sophisticated resistance measurements by Ge *et al* (2015). They performed electrical transport measurements on MBE-grown 1-UC FeSe on Nb-doped SrTiO_3 using an *in situ* four-point probe (4PP) technique. They traced the I - V curves at fixed temperatures. The data showed nonlinear I - V curves, namely, finite current at zero voltage, similar to those observed in superconductors, although linear I - V curves were obtained occasionally at different locations in the same sample. They moved the 4PP to various locations to collect I - V curves at a fixed temperature, and the film was designated superconducting when the superconducting I - V curves were at least one location. Then they found that superconductivity could be obtained at a temperature as high as 109 K.

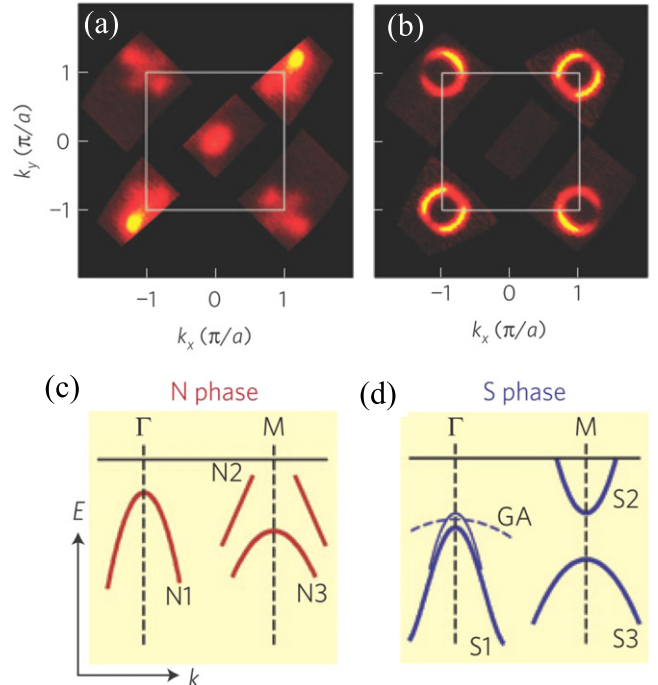


Figure 58. Fermi surface of the 1-UC FeSe before (a) and after (b) the annealing process. The annealing sequence is 190 °C/2 h + 250 °C/2 h + 190 °C/10 h + 360 °C/2 h in vacuum. In these figures, the Fermi surfaces are drawn in the folded BZ. (c), (d) Schematic band structures corresponding to (a) and (b). The band structure in (c) represents the N phase, whereas that in (d) the S phase. Reprinted by permission from Springer Nature: Nature Materials (He *et al* 2013). Copyright 2013.

As-grown 1-UC FeSe films are non-superconducting, and they are converted to a superconductor after subsequent annealing in vacuum at a relatively high temperature, which was mentioned explicitly in the first article by Wang *et al* (2012). Therefore, later (2013–2014) systematic ARPES and STM studies on the annealing effect have been performed. He *et al* (2013) investigated the evolution with annealing of the electronic structure and superconductivity by ARPES. The Fermi surface and the band structure of the 1-UC FeSe film experienced a pronounced change during the annealing process that induced electron doping. They identified two distinct phases, which compete during the annealing process: N and S phases. The N phase is dominant in as-grown or insufficiently annealed samples, whereas the S phase is dominant in well-annealed samples. The electronic structure of the N phase bears a clear resemblance to the antiferromagnetic parent compounds of Fe-based superconductors. The S phase emerges with the increase in doping and the suppression of the N phase. The band structures and Fermi surfaces of the two phases are compared in figure 58. The ARPES for the S phase shows an electron-like Fermi surface around X_{unfold} with no Fermi surface around the zone center (figure 58(b)), which is identical to the first observation by Liu *et al* (2012). The S phase is characterized by substantial electron doping and its concentration gradually increases with the annealing process. One immediate question that arises is what is happening during the annealing process. A few scenarios are possible. The first is the loss of Se by evaporation, which

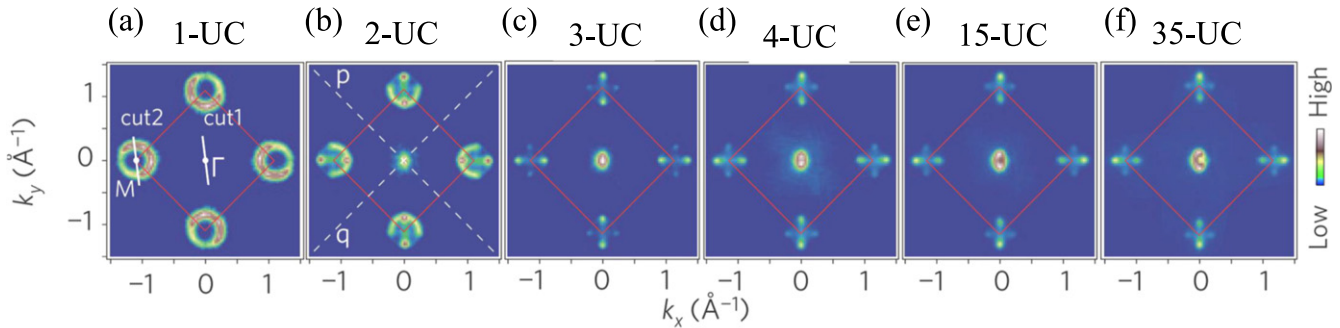


Figure 59. Electronic structure of FeSe films as a function of thickness. Reprinted by permission from Springer Nature: Nature Materials (Tan *et al* 2013). Copyright 2013.

would give rise to electron doping in FeSe. An indication of Se vacancy in FeSe films are also observed in STM (Zhang *et al* 2014). The second possibility is the loss of oxygen in SrTiO₃ near the interface between FeSe and SrTiO₃, which would also lead to electron doping. He *et al* (2013) obtained T_c as high as 65 K and Δ as large as 19 meV by optimizing the annealing condition. However, excess annealing leads to the deterioration of superconductivity such as the broadened and weakened the coherence peak.

As mentioned above, 1-UC FeSe is superconducting but a thickness higher than 1-UC kills superconductivity. Tan *et al* (2013) investigated the Fermi surface and band structure of FeSe as a function of thickness by ARPES. The 1- to 50-UC FeSe films were grown by MBE, subsequently annealed at 600 °C in vacuum, and directly transferred into the ARPES chamber in vacuum. The results are summarized in figure 59. The Fermi surface of the 1-UC FeSe is composed of four electron pockets at X_{unfold} as shown figure 59(a), which is identical to the above observation by Liu *et al* (2012) and He *et al* (2013). The Fermi surface topology changes dramatically for the FeSe films with increasing thickness. For the thickness ≥ 3 -UC, the hole pockets at Γ cross at E_F and simultaneously the band structure near X_{unfold} becomes complicated, giving four small electron pockets that make a cross mark. Similar pockets are observed in BaFe₂As₂ in the SDW state (Yang *et al* 2009), suggesting the presence of SDW in ≥ 3 -UC FeSe but not in 1-UC FeSe. They also took the photoemission data before and after the deposition of 1-UC FeSe and compared them. The SrTiO₃ surface pre-annealed in Se flux shows a metal-like Fermi step, which is owing to oxygen vacancies. After the 1-UC FeSe deposition, this Fermi step disappears almost entirely. From these observations, they concluded that the electrons in the localized oxygen-vacancy-induced states are transferred to the FeSe layer, and thus are responsible for the electron doping in 1-UC FeSe.

If the above scenario by Tan *et al* (2013) is correct, one may speculate that the absence of superconductivity in multilayer (≥ 2 -UC) FeSe is due to insufficient carrier transfer from a SrTiO₃ substrate. It has been demonstrated by the recent ARPES study by Miyata *et al* (2015) that this may be the case. They showed that 3-UC FeSe films, once coated with potassium (K) atoms, exhibit a pairing formation below $48 \text{ K} \pm 3 \text{ K}$. A similar observation has been reported from the

STS study by Tang *et al* (2016) that K-coated 2 ~ 4-UC FeSe films on SrTiO₃ exhibit T_c higher than 30 K and thickness-dependent superconducting gaps larger than 11 meV under optimal surface doping of K atoms/clusters. The T_c and Δ values should be compared with $T_c \sim 30 \text{ K}$ and $\Delta \sim 10 \text{ meV}$ in bulk $A_x\text{Fe}_2\text{Se}_2$ ($A = \text{K}, \text{Cs}$) (Zhang *et al* 2011b).

The origin of high- T_c superconductivity for ultrathin FeSe is currently being debated, and at present the following possibilities have been proposed.

- Alteration of the band structure or suppression of SDW in single layer.
- Electron transfer from a SrTiO₃ substrate and/or via Se vacancies.
- Interfacial coupling between electrons in 1-UC FeSe and oxygen optical phonons in SrTiO₃.

As shown in the next section, a high- T_c of FeSe was observed in films not only on a SrTiO₃ substrate but also on a MgO substrate by EDLT experiments. Therefore, it may not be confirmed that SrTiO₃ as a substrate is prerequisite in achieving high- T_c superconductivity.

6.7. Electric field effect for FeSe

A few groups have achieved $T_c \sim 40 \text{ K}$ in FeSe ultrathin films using an EDLT configuration (Hanzawa *et al* 2016, Shiogai *et al* 2016, Lei *et al* 2016). In EDLT experiments, by using ionic liquids, strong electric fields can be applied and thereby dope carriers on the surface of samples. The concept of EDLT, which is an old idea, aims at electrostatic charge carrier doping based on gigantic capacitance originating from a very thin (<10 Å) electric-double layer. Based on this concept, various kinds of physical properties such as superconductivity, magnetism, and metal-insulator (MI) transition, have been induced or controlled electrostatically. The storage of carrier density as high as $\sim 10^{15} \text{ cm}^{-2}$ on the surface of films is possible by using some special ionic liquids such as *N,N*-diethyl-*N*-methyl-*N*-(2-methoxyethyl)ammonium bis(trifluoromethanesulfonyl)imide (DEME-TFSI). With ionic liquids, it is also possible to etch films electrochemically by applying strong electric fields at high temperature. In section 6.6, ultrathin FeSe films were prepared by a bottom-up approach using MBE. Ultrathin FeSe can also be prepared by an alternative top-down approach using electrochemical

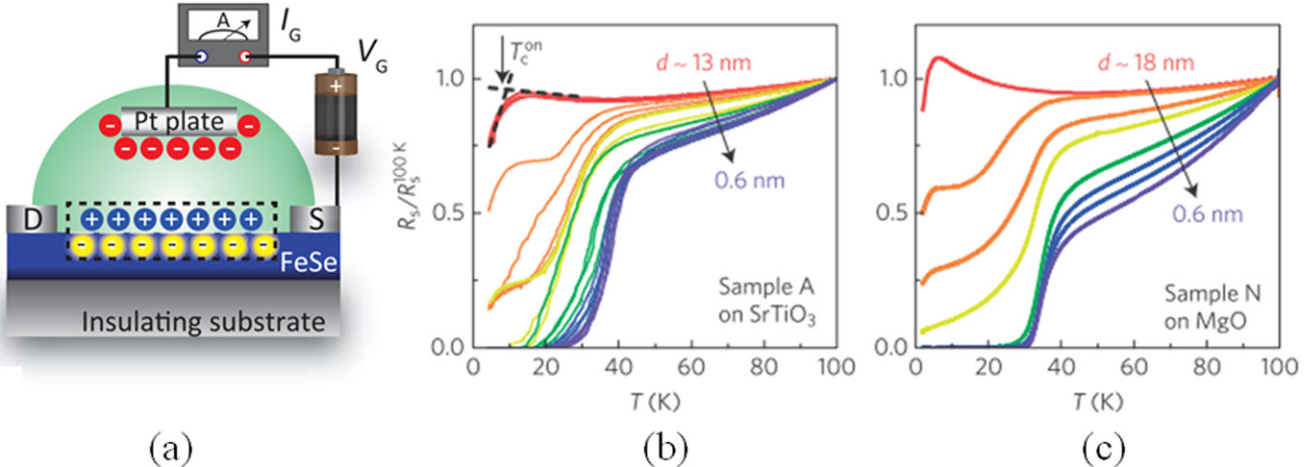


Figure 60. (a) Schematic of the EDLT composed of FeSe films on insulating substrates. Thickness tuning of FeSe films on SrTiO_3 (b) and MgO (c) via electrochemical etching. Sheet resistance normalized to the value at $T = 100 \text{ K}$, $R_s/R_s(100 \text{ K})$, is plotted as a function of temperature T during the continuing etching process, where the film thickness is continuously reduced. The T_c^{on} is defined by the intersection of the two dashed linear extrapolation lines as shown in the inset of (b). Reprinted by permission from Springer Nature: *Nature Physics* (Shiozai *et al* 2016). Copyright 2016.

etching that employs EDLT. The two features, electrostatic doping and electrochemical etching, of EDLT appear separately, depending on the temperature of ion liquids and on the applied gate voltage. Namely, doping primarily takes place at low temperature ($<220 \text{ K}$) and low applied voltage ($<5 \text{ V}$), whereas etching primarily takes place at a higher temperature ($>240 \text{ K}$) and voltage ($\geq 5 \text{ V}$).

Shiozai *et al* (2016) performed such an investigation and examined a possible occurrence of high- T_c superconductivity in ultrathin FeSe films etched by EDLT. They fabricated EDLT using 130 and 180 Å thick FeSe films grown on insulating SrTiO_3 and MgO substrates, respectively, by PLD. The initial T_c 's were 8.2 K and 4.8 K, respectively. The films and Pt gate electrode were covered with an ionic liquid of DEME-TFSI as schematically shown in figure 60(a). They first investigated the electrostatic doping effect at $T = 220 \text{ K}$, but no significant change in the $R-T$ curves was observed up to $V_G = +5 \text{ V}$. Subsequently, they etched films at $T = 245 \text{ K}$ with $V_G = +5 \text{ V}$. The averaged thickness of the etched films can be estimated from the etching rate in electrochemical reaction via the gate leakage current. After etching, the films were cooled, and the $R-T$ measurements were performed with V_G kept on (+5 V). The positive V_G depletes holes and accumulates electrons. A high T_c of 30 K–40 K appears after a series of etching as shown in figures 60(b) and (c). The T_c reached 43 K in the 1-UC ($\sim 5.5 \text{ \AA}$ thick) film on SrTiO_3 and 39 K in the 1-UC film on MgO . It is surprising that (i) the film on MgO is also superconducting with a comparable T_c and (ii) high- T_c emerges at thickness as large as $\sim 10\text{-UC}$, below which the thickness dependence is rather weak. Finally, they examined the electrostatic doping effect on the superconductivity. In the 1-UC film on SrTiO_3 , superconductivity with $T_c \sim 40 \text{ K}$ was retained even with V_G turned off. On the other hand, in the thicker (94 Å thick) film on SrTiO_3 ,

superconductivity disappeared with V_G turned off and reappeared with V_G turned on, demonstrating reversible electrostatic control of superconductivity. The T_c is also controlled continuously with V_G in the film (37 Å thick) on MgO . Unfortunately, there is no data on 1-UC FeSe on MgO .

Hanzawa *et al* (2016) grew 100 Å thick FeSe films on SrTiO_3 by MBE, which were used as a channel layer in their EDLT to induce high- T_c superconductivity. Upon applying $V_G = +5.0 \text{ V}$, a semiconductor–superconductor transition was induced with $T_c^{\text{on}} = 24 \text{ K}$. The highest T_c^{on} of 35 K was obtained by applying $V_G = +5.5 \text{ V}$. Their Hall effect measurements suggested that the high- T_c superconductivity comes from the highly accumulated electron carriers in the FeSe channel surface. The relationship between T_c and accumulated carrier density indicates that T_c in FeSe channel increases monotonically with V_G up to a breakdown voltage ($V_G > +5.5 \text{ V}$).

Lei *et al* (2016) did similar EDLT experiments using FeSe single crystals. The FeSe single crystals were grown by a flux method. FeSe thin flakes with a typical thickness of about 100 Å were used for the fabrication of EDLT devices. Before the gate voltage is applied, the FeSe flake showed $T_c^{\text{on}} = 5.2 \text{ K}$. With increasing V_G , T_c^{on} slowly increases and reaches 7.5 K at $V_G = 4.0 \text{ V}$. A further increase of V_G gives rise to a two-step superconducting transition in the sample. The low superconducting transition temperature nearly does not change, while the high one increases significantly from $\sim 30 \text{ K}$ to $\geq 40 \text{ K}$. Such a two-step transition should originate from the inhomogeneity of the carrier distribution. With $V_G > 5.0 \text{ V}$, only the superconducting transition with T_c above 40 K was observed and T_c^{on} continuously increases with increasing V_G . They also measured the Hall effect in their EDLT. Upon applying V_G , the effective carrier density (n_H) is initially positive and decreases in accord with an electron doping process. The n_H shows a sudden sign reversal

Table 6. Superconducting transition temperatures of Ln -1111 thin films fabricated by MBE and PLD.

Materials	Substrate	Method	Transition temperature (K) ^a	References
LaFeAs(O,F)	LaAlO ₃	PLD	T_c onset = 11.1 K $T_{c,90}$ = 28 K $T_{c,90}$ = 25 K, T_c end = 17 K T_c onset = 4.5 K, T_c end = 2 K T_c onset = 56 K, T_c end = 52 K T_c onset = 45 K, T_c end = 41 K T_c onset = 44 K, T_c end = 39 K T_c onset = 45 K, T_c end = 41 K $T_{c,90}$ = 47.1 K, T_c end = 42.5 K T_c onset = 50 K	Backen <i>et al</i> 2008 Haindl <i>et al</i> 2010 Kidszun <i>et al</i> 2010 Kawaguchi <i>et al</i> 2011b Uemura <i>et al</i> 2012 Uemura <i>et al</i> 2012 Uemura <i>et al</i> 2012 Kawaguchi <i>et al</i> 2011a Tarantini <i>et al</i> 2016 Chihara <i>et al</i> 2015
NdFeAs(O,F)	GaAs	MBE	T_c onset = 48 K, T_c end = 42 K T_c onset = 37 K, T_c end = 26 K	Kawaguchi <i>et al</i> 2010 Uemura <i>et al</i> 2012
	CaF ₂		T_c onset = 57.8 K, T_c end = 56.4 K	Ueda <i>et al</i> 2011a
	BaF ₂		T_c onset = 56.7 K, T_c end = 54.2 K	Ueda <i>et al</i> 2011a
	LaAlO ₃		T_c onset = 55.3 K, T_c end = 41.8 K	Ueda <i>et al</i> 2011a
SmFeAs(O,F)	Al ₂ O ₃	MBE + F diffusion	T_c onset = 50.3 K, T_c end = 49.3 K	Takeda <i>et al</i> 2012
	CaF ₂ -buffered LaAlO ₃		T_c onset = 52 K, T_c end = 48.6 K	Ueda <i>et al</i> 2011b
	YAlO ₃		T_c onset = 52.2 K, T_c end = 49.7 K	Ueda <i>et al</i> 2012a
	CaF ₂		T_c onset = 48.7 K, T_c end = 45.1 K	Ueda <i>et al</i> 2012b
	CaF ₂	MBE with FeF ₂	T_c onset = 56.1 K, T_c end = 54.0 K	Sugawara <i>et al</i>
	CaF ₂		T_c onset = 57.0 K, T_c end = 53.9 K	This review
	CaF ₂	MBE with FeF ₃	T_c onset = 55.9 K, T_c end = 52.3 K	Sakoda <i>et al</i>
	CaF ₂		$T_{c,90}$ = 35 K, $T_{c,10}$ = 24 K	Haindl <i>et al</i> 2016

^a $T_{c,90}$ and $T_{c,10}$ indicate the temperatures at which the sample resistance becomes 90% and 10% of the normal-state resistance, respectively.

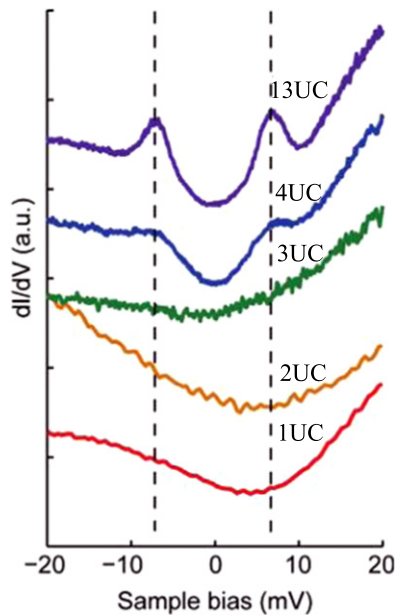


Figure 61. Thickness dependence of the dI/dV spectra for LiFeAs from -20 to 20 mV. The spectra are vertically shifted for clarity. The dashed line indicates the coherence peak. Reproduced from Chang *et al* (2015). Copyright © EPLA, 2015.

at $V_G = 4.25$ V. They confirm that the high- T_c phase starts to show up at the same voltage as the n_H shows a sign reversal. They pointed out a close connection between the enhanced T_c and the electron-dominated transport properties.

6.8. Ultrathin LiFeAs films by MBE

LiFeAs takes the PbFCl structure as shown in figure 1(d). Chang *et al* (2015) successfully fabricated LiFeAs epitaxial thin films on SrTiO₃(001) by MBE. Solid sources of Li, Fe, and FeAs were used. Because of a large difference in vapor pressure between Fe (10^{-4} torr at 1220 °C) and As (10^{-4} torr at 200 °C), almost pure As flux comes out from an FeAs source. The respective evaporation temperatures for Li, Fe, and FeAs were 400 °C, 1100 °C, and ≥ 400 °C. The optimum growth temperature for LiFeAs was determined as 450 °C and the growth rate was $0.2 \sim 0.4$ -UC ($c_0 \sim 6.3$ Å for LiFeAs) per min. A uniform film of LiFeAs was realized down to 3-UC, although the thickness could be reduced down to 1-UC. The in-plane lattice parameter determined by RHEED was relaxed as the film thickness reached 15-UC.

Shown in figure 61 is the evolution of dI/dV spectra for LiFeAs as a function of thickness measured at 4.2 K. It is clear that the superconducting gap sets in at the film thickness of 4-UC. Unlike monolayer FeSe, an enhanced superconducting gap was not observed in LiFeAs even with a thickness as thin as 1-UC. The peak-to-peak distance is $2\Delta \sim 14$ meV, which is close to the single-crystal value.

7. Summary and future prospects

In this article, we reviewed the progress in the synthesis of thin films of Fe-based superconductors over the decade since

their discovery. The growth of thin films of all of the representative Fe pnictides and chalcogenides has been achieved, and the following results have been obtained.

(a) 1111 compounds (see table 6):

1. $T_c^{\text{end}} > 56$ K was demonstrated for SmFeAs(O,F) films grown by the two-step growth using SmF₃ overlayer.
2. CaF₂ turned out to be a superior substrate.
3. One-step growth of SmFeAs(O,F) films was achieved using SmF₃, FeF₂, FeF₃ as a fluorine source. Their T_c^{end} is >52 K.
4. One-step growth of NdFeAs(O,F) films was also achieved via a different route, namely, by the codeposition of Fe, NdF₃, Ga, As in oxygen atmosphere, where Ga plays the role of F-getter.
5. J_c for $H \parallel ab$ is insensitive against applied magnetic field due to the presence of intrinsic pinning, which originates from the modulation of the superconducting order parameter along the crystallographic direction. Additionally, a J_c of over 10^5 A cm⁻² at 45 T and 4.2 K was recorded for both $H \parallel ab$ and $H \parallel c$, which is beyond the required level for practical applications.
6. Both point-like-pinning and surface pinning are present in SmFeAs(O,F) and NdFeAs(O,F).

(b) 122 compounds (see table 7):

1. $T_c^{\text{end}} > 31$ K and > 35 K were demonstrated for the (Sr,K)Fe₂As₂ and (Ba,K)Fe₂As₂ films, respectively, grown by MBE to codeposit Fe, Sr (Ba), K, and As. The key to the growth is reduced P_{As} .
2. Optimally P-doped BaFe₂As₂ inherently possesses high J_c due to a strong enhancement of the vortex core energy.
3. The critical angle for which inter-grain J_c starts to fall exponentially is as large as 9° (Ba(Fe,Co)₂As₂). Additionally, the inter-grain J_c beyond $\theta_{\text{GB}} = 30^\circ$ is almost constant. These properties may be generic properties for the 122 compounds, including BaFe₂(As,P)₂.
4. Low angle grain boundaries work as pinning centers.
5. Ba(Fe,Co)₂As₂ and BaFe₂(As,P)₂ thin films have been realized on technical substrates.
6. Artificial and naturally grown pinning centers can be introduced in both P- and Co-doped Ba-122 superconducting matrices, leading to high J_c –H performances.
7. Ba(Fe,Co)₂As₂ can accept a large volume fraction of secondary phase ($\sim 20\%$) without reducing T_c .

(c) 11 compounds (see table 8):

1. MBE growth of FeSe (except for ultrathin films) is not easy since the Se sticking is not self-limited as in the growth of GaAs.
2. Similarly to the 122 systems, Fe(Se,Te) possesses a high critical angle ($\sim 9^\circ$) as well as nearly constant inter-grain J_c above $\theta_{\text{GB}} = 30^\circ$.
3. Fe(Se,Te) thin films on both IBAD-MgO and RABiTS substrates have been realized.

4. Low-temperature thin-film synthesis suppresses the phase separation occurring at $0.1 \leq x \leq 0.4$ in FeSe_{1-x}Te_x. The highest $T_c \sim 23$ K is achieved at $x = 0.2$ on CaF₂.
5. $T_c > 50$ K has been suggested for MBE-grown monolayer FeSe on SrTiO₃ from several experiments (STS, ARPES, and also transport) although the origin of high- T_c superconductivity is being debated.
6. Using EDLT configuration, FeSe can be etched down to 1-UC. The T_c reached 43 K in the 1-UC film on SrTiO₃ and 39 K in the 1-UC film on MgO with V_G kept on (+5 eV).

These films are now being used in various research studies in materials science including the strain effects, pinning studies, improved superconductivity in ultrathin films, carrier doping by field-effect transistor configuration, etc. The large values and the weak magnetic field dependence of the J_c are promising for practical high-field applications. Furthermore, excellent quality epitaxial films have also been used in the research on basic physics such as transport, optics, *in situ* ARPES, and tunneling spectroscopy including *in situ* STS/STM. The current thin-film technology for Fe-based superconductors has reached a fairly mature level.

Now it is time to explore new directions of research. One candidate is to control the heterogeneous interface between Fe-based compounds and other materials and to discover new phenomena or to create superior functions in such interface. There have already been some indications that the interface seems to play an important role. The interface control should be performed by a scientific approach, namely, characterizing the interface carefully by *in situ* ARPES, *in situ* STS/STM, slow-muon μ SR, etc. The interface control may also enable us to fabricate high-quality JJs of Fe-based superconductors.

Historically speaking, there have been many struggles in the fabrication of JJs over 50 years. In the first Pb-based JJs, since the PbO_x barrier is thermally unstable, the JJ characteristics varied in time (Basavaiah and Greiner 1977). This unfavorable property of the barrier made it impossible to manufacture integrated JJ circuits. The second Nb-based JJ technology is the sole successful one in the history of superconducting electronics. Initial Nb JJs using the NbO_x barrier suffer from two major problems: the large dielectric constant of NbO_x and the existence of interfacial conducting Nb suboxides between insulating Nb₂O₅ pentoxide and metallic Nb. The dramatic improvement in the characteristics of Nb JJs was triggered by changing the barrier from NbO_x to Al₂O₃, which was proposed and attempted in the early 1980s (Rowell *et al* 1981, Gurvitch and Kwo 1984). Using the Al₂O₃ barrier, the interface becomes quite sharp as demonstrated by the photoemission experiments (Kwo *et al* 1982). The next was cuprates. With regard to the nonideal characteristics of cuprate-based JJs, we have pointed out one intrinsic problem with cuprates which is that the Cu–O bond responsible for superconductivity is weak (Yamamoto *et al* 1997, Naito *et al* 2000). Therefore, the redox reaction easily takes place at the interface between the cuprate surface and the overlayers. It causes severe oxygen depletion in the CuO₂ planes, leading to serious degradation or even the destruction of

Table 7. Superconducting transition temperatures of doped and undoped Ae -122 thin films fabricated by MBE and PLD. Since many studies on Co-doped Ba-122 have been reported, the highest T_c 's of the films have been tabulated.

Materials	Substrate	Method	Transition temperature (K)	References
K:Ba-122	Al_2O_3	MBE	$T_c^{\text{onset}} = 38.3 \text{ K}, T_c^{\text{end}} = 35.5 \text{ K}$	Takeda <i>et al</i> 2010
	Al_2O_3	Solid-state epitaxy	$T_c^{\text{onset}} = 40 \text{ K}$	Lee <i>et al</i> 2010a
	LaAlO_3		$T_c^{\text{onset}} = 39 \text{ K}$	Lee <i>et al</i> 2010a
K:Sr-122	Al_2O_3	MBE	$T_c^{\text{onset}} = 30.3 \text{ K}, T_c^{\text{end}} = 22.9 \text{ K}$	Agatsuma <i>et al</i> 2010
	Al_2O_3	MBE	$T_c^{\text{onset}} = 33.2 \text{ K}, T_c^{\text{end}} = 30 \text{ K}$	Takeda <i>et al</i> 2010
Co:Sr-122	LSAT	PLD	$T_c^{\text{onset}} = 20 \text{ K}$	Hiramatsu <i>et al</i> 2008b
	LaAlO_3		$T_{c,50} = 18.1 \text{ K}, T_{c,0} = 16.4 \text{ K}$	Choi <i>et al</i> 2009
	LSAT	PLD	$T_c^{\text{onset}} = 20.8 \text{ K}$	Hiramatsu <i>et al</i> 2013
P:Ba-122	MgO	MBE	$T_c^{\text{onset}} = 30.5 \text{ K}$	Sakagami <i>et al</i> 2013
	LSAT	PLD	$T_c^{\text{onset}} = 30.6 \text{ K}, T_c^{\text{end}} = 27.4 \text{ K}$	Adachi <i>et al</i> 2014
	MgO	PLD	$T_c^{\text{onset}} = 26.5 \text{ K}, T_c^{\text{end}} = 27.4 \text{ K}$	Sato <i>et al</i> 2014
Ni:Ba-122			$T_{c,90} = 28.9 \text{ K}$	Miura <i>et al</i> 2013a
	CaF_2	PLD	$T_c^{\text{end}} = 20.5 \text{ K}$	Yoon <i>et al</i> 2017
La:Ba-122			$T_{c,90} = 17.3 \text{ K}$	Richter <i>et al</i> 2017
	MgO	PLD	$T_c^{\text{onset}} = 22.4 \text{ K}$	Katase <i>et al</i> 2012a
Ce:Ba-122			$T_c^{\text{onset}} = 13.4 \text{ K}$	Katase <i>et al</i> 2013
Pr:Ba-122			$T_c^{\text{onset}} = 6.2 \text{ K}$	Katase <i>et al</i> 2013
Co:Ba-122	CaF_2	PLD	$T_{c,90} = 27.9 \text{ K}$	Kurth <i>et al</i> 2013
	MgO		$T_c = 25.5 \text{ K}$	Katase <i>et al</i> 2012b
	SrTiO ₃ -buffered LSAT		$T_c^{\text{end}} = 21.5 \text{ K}$	Lee <i>et al</i> 2010b
Ba-122	SrTiO_3		$T_c^{\text{onset}} = 24.5 \text{ K}$	Iida <i>et al</i> 2009
	Fe-buffered MgAl_2O_4		$T_{c,90} = 29.4 \text{ K}$	Engelmann <i>et al</i> 2013a
	Fe-buffered MgAl_2O_4		$T_c^{\text{end}} = 10 \text{ K}$	Engelmann <i>et al</i> 2013b
K-122	LSAT	Solid-state epitaxy	$T_c^{\text{onset}} = 3.7 \text{ K}$	Hiramatsu <i>et al</i> 2014b

Table 8. Superconducting transition temperatures of FeSe and Fe(Se,Te) thin films fabricated by MBE and PLD. Some of the studies particularly before 2012 are not shown in the table. Interested readers may refer to Li *et al* (2011) and Mele (2012). The results obtained from EDLTs in FeSe are also not tabulated.

Materials	Substrate	Method ^a	Transition temperature (K)	References
FeSe	r -cut Al_2O_3	MBE	$T_c^{\text{onset}} \sim 13 \text{ K}$	Agatsuma <i>et al</i> 2010
	CaF_2	PLD	$T_c^{\text{onset}} = 12.4 \text{ K}, T_c^{\text{end}} = 11.9 \text{ K}$	Nabeshima <i>et al</i> 2013
Monolayer FeSe	SrTiO_3	MBE	$T_c = 42 \text{ K}$	Wang <i>et al</i> 2012
	SrTiO_3	MBE	$T_c = 65 \pm 5 \text{ K}$	He <i>et al</i> 2013
FeSe _{1-x} Te _x $x = 0.0 \sim 1.0$	Nb-doped SrTiO_3	MBE	$T_c = 109 \text{ K}$	Ge <i>et al</i> 2015
	MgO	PLD	$T_c^{\text{onset}} \sim 14 \text{ K}, T_c^{\text{end}} \sim 12 \text{ K}$ at $x = 0.5$	Wu <i>et al</i> 2009
FeSe _{0.5} Te _{0.5}	SrTiO_3	PLD	$T_c = 17 \text{ K}$	Bellingeri <i>et al</i> 2009
FeSe _{0.5} Te _{0.5}	LaAlO_3	PLD	$T_c = 21 \text{ K}$	Bellingeri <i>et al</i> 2010
FeSe _{0.5} Te _{0.5}	CaF_2	PLD	$T_c^{\text{onset}} = 16.3 \text{ K}, T_c^{\text{end}} = 15.3 \text{ K}$	Tsukada <i>et al</i> 2011
FeSe _{0.5} Te _{0.2}		PLD	$T_c = 23 \text{ K}$	Imai <i>et al</i> 2015
FeSe _{0.72} Te _{0.18} ^b		PLD	$T_c^{\text{onset}} = 22 \text{ K}, T_c^{\text{end}} = 20.5 \text{ K}$	Seo <i>et al</i> 2017
FeSe _{0.5} Te _{0.5}	SrF_2	PLD	$T_c^{\text{onset}} = 15.7 \text{ K}$	Hanawa <i>et al</i> 2012
	BaF_2	PLD	$T_c^{\text{onset}} = 12.8 \text{ K}$	Hanawa <i>et al</i> 2012
FeSe _{0.5} Te _{0.5}	Fe-buffered MgO	PLD	$T_c^{\text{onset}} = 17.7 \text{ K}$	Iida <i>et al</i> 2011a
FeSe _{0.5} Te _{0.5}	CeO ₂ -buffered YSZ, RABiTS	PLD	$T_c^{\text{onset}} > 20 \text{ K}, T_c^{\text{end}} > 18 \text{ K}$	Si <i>et al</i> 2013
FeSe _{0.5} Te _{0.5}	CeO ₂ -buffered SrTiO_3	PLD	$T_c^{\text{onset}} = 18.5 \text{ K}, T_c^{\text{end}} = 18 \text{ K}$	Ozaki <i>et al</i> 2016
FeSe _{0.5} Te _{0.5}	FeSe _{1-x} Te _x -buffered MgO	PLD	$T_c^{\text{onset}} \geqslant 17 \text{ K}$,	Molatta <i>et al</i> 2015

^a The methods of how to determine the T_c of mono-layer FeSe films are described in the main text.^b The composition of this data is the film's composition determined by wavelength dispersive spectroscopy, but the compositions indicated in all of the other data are the target's composition.

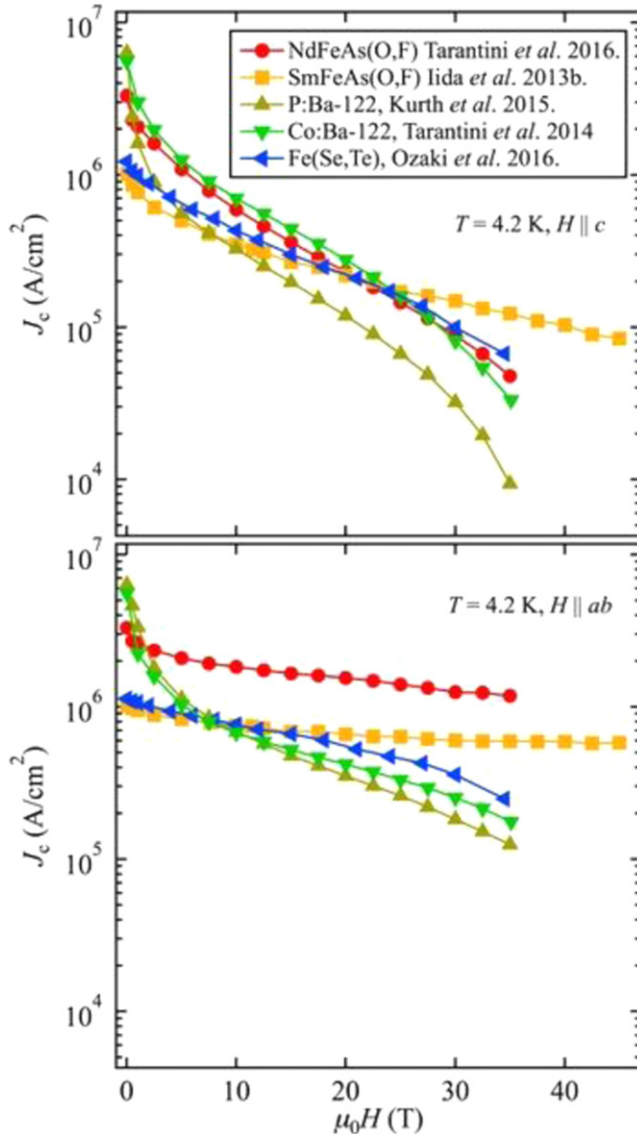


Figure 62. In-field J_c - H properties of various Fe-based superconducting thin films at 4.2 K for $H \parallel c$ and $H \parallel ab$. All measurements were conducted at the National High Magnetic Field Laboratory, FL, USA.

superconductivity. Loss of superconductivity at the interface is a new type of problem with JJs, which is different from the barrier non-ideality (leaky, thermally unstable, high dielectric constant, conducting, etc) encountered in Pb-based JJs and Nb-based JJs with a NbO_x barrier. As compared with the $\text{Cu}-\text{O}$ bond in the CuO_2 plane, the $\text{Fe}-\text{As}$ bond in the Fe_2As_2 layer appears to be stronger, suggesting that the interface issue may be lessened in Fe-based superconductors. We may see promising results for Fe-based JJs in the near future. Toward this goal, prerequisite are the scientific characterization and control of the heterogeneous interface between Fe pnictides/chalcogenides and other compounds.

Another candidate for new directions of research is to utilize ultrahigh H_{c2} of Fe-based superconducting films. One example toward this direction is coated conductors. As has already been mentioned in the recent review article by

Hosono *et al* (2017), Fe-based superconductors have great potential for wire applications for various reasons: high upper critical field (H_{c2}), low anisotropy, large critical angle (θ_c), and high tolerance to large concentration of the secondary phase. Large θ_c leads to the cost-effective production of wires. With high tolerance to large concentration of the secondary phase, there is still much room for further improvement of superconducting properties. Indeed, the depairing current density for ‘122’ is around 100 MA cm^{-2} at $T = 0 \text{ K}$, which is more than one order of magnitude higher than the J_c realized in pinning-enhanced Co-doped Ba-122 thin films.

For high-field magnet applications, it is desirable to compare the high-field J_c - H curves at 4.2 K for various Fe-based superconducting thin films (see figure 62). For $H \parallel c$, all films except for $\text{BaFe}_2(\text{As},\text{P})_2$ have a high J_c of $\sim 10^5 \text{ A cm}^{-2}$ at 30 T, albeit the self-field J_c of $\text{BaFe}_2(\text{As},\text{P})_2$ shows the highest of 6.5 MA cm^{-2} . Since $\text{BaFe}_2(\text{As},\text{P})_2$ is microstructurally clean (i.e., small density of pinning centers), J_c is monotonously decreased with fields. In the range of $0 \leq \mu_0 H \leq 20 \text{ T}$, the pinning enhanced $\text{Ba}(\text{Fe},\text{Co})_2\text{As}_2$ film exhibits the highest J_c , whilst in $\mu_0 H > 20 \text{ T}$, $\text{SmFeAs}(\text{O},\text{F})$ takes over. Although proton-irradiated $\text{Fe}(\text{Se},\text{Te})$ has a T_c of only 18.5 K, J_c - H properties up to $\mu_0 H = 20 \text{ T}$ are almost comparable to high- T_c $\text{SmFeAs}(\text{O},\text{F})$. Over 20 T, the level of J_c is the same as that of $\text{NdFeAs}(\text{O},\text{F})$ and $\text{Ba}(\text{Fe},\text{Co})_2\text{As}_2$. These results indicate that low-energy proton irradiation is very effective for pinning enhancement. For $H \parallel ab$, $\text{NdFeAs}(\text{O},\text{F})$ and $\text{SmFeAs}(\text{O},\text{F})$ exhibit almost constant J_c due to the intrinsic pinning. At present it is not easy to say which material is optimum for high-field applications.

Finally, we apologize that many new important reports could not be included in this article largely due to our limited capacity.

Acknowledgments

It is a pleasure to thank our coworkers and various close collaborators on this subject, including S Ueda, A Yamamoto, A Mitsuda, S Agatsuma, T Yamagishi, S Takeda, S Takano, H Sugawara, T Tsuneki, D Watanabe, F Kurth, S Trommler, J Engelmann, M Kidszun, S Haindl, S Richter, M Langer, F Yuan, J Hänsch, V Grinenko, S Aswartham, R Hühne, B Holzapfel, P Seidel, D Daghero, R Gonnelli, S Pagano, A Plecenik, A Golubov, M Putti, C Tarantini, J Jaroszynski, D C Larbalestier, and H Ikuta. We gratefully acknowledge many helpful discussions with A Maeda, Y Imai, I Tsukada, A Ichinose, S Lee, C B Eom, and Q Li. K I was supported by the European Union’s Seventh Framework Programme (FP7/2007-2013) under Grant No. 283141 and the Japan Society for the Promotion of Science (JSPS) through a Grant-in-Aid for Scientific Research (B) (Grant No. 16H04646). The work done at TAT was supported by the Transformative Research Project on Iron Pnictides (TRIP) and Strategic International Collaborative Research Program (SICORP), Japan Science and Technology Agency. The work done at the National High Magnetic Field Laboratory was supported by the National Science Foundation Cooperative Agreement No. DMR-1157490 and the State of Florida.

ORCID iDs

Kazumasa Iida <https://orcid.org/0000-0003-1038-9630>
 Michio Naito <https://orcid.org/0000-0002-7581-889X>

References

- Adachi S, Shimode T, Miura M, Chikumoto N, Takemori A, Nakao K, Oshikubo Y and Tanabe K 2012 Pulsed laser deposition of BaFe₂(As,P)₂ superconducting thin films with high critical current density *Supercond. Sci. Technol.* **25** 105015
- Adachi S, Shimode T, Murai Y, Chikumoto N and Tanabe K 2014 Chemical reaction between BaFe₂(As,P)₂ superconducting thin film and LSAT substrate *Physica C* **502** 31–5
- Agatsuma S, Yamagishi T, Takeda S and Naito M 2010 MBE growth of FeSe and Sr_{1-x}K_xFe₂As₂ *Physica C* **470** 1468–72
- Awaji S, Watanabe K and Kobayashi N 1999 Crossover from intrinsic to extrinsic pinning for YBa₂Cu₃O₇ *Cryogenics* **39** 569–77
- Awaji S, Ishihara R, Watanabe K, Shikimachi K, Hirano N and Nagaya S 2011 Anisotropy of the critical current density and intrinsic pinning behaviors of YBa₂Cu₃O_y coated conductors *Appl. Phys. Express* **4** 013101
- Backen E, Haindl S, Niemeier T, Hühne R, Freudenberg T, Werner J, Behr G, Schultz L and Holzapfel B 2008 Growth and anisotropy of La(O,F)FeAs thin films deposited by pulsed laser deposition *Supercond. Sci. Technol.* **21** 122001
- Basavaiah S and Greiner J H 1977 An investigation of the thermal cycling of Pb-alloy Josephson tunneling gates *J. Appl. Phys.* **48** 4630–3
- Bellingeri E, Buzio R, Gerbi A, Marrè D, Congiu S, Cimberle M R, Tropeano M, Siri A S, Palenzona A and Ferdeghini C 2009 High quality epitaxial FeSe_{0.5}Te_{0.5} thin films grown on SrTiO₃ substrates by pulsed laser deposition *Supercond. Sci. Technol.* **22** 105007
- Bellingeri E, Pallecchi I, Buzio R, Gerbi A, Marrè D, Cimberle M R, Tropeano M, Putti M, Palenzona A and Ferdeghini C 2010 $T_c = 21$ K in epitaxial FeSe_{0.5}Te_{0.5} thin films with biaxial compressive strain *Appl. Phys. Lett.* **96** 102512
- Bellingeri E *et al* 2012 Strong vortex pinning in FeSe_{0.5}Te_{0.5} epitaxial thin film *Appl. Phys. Lett.* **100** 082601
- Benerofe S J, Ahn C H, Wang M M, Kihlstrom K E, Do K B, Arnason S B, Fejer M M, Geballe T H, Beasley M R and Hammond R H 1994 Dual beam atomic absorption spectroscopy for controlling thin film deposition rates *J. Vac. Sci. Technol. B* **12** 1217–20
- Boutboul T, Le Naour S, Leroy D, Oberli L and Previtali V 2006 Critical current density in superconducting Nb-Ti strands in the 100 mT to 11 T applied field range *IEEE Trans. Appl. Supercond.* **16** 1184–7
- Braccini V *et al* 2013 Highly effective and isotropic pinning in epitaxial Fe(Se,Te) thin films grown on CaF₂ substrates *Appl. Phys. Lett.* **103** 172601
- Burrard-Lucas M *et al* 2013 Enhancement of the superconducting transition temperature of FeSe by intercalation of a molecular spacer layer *Nat. Mater.* **12** 15
- Cava R J *et al* 1994a Superconductivity at 23 K in yttrium palladium boride carbide *Nat.* **367** 146–8
- Cava R J *et al* 1994b Superconductivity in the quaternary intermetallic compounds LnNi₂B₂C *Nat.* **367** 252–3
- Chanda G, Lobo R P S M, Schachinger E, Wosnitza J, Naito M and Pronin A V 2014 Optical study of superconducting Pr₂CuO_x with $x \approx 4$ *Phys. Rev. B* **90** 024503
- Chang K *et al* 2015 Molecular beam epitaxy growth of superconducting LiFeAs film on SrTiO₃(001) substrate *Europhys. Lett.* **109** 28003
- Chang L L, Esaki L, Howard W E and Ludeke R 1973 The growth of a GaAs-GaAlAs superlattice *J. Vac. Sci. Technol.* **10** 11–6
- Chen C T, Tsuei C C, Ketchen M B, Ren Z A and Zhao Z X 2010 Integer and half-integer flux-quantum transitions in a niobium-iron pnictide loop *Nat. Phys.* **6** 260–4
- Chen H *et al* 2009 Coexistence of the spin-density wave and superconductivity in Ba_{1-x}K_xFe₂As₂ *Europhys. Lett.* **85** 17006
- Chen K, Cui Y, Li Q, Zhuang C G, Liu Z-K and Xi X X 2008 Study of MgB₂/I/Pb tunnel junctions on MgO (211) substrates *Appl. Phys. Lett.* **93** 012502
- Chen L, Tsai C F, Zhu Y, Chen A, Bi Z, Lee J and Wang H 2012 Enhanced flux pinning properties in superconducting FeSe_{0.5}Te_{0.5} thin films with secondary phases *Supercond. Sci. Technol.* **25** 025020
- Chew N G, Goodyear S W, Edwards J A, Satchell J S, Blenkinsop S E and Humphreys R G 1990 Effect of small changes in composition on the electrical and structural properties of YBa₂Cu₃O₇ thin films *Appl. Phys. Lett.* **57** 2016–8
- Chihara M, Sumiya N, Arai K, Ichinose A, Tsukada I, Hatano T, Iida K and Ikuta H 2015 Direct growth of superconducting NdFeAs(O,F) thin films by MBE *Physica C* **518** 69–72
- Choi E M, Jung S G, Lee N H, Kwon Y S, Kang W N, Kim D H, Jung M H, Lee S I and Sun L 2009 *In situ* fabrication of cobalt-doped SrFe₂As₂ thin films by using pulsed laser deposition with excimer laser *Appl. Phys. Lett.* **95** 062507
- Civale L, Maiorov B, MacManus-Driscoll J L, Wang H, Holesinger T G, Folty S R, Serquis A and Arendt P N 2005 Identification of intrinsic *ab*-plane pinning in YBa₂Cu₃O₇ thin films and coated conductors *IEEE Trans. Appl. Supercond.* **15** 2808
- de la Cruz C *et al* 2008 Magnetic order close to superconductivity in the iron-based layered LaO_{1-x}F_xFeAs systems *Nat.* **453** 899–902
- Dew-Hughes D 1974 Flux pinning mechanisms in type II superconductors *Phil. Mag.* **30** 293–305
- Drozdov A P, Erements M I, Troyan I A, Ksenofontov V and Shylin S I 2015 Conventional superconductivity at 203 kelvin at high pressures in the sulfur hydride system *Nat.* **525** 73–6
- Duncan W J, Welzel O P, Harrison C, Wang X F, Chen X H, Grosche F M and Niklowitz P G 2010 High pressure study of BaFe₂As₂: the role of hydrostaticity and uniaxial stress *J. Phys. Condens. Matter* **22** 052201
- Edlinger J, Fischer H, Koprio J A, Peter G and Ramm J 1988 Coevaporation of Y-Ba-Cu-O films in an ultra high vacuum plant *Physica C* **153-155** 778–9
- Engelmann J, Iida K, Kurth F, Behler C, Oswald S, Hühne R, Holzapfel B, Schultz L and Haindl S 2013a Fe/Ba(Fe_{1-x}Co_x)₂As₂ multilayers and quasi-multilayers with $T_c = 29$ K *Physica C* **494** 185–8
- Engelmann J *et al* 2013b Strain induced superconductivity in the parent compound BaFe₂As₂ *Nat. Commun.* **4** 2877
- Fernandes R M, Böhmer A, Meingast C and Schmalian J 2013 Scaling between magnetic and lattice fluctuations in iron pnictide superconductors *Phys. Rev. Lett.* **111** 137001
- Fischer H, Grob M, Peter G and Koprio J A 1988 Microprocessor controlled ultrahigh vacuum evaporation of critical thin films, multilayer structures, and coevaporated materials *J. Vac. Sci. Technol. A* **6** 2103
- Fujioka M *et al* 2013 Phase diagram and superconductivity at 58.1 K in α -FeAs-free SmFeAsO_{1-x}F_x *Supercond. Sci. Technol.* **26** 085023
- Gao Z, Qi Y, Wang L, Wang D, Zhang X, Yao C, Wang C and Ma Y 2011 Synthesis and properties of La-doped CaFe₂As₂ single crystals with $T_c = 42.7$ K *Europhys. Lett.* **95** 67002
- Ge J F, Liu Z L, Liu C, Gao C L, Qian D, Xue Q K, Liu Y and Jia J F 2015 Superconductivity above 100 K in single-layer FeSe films on doped SrTiO₃ *Nat. Mater.* **14** 285–9
- Giannozzi P, Baroni S, Bonini N, Calandra M, Car R, Cavazzoni C, Ceresoli D, Chiarotti G L, Cococcioni M and Dabo I 2009

- QUANTUM ESPRESSO: a modular and open-source software project for quantum simulations of materials *J. Phys. Condens. Matter* **21** 395502
- Goldman A I, Argyriou D N, Ouladdiaf B, Chatterji T, Kreyssig A, Nandi S, Ni N, Bud'ko S L, Canfield P C and McQueeney R J 2008 Lattice and magnetic instabilities in CaFe_2As_2 : A single-crystal neutron diffraction study *Phys. Rev. B* **78** 100506(R)
- Golubov A A and Mazin I I 2012 Designing phase-sensitive tests for Fe-based superconductors *Appl. Phys. Lett.* **102** 032601
- Gurvitch M and Kwo J 1984 Tunneling and surface properties of oxidized metal overlayers on Nb *Advances in Cryogenic Engineering Materials* vol 30 ed A F Clark and R P Reed (Berlin: Springer) pp 509–33
- Haindl S *et al* 2010 High upper critical fields and evidence of weak-link behavior in superconducting $\text{LaFeAsO}_{1-x}\text{F}_x$ thin films *Phys. Rev. Lett.* **104** 077001
- Haindl S *et al* 2014 Thin film growth of Fe-based superconductors: from fundamental properties to functional devices: a comparative review *Rep. Prog. Phys.* **77** 046502
- Haindl S, Hanzawa K, Sato H, Hiramatsu H and Hosono H 2016 *In-situ* growth of superconducting $\text{SmO}_{1-x}\text{F}_x\text{FeAs}$ thin films by pulsed laser deposition *Sci. Rep.* **6** 35797
- Han Y, Li W Y, Cao L X, Wang X Y, Xu B, Zhao B R, Guo Y Q and Yang J L 2010 Superconductivity in iron telluride thin films under tensile stress *Phys. Rev. Lett.* **104** 017003
- Hanawa M, Ichinose A, Komiya S, Tsukada I, Imai Y and Maeda A 2012 Empirical selection rule of substrate materials for iron chalcogenide superconducting thin films *Jpn. J. Appl. Phys.* **51** 010104
- Hänisch J, Iida K, Haindl S, Kurth F, Kaufmann A, Kidszun M, Thersleff T, Freudenberger J, Schultz L and Holzapfel B 2011 J_c scaling and anisotropies in Co-doped Ba-122 thin films *IEEE Trans. Appl. Supercond.* **21** 2887–90
- Hänisch J, Iida K, Kurth F, Thersleff T, Trommler S, Reich E, Hühne R, Schultz L and Holzapfel B 2014 The effect of 45° grain boundaries and associated Fe particles on J_c and resistivity in $\text{Ba}(\text{Fe}_{0.9}\text{Co}_{0.1})_2\text{As}_2$ thin films *AIP Conf. Proc.* **1574** 260
- Hanzawa K, Sato H, Hiramatsu H, Kamiya T and Hosono H 2016 Electric field-induced superconducting transition of insulating FeSe thin film at 35 K *Proc. Natl Acad. Sci. USA* **113** 3986–90
- Hatakeyama T, Sato H, Hiramatsu H, Kamiya T and Hosono H 2016 Novel solid-phase epitaxy for multi-component materials with extremely high vapor pressure elements: An application to KFe_2As_2 *Appl. Phys. Express* **9** 055505
- Hatano T, Kawaguchi T, Fujimoto R, Nakamura I, Mori Y, Harada S, Ujihara T and Ikuta H 2016 Thin film growth of CaFe_2As_2 by molecular beam epitaxy *Supercond. Sci. Technol.* **29** 015013
- Haule K, Shim J H and Kotliar G 2008 Correlated electronic structure of $\text{LaO}_{1-x}\text{F}_x\text{FeAs}$ *Phys. Rev. Lett.* **100** 226402
- He S *et al* 2013 Phase diagram and electronic indication of high-temperature superconductivity at 65 K in single-layer FeSe films *Nat. Mater.* **12** 605–10
- Hiramatsu H, Katase T, Kamiya T, Hirano M and Hosono H 2008a Heteroepitaxial growth and optoelectronic properties of layered iron oxyarsenide, LaFeAsO *Appl. Phys. Lett.* **93** 162504
- Hiramatsu H, Katase T, Kamiya T, Hirano M and Hosono H 2008b Superconductivity in epitaxial thin films of Co-doped SrFe_2As_2 with bilayered FeAs structures and their magnetic anisotropy *Appl. Phys. Express* **1** 101702
- Hiramatsu H, Kamiya T, Hirano M and Hosono H 2009 Heteroepitaxial film growth of layered compounds with the ZrCuSiAs -type and ThCr_2Si_2 -type structures: from Cu-based semiconductors to Fe-based superconductors *Physica C* **469** 657–66
- Hiramatsu H, Katase T, Kamiya T and Hosono H 2012 Thin film growth and device fabrication of iron-based superconductors *J. Phys. Soc. Jpn.* **81** 011011
- Hiramatsu H, Katase T, Kamiya T and Hosono H 2013 Superconducting properties and phase diagram of indirectly electron-doped $(\text{Sr}_{1-x}\text{La}_x)\text{Fe}_2\text{As}_2$ epitaxial films grown by pulsed laser deposition *IEEE Trans. Appl. Supercond.* **23** 7300405
- Hiramatsu H, Sato H, Katase T, Kamiya T and Hosono H 2014a Critical factor for epitaxial growth of cobalt-doped BaFe_2As_2 films by pulsed laser deposition *Appl. Phys. Lett.* **104** 172602
- Hiramatsu H, Matsuda S, Sato H, Kamiya T and Hosono H 2014b Growth of c -axis-oriented superconducting KFe_2As_2 thin films *ACS Appl. Mater. Interfaces* **6** 14293–301
- Hirschfeld P J, Korshunov M M and Mazin I I 2011 Gap symmetry and structure of Fe-based superconductors *Rep. Prog. Phys.* **74** 124508
- Hosono H 2007 Recent progress in transparent oxide semiconductors: materials and device application *Thin Solid Films* **515** 6000–14
- Hosono H and Kuroki K 2015 Iron-based superconductors: current status of materials and pairing mechanism *Physica C* **514** 399–422
- Hosono H, Tanabe K, Takayama-Muromachi E, Kageyama H, Yamanaka S, Kumakura H, Nohara M, Hiramatsu H and Fujitsu S 2015 Exploration of new superconductors and functional materials, and fabrication of superconducting tapes and wires of iron pnictides *Sci. Technol. Adv. Mater.* **16** 033503
- Hosono H, Yamamoto A, Hiramatsu H and Ma Y 2018 Recent advances in iron-based superconductors toward applications *Mater. Today* **21** 278–302
- Hsu F C *et al* 2008 Superconductivity in the PbO-type structure α -FeSe *Proc. Natl. Acad. Sci.* **105** 14262–4
- Huang Q, Zhao J, Lynn J W, Chen G F, Luo J L, Wang N L and Dai P 2008a Doping evolution of antiferromagnetic order and structural distortion in $\text{LaFeAsO}_{1-x}\text{F}_x$ *Phys. Rev. B* **78** 054529
- Huang Q, Qiu Y, Bao W, Green M A, Lynn J W, Gasparovic Y C, Wu T, Wu G and Chen X H 2008b Neutron-diffraction measurements of magnetic order and a structural transition in the parent BaFe_2As_2 compound of FeAs-based high-temperature superconductors *Phys. Rev. Lett.* **101** 257003
- Ichinose A, Nabeshima F, Tsukada I, Hanawa M, Komiya S, Akiike T, Imai Y and Maeda A 2013 Microscopic analysis of the chemical reaction between $\text{Fe}(\text{Te},\text{Se})$ thin films and underlying CaF_2 *Supercond. Sci. Technol.* **26** 075002
- Iida K, Hänisch J, Hühne R, Kurth F, Kidszun M, Haindl S, Werner J, Schultz L and Holzapfel B 2009 Strong T_c dependence for strained epitaxial $\text{Ba}(\text{Fe}_{1-x}\text{Co}_x)_2\text{As}_2$ thin films *Appl. Phys. Lett.* **95** 192501
- Iida K, Hänisch J, Thersleff T, Kurth F, Kidszun M, Haindl S, Hühne R, Schultz L and Holzapfel B 2010 Scaling behavior of the critical current in clean epitaxial $\text{Ba}(\text{Fe}_{1-x}\text{Co}_x)_2\text{As}_2$ thin films *Phys. Rev. B* **81** 100507(R)
- Iida K, Hänisch J, Schulze M, Aswartham S, Wurmehl S, Büchner B, Schultz L and Holzapfel B 2011a Generic Fe buffer layers for Fe-based superconductors: epitaxial $\text{FeSe}_{1-x}\text{Te}_x$ thin films *Appl. Phys. Lett.* **99** 202503
- Iida K *et al* 2011b Epitaxial growth of superconducting $\text{Ba}(\text{Fe}_{1-x}\text{Co}_x)_2\text{As}_2$ thin films on technical ion beam assisted deposition MgO substrates *Appl. Phys. Express* **4** 013103
- Iida K *et al* 2013a Intrinsic pinning and the critical current scaling of clean epitaxial $\text{Fe}(\text{Se},\text{Te})$ thin films *Phys. Rev. B* **87** 104510
- Iida K *et al* 2013b Oxypnictide SmFeAs(O,F) superconductor: a candidate for high-field magnet applications *Sci. Rep.* **3** 2139
- Iida K *et al* 2016 Hall-plot of the phase diagram for $\text{Ba}(\text{Fe}_{1-x}\text{Co}_x)_2\text{As}_2$ *Sci. Rep.* **6** 28390
- Iida K *et al* 2018 unpublished
- Iida K, Sato H, Tarantini C, Hänisch J, Jaroszynski J, Hiramatsu H, Holzapfel B and Hosono H 2017 High-field transport

- properties of a P-doped BaFe₂As₂ film on technical substrate *Sci. Rep.* **7** 39951
- Imai Y, Akiike T, Hanawa M, Tsukada I, Ichinose A, Maeda A, Hikage T, Kawaguchi T and Ikuta H 2010 Systematic comparison of eight substrates in the growth of FeSe_{0.5}Te_{0.5} superconducting thin films *Appl. Phys. Express* **3** 043102
- Imai Y, Sawada Y, Nabeshima F and Maeda A 2015 Suppression of phase separation and giant enhancement of superconducting transition temperature in FeSe_{1-x}Te_x thin films *Proc. Natl Acad. Sci.* **112** 1937–40
- Imai Y, Nabeshima F and Maeda A 2017 Comparative review on thin film growth of iron-based superconductors *Condens. Matter.* **2** 25
- Izyumov Y and Kurmaev E 2010 High- T_c superconductors based on FeAs compounds *Springer Series in Materials Science* vol 143 (Berlin: Springer)
- James A C W P, Murphy D W and Zahurak S M 1989 Superconductivity at 27 K in fluorine-doped Nd₂CuO₄ *Nat.* **338** 240
- Jeitschko W, Glaum R and Boonk L 1987 Superconducting LaRu₂P₂ and other alkaline earth and rare earth metal ruthenium and osmium phosphides and arsenides with ThCr₂Si₂ structure *J. Solid State Chem.* **69** 93–100
- Johnson V and Jeitschko W 1974 ZrCuSiAs: a ‘filled’ PbFCl type *J. Solid State Chem.* **11** 161–6
- Johnston D C 2010 The puzzle of high temperature superconductivity in layered iron pnictides and chalcogenides *Adv. Phys.* **59** 803–1061
- Johrendt D and Pöttgen R 2009 Superconductivity, magnetism and crystal chemistry of Ba_{1-x}K_xFe₂As₂ *Physica C* **469** 332–9
- Johrendt D, Hosono H, Hoffmann R D and Rainer Pöttgen R 2011 Structural chemistry of superconducting pnictides and pnictide oxides with layered structures *Z. Kristallogr.* **226** 435–46
- Kamihara Y, Hiramatsu H, Hirano M, Kawamura R, Yanagi H, Kamiya T and Hosono H 2006 Iron-based layered superconductor: LaOFeP *J. Am. Chem. Soc.* **128** 10012–3
- Kamihara Y, Watanabe T, Hirano M and Hosono H 2008 Iron-based layered superconductor La[O_{1-x}F_x]FeAs ($x = 0.05\text{--}0.12$) with $T_c = 26$ K *J. Am. Chem. Soc.* **130** 3296–7
- Kamihara Y *et al* 2010 Electronic and magnetic phase diagram of superconductors, SmFeAsO_{1-x}F_x *New J. Phys.* **12** 033005
- Kanithi H, Blasiak D, Lajewski J, Berriaud C, Vedrine P and Gilgrass G 2014 Production results of 11.75 tesla Iseult/INUMAC MRI conductor at Luvata *IEEE Trans. Appl. Supercond.* **24** 6000504
- Karpinski J *et al* 2009 Single crystals of LnFeAsO_{1-x}F_x (Ln = La, Pr, Nd, Sm, Gd) and Ba_{1-x}Rb_xFe₂As₂: growth, structure and superconducting properties *Physica C* **469** 370
- Kasahara S *et al* 2010 Evolution from non-Fermi- to Fermi-liquid transport via isovalent doping in BaFe₂(As_{1-x}P_x)₂ superconductors *Phys. Rev. B* **81** 184519
- Katase T, Hiramatsu H, Yanagai H, Kamiya T, Hirano M and Hosono H 2009 Atomically-flat, chemically-stable, superconducting epitaxial thin film of iron-based superconductor, cobalt-doped BaFe₂As₂ *Solid State Commun.* **149** 2121–4
- Katase T, Hiramatsu H, Kamiya T and Hosono H 2010 High critical current density 4 MA/cm² in Co-doped BaFe₂As₂ epitaxial films grown on (La,Sr)(Al,Ta)O₃ substrates without buffer layers *Appl. Phys. Express* **3** 063101
- Katase T, Hiramatsu H, Matias V, Sheehan C, Ishimaru Y, Kamiya T, Tanabe K and Hosono H 2011a Biaxially textured cobalt-doped BaFe₂As₂ films with high critical current density over 1 MA/cm² on MgO-buffered metal-tape flexible substrates *Appl. Phys. Lett.* **98** 242510
- Katase T, Ishimaru Y, Tsukamoto A, Hiramatsu H, Kamiya T, Tanabe K and Hosono H 2011b Advantageous grain boundaries in iron pnictide superconductors *Nat. Commun.* **2** 409
- Katase T, Iimura S, Hiramatsu H, Kamiya T and Hosono H 2012a Identical effects of indirect and direct electron doping of superconducting BaFe₂As₂ thin films *Phys. Rev. B* **85** 140516
- Katase T, Hiramatsu H, Kamiya T and Hosono H 2012b Thin film growth by pulsed laser deposition and properties of 122-type iron-based superconductor AE(Fe_{1-x}Co_x)₂As₂ (AE=alkaline earth) *Supercond. Sci. Technol.* **25** 084015
- Katase T, Hiramatsu H, Kamiya T and Hosono H 2013 Magnetic scattering and electron pair breaking by rare-earth-ion substitution in BaFe₂As₂ epitaxial films *New J. Phys.* **15** 073019
- Kawaguchi T, Uemura H, Ohno T, Watanabe R, Tabuchi M, Ujihara T, Takenaka K, Takeda Y and Ikuta H 2009 Epitaxial growth of NdFeAsO thin films by molecular beam epitaxy *Appl. Phys. Express* **2** 093002
- Kawaguchi T, Uemura H, Ohno T, Tabuchi M, Ujihara T, Takenaka K, Takeda Y and Ikuta H 2010 *In situ* growth of superconducting NdFeAs(O,F) thin films by molecular beam epitaxy *Appl. Phys. Lett.* **97** 042509
- Kawaguchi T, Uemura H, Ohno T, Tabuchi M, Ujihara T, Takeda Y and Ikuta H 2011a Molecular beam epitaxy growth of superconducting NdFeAs(O,F) thin films using a F-getter and a novel F-doping method *Appl. Phys. Express* **4** 083102
- Kawaguchi T, Uemura H, Ohno T, Tabuchi M, Ujihara T, Takenaka K, Takeda Y and Ikuta H 2011b Epitaxial growth of LaFeAs(O,F) thin films by molecular beam epitaxy *Physica C* **471** 1174–6
- Kawaguchi T, Sakagami A, Mori Y, Tabuchi M, Ujihara T, Takeda Y and Ikuta H 2014 The strain effect on the superconducting properties of BaFe₂(As, P)₂ thin films grown by molecular beam epitaxy *Supercond. Sci. Technol.* **27** 065005
- Kayanuma K, Kawamura R, Hiramatsu H, Yanagi H, Hirano M, Kamiya T and Hosono H 2008 Heteroepitaxial growth of layered semiconductors, LaZnOPn (Pn = P and As) *Thin Solid Films* **516** 5800–4
- Kidszun M, Haindl S, Reich E, Hänsch J, Iida K, Schultz L and Holzapfel B 2010 Fabrication of superconducting oxypnictide thin films *Supercond. Sci. Technol.* **23** 022002
- Kidszun M, Haindl S, Thersleff T, Hänsch J, Kauffmann A, Iida K, Freudenberg J, Schultz L and Holzapfel B 2011 Critical current scaling and anisotropy in oxypnictide superconductors *Phys. Rev. Lett.* **106** 137001
- Kim M-S, Skinta J A, Lemberger T R, Tsukada A and Naito M 2003 Magnetic penetration depth measurements of Pr_{2-x}Ce_xCuO_{4-d} films on buffered substrates: evidence for a nodeless gap *Phys. Rev. Lett.* **91** 087001
- Kimber S A J *et al* 2009 Similarities between structural distortions under pressure and chemical doping in superconducting BaFe₂As₂ *Nat. Mater.* **8** 471–5
- Klausmeier-Brown M E, Eckstein J N, Bozovic I and Virshup G F 1992 Accurate measurement of atomic beam flux by pseudo-double-beam atomic absorption spectroscopy for growth of thin-film oxide superconductors *Appl. Phys. Lett.* **60** 657
- Kojima K M *et al* 2014 Bulk superconductivity in undoped T'-La_{1.9}Y_{0.1}CuO₄ probed by muon spin rotation *Phys. Rev. B* **89** 180508(R)
- Koprio J A, Peter G and Fischer H 1988 Quadrupole mass spectrometer monitored and controlled thin film deposition processes under ultrahigh vacuum conditions *Vacuum* **38** 783–6
- Kudo K, Iba K, Takasuga M, Kitahama Y, Matsumura J, Danura M, Nogami Y and Nohara M 2013 Emergence of superconductivity at 45 K by lanthanum and phosphorus co-doping of CaFe₂As₂ *Sci. Rep.* **3** 1478
- Kuroki K, Onari S, Arita R, Usui H, Tanaka Y, Kontani H and Aoki H 2008 Unconventional pairing originating from the

- disconnected Fermi surfaces of superconducting $\text{LaFeAsO}_{1-x}\text{F}_x$ *Phys. Rev. Lett.* **101** 087004
- Kuroki K, Usui H, Onari S, Arita R and Aoki H 2009 Pnictogen height as a possible switch between high- T_c nodeless and low- T_c nodal pairings in the iron-based superconductors *Phys. Rev. B* **79** 224511
- Kurth F *et al* 2013 Versatile fluoride substrates for Fe-based superconducting thin films *Appl. Phys. Lett.* **102** 142601
- Kurth F *et al* 2015 Unusually high critical current of clean P-doped BaFe_2As_2 single crystalline thin film *Appl. Phys. Lett.* **106** 072602
- Kwo J, Wertheim G K, Gurvitch M and Buchanan D N E 1982 X-ray photoemission spectroscopy study of surface oxidation of Nb/Al overlayer structures *Appl. Phys. Lett.* **40** 675
- Lebègue S 2007 Electronic structure and properties of the Fermi surface of the superconductor LaOFeP *Phys. Rev. B* **75** 035110
- Lee C H *et al* 2008 Relationship between crystal structure and superconductivity in LnFeAsO_{1-y} (Ln =lanthanide) *J. Phys. Soc. Jpn.* **77** 44
- Lee C H, Kihou K, Iyo A, Kito H, Shirage P M and Eisaki H 2012 Relationship between crystal structure and superconductivity in iron-based superconductors *Solid State Commun.* **152** 644
- Lee J *et al* 2017 High critical current density over 1 MAcm⁻² at 13 T in BaZrO_3 incorporated $\text{Ba}(\text{Fe}, \text{Co})_2\text{As}_2$ thin film *Supercond. Sci. Technol.* **30** 085006
- Lee N H, Jung S-G, Kim D H and Kang W N 2010a Potassium-doped BaFe_2As_2 superconducting thin films with a transition temperature of 40 K *Appl. Phys. Lett.* **96** 202505
- Lee N H, Jung S-G, Ranot M and Kang W N 2014 Fabrication details of $\text{Ba}_{1-x}\text{K}_x\text{Fe}_2\text{As}_2$ films by pulsed laser deposition technique *Prog. Supercond. Cryog.* **6** 4–6
- Lee S *et al* 2009 Weak-link behavior of grain boundaries in superconducting $\text{Ba}(\text{Fe}_{1-x}\text{Co}_x)_2\text{As}_2$ bicrystals *Appl. Phys. Lett.* **95** 212505
- Lee S *et al* 2010b Template engineering of Co-doped BaFe_2As_2 single-crystal thin films *Nat. Mater.* **9** 397–402
- Lee S *et al* 2013 Artificially engineered superlattices of pnictide superconductors *Nat. Mater.* **12** 392–6
- Lei B, Cui J H, Xiang Z J, Shang C, Wang N Z, Ye G J, Luo X G, Wu T, Sun Z and Chen X H 2016 Evolution of high-temperature superconductivity from a low- T_c phase tuned by carrier concentration in FeSe thin flakes *Phys. Rev. Lett.* **116** 077002
- Lei Q Y *et al* 2014 Structural and transport properties of epitaxial $\text{Ba}(\text{Fe}_{1-x}\text{Co}_x)_2\text{As}_2$ thin films on various substrates *Supercond. Sci. Technol.* **27** 115010
- Li G Z, Sumption M D, Zwayer J B, Susner M A, Rindfleish M A, Thong C J, Tomsic M J and Collings E W 2013 Effects of carbon concentration and filament number on advanced internal Mg infiltration-processed MgB_2 strands *Supercond. Sci. Technol.* **26** 095007
- Li Q, Si W and Dimitrov I K 2011 Films of iron chalcogenide superconductors *Rep. Prog. Phys.* **74** 124510
- Liu D *et al* 2012 Electronic origin of high-temperature superconductivity in single-layer FeSe superconductor *Nat. Commun.* **3** 931
- Liu K W, Zhang J Y, Shen D Z, Shan C X, Li B H, Lu Y M and Fan W X 2007 Electronic and magnetic properties of FeSe thin film prepared on GaAs (001) substrate by metal-organic chemical vapor deposition *Appl. Phys. Lett.* **90** 262503
- Liu R H *et al* 2008 transport properties and phase diagram of the FeAs-based $\text{SmFeAsO}_{1-x}\text{F}_x$ superconductors *Phys. Rev. Lett.* **101** 087001
- Lu C and Guan Y 1995 Improved method of nonintrusive deposition rate monitoring by atomic absorption spectroscopy for physical vapor deposition processes *J. Vac. Sci. Technol. A* **13** 1797
- Lu C and Lightner M J 1977 Rate controlling and composition analysis of alloy deposition processes by electron impact emission spectroscopy (EIES) *J. Vac. Sci. Technol.* **14** 103
- Lu C, Blissett C D and Diehl G 2008 An electron impact emission spectroscopy flux sensor for monitoring deposition rate at high background gas pressure with improved accuracy *J. Vac. Sci. Technol. A* **26** 956
- Luetkens H *et al* 2008 The electronic phase diagram of the $\text{LaO}_{1-x}\text{Fe}_2\text{As}_2$ superconductor *Nat. Mater.* **8** 305
- Luo H, Wang Z, Yang H, Cheng P, Zhu X and Wen H-H 2008 Growth and characterization of $\text{A}_{1-x}\text{K}_x\text{Fe}_2\text{As}_2$ (A =Ba, Sr) single crystals with x =0–0.4 *Supercond. Sci. Technol.* **21** 125014
- Lv B, Gooch M, Lorenz B, Chen F, Guloy A M and Chu C W 2009 The superconductor $\text{K}_x\text{Sr}_{1-x}\text{Fe}_2\text{As}_2$: normal state and superconducting properties *New J. Phys.* **11** 025013
- Lv B, Deng L, Gooch M, Wei F, Sun Y, Meen J K, Xue Y Y, Lorenz B and Chu C W 2011 Unusual superconducting state at 49 K in electron-doped CaFe_2As_2 at ambient pressure *Proc. Natl. Acad. Sci.* **108** 15705
- Lynn J W and Dai P 2009 Neutron studies of the iron-based family of high- T_c magnetic superconductors *Physica C* **469** 469–76
- MacManus-Driscoll J L, Folty S R, Jia Q X, Wang H, Serquis A, Maiorov B, Cicale L, Hawley M E and Peterson D E 2004 Strongly enhanced current densities in superconducting coated conductors of $\text{YBa}_2\text{Cu}_3\text{O}_{7-x}$ + BaZrO_3 *Nat. Mater.* **3** 439
- Maeter H *et al* 2012 Structural and electronic phase diagrams of $\text{CeFeAsO}_{1-x}\text{F}_x$ and $\text{SmFeAsO}_{1-x}\text{F}_x$ (arXiv:1210.6959v1)
- Maiorov B, Katase T, Baily S A, Hiramatsu H, Holesinger T G, Hosono H and Civale L 2011 Liquid vortex phase and strong *c*-axis pinning in low anisotropy $\text{BaCo}_x\text{Fe}_{2-x}\text{As}_2$ pnictide films *Supercond. Sci. Technol.* **24** 055007
- Margadonna S, Takabayashi Y, McDonald M T, Brunelli M, Wu G, Liu R H, Chen X H and Prassides K 2009a Crystal structure and phase transitions across the metal-superconductor boundary in the $\text{SmFeAsO}_{1-x}\text{F}_x$ ($0 \leq x \leq 0.20$) family *Phys. Rev. B* **79** 014503
- Margadonna S, Takabayashi Y, Ohishi Y, Mizuguchi Y, Takano Y, Kagayama T, Nakagawa T, Takata M and Prassides K 2009b Pressure evolution of the low-temperature crystal structure and bonding of the superconductor FeSe ($T_c = 37$ K) *Phys. Rev. B* **80** 064506
- Martinelli A, Palenzona A, Tropeano M, Putti M, Ferdeghini C, Profeta G and Emerich E 2011 Retention of the tetragonal to orthorhombic structural transition in F-Substituted SmFeAsO : a new phase diagram for $\text{SmFeAs(O}_{1-x}\text{F}_x)$ *Phys. Rev. Lett.* **106** 227001
- Matijasevic V, Rosenthal P, Shinohara K, Marshall A F, Hammond R H and Beasley M R 1991 Reactive coevaporation of YBaCuO superconducting films *J. Mater. Res.* **6** 682–98
- Mattheiss L F, Siegrist T and Cava R J 1994 Superconductivity in the $\text{LnNi}_2\text{B}_2\text{C}$ intermetallics via boron A1g phonons *Solid State Commun.* **91** 587
- Mazumdar C, Nagarajana R, Godart C, Gupta L C, Latroche M, Dhara S K, Clement C L, Padalia B D and Vijayaraghavan R 1993 Superconductivity at 12 K in Y-Ni-B system *Solid State Commun.* **87** 413
- McQueen T M *et al* 2009 Extreme sensitivity of superconductivity to stoichiometry in $\text{Fe}_{1+\delta}\text{Se}$ *Phys. Rev. B* **79** 014522
- Medvedev S *et al* 2009 Electronic and magnetic phase diagram of $\beta\text{-Fe}_{1.01}\text{Se}$ with superconductivity at 36.7 K under pressure *Nat. Mater.* **8** 630–3
- Meingast C, Hardy F, Heid R, Adelmann P, Böhmer A, Burger P, Ernst D, Fromknecht R, Schweiss P and Wolf T 2012 Thermal expansion and Grüneisen parameters of $\text{Ba}(\text{Fe}_{1-x}\text{Co}_x)_2\text{As}_2$: a thermodynamic quest for quantum criticality *Phys. Rev. Lett.* **108** 177004
- Mele P 2012 Superconducting properties of iron chalcogenide thin films *Sci. Technol. Adv. Mater.* **13** 054301
- Mele P, Matsumoto K, Fujita K, Yoshida Y, Kiss T, Ichinose A and Mukaida M 2012 Fe–Te–Se epitaxial thin films with enhanced superconducting properties *Supercond. Sci. Technol.* **25** 084021

- Mewis A 1980 Ternary phosphides with the ThCr₂Si₂ structure *Z. Naturforsch. B* **35** 141
- Miura M, Adachi S, Shimode T, Wada K, Takemori A, Chikumoto N, Nakao K and Tanabe K 2013a Anisotropy and superconducting properties of BaFe₂(As_{1-x}P_x)₂ films with various phosphorus contents *Appl. Phys. Express* **6** 093101
- Miura M, Maiorov B, Kato T, Shimode T, Wada K, Adachi S and Tanabe K 2013b Strongly enhanced flux pinning in one-step deposition of BaFe₂(As_{0.66}P_{0.33})₂ superconductor films with uniformly dispersed BaZrO₃ nanoparticles *Nat. Commun.* **4** 2499
- Miyake K, Matsuura T, Sano T and Nagaoka Y 1988 Copper-oxide superconductors as mixed-valence heavy fermions: spin-fluctuation mechanism of superconductivity *J. Phys. Soc. Jpn.* **57** 722
- Miyata Y, Nakayama K, Sugawara K, Sato T and Takahashi T 2015 High-temperature superconductivity in potassium-coated multilayer FeSe thin films *Nat. Mater.* **14** 775
- Mizuguchi Y, Tomioka F, Tsuda S, Yamaguchi I, T and Takano Y 2008 Superconductivity at 27K in tetragonal FeSe under high pressure *Appl. Phys. Lett.* **93** 152505
- Mizuguchi Y, Hara Y, Deguchi K, Tsuda S, Yamaguchi T, Takeda K, Kotegawa H, Tou H and Takano Y 2010 Anion height dependence of T_c for the Fe-based superconductor *Supercond. Sci. Technol.* **23** 054013
- Mizuguchi Y and Takano Y 2010 Review of Fe chalcogenides as the simplest Fe-based superconductor *J. Phys. Soc. Jpn.* **79** 102001
- Mohan S, Taen T, Yagyuda H, Nakajima Y, Tamegai T, Katase T, Hiramatsu H and Hosono H 2010 Transport and magnetic properties of Co-doped BaFe₂As₂ epitaxial thin films grown on MgO substrate *Supercond. Sci. Technol.* **23** 105016
- Mohan S, Taen T, Yagyuda H, Nakajima Y, Tamegai T, Katase T, Hiramatsu H and Hosono H 2011 Characterization of epitaxial Co-doped BaFe₂As₂ thin films *Physica C* **471** 1181–4
- Molatta S, Haindl S, Trommler S, Schulze M, Wurmehl S and Hühne R 2015 Interface control by homoepitaxial growth in pulsed laser deposited iron chalcogenide thin films *Sci. Rep.* **5** 16334
- Moll P J W, Puzniak R, Balakirev F, Rogacki K, Karpinski J, Zhigadlo N D and Batlogg B 2010 High magnetic-field scales and critical currents in SmFeAs(O,F) crystals *Nat. Mater.* **9** 628–33
- Moll P J W, Balicas L, Geshkenbein V, Blatter G, Karpinski J, Zhigadlo N D and Batlogg B 2013 Transition from slow Abrikosov to fast moving Josephson vortices in iron pnictide superconductors *Nat. Mater.* **12** 134–8
- Müller-Buschbaum H M and Wollschläger M W 1975 Über ternäre oxocuprate. VII. zur Kristallstruktur von Nd₂CuO₄ *Z. Anorg. Allg. Chem.* **414** 76
- Nabeshima F, Imai Y, Hanawa M, Tsukada I and Maeda A 2013 Enhancement of the superconducting transition temperature in FeSe epitaxial thin films by anisotropic compression *Appl. Phys. Lett.* **103** 172602
- Naito M, Sato H and Yamamoto H 1997 MBE growth of (La,Sr)₂CuO₄ and (Nd,Ce)₂CuO₄ thin films *Physica C* **293** 36–43
- Naito M, Yamamoto H and Sato H 2000 Intrinsic problem of cuprate surface and interface: why good tunnel junctions are difficult to fabricate *Physica C* **335** 201–6
- Naito M, Krockenberger Y, Ikeda A and Yamamoto H 2016 Reassessment of the electronic state, magnetism, and superconductivity in high- T_c cuprates with the Nd₂CuO₄ structure *Physica C* **523** 28–54
- Nakajima M, Uchida S, Kihou K, Lee C H, Iyo A and Eisaki H 2012 Growth of BaFe₂(As_{1-x}P_x)₂ single crystals ($0 \leq x \leq 1$) by Ba₂As₃/Ba₂P₃-flux method *J. Phys. Soc. Jpn.* **81** 104710
- Nandi S *et al* 2010 Anomalous suppression of the orthorhombic lattice distortion in superconducting Ba(Fe_{1-x}Co_x)₂As₂ single crystals *Phys. Rev. Lett.* **104** 057006
- Ni N, Nandi S, Kreyssig A, Goldman A I, Mun E D, Bud'ko S L and Canfield P C 2008 First-order structural phase transition in CaFe₂As₂ *Phys. Rev. B* **78** 014523
- Ning F L, Fu M, Torchetti D A, Imai T, Sefat A S, Cheng P, Shen B and Wen H-H 2014 Critical behavior of the spin density wave transition in underdoped Ba(Fe_{1-x}Co_x)₂As₂ ($x \leq 0.05$): ⁷⁵As NMR investigation *Phys. Rev. B* **89** 214511
- Noji T, Hatakeyama T, Hosono S, Kawamata T, Kato M and Koike Y 2014 Synthesis and post-annealing effects of alkaline-methylethylenediamine-intercalated superconductors A_x(C₂H₈N₂)_yFe_{2-z}Se₂ ($A = Li, Na$) with $T_c = 45$ K *Physica C* **504** 8
- Okabe H, Takeshita N, Horigane K, Muranaka T and Akimitsu J 2010 Pressure-induced high- T_c superconducting phase in FeSe: correlation between anion height and T_c *Phys. Rev. B* **81** 205119
- Oyanagi H, Tsukada A, Naito M and Saini N L 2007 Local structure of superconducting (La,Sr)₂CuO₄ under strain: microscopic mechanism of strain-induced T_c variation *Phys. Rev. B* **78** 024511
- Oyanagi H, Tsukada A and Naito M 2012 XAS study of superconducting thin film single crystals without doping *Proc. SPIE* **8263** 82631F
- Ozaki T, Wu L, Zhang C, Jaroszynski J, Si W, Zhou J, Zhu Y and Li Q 2016 A route for a strong increase of critical current in nanostrained iron-based superconductors *Nat. Commun.* **7** 13036
- Paglione J and Greene R L 2010 High-temperature superconductivity in iron-based superconductors *Nat. Phys.* **6** 645
- Parrell J A, Field M B, Zhang Y and Hong S 2005 Nb₃Sn conductor development for fusion and particle accelerator applications *AIP Conf. Proc.* **711** 369
- Putzke C *et al* 2014 Anomalous critical fields in quantum critical superconductors *Nat. Commun.* **5** 5679
- Rehm L *et al* 2013 Infrared photo-response of Fe-shunted Ba-122 thin film microstructures *IEEE Trans. Appl. Supercond.* **23** 7300104
- Ren Z A *et al* 2008a Superconductivity in the iron-based F-doped layered quaternary compound Nd[O_{1-x}F_x]FeAs *Europhys. Lett.* **82** 57002
- Ren Z A *et al* 2008b Superconductivity at 55 K in iron-based F-doped layered quaternary compound Sm[O_{1-x}F_x]FeAs *Chin. Phys. Lett.* **25** 2215
- Ren Z A *et al* 2008c Superconductivity and phase diagram in iron-based arsenic-oxides ReFeAsO_{1-δ} (Re = rare-earth metal) without fluorine doping *Europhys. Lett.* **83** 17002
- Richter S *et al* 2017 Superconducting properties of Ba(Fe_{1-x}Ni_x)₂As₂ thin films in high magnetic fields *Appl. Phys. Lett.* **110** 022601
- Ronning F, Klimczuk T, Bauer E D, Volz H and Thompson J D 2008 Synthesis and properties of CaFe₂As₂ single crystals *J. Phys. Condens. Matter* **20** 322201
- Rotter M, Tegel M and Johrendt D 2008a Superconductivity at 38 K in the iron arsenide (Ba_{1-x}K_x)Fe₂As₂ *Phys. Rev. Lett.* **101** 107006
- Rotter M, Pangerl M, Tegel M and Johrendt D 2008b Superconductivity and crystal structures of (Ba_{1-x}K_x)Fe₂As₂ ($x=0-1$) *Angew. Chem. Int. Ed.* **47** 7949–52
- Rowell J M, Gurvitch M and Geerk J 1981 Modification of tunneling barriers on Nb by a few monolayers of Al *Phys. Rev. B* **24** 2278(R)
- Sadovskii M V 2016 High-temperature superconductivity in FeSe monolayers *Phys.-Usp.* **59** 947–67
- Saha S R, Butch N P, Drye T, Magill J, Ziemak S, Kirshenbaum K, Zavalij P Y, Lynn J W and Paglione J 2012 Structural collapse and superconductivity in rare-earth-doped CaFe₂As₂ *Phys. Rev. B* **85** 024525

- Sakagami A, Kawaguchi T, Tabuchi M, Ujihara T, Takeda Y and Ikuta H 2013 Critical current density and grain boundary property of BaFe₂(As,P)₂ thin films *Physica C* **494** 181–4
- Sakoda M, Ishii A, Takinaka K and Naito M 2017 Molecular beam epitaxy growth of SmFeAs(O,F) films with $T_c = 55$ K using the new fluorine source FeF₃ *J. Appl. Phys.* **122** 015306
- Sarnelli E, Adamo M, Nappi C, Braccini V, Kawale S, Bellingeri E and Ferdeghini C 2014 Properties of high-angle Fe(Se,Te) bicrystal grain boundary junctions *Appl. Phys. Lett.* **104** 162601
- Sarnelli E, Nappi C, Camerlingo C, Enrico E, Bellingeri E, Kawale S, Braccini V, Leveratto A and Ferdeghini C 2017 Properties of Fe(Se,Te) bicrystal grain boundary junctions, SQUIDs, and nanostrips *IEEE Trans. Appl. Supercond.* **27** 7400104
- Sasmal K, Lv B, Lorenz B, Guloy A M, Chen F, Xue Y Y and Chu C W 2008 Superconducting Fe-based compounds (A_{1-x}Sr_x)Fe₂As₂ with A = K and Cs with transition temperatures up to 37 K *Phys. Rev. Lett.* **101** 107007
- Sato H and Naito M 1997 Increase in the superconducting transition temperature by anisotropic strain effect in (001) La_{1.85}Sr_{0.15}CuO₄ thin films on LaSrAlO₄ substrates *Physica C* **274** 221–6
- Sato H, Hiramatsu H, Kamiya T and Hosono H 2014 High critical-current density with less anisotropy in BaFe₂(As, P)₂ epitaxial thin films: Effect of intentionally grown *c*-axis vortex-pinning centers *Appl. Phys. Lett.* **104** 182603
- Sato H, Hiramatsu H, Kamiya T and Hosono H 2016 Enhanced critical-current in P-doped BaFe₂As₂ thin films on metal substrates arising from poorly aligned grain boundaries *Sci. Rep.* **6** 36828
- Sefat A S 2011 Pressure effects on two superconducting iron-based families *Rep. Prog. Phys.* **74** 124502
- Seidel P 2011 Josephson effects in iron based superconductors *Supercond. Sci. Technol.* **24** 043001
- Seo S *et al* 2017 Origin of the emergence of higher T_c than bulk in iron chalcogenide thin films *Sci. Rep.* **7** 9994
- Shein I R and Ivanovskii A L 2009 Chemical bonding in LaFeAsO, SrFe₂As₂, and LiFeAs: Basic phases of new 18–56 K superconductors *J. Struct. Chem.* **50** 552–5
- Shiozai J, Ito Y, Mitsuhashi T, Nojima T and Tsukazaki A 2016 Electric-field-induced superconductivity in electrochemically etched ultrathin FeSe films on SrTiO₃ and MgO *Nat. Phys.* **12** 42–6
- Si W, Lin Z-W, Jie Q, Yin W-G, Zhou J, Gu G, Johnson P D and Li Q 2009 Enhanced superconducting transition temperature in FeSe_{0.5}Te_{0.5} thin films *Appl. Phys. Lett.* **95** 052504
- Si W, Zhou J, Jie Q, Dimitrov I, Solovyov V, Johnson P D, Jaroszynski J, Matias V, Sheehan C and Li Q 2011 Iron-chalcogenide FeSe_{0.5}Te_{0.5} coated superconducting tapes for high field applications *Appl. Phys. Lett.* **98** 262509
- Si W, Han S J, Shi X, Ehrlich S N, Jaroszynski J, Goyal A and Li Q 2013 High current superconductivity in FeSe_{0.5}Te_{0.5}-coated conductors at 30 tesla *Nat. Commun.* **4** 1347
- Si W, Zhang C, Shi X, Ozaki T, Jaroszynski J and Li Q 2015 Grain boundary junctions of FeSe_{0.5}Te_{0.5} thin films on SrTiO₃ bicrystal substrates *Appl. Phys. Lett.* **106** 032602
- Siegrist T, Zahurak S M, Murphy D W and Roth R S 1988 The parent structure of the layered high-temperature superconductors *Nat.* **334** 231–2
- Siegrist T, Zandbergen H W, Cava R J, Krajewski J J and Peck W F Jr 1994 The crystal structure of superconducting LuNi₂B₂C and the related phase LuNiBC *Nat.* **367** 254–6
- Smith M G, Manthiram A, Zhou J, Goodenough J B and Markert J T 1991 Electron-doped superconductivity at 40 K in the infinite-layer compound Sr_{1-x}Nd_xCuO₂ *Nat.* **351** 549–51
- Singh D I and Du M-H 2008 Density functional study of LaFeAsO_{1-x}F_x: a low carrier density superconductor near itinerant magnetism *Phys. Rev. Lett.* **100** 237003
- Skinta J A, Lemberger T R, Greibe T and Naito M 2002a Evidence for a nodeless gap from the superfluid density of optimally doped Pr_{1.855}Ce_{0.145}CuO_{4-y} films *Phys. Rev. Lett.* **88** 207003
- Skinta J A, Kim M-S, Lemberger T R, Greibe T and Naito M 2002b Evidence for a transition in the pairing symmetry of the electron-doped cuprates La_{2-x}Ce_xCuO_{4-y} and Pr_{2-x}Ce_xCuO_{4-y} *Phys. Rev. Lett.* **88** 207005
- Song C-L *et al* 2011 Direct observation of nodes and twofold symmetry in FeSe superconductor *Science* **332** 1410–3
- Sugawara H, Tsuneki T, Watanabe D, Yamamoto A, Sakoda M and Naito M 2014 One-step growth of SmFeAs(O,F) films by molecular beam epitaxy using FeF₂ as a fluorine source *Supercond. Sci. Technol.* **28** 015005
- Takano S, Ueda S, Takeda S, Sugawara H and Naito M 2012 Substrate effect on structure and superconductivity in SmFeAs (O,F) epitaxial films *Physica C* **475** 10–3
- Takeda S, Ueda S, Yamagishi T, Agatsuma S, Takano S, Mitsuda A and Naito M 2010 Molecular beam epitaxy growth of superconducting Sr_{1-x}K_xFe₂As₂ and Ba_{1-x}K_xFe₂As₂ *Appl. Phys. Express* **3** 093101
- Takeda S, Ueda S, Takano S, Yamamoto A and Naito M 2012 Growth of superconducting SmFeAs(O, F) epitaxial films by F diffusion *Supercond. Sci. Technol.* **25** 035007
- Takemura Y, Suto H, Honda N and Kakuno K 1997 Characterization of FeSe thin films prepared on GaAs substrate by selenization technique *J. Appl. Phys.* **81** 5177
- Tan S *et al* 2013 Interface-induced superconductivity and strain-dependent spin density waves in FeSe/SrTiO₃ thin films *Nat. Mater.* **12** 634–40
- Tang C *et al* 2016 Interface-enhanced electron-phonon coupling and high-temperature superconductivity in potassium-coated ultrathin FeSe films on SrTiO₃ *Phys. Rev. B* **93** 020507(R)
- Tanabe K and Hosono H 2012 Frontiers of research on iron-based superconductors toward their application *Jpn. J. Appl. Phys.* **51** 010005
- Tapp J H, Tang Z, Lv B, Sasmal K, Lorenz B, Chu P C W and Guloy A M 2008 LiFeAs: An intrinsic FeAs-based superconductor with $T_c = 18$ K *Phys. Rev. B* **78** 060505(R)
- Tarantini C *et al* 2010 Strong vortex pinning in Co-doped BaFe₂As₂ single crystal thin films *Appl. Phys. Lett.* **96** 142510
- Tarantini C, Gurevich A, Jaroszynski J, Balakirev F, Bellingeri E, Palleggi I, Ferdeghini C, Shen B, Wen H H and Larbalestier D C 2011 Significant enhancement of upper critical fields by doping and strain in iron-based superconductors *Phys. Rev. B* **84** 184522
- Tarantini C, Lee S, Kametani F, Jiang J, Weiss J D, Jaroszynski J, Folkman C M, Hellstrom E E, Eom C B and Larbalestier D C 2012 Artificial and self-assembled vortex-pinning centers in superconducting Ba(Fe_{1-x}Co_x)₂As₂ thin films as a route to obtaining very high critical-current densities *Phys. Rev. B* **86** 214504
- Tarantini C, Kametani F, Lee S, Jiang J, Weiss J D, Jaroszynski J, Hellstrom E E, Eom C B and Larbalestier D C 2014 Development of very high J_c in Ba(Fe_{1-x}Co_x)₂As₂ thin films grown on CaF₂ *Sci. Rep.* **4** 7305
- Tarantini C *et al* 2016 Intrinsic and extrinsic pinning in NdFeAs(O, F): vortex trapping and lock-in by the layered structure *Sci. Rep.* **6** 36047
- Thersleff T *et al* 2010 Coherent interfacial bonding on the FeAs tetrahedron in Fe/Ba(Fe_{1-x}Co_x)₂As₂ bilayers *Appl. Phys. Lett.* **97** 022506
- Trommler S, Hühne R, Iida K, Pahlke P, Haindl S, Schultz L and Holzapfel B 2010 Reversible shift in the superconducting transition for La_{1.85}Sr_{0.15}CuO₄ and BaFe_{1.8}Co_{0.2}As₂ using piezoelectric substrates *New J. Phys.* **12** 103030
- Trommler S, Hänisch J, Iida K, Kurth F, Schultz L, Holzapfel B and Hühne R 2014 Investigation of the strain-sensitive

- superconducting transition of $\text{BaFe}_{1.8}\text{Co}_{0.2}\text{As}_2$ thin films utilizing piezoelectric substrates *J. Phys.: Conf. Ser.* **507** 012049
- Tsuei C C, Kirtley J R, Chi C C, Yu-Jahnes L S, Gupta A, Shaw T, Sun J Z and Ketchen M B 1994 Pairing symmetry and flux quantization in a tricrystal superconducting ring of $\text{YBa}_2\text{Cu}_3\text{O}_{7-\delta}$ *Phys. Rev. Lett.* **73** 593
- Tsuei C C and Kirtley J R 2000 Pairing symmetry in cuprate superconductors *Rev. Mod. Phys.* **72** 969
- Tsukada I *et al* 2011 Epitaxial growth of $\text{FeSe}_{0.5}\text{Te}_{0.5}$ thin films on CaF_2 substrates with high critical current density *Appl. Phys. Express* **4** 053101
- Ueda K and Naito M 2003 *In situ* growth of superconducting MgB_2 thin films by molecular-beam epitaxy *J. Appl. Phys.* **93** 2113–20
- Ueda K, Saito S, Semba K, Makimoto T and Naito M 2005 All- MgB_2 Josephson junctions *Appl. Phys. Lett.* **86** 172502
- Ueda S, Takeda S, Takano S, Yamamoto A and Naito M 2011a High- T_c and high- J_c SmFeAs(O,F) films on fluoride substrates grown by molecular beam epitaxy *Appl. Phys. Lett.* **99** 232505
- Ueda S, Yamagishi T, Takeda S, Agatsuma S, Takano S, Mitsuda A and Naito M 2011b MBE growth of Fe-based superconducting films *Physica C* **471** 1167–73
- Ueda S, Takeda S, Takano S and Naito M 2012a As-grown superconducting SmFeAs(O,F) thin films by molecular beam epitaxy *Appl. Phys. Express* **5** 053101
- Ueda S, Takeda S, Takano S, Mitsuda A and Naito M 2012b Molecular beam epitaxy growth of superconducting $\text{Ba}_{1-x}\text{K}_x\text{Fe}_2\text{As}_2$ and SmFeAs(O,F) films *Jpn. J. Appl. Phys.* **51** 010103
- Uemura H, Kawaguchi T, Ohno T, Tabuchi M, Ujihara T, Takeda Y and Ikuta H 2012 Substrate dependence of the superconducting properties of NdFeAs(O,F) thin films *Solid State Commun.* **152** 735–9
- Vildosola V, Pourovskii L, Arita R, Biermann S and Georges A 2008 Bandwidth and Fermi surface of iron oxypnictides: covalency and sensitivity to structural changes *Phys. Rev. B* **78** 064518
- Wang Q-Y *et al* 2012 Interface-induced high-temperature superconductivity in single unit-cell FeSe films on SrTiO_3 *Chin. Phys. Lett.* **29** 037402
- Wang W, Hammond R H, Fejer M M, Ahn C H and Beasley M R 1995 Diode-laser-based atomic absorption monitor using frequency-modulation spectroscopy for physical vapor deposition process control *Appl. Phys. Lett.* **67** 1375
- Wang W, Fejer M M, Hammond R H, Beasley M R and Ahn C H 1996 Atomic absorption monitor for deposition process control of aluminum at 394 nm using frequency-doubled diode laser *Appl. Phys. Lett.* **68** 729
- Wang W, Hammond R H, Fejer M M, Arnason S and Beasley M R 1997 Direct atomic flux measurement of electron-beam evaporated yttrium with a diode-laser-based atomic absorption monitor at 668 nm *Appl. Phys. Lett.* **71** 31
- Wang W, Hammond R H, Fejer M M and Beasley M R 1999 Atomic flux measurement by diode-laser-based atomic absorption spectroscopy *J. Vac. Sci. Technol. A* **17** 2676
- Watanabe T, Yanagi H, Kamiya T, Kamihara Y, Hiramatsu H, Hirano M and Hosono H 2007 Nickel-based oxyphosphide superconductor with a layered crystal structure, LaNiOP *Inorg. Chem.* **46** 7719–21
- Watanabe T, Yanagi H, Kamihara Y, Kamiya T, Hirano M and Hosono H 2008 Nickel-based layered superconductor, LaNiOAs *J. Solid State Chem.* **181** 2117–20
- Wu M K *et al* 2009 The development of the superconducting PbO -type $\beta\text{-FeSe}$ and related compounds *Physica C* **469** 340–9
- Yamagishi T, Ueda S, Takeda S, Takano S, Mitsuda A and Naito M 2011 A study of the doping dependence of T_c in $\text{Ba}_{1-x}\text{K}_x\text{Fe}_2\text{As}_2$ and $\text{Sr}_{1-x}\text{K}_x\text{Fe}_2\text{As}_2$ films grown by molecular beam epitaxy 2011 *Physica C* **471** 1177–80
- Yamamoto H, Naito M and Sato M 1997 Surface and interface study on MBE-grown $\text{Nd}_{1.85}\text{Ce}_{0.15}\text{CuO}_4$ thin films by photoemission spectroscopy and tunnel spectroscopy *Phys. Rev. B* **56** 2852
- Yamamoto H, Naito M, Tsukada A and Suzuki S 2004a *In situ* angle-resolved photoemission study of MBE-grown $(\text{La}, \text{Ce})_2\text{CuO}_4$ thin films *Physica C* **412–414** 134–8
- Yamamoto H, Aoki K, Tsukada A and Naito M 2004b Growth of $\text{Ba}_{1-x}\text{K}_x\text{BiO}_3$ thin films by molecular beam epitaxy *Physica C* **412–414** 192–5
- Yamamoto H, Krockenberger Y and Naito M 2013 Multi-source MBE with high-precision rate control system as a synthesis method *sui generis* for multi-cation metal oxides *J. Cryst. Growth* **378** 184–8
- Yamazaki T, Takeshita N, Kobayashi R, Fukazawa H, Kohori Y, Kihou K, Lee C-H, Kito H, Iyo A and Eisaki H 2010 Appearance of pressure-induced superconductivity in BaFe_2As_2 under hydrostatic conditions and its extremely high sensitivity to uniaxial stress *Phys. Rev. B* **81** 224511
- Yang L X *et al* 2009 Electronic structure and unusual exchange splitting in the spin-density-wave state of the BaFe_2As_2 parent compound of iron-based superconductors *Phys. Rev. Lett.* **102** 107002
- Yeh K-W *et al* 2008 Tellurium substitution effect on superconductivity of the α -phase iron selenide *Europhys. Lett.* **84** 37002
- Yoon S *et al* 2017 Structural, electro-magnetic, and optical properties of $\text{Ba}(\text{Fe},\text{Ni})_2\text{As}_2$ single-crystal thin film *Supercond. Sci. Technol.* **30** 035001
- Yuan F *et al* 2015a Influence of substrate type on transport properties of superconducting $\text{FeSe}_{0.5}\text{Te}_{0.5}$ thin films *Supercond. Sci. Technol.* **28** 065005
- Yuan F *et al* 2017a The influence of the in-plane lattice constant on the superconducting transition temperature of $\text{FeSe}_{0.7}\text{Te}_{0.3}$ thin films *AIP Adv.* **7** 065015
- Yuan P, Xu Z, Zhang H, Wang D, Ma Y, Zhang M and Li J 2015b High performance $\text{FeSe}_{0.5}\text{Te}_{0.5}$ thin films grown at low temperature by pulsed laser deposition *Supercond. Sci. Technol.* **28** 065009
- Yuan P, Xu Z, Wang D, Zhang M, Li J and Ma Y 2017b Vortex pinning properties in Co-doped BaFe_2As_2 thin films with a high critical current density over 2 MA cm^{-2} at 9 T *Supercond. Sci. Technol.* **30** 025001
- Zhang W *et al* 2014 Interface charge doping effects on superconductivity of single-unit-cell FeSe films on SrTiO_3 substrates *Phys. Rev. B* **89** 060506(R)
- Zhang Y *et al* 2011a Self-assembled oxide nanopillars in epitaxial BaFe_2As_2 thin films for vortex pinning *Appl. Phys. Lett.* **98** 042509
- Zhang Y *et al* 2011b Nodeless superconducting gap in $\text{A}_x\text{Fe}_2\text{Se}_2$ ($\text{A} = \text{K}, \text{Cs}$) revealed by angle-resolved photoemission spectroscopy *Nat. Mater.* **10** 273–7
- Zhao J *et al* 2008 Structural and magnetic phase diagram of $\text{CeFeAsO}_{1-x}\text{F}_x$ and its relation to high-temperature superconductivity *Nat. Mater.* **7** 953–9
- Zhigadlo N D, Weyeneth S, Katrych S, Moll P J W, Rogacki K, Bosma S, Puzniak R, Karpinski J and Batlogg B 2012 High-pressure flux growth, structural, and superconducting properties of LnFeAsO ($\text{Ln} = \text{Pr}, \text{Nd}, \text{Sm}$) single crystals *Phys. Rev. B* **86** 214509
- Zimmer B I, Jeitschko W, Albering J H, Glaum R and Reehuis M 1995 The rare earth transition metal phosphide oxides LnFePO , LnRuPO and LnCoPO with ZrCuSiAs type structure *J. Alloys Comp.* **229** 238–42